INAUGURAL-DISSERTATION

zur Erlangung der Doktorwürde der

NATURWISSENSCHAFTLICH - MATHEMATISCHEN
GESAMTFAKULTÄT

der

RUPRECHT-KARLS-UNIVERSITÄT
HEIDELBERG

vorgelegt von
Diplom-Mathematiker

Felix Brinkmann

aus Geseke (NRW)

Tag der mündlichen Prüfung: _____

Mathematical models and numerical simulation of mechanochemical pattern formation in biological tissues

Gutachter: **Prof. Dr. Thomas Richter**

Abstract

Mechanical and chemical pattern formation in the development of biological tissue is a fundamental and fascinating process of self-complexation and self-organization. Yet, the understanding of the underlying mechanisms and their mathematical description still lacks in many interesting cases such as embryogenesis. In this thesis, we combine recent experimental and theoretical insights and numerically investigate the capacity of mechano-chemical processes to spontaneously generate patterns in biological tissue.

Firstly, we develop and numerically analyze a prototypical system of partial differential equations (PDEs) leading to mechanochemical pattern formation in evolving tissues. Based on recent experimental data, we propose a novel coupling by tensor invariants describing stretch, stress or strain of tissue mechanics on the production of signaling molecules (morphogens). In turn, morphogen leads to piecewise-defined active deformations of individual biological cells. The presented approach is flexible and applied to two prominent examples of evolving tissue: We show how these simple interaction rules ("feedback loops") lead to spontaneous, robust mechanochemical patterns in the applications to embryogenesis and to symmetry breaking in the sweet water polyp *Hydra*. Our results reveal that the full 3D model geometry is essential to obtain realistic results such as gastrulation events. Also, we highlight predictive numerical experiments that assess the sensitivity of biological tissue with regard to mechanical stimuli, namely to micropipette aspiration. These numerical experiments allow for a cross-validation with experimental observations. Besides, we apply our modeling approach to growing tips in colonial hydroids and investigate the role of rotational and shearing active deformations by a comparison to experimental data.

Secondly, we develop an efficient, numerical method to reliably solve these strongly coupled, prototypical systems of PDEs that model mechanochemical long-term problems. We employ state-of-the-art finite element methods, parallel geometric multigrid solvers and present a simple, local mesh refinement strategy to obtain an efficient solution approach. Parallel solvers are essential to deal with the huge problem size in 3D and were modified to keep track of biological cells. Further, we propose a stabilization of the structural equation to deal with the strongly coupled system of equations and the challenges of the different timescales of growth (days) and nonlinear elasticity (seconds). Also, this addresses the instabilities which result form the description of homogeneous Neumann values on the entire boundary that is necessary since the locations of patterns is *a priori* unknown.

Zusammenfassung

Mechanische und chemische Musterbildung ist ein fundamentaler und faszinierender Prozess der Selbstorganisation und Selbststrukturierung bei der Entwicklung von biologischem Gewebe. In vielen Organismen sind die dabei zugrundeliegenden Mechanismen allerdings noch immer unverstanden, beispielsweise in der Embryonalentwicklung. In dieser Doktorarbeit kombinieren

wir neuste experimentelle und theoretische Erkenntnisse und untersuchen numerisch wie mechanisch-chemische Prozesse spontan Muster in biologischem Gewebe erzeugen.

Zunächst entwickeln und analysieren wir Systeme partieller Differentialgleichungen (PDEs), welche mechanisch-chemische Muster in biologischem Gewebe beschreiben und erzeugen. Basierend auf neuesten Experimenten präsentieren wir dabei eine neuartige Kopplung mechanischer Tensorinvarianten, welche Verformungen, mechanische Spannungen oder Kompression beschreiben, auf die Produktion von Signalmolekülen (Morphogene). Im Gegenzug führen Konzentrationen von Morphogen zu diskreten, aktiven Deformationen einzelner biologischer Zellen. Unser Ansatz ist flexibel und wird exemplarisch auf sich entwickelnden Gewebes angewendet: Wir zeigen am Beispiel der Embryonalentwicklung im Stadium der Blastula sowie der Symmetriebrechung in dem Süßwasserpolüpen *Hydra*, wie diese einfachen Interaktionen spontan zur Bildung robuster mechanisch-chemische Muster führen. Insbesondere zeigen unsere Resultate, dass die gesamte 3D-Geometrie entscheidend für die Simulation biologische Vorgänge wie der Gastrulation sind. Interessant sind zudem unsere numerischen Experimente, in denen wir den Einfluss mechanischer Stimuli, beispielsweise von Mikropipetten, auf die Entwicklung des Gewebes untersuchen. Diese numerischen Experimente unterstreichen die entscheidende Bedeutung der Mechanik in der Entwicklung biologischen Gewebes und ermöglichen den direkten Vergleich mit biologischen Experimenten. Schließlich wenden wir unsere Modellsysteme auf Wachstum in Hydroiden an und untersuchen die Rolle rotierender und scherender aktiver Deformationen durch einen Vergleich mit experimentellen Ergebnissen.

Zweitens entwickeln wir effiziente, verlässliche numerische Methoden zur Lösung dieser stark gekoppelten mechanisch-chemischen Systeme von Differentialgleichungen. Wir verwenden moderne Finite-Elemente-Methoden mit einem parallelisierten, geometrischen Mehrgitterlöser. Zudem präsentieren wir eine einfache Strategie zur lokalen Gittersteuerung. Dabei sind parallelisierte Mehrgittermethoden zur effizienten Lösung der großen, gekoppelten Systeme in 3D unerlässlich. Schließlich schlagen wir eine Stabilisierung der Strukturgleichung vor, welche Instabilitäten durch das stark gekoppelte Gleichungssystem und der unterschiedlichen Zeitskalen von Wachstum (in Tagen) und nichtlinearem, elastischem Materialverhalten (in Sekunden) reduziert. Ebenso stabilisieren wir dabei unser Gleichungssystem gegenber Instabilitäten, welche durch das ausschließliche vorschreiben homogener Neumannwerte auf dem gesamten Rand entstehen. Diese müssen wir vorschrieben, da *a priori* der Ort der Musterbildung nicht bekannt ist.

Contents

1 Introduction

This thesis is devoted to the mathematical modeling and the numerical simulation of prototypical and strongly coupled systems of partial differential equations (PDEs) that describe mechanochemical pattern formation in biological tissue. Firstly, inspired by recent experimental findings, we propose a novel modeling approach based on simple mechanochemical interaction rules (mechanochemical coupling) which helps to unravel the complex processes involved in spontaneous and self organized pattern formation. Secondly, the numerical treatment of the resulting strongly coupled systems of PDEs including parallelization and stabilization techniques is a key aspect of this work.

Mechanochemical pattern formation is a fascinating feature of biological tissues. It describes the capacity of self-complexation respectively self-organization during tissue development, which leads to mechanical and chemical patterns. A prominent example is embryogenesis, where we will focus on the *gastrulation* event, during which a hollow sphere (*blastula*) of tissue cells reorganizes and folds inwards (gastrula). This process breaks the symmetry of the embryo and is observed in all multicellular organisms from fruit flies to mammals. A second, important application is mechanochemical pattern formation in the symmetry breaking of the fresh-water polyp *Hydra*. In this process, the *Hydra* cells aggregate to a tissue sphere, which then spontaneously develops a head. Despite substantial progress in recent years, the underlying chemical and mechanical mechanisms involved in spontaneous pattern formation are still elusive in many interesting cases.

In this thesis, we present a novel mechanochemical modeling approach based on the coupling of mechanical cues expressed by tensor invariants on the dynamics of signaling molecules (*morphogens*). This approach might serve as a blueprint to understand mechanochemical pattern formation in many organisms and to develop new experimental methods in coherence with our simulations.

Objectives

The modeling and the numerical simulation of our prototypical system of PDEs and their application to mechanochemical pattern formation pose a number of typical challenges:

- Finding suitable couplings (feedback loops) between tissue mechanics and morphogen dynamics that robustly lead to spontaneous (*de novo*) pattern formation and the need of an efficient, monolithic numerical approach to solve the resulting strongly coupled systems of PDEs;

- Numerically resolving the full 3D tissue geometry requires efficient, parallel solvers;

- Pattern formation takes place on considerably different timescales, the timescale of growth (days) and the timescale of the elastic material response (seconds), which requires stable solvers and a sufficient resolution in time;
- The continuous model equations are preferably blended with an explicit, discontinuous description of active deformations for each biological cell, which results in a semi-discrete model;
- Our systems of PDEs might not be well-posed due to nonlinear elasticity and homogeneous Neumann values on the entire boundary (the latter has to be assumed since it is *a priori* not known where patterns will emerge). Both require the stabilization of the structural equation;
- And finally, our approach should be flexible since different mechanical cues such as strain, stress or stretch have been shown to influence morphogen dynamics. Also, we want to consider different active cell shape changes and cover a large variety of possible applications, particularly, growth pulsations in colonial hydroids, embryogenesis or symmetry breaking in *Hydra*.

Unfortunately, these challenges can be incompatible. For instance, the objectives of not resolving the elastic timescale and of stabilization by the time derivative oppose one another and have to be resolved.

Structure of the thesis

The main target of this work is the derivation and the efficient, reliable numerical simulation of novel prototypical systems of PDEs that model mechanochemical interactions in biological tissue. Namely, we focus on the mechanochemical self-organization during tissue development in embryogenesis and symmetry breaking in *Hydra*. Yet, the underlying molecular and cellular mechanisms are still elusive in many cases and the crucial role of mechanics is mostly neglected in hitherto existing models. Accordingly, the need for new modeling approaches was recently stressed [152].

Based on recent experimental findings, we propose a novel modeling approach and demonstrate how simple, mechanochemical interaction rules ("feedback loops") lead to *spontaneous* and *robust* pattern formation. These simple, positive feedback loops are based on a novel coupling of mechanics on morphogen dynamics where we use tensor invariants describing strain, stress or stretch to trigger the production of signaling molecules (morphogens). Vice versa, morphogens lead to piecewise-defined, active cell-shape changes of individual biological cells.

In this thesis, we develop an comprehensive framework that is designed as a blueprint to model tissue development. We apply our approach to embryogenesis and symmetry breaking in *Hydra* to gain valuable insights into developmental self-organization. Moreover, we develop an efficient, monolithic numerical solution approach to robustly solve the strongly coupled mechanochemical long-term problems. The parallelization of our solvers is essential to tackle the large problem size and a stabilization based on the time derivative in the structural equation is introduced to deal with the strong coupling, the different timescales and the sole prescription of Neumann boundary values.

Lastly, we highlight our predictive numerical experiments where we focus on the mechanical sensitivity of biological tissue with respect to micropipette aspiration. Here, we focus on tissue strain and subsequent head formation in *Hydra* aggregates. Notably, these mechanical manipulations allow for a cross-validation with experiments such as a qualitative comparison to experimental micropipette aspiration of *Hydra* aggregates by Heike Sander [133].

Chapter 2 is dedicated to the derivation of our prototypical system of PDEs modeling tissue development. In particular, we follow the idea of Rodriguez *et al.* [128] to multiplicatively decompose the deformation gradient into an active part and an elastic response, the latter ensuring continuity of the deformation. The active part prescribes active cell shape changes such as apical/basal constriction (wedging) of biological cells. In the decomposition, the key assumption is that all stresses are produced by the elastic material response. Incorporating growth, this is also reflected in the description of the material laws. The centerpiece of this chapter is the design of mechanochemical feedback loops where we blend morphogen-induced discrete, active deformations with a novel description of mechanical feedback on morphogen dynamics via tensor invariants describing strain, stress or stretch. Also, we will provide an overview of related approaches regarding tissue development and active deformations, where we elaborate on the key differences in the conception and the objectives in comparison to the goals of this thesis.

In Chapter 3, we present the temporal and spatial discretizations of our strongly coupled system of PDEs. In time, we employ θ-time-stepping methods for the reaction-diffusion equations modeling morphogen dynamics. In space, we examine discretizations by linear and bilinear finite elements (Q_1- and Q_2-FE), where we show quadratic and cubic convergence, respectively. In three dimensions, it is essential to employ Q_2-FE to profit from the cubic convergence of this approach for the available spacial discretizations. Further, in case of stress-based mechanical feedback, we propose a local, adaptive mesh refinement strategy to accurately resolve the discontinuous invariants of the Piola-Kirchhoff stress tensor, which is based on a discontinuous material response when piecewise-defined active deformations are considered.

Finally, we develop and analyze a stabilization of the structural equation based on the time derivative. This stabilization tackles the challenge of keeping the system of PDEs well-posed while solving mechanochemical long-term problems. In particular, we treat the instabilities introduced by prescribing homogeneous Neumann values only and by just resolving the elastic time scale to the smallest possible extent. A numerical analysis of the stabilization error reveals that the error is sufficiently small compared to the discretization errors.

In Chapter 4, we present efficient solution techniques and their parallelization to solve our strongly coupled system of PDEs. We consider a monolithic solution approach based on the state-of-the-art finite element (FE) library Gascoigne3D [9]. The system matrix to solve in each time step is strongly coupled and of considerable size, particularly in 3D. The system is linearized by Newton's method and solved by GMRES [132] iterations that are preconditioned by a geometric multigrid method [57]. To reduce the computational effort, a parallelized ILU factorization based on domain decomposition was used as a smoother in the multigrid method [78, 127]. In this chapter, we will demonstrate that this parallelization leads to a considerable

speedup of our computations. For instance, on an Intel(R) Xeon(R) CPU E5-2690 0 @ 2.90 GHz with 16 physical cores the computational time per time-step reduces from 49 seconds in a sequential solution approach to only 4 seconds on 15 CPU cores - an impressive speedup of factor twelve. Finally, we quantify the efficiency of the parallelization by plotting the speedup per number of CPU cores.

In Chapter 5, we apply our modeling framework to simulate growth pulsations in hydroid tips as well as mechanochemical long-term problems during embryogenesis and symmetry breaking in *Hydra*. In particular, we demonstrate that our system of prototypical equations is flexible and spontaneously leads to robust mechanochemical pattern formation.

In the first application, we focus on growth processes in the development of tips in colonial hydroids, where we reduce the model to the structural equation only. We investigate how active deformation tensors describing rotational and shearing movements of ectodermal cells lead to very different deformations in the growing hydroid tips. This application is particularly appealing since we compare our numerical results to experimental data on growth pulsations in the morphogenesis of colonial hydroids, which was kindly provided by Igor Kosevich [81].

Next, we apply our system to embryogenesis in the blastula stage and demonstrate how simple interaction rules based on strain-, stress- or stretch-mediated mechanical feedback lead to robust mechanochemical patterns. Here, the full 3D geometry of the tissue seems crucial to obtain a realistic mechanochemical behavior such as gastrulation events. In this application, we demonstrate the robustness of our approach with regard to the initial conditions, the model geometry, the system size as well as the parameters, most importantly the diffusion rates. Further, we develop an inner volume constrained that accounts for the fluid inside the biological tissue, stops invagination processes and hence ensures stationary solutions during gastrulation. Finally, an enhanced model is presented, which is more accurate on the cellular level due to integrated mechanical feedback and uniform morphogen production in each biological cell. This enhanced approach further underlines the accuracy of our models on the tissue level.

Finally, we simulate symmetry breaking in the development of the fresh-water polyp *Hydra*. Clearly, the highlight in this application are our predictive numerical experiments, where we explore the sensitivity of biological tissue with regard to mechanical stimuli, namely micropipette aspiration. Indeed, these numerical results might inspire cross-validations between numerical experiments and the field of developmental biology, particularly since recent experimental efforts to visualize and study tissue mechanics are promising [55, 101, 102, 159]. In this thesis, we qualitatively compare our numerical results to micropipette experiments as presented in Ref. [133].

In summary, the developed modeling approach is robust, sustainable and flexible, i.e. it is simple to prescribe different active deformations, to add further equations or to employ various mechanical tensor invariants (describing e.g. stress, stretch or strain) to influence morphogen dynamics. Thus, our approach might serve as a blueprint to simulate pattern formation in many applications and might help to unravel one of the biggest mysteries in biology: Self-organized pattern formation during tissue development.

State of developmental biology

Mechanochemical pattern formation is the fascinating process of self-organization and self-complexation in biological tissue. Yet, the understanding of the underlying mechanical and molecular mechanisms is still sparse and the need for new modeling approaches combining morphogen dynamics and tissue mechanics has been recently stressed [152].

In the last decades, pure chemical theories and modeling approaches have been dominating the scientific discussion, mostly due to the lack of mechanical tissue modification tools, molecule markers for mechanical cues as well as the huge computational effort to consider mechanics on the full 3D tissue geometry. Although many recent studies stress the active involvement of mechanics in tissue morphogenesis [13, 24, 35, 105, 117], mechanochemical modeling is still in its infancy [20, 103] .

First steps into implementing growth and remodeling in biological tissue were taken by Rodriguez *et al.* [128], who introduced the idea of multiplicatively decomposing the deformation gradient into an active, prescribed part and an elastic response to examine ventricular hypertrophy (pathological growth of the heart muscle). This idea was successfully adapted by Lubarda and Hoger [92] and Himpel *et al.* [63], who present a constitutive theory of stress-modulated growth. All these works have yet in common that they consider growth as a mere consequence of mechanical or chemical pre-patterns, i.e. active deformations depending on time or local morphogen gradients are prescribed in parts of the domain only to predetermine regions of pattern formation. One exception is the recent work by Mercker *et al.* [104, 105] who describe the tissue as an infinitely thin deforming surface and propose simple feedback loops between morphogen dynamics and tissue curvature. In this thesis, we use the deformation gradient decomposition to prescribe piecewise-defined apical/basal constriction (wedging) or apico-basal shortening (thinning) of individual, biological cells, similar to Conte *et al.* [29] and Muñoz [106]. Further, we define shearing and rotating active deformations in our application to growth processes in tips of colonial hydroids. Also, we will rather focus on a novel mechanical feedback via tensor invariants describing strain, stress or compression, which, in combination with the full 3D tissue geometry, are crucial to obtain spontaneous pattern formation leading to gastrulation or symmetry breaking.

Classical, purely chemical approaches dominated the scientific discussions during the last decades. Turing patterns are particularly fascinating since they can lead to self-organized pattern formation for merely two or three chemical species. Also, they easily scale with the system size and simulating Turing patterns demands only little computational effort. Hence, it is no wonder that Turing patterns are a favorite explanation of many morphogenic phenomena. Yet, Turing patterns usually suffer from severe drawbacks. In particular, they are not robust, i.e. they are only stable over narrow parameter ranges, which raises the question how these mechanisms could ever be discovered by evolution [136]. Further, inhibitor molecules involved often demand diffusion rates beyond the limit of measured rates [68] and the underlying complexity in morphgenic processes complicates the identification of activator/inhibitor molecule pairs that are still elusive in many interesting cases [64, 80, 136]. A full historic overview of alternative modeling approaches is given in Chapter 5.

In Brinkmann *et al.* [20], we have published our coupled system of PDES applied to embryogenesis. In particular, we demonstrated that simple, positive feedback loops based on the novel coupling of mechanical stretch on the morphogen production lead to spontaneous mechanochemical pattern formation such as gastrulation if the full 3D tissue geometry is considered. First results on 2D cross-sections were published in Mercker et al [103]. In this thesis, our research is extended by a comprehensive convergence and a stabilization analysis, an investigation of speedup and efficiency of the parallel solvers as well as an adaptive, local mesh refinement strategy. Further, the applications to symmetry breaking in *Hydra* based on active apico-basal shortening of biological cells and the application to growth pulsations in hydroid tips are exclusive to this thesis. Regarding embryogenesis, we further present a stress-mediated feedback loop and an enhanced modeling approach based on integrated mechanical feedback which is more accurate on the cellular level. Also, we have implemented an inner volume constraint that accounts for the fluid contained inside the tissue sphere and leads to stationary invaginations during gastrulation events. Finally, a novel highlight of this thesis are our predictive, numerical experiments on the impact of micropipette aspiration on biological tissue that we compare to experiments by Heike Sander [133].

Mathematical state of science

In literature, results on a theoretical analysis of our prototypical system of PDEs are sparse. Here, the structural equation is based on the simple Saint-Venant-Kirchhoff model for compressible, hyperelastic materials. Reducing this model to linear elasticity, Riesz representation theorem guarantees the existence and the uniqueness of a minimizer of a coercive and quadratic functional over a suitable Hilbert space. Yet, the "question of finding reasonable conditions under which the minimizers are (even weak) solutions of the associated boundary value problems stands as a major unresolved issue."(Ciarlet [27, p. 346]). In this thesis, matters are complicated as we introduce active deformations into the structural equations via the decomposition of the active deformation gradient. Further, in finite strain theory and on multiply-connected domains such as our spherical tissue shell, theoretical results on the properties of active deformation tensors are only known in specific cases [138]. From a mathematical point of view, it is amazing that a dynamic process of mechanochemical pattern formation modeled by feedback loops of strongly coupled equations robustly leads to stationary results. Then again, it is objectively difficult to perform a theoretical convergence and stability analysis and to hope for *a priori* convergence estimates.

In Chapter 3, we will provide a comprehensive, numerical convergence and stability analysis of our prototypical system, where quadratic and cubic convergence as well as a small stabilization error are observed for Q_1 and Q_2 finite elements, respectively. In the course of this dissertation, we have implemented new features in finite element (FE) library Gascoigne3D [9]. These features range from the implementation of the model and growth itself over template classes to dynamically switch between 2D and 3D scenarios, material IDs to keep track of biological cells through discretization and parallelization, discretization over spheres, cylinders and spheroids and, finally, over an adaptive mesh refinement strategy to the integration of the mechanical feedback over biological cells.

2 Continuum mechanics, active deformations and mechanochemical interaction

This chapter is split into three major parts: Firstly, we introduce our prototypical, structural equation to model continuum mechanics of hyperelastic solids such as biological tissue. Secondly, in Section 2.2, we develop how active deformations ("growth") are incorporated in our equations. Thereby, we follow the work of Rodriguez *et al.* [128] and use a multiplicative decomposition of the deformation gradient into a prescribed, active part that leads to active deformations of individual biological cells and an elastic response which ensures the continuity of the overall deformation. Lastly, in Section 2.3, we present the fully coupled, prototypical system of PDEs. In particular, we propose a novel coupling of tensor invariants describing stress, strain or stretch on the production of signaling molecules (morphogens) that are described by reaction-diffusion equations. In turn, morphogen concentrations lead to active deformations of the biological cells via the decomposed deformation gradient. These couplings result in simple, mechanochemical interaction rules ("positive feedback loops"), which lead to robust, mechanochemical pattern formation in our simulations.

We already published our prototypical system of PDEs including the novel mechanochemical coupling and a presentation of the resulting positive feedback loops in Brinkmann *et al.* [20] and, restricted to two dimensions, in Mercker et al [103]. In Section 2.1, we replace the short derivations of the structural equation that were given in these publications by a variational approach that requires less regularity of our solution components and is more physical in our opinion. In Section 2.2, we now give a complete derivation of incorporating growth in our variational, structural equation. In this thesis, we enhance our framework for investigating mechanochemical pattern formation from Brinkmann *et al.* [20] by a more general description of our equations. In particular, we consider a wider range of applications such as symmetry breaking in *Hydra* aggregates, which includes new active deformations as well as stress- and strain-based mechanochemical feedback loops. The differences to our previous publications are highlighted in Section 2.3.

Throughout this chapter, we use the notation of the textbook on fluid structure interactions by Thomas Richter [126] and the textbook on nonlinear solid mechanics by Holzapfel [66] to the greatest possible extent.

2.1 Structural mechanics

In this section, we introduce the basics of displacement, strain and stress as well as the deformation gradient. In particular, we focus on the conservation principles of mass and momentum and present the nonlinear *Saint-Venant-Kirchhoff model* to model biological tissue. This section is structured as follows:

Firstly, we study kinematics, where we introduce displacement, deformation and strain. Strain measures deformation by comparing relative length changes during tissue motion. Secondly, we focus on the concept of stress to express internal forces within the material body. We introduce the important Cauchy stress tensor as well as the the first and second Piola-Kirchhoff stress tensors, which are common measures for stress in the Eulerian and the Lagrangian coordinate systems. Thirdly, we briefly discuss the conservation principles of mass and momentum, which are fundamental physical principles and assumed to be exact for all continuum bodies at all times. Yet, these conservation principles by themselves are not sufficient to predict the mechanical material response, which is finally given by constitutive laws: Hooke's law proposes a linear relation between stress and strain and is only a first-order, linear approximation to the response of elastic materials. Together, we derive the nonlinear *Saint-Venant-Kirchhoff model* for compressible, hyperelastic materials to describe biological tissue. Finally, this section is dedicated to introducing the concept of objectivity where we focus on the invariants of strain, stress and stretch tensor that are used in the description of the mechanical tissue response on morphogen dynamics.

Since there is a vast amount of literature on solid mechanics, we keep this section short and refer to textbooks such as Ciarlet [27], Holzapfel [66], Richter [126] or Truesdell [148] for more details.

2.1.1 Kinematics

In finite strain theory, structural dynamics are expressed in the *Lagrangian* or particle-centered coordinate system $\mathbf{X}$. The Lagrangian viewpoint follows material particles and their paths over time. These particles are connected in a solid, elastic material body $\Omega(t)$, which will return to the (initial) reference state Ω if all external forces are removed. This framework is opposed to the spatial-centered *Eulerian* framework where a fixed point $\mathbf{x}$ in space is observed. Hence, the Eulerian approach is the natural one for modeling fluids where particles moving through a fixed point are considered.

Let $\mathbf{X}$ be a particle in the undeformed, initial configuration $\Omega \subset \mathbb{R}^d$ with $d = 2, 3$. Also, let $\mathbf{x} = \mathbf{x}(\mathbf{X}, t)$ be its current position in the deformed configuration $\Omega(t) \subset \mathbb{R}^d$ at time t. Then, the *motion* of this particle in a continuum body at time $t \in I$ is called *deformation* and is defined by $\chi(t)\colon \Omega \to \Omega(t)$ with

$$\mathbf{x} = \chi(t)(\mathbf{X}) =: \chi(\mathbf{X}, t). \tag{2.1}$$

The deformation is assumed to be continuously differentiable in space and time and to be invertible for the purpose of the following definitions. Next, we define the *displacement* in the

Lagrangian description as the vector field $\mathbf{U}\colon \Omega \to \mathbb{R}^d$ joining the current position $\mathbf{x}(\mathbf{X}, t)$ with the reference (and in our case always initial) position $\mathbf{X}$ of a particle by

$$\mathbf{U}(\mathbf{X}, t) \coloneqq \mathbf{x}(\mathbf{X}, t) - \mathbf{X}.$$

In the current configuration, the displacement $\mathbf{u}\colon \Omega(t) \to \mathbb{R}^d$ is given by

$$\mathbf{u}(\mathbf{x}, t) \coloneqq \mathbf{x} - \mathbf{X}(\mathbf{x}, t).$$

This directly yields the relation

$$\mathbf{u}(\mathbf{x}, t) = \mathbf{U}(\chi^{-1}(\mathbf{x}, t), t) = \mathbf{U}(\mathbf{X}, t), \tag{2.2}$$

which allows us to state all results in terms of $\mathbf{u}$ in the following. The same holds for the Lagrangian velocity field $\mathbf{V}(\mathbf{X}, t)$ and its Eulerian counterpart $\mathbf{v}(\mathbf{x}, t)$. If the deformation $\chi(\mathbf{X}, t)$ and the vector-valued displacement field $\mathbf{u}(\mathbf{x}, t)$ are differentiable in time, it holds

$$\mathbf{V}(\mathbf{X}, t) \coloneqq \partial_t \chi(\mathbf{X}, t) = \partial_t \mathbf{u}(\mathbf{x}, t) = \mathbf{v}(\mathbf{x}, t). \tag{2.3}$$

Deformation gradient

The Jacobian matrix $\mathbf{F}$ of the deformation χ is called the *deformation gradient*. For a differentiable displacement field $\mathbf{u}\colon \Omega \to \mathbb{R}^d$, the deformation gradient and its determinant are defined as

$$\begin{aligned} \mathbf{F}(\mathbf{X}, t) &\coloneqq \nabla \chi(\mathbf{X}, t) = \nabla \mathbf{u}(\mathbf{x}, t) + \mathbf{I}, \\ J(\mathbf{X}, t) &\coloneqq \det(\mathbf{F}(\mathbf{X}, t)), \end{aligned}$$

with $\mathbf{I}$ being the identity matrix. The deformation gradient is an important measure of deformation. Its decomposition into a prescribed active part and an elastic response is key to our implementation of growth in Section 2.2.

Coordinate transformations

When dealing with material bodies, it is usually more convenient to express structural dynamics in the Lagrangian configuration. In contrast, the natural approach to state the conservation principles of mass and momentum is the Eulerian one. Thus, we need conversion rules which transform functions from the Eulerian to the Lagrangian setting. To begin with, let us consider a vector-valued, continuously differentiable function, for instance the velocity field $\mathbf{v}(\mathbf{x}, t)\colon \Omega(t) \to \mathbb{R}^d$. Using integration by substitution, integrals can be transformed from the Lagrangian to the Eulerian configuration by

$$\int_\Omega J\, \mathbf{V}(\mathbf{X}, t)\, \mathrm{d}\mathbf{X} = \int_\Omega |\det(\nabla \chi(\mathbf{X}))|\, \mathbf{v}(\chi(\mathbf{X}))\, \mathrm{d}\mathbf{X} = \int_{\Omega(t)} \mathbf{v}(\mathbf{x}, t)\, \mathrm{d}\mathbf{x}. \tag{2.4}$$

Further, the transformation of spatial derivatives is attained by employing the chain rule, which yields

$$\partial_{\mathbf{X},i} \mathbf{V}(\mathbf{X}, t) = \sum_j \partial_{\mathbf{x},j} \mathbf{v}(\chi(\mathbf{X}), t) \frac{\partial \chi(\mathbf{X}, t)}{\partial \mathbf{X}_i}.$$

Thus, the gradient transforms as

$$\nabla_{\mathbf{X}} \mathbf{V}(\mathbf{X}, t) = \mathbf{F}^T \nabla_{\mathbf{x}} \mathbf{v}(\boldsymbol{\chi}(\mathbf{X}, t)). \tag{2.5}$$

Next, the transformation of the divergence is given by

$$J \nabla_{\mathbf{x}} \cdot \mathbf{v}(\mathbf{x}, t) = \nabla_{\mathbf{X}} \cdot (J \mathbf{F}^{-1} \mathbf{V}(\mathbf{X}, t)). \tag{2.6}$$

For the (simple) proof of this transformation we refer to literature, e.g. see Richter [126]. Also, we require the transformation of the partial time derivative of a continuously differentiable, scalar function $c(\mathbf{x}, t)$. Using the transformation of gradients (2.5), it is easy to show that the partial time derivative of its Lagrangian counterpart $C(\mathbf{X}, t)$ is given by

$$\begin{aligned} \partial_t C(\mathbf{X}, t) &= \partial_t c(\boldsymbol{\chi}(\mathbf{X}), t) + (\mathbf{V}(\mathbf{X}, t) \cdot \nabla_{\mathbf{x}}) c(\boldsymbol{\chi}(\mathbf{X}), t) \\ &= \partial_t c(\mathbf{x}, t) + (\mathbf{v}(\mathbf{x}, t) \cdot \nabla_{\mathbf{x}}) c(\mathbf{x}, t), \end{aligned} \tag{2.7}$$

where we used the relation (2.3) for the velocity and the definition of the deformation to simplify the notation.

In general, we neglect the index of the gradient operator if the direction of the derivative is obvious from the context. Further, we often omit the deformation $\boldsymbol{\chi}$ for the sake of a simpler presentation. For instance, this simplifies the transformation of the gradient, which reads $\nabla \mathbf{V}(\mathbf{X}, t) = \mathbf{F}^T \nabla \mathbf{v}(\mathbf{x}, t)$ in short. For details on these derivations, we refer to literature, e.g., to the textbook on fluid structure interactions by Thomas Richter [126].

Strain tensors

Strain is a measure of deformation which characterizes the change of relative distances between particles under deformation. Various concepts of strain have been proposed in literature. Here, we briefly present the *right Cauchy-Green tensor* and the *Green-Lagrange strain tensor*, which are important in modeling the elastic tissue response.

We follow the presentation in Truesdell [148] (Chapter II) and use the fact that the deformation $\boldsymbol{\chi}$ and thus the deformation gradient $\mathbf{F}$ are invertible. Then, Cauchy's polar decomposition theorem yields a unique decompositions of $\mathbf{F}$, namely

$$\mathbf{F} = \mathbf{R}\mathbf{U} = \mathbf{V}\mathbf{R}, \tag{2.8}$$

into an orthogonal *rotation tensor* $\mathbf{R}$ and positive, symmetric *left and right stretch tensors* $\mathbf{U}$ and $\mathbf{V}$. For the rotation $\mathbf{R}$ it holds $\mathbf{R}\mathbf{R}^T = 1$ which implies $\det(\mathbf{U}) = \det(\mathbf{V}) = |\det(\mathbf{F})| = J$. Since $\mathbf{U}$ and $\mathbf{V}$ are symmetric, they have a corresponding basis of orthogonal eigenvectors (also referred to as "principal axes of strain") in the reference system $\mathbf{X}$ and the current one $\mathbf{x}$, respectively. The rotation $\mathbf{R}$ carries principle axes of strain in $\mathbf{X}$ to principle axes of strain in $\mathbf{x}$. Also, we conclude from the obvious relation $\mathbf{V} = \mathbf{R}\mathbf{U}\mathbf{R}^T$ that $\mathbf{U}$ and $\mathbf{V}$ have the same eigenvalues (or "principle stretches").

So let $\mathbf{e}_k$ be a vector that points along the k^{th} eigenvector in the reference configuration. Then, the corresponding eigenvalue λ_k is the ratio (or the *stretch*) of the length of the image $\mathbf{F}\mathbf{e}_k$ to the length of the original $\mathbf{e}_k$:

$$\lambda_k = \frac{\mathbf{F}\mathbf{e}_k}{\mathbf{e}_k}.$$

Since it is inconvenient to calculate $\mathbf{U}$, $\mathbf{V}$ and $\mathbf{R}$ from $\mathbf{F}$ and rotations do not induce strain, the *right Cauchy-Green tensor* is merely defined (rotation-independently) by

$$\mathbf{C} \coloneqq \mathbf{F}^T\mathbf{F} = \mathbf{U}^2, \tag{2.9}$$

with the determinant $\det(\mathbf{C}) = det(\mathbf{F})^2 = J^2$. Its eigenvalues are the squares λ_k^2 of the principle stretches, i.e., it measures the square of changes (stretches) due to the deformation.

Another important measure of strain is the *Green-Lagrange strain tensor*, which often simplifies the notation and is defined as

$$\mathbf{E} \coloneqq \frac{1}{2}(\mathbf{C} - \mathbf{I}) = \frac{1}{2}(\mathbf{F}^T\mathbf{F} - \mathbf{I}). \tag{2.10}$$

For further details on strain tensors we refer once again to literature, e.g. see Holzapfel [66] (Chapter 2), Richter [126] (Chapter 2) or Truesdell [148] (Chapter II).

2.1.2 Stress

In continuum mechanics, *stress* characterizes an internal infinitesimal force across an imaginary surface per unit area of that surface within a material body. It is a kinematic principle and does not depend on the material model under consideration. Stress is a consequence of interactions between particles due to deformations inside a material body. Hence, stress can be the result of external forces, the elastic material response due to active deformations, or it can be built into the system (the latter is not considered in this work). We want to introduce stress tensors related to the current and to the reference configuration.

So let the material body $V(t) \subset \Omega(t)$ be a part of the current configuration $\Omega(t)$ at time t. Then, the applied force acting on $V(t)$ is assumed to be the sum of the volume- and surface-forces $K(V(t))$ and $K(\partial V(t))$ given by

$$\begin{aligned} K(V(t)) &= \int_{V(t)} \rho(\mathbf{x}, t)\mathbf{f}(\mathbf{x}, t)\,\mathrm{d}\mathbf{x}, \\ K(\partial V(t)) &= \int_{\partial V(t)} \mathbf{t}(\mathbf{x}, t, \mathbf{n})\,\mathrm{d}s = \int_{\partial V} \mathbf{T}(\mathbf{X}, t, \mathbf{N})\,\mathrm{d}S, \end{aligned} \tag{2.11}$$

with the prescribed external body-force density $\mathbf{f}(\mathbf{x}, t)$ acting within the volume of the biological tissue. Moreover, $\mathbf{t}(\mathbf{x}, t, \mathbf{n})$ is the *surface stress density* (or *Cauchy traction field*) in direction $\mathbf{n}$ of the current configuration $\Omega(t)$ and $\mathbf{T}(\mathbf{X}, t, \mathbf{N})$ is the *surface stress density* (or *first Piola-Kirchhoff traction field*) in direction $\mathbf{N}$ of the reference configuration Ω.

We employ *Cauchy's stress theorem* which states that there exist unique second order tensor fields $\boldsymbol{\sigma}(\mathbf{x}, t)$ and $\mathbf{P}(\mathbf{X}, t)$ such that

$$\mathbf{t}(\mathbf{x}, t, \mathbf{n}) = \boldsymbol{\sigma}(\mathbf{x}, t)\mathbf{n}, \quad \mathbf{T}(\mathbf{X}, t, \mathbf{N}) = \mathbf{P}(\mathbf{X}, t)\mathbf{N}. \tag{2.12}$$

The symmetric, spatial tensor field $\boldsymbol{\sigma}(\mathbf{x}, t)$ is called the *Cauchy stress tensor* and describes the stress in the current configuration. In particular, it is defined in a way that $\boldsymbol{\sigma}\mathbf{n}$ is the force in

the current configuration per unit area with normal direction $\mathbf{n}$, the latter also with regard to the current configuration. Next, $\mathbf{P}(\mathbf{X}, t)$ is called the *first Piola-Kirchhoff stress tensor* and is defined such that $\mathbf{PN}$ is the force in the current framework per unit area with normal direction $\mathbf{N}$ in the reference configuration. Finally, we introduce $\mathbf{\Sigma}(\mathbf{X}) = \mathbf{F}^{-1}(\mathbf{x}, t)\mathbf{P}(\mathbf{X}, t)$ which is the transformation of $\mathbf{P}$ to the reference configuration. It is called *second Piola-Kirchhoff stress tensor* and expresses the stress solely in the reference configuration. These stress tensors are related by the transformations

$$\mathbf{P} = J\boldsymbol{\sigma}\mathbf{F}^{-T}, \quad \mathbf{F\Sigma} = \mathbf{P}, \tag{2.13}$$

which emerges once we transform our conservation equations to the reference configuration, see Eq. (2.18) and Eq. (2.19). For further details on the concept of stress and the different stress tensors we refer to literature, namely to Holzapfel [66] (Chapter 3), Richter [126] (Chapter 2) or Truesdell [148] (Chapter III).

2.1.3 Conservation of mass and momentum

The shape of structural equations is determined by the two principles of *conservation of mass and momentum*. Conservation of mass states that mass is preserved that is mass is neither destroyed nor created. Conservation of mass reads

$$d_t \int_{\Omega(t)} \rho(\mathbf{x}, t)\, \mathrm{d}\mathbf{x} = d_t \int_{\Omega} J\rho^0(\mathbf{X})\, \mathrm{d}\mathbf{X} = 0, \tag{2.14}$$

for current and initial mass distributions $\rho(\mathbf{x}, t)$ and $\rho^0(\mathbf{X}) \coloneqq \rho(\mathbf{x}, 0)$. Conservation of momentum says that the change in momentum is equivalent to the sum of body and surface forces. In the Eulerian framework, Conservation of momentum (or *Cauchy's first equation of motion*) reads

$$\begin{aligned} d_t \int_{\Omega(t)} \rho(\mathbf{x}, t)\mathbf{v}(\mathbf{x}, t)\, \mathrm{d}\mathbf{x} &= K(V(t)) + K(\partial V(t)) \\ &= \int_{\Omega(t)} \rho(\mathbf{x}, t)\mathbf{f}(\mathbf{x}, t)\, \mathrm{d}\mathbf{x} + \int_{\partial V(t)} \boldsymbol{\sigma}(\mathbf{x}, t)\mathbf{n}\, \mathrm{d}\mathbf{x}, \end{aligned} \tag{2.15}$$

with external volume force $\mathbf{f}(\mathbf{x}, t)$ and surface forces $\boldsymbol{\sigma}(\mathbf{x}, t)\mathbf{n}$, which were expressed by the stress tensor $\boldsymbol{\sigma}$ using Cauchy's stress theorem, see Eq. (2.11) and Eq. (2.12). We have assumed that all these functions are in $L^2(\Omega(t))$ which denotes the Lebesgue space of measurable square integrable functions on $\Omega(t)$. Additionally, we have assumes that $\rho(\mathbf{x}, t)$ and $\mathbf{v}(\mathbf{x}, t)$ are additionally differentiable in time.

In continuum mechanics it is usually more convenient to express the structural equations in the reference configuration $\Omega \subset \mathbb{R}^d$. We use a variational formulation of the conservation equations, which leads to a simpler and more elegant transformation to the Lagrangian setting. From a physical point of view, a variational approach is more natural, since the classical elasticity theory stems from energy minimization, which leads to variational equations. Besides, real world problems usually posses solutions of limited regularity. In a variational approach, this is reflected by the concept of weak solutions that require less regularity of the model geometry or the data. Details on the variational formulation are provided in Chapter 3.

To state the variational formulation, we have to specify suitable function spaces: We choose the velocity $\mathbf{v}$ and a test function $\boldsymbol{\varphi}$ as

$$\mathbf{v}, \boldsymbol{\varphi} \in V^d_{\Omega(t)} := H^1(\Omega(t))^d, \tag{2.16}$$

where $H^1(\Omega(t))$ is the Sobolev space of functions with first, generalized derivatives in $L^2(\Omega(t))$. We consider an approach that is weak (variational) in space and strong in time, i.e. our equation holds pointwise in time. Hence, we further assume that the velocity is differentiable in time and that

$$\partial \mathbf{v} \in H^{-1}(\Omega(t))^d \quad \forall t \in [0, T],$$

where $H^{-1}(\Omega(t))$ denotes the dual space of $H^1(\Omega(t))$. That way, a simple discretization by finite differences in time, e.g. by the implicit Euler method, is possible. In the following, we skip the $\Omega(t)$-indices if the examined computational domain is obvious from the context. Details on the function spaces introduced above are given in Chapter 3 or in literature, e.g. see Alt [2], Braess [14], Brenner & Scott [18] or Wloka [154].

Firstly, we apply Reynolds transport theorem to the first integral in the conservation of momentum equation to derive under the integral sign, namely, for a differentiable, scalar function f it holds $d_t \int_{\Omega(t)} f \, \mathrm{d}\mathbf{x} = \int_{\Omega(t)} \partial_t f + \nabla \cdot (f\mathbf{v}) \, \mathrm{d}\mathbf{x}$. The proof of this theorem is based on transforming both integrals to the reference configuration (cf. Eq. (2.4)), where the integration is independent of time, and elementary reformulations, e.g. by the product rule, are used. We refer to Holzapfel [66] for a complete proof. Secondly, we use Gauss's theorem to transform the boundary integral which describes the surface forces.

Then, we obtain the equation for conservation of momentum in non-conservative, variational formulation, which reads

$$\begin{aligned} &\int_{\Omega(t)} \rho(\mathbf{x}, t)\partial_t \mathbf{v}(\mathbf{x}, t)\boldsymbol{\varphi} + \rho(\mathbf{x}, t)(\mathbf{v}(\mathbf{x}, t) \cdot \nabla)\mathbf{v}(\mathbf{x}, t)\boldsymbol{\varphi} \, \mathrm{d}\mathbf{x} + \int_{\Omega(t)} \boldsymbol{\sigma}(\mathbf{x}, t)\nabla\boldsymbol{\varphi} \, \mathrm{d}\mathbf{x} \\ &= \int_{\Omega(t)} \rho(\mathbf{x}, t)\mathbf{f}(\mathbf{x}, t)\boldsymbol{\varphi} \, \mathrm{d}\mathbf{x}, \end{aligned} \tag{2.17}$$

for all test functions $\boldsymbol{\varphi}(\mathbf{x}) \in V^d$. We point out that this is a variational approach in space that is strong in time since we did not integrate over time using time-dependent test functions. When discretizing in space, we therefore obtain an ODE in time which is discretized by simple finite difference methods, such as the implicit Euler scheme or multi-step methods. We prefer this ansatz for the sake of a simple presentation over a fully variational approach, which implies an additional integration in time with velocity and test functions given in *Bochner spaces*. A fully variational approach based on a discontinuous Galerkin method ($dG(0)$) is then equivalent to the approach presented above. Details on the variational formulation are presented in Chapter 3.

Next, we transform Eq. (2.17) from the Eulerian to the Lagrangian configuration, which is essential to include active deformations into our equation (cf. Subsection 2.2.3). We thus carry along the arguments of all functions for a better perception of these two configurations. Firstly, we apply the transformation of the time derivative (2.7) to the first integral, secondly,

the transformation of the gradient (2.5) is applied to the test function in the second integral and thirdly, all integrals are transformed using the relation (2.4). Then, conservation of momentum in the reference configuration reads in variational form

$$\begin{aligned}&\int_\Omega J(\mathbf{X},t)\rho(\boldsymbol{\chi}(\mathbf{X}),t)\partial_t \mathbf{V}(\mathbf{X},t)\boldsymbol{\Phi}\,\mathrm{d}\mathbf{X} + \int_\Omega J(\mathbf{X},t)\boldsymbol{\sigma}(\boldsymbol{\chi}(\mathbf{X}),t)\mathbf{F}^{-T}(\boldsymbol{\chi}(\mathbf{X}),t)\nabla\boldsymbol{\Phi}\,\mathrm{d}\mathbf{X}\\ &= \int_\Omega J(\mathbf{X},t)\rho(\boldsymbol{\chi}(\mathbf{X}),t)\mathbf{f}(\boldsymbol{\chi}(\mathbf{X}),t)\boldsymbol{\Phi},\mathrm{d}\mathbf{X},\end{aligned} \tag{2.18}$$

for all test functions $\boldsymbol{\Phi}(\mathbf{X}) \coloneqq \boldsymbol{\varphi}(\boldsymbol{\chi}(\mathbf{X})) \in V^d_\Omega$. Finally, we insert the balance equation for mass conservation (2.14), drop the arguments and use the relation $\boldsymbol{\Sigma} = J\mathbf{F}^{-1}\boldsymbol{\sigma}\mathbf{F}^{-T}$ with the symmetric, second Piola-Kirchhoff stress tensor to express the stress in the reference configuration. Then, conservation of momentum (or Cauchy's first equation of motion) reads in the reference domain

$$\int_\Omega \rho^0 \partial_{tt}\mathbf{u}\boldsymbol{\Phi}\,\mathrm{d}\mathbf{X} + \int_\Omega \mathbf{F}\boldsymbol{\Sigma}\nabla\boldsymbol{\Phi}\,\mathrm{d}\mathbf{X} = \int_\Omega \rho^0\mathbf{f}\boldsymbol{\Phi}\,\mathrm{d}\mathbf{X} \quad \forall\boldsymbol{\Phi}\in V^d. \tag{2.19}$$

Sufficient regularity provided, we can integrate the second integral by parts and employ the fundamental lemma of calculus of variations (cf. Gelfand *et al.*[44, p. 9] (Lemma 1)): Together, Eq. (2.19) is then almost everywhere equivalent to the conservation of momentum in strong formulation given by

$$\begin{aligned}\rho^0\partial_{tt}\mathbf{u} - \nabla\cdot(\mathbf{F}\boldsymbol{\Sigma}) &= \rho^0\mathbf{f} && \text{in } \Omega,\\ \mathbf{F}\boldsymbol{\Sigma}\mathbf{N} &= 0 && \text{on } \partial\Omega,\end{aligned} \tag{2.20}$$

assuming homogeneous Neumann values on the entire boundary $\partial\Omega$ for the moment and where the divergence is meant in a row-wise sense. Homogeneous Neumann values are indeed a reasonable choice and Dirichlet values cannot be prescribed, since it is *a priori* not known where patterns will emerge.

We emphasize that this equation was derived from the physical principles of conservation of mass and momentum only. Especially, they have to be valid for all materials at all times and involve no modeling. On the other hand, they do not distinguish between different materials. We still need a constitutive law which describes the observed physical behavior of biological tissue. Then, we finally obtain a model which is capable of approximating the real tissue response to active deformations or external forces.

2.1.4 Objectivity and tensor invariants

It is a fundamental physical principle that the material response should not depend on the choice of an observer. This property is usually called *material frame-indifference* or *objectivity of a material*, see Truesdell and Noll [149] (Sections 19, 19A). If the constitutive equation was not objective, the material response would change under rigid body motions such as rotations and translations, which is physically impossible.

In the following, we briefly introduce the concept of objectivity and give a short list of objective tensors, similar to the presentation in Holzapfel [66]. Based on these objective tensors, we formulate our objective constitutive material law (2.23) that we present in the next subsection.

Subsequently, we define the principal invariants of a tensor. These scalar invariants of an objective tensor are objective and be essential in describing the (objective) material response on the morphogen dynamics in our coupled system of prototypical equations.

So let O and O^+ be two different observers at $\mathbf{x}$ and $\mathbf{x}^+$ with assigned basis vectors (or reference frames) $\{\mathbf{e}_i\}$ and $\{\mathbf{e}_i^+\}$ such that $\mathbf{x} = x_i\mathbf{e}_i$ and $\mathbf{x}^+ = x_i^+\mathbf{e}_i^+$. If the relative rotation between the two observers is given by $\mathbf{Q}(t)$ with $\mathbf{Q}^T\mathbf{Q} = \mathbf{I}$ and $\det(\mathbf{Q}) = 1$, the distance between two material points is preserved and we find $\mathbf{e}_i^+ = \mathbf{Q}(t)\mathbf{e}_i$. With these preparations we obtain that a vector field $\mathbf{u}$ and a tensor $\mathbf{A}$ are objective if they transform under changes of observer according to the relations

$$\begin{aligned}\mathbf{A}^+(\mathbf{x}^+, t^+) &= \mathbf{Q}(t)\mathbf{A}(\mathbf{x}, t)\mathbf{Q}(t)^T,\\ \mathbf{u}^+(\mathbf{x}^+, t^+) &= \mathbf{Q}(t)\mathbf{u}(\mathbf{x}, t).\end{aligned} \tag{2.21}$$

For instance, we consider the deformation gradient at the points $\mathbf{x}$ and $\mathbf{x}^+$ and recall that the reference configuration is unaffected by a rigid body motion, i.e.

$$\mathbf{F}(\mathbf{X}, t) = \frac{\partial \mathbf{x}(\mathbf{X}, t)}{\partial \mathbf{X}}, \quad \mathbf{F}^+(\mathbf{X}, t) = \frac{\partial \mathbf{x}^+(\mathbf{X}, t)}{\partial \mathbf{X}}.$$

Then, differentiation yields

$$\mathbf{F}^+(\mathbf{X}, t) = \frac{\partial \mathbf{x}^+}{\partial \mathbf{X}} = \mathbf{Q}\frac{\partial \mathbf{x}}{\partial \mathbf{X}} = \mathbf{Q}\mathbf{F},$$

which shows that the deformation gradient transforms like a vector (cf. Eq. 2.21). Notably, the deformation gradient is still objective, since it is a two-point tensor with one argument in the reference configuration, which is intrinsically objective. Clearly, the second Piola-Kirchhoff stress tensor $\mathbf{\Sigma}$ is also objective, since it is parameterized by material coordinates only. Simple argumentation shows that the Cauchy stress tensor $\boldsymbol{\sigma}$ and the Green-Lagrange strain tensor $\mathbf{E}$ are objective as well. Since our equations are given in the reference configuration, stress-based mechanical feedback is expressed in terms of $\mathbf{\Sigma}$. For more details on the objectivity of these tensors, we refer to Holzapfel [66]. The objectivity requirement (Eq. (2.21)) restricts the possible shape of the material response: In the next subsection, our constitutive equation (2.23) is based on objective tensors only.

Tensor invariants Throughout this thesis, the mechanochemical coupling of our prototypical equations is essential to observe pattern formation. In particular, we use tensor invariants to express the material response (to active deformations) that triggers morphogen production. Here, we give a short overview of tensor invariants that we use as objective scalar measures of stress, strain and stretch.

A tensor $\mathbf{A}$ in d dimensions possesses d so-called principal scalar invariants I_i, $i = 1, \cdots, d$, where we only consider $d = 2, 3$ for the purposes of this thesis. Per definition, the first invariant of a tensor $\mathbf{A}$ is always the trace and the last invariant is always the determinant. In two and three dimensions, this gives the common invariants

$$I_1(\mathbf{A}) = \mathrm{tr}(\mathbf{A}) = \sum_i A_{ii}, \quad I_d(\mathbf{A}) = \det(\mathbf{A}) = \sum_{i,j,k} \epsilon_{ijk} A_{1i} A_{2,j} A_{3,k},$$

where ϵ_{ijk} denotes the Levi-Civita symbol. In three dimensions, the additional dimension gives a third invariant which takes the form:

$$\begin{aligned} I_2(\mathbf{A}) &= \frac{1}{2}(tr(\mathbf{A})^2 - tr(\mathbf{A}^2)) \\ &= A_{00}A_{11} + A_{11}A_{22} + A_{00}A_{22} - A_{01}A_{10} - A_{12}A_{21} - A_{02}A_{20} \end{aligned}$$

For further details on tensor invariants, we refer to literature, e.g. see Ciarlet [27] (Section 3.5) or Holzapfel [66] (Section 1.4). In summary, our mechanical feedback influencing the production of morphogen is objective under a change of observer, e.g. under a rotation of the coordinate system, if it merely depends on these scalar invariants. Since we dealt with the question of objectivity, we can now formulate our constitutive equations.

2.1.5 Material laws

Cauchy's first equation of motion (2.15) is based on physical balance principles and is valid for all materials in continuum mechanics. If we want to predict the material response of a particular material such as biological tissue, we need to specify a material law. Mathematically speaking, Eq. (2.20) is highly under-determined: In three dimensions, there are three unknown components of $\mathbf{u}$ and six unknowns in the symmetric Cauchy stress tensor $\boldsymbol{\sigma}$ but only the three dimensional equation. What we need is a material law which states the stress in terms of the deformation gradient $\mathbf{F}$.

Biological tissue is often assumed to be incompressible due to its high water content, although there is little experimental data supporting this assumption [48]. On the contrary, water can leave biological cells through pores and channels in the cell membranes, comparable to a sponge. Correspondingly, biological tissue is assumed to be compressible and elastic in many studies [1, 29, 48] and viscoelastic behavior of biological tissue is still a controversial topic [1]. In experiments, Farge [36] observes that deformed *Drosophila* embryos recover their initial shape after external forces are removed. The difficulty to model biological material further increases as material constants of biological tissue may depend "on its stress- and strain-history [which] makes direct measurements of compressibility technically challenging" (Labouesse [83, p. 226]). Besides, we observe that hardly any tissue volume (less than one percent in randomly tested calculations) is lost when the Saint-Venant-Kirchhoff model is employed.

Here, we focus our attention on compressible, elastic material models. The main assumption in elasticity is that the stress does not depend on the deformation history. Regarding the previous quotation from Labouesse, this is the first major simplification that has to be made for the sake of a simple material model. In particular, we restrict ourselves to *hyperelastic materials* and assume the existence of a scalar-valued stored-energy function $\Psi = \Psi(\mathbf{F})$ analog to the assumptions in Ciarlet [27] or Holzapfel [66]. There are many equivalent forms of the stored-energy function. Here, we postulate that the stored-energy function can be expressed by $\Psi(\mathbf{F}) = \Psi(\mathbf{E}) = \Psi(\mathbf{C})$ and that it does not depend on the current position $\mathbf{X}$, which implies that the material is homogeneous.

We also assume that our biological tissue is isotropic and isothermal, i.e. we assume that the material response is the same in all directions and for all temperatures. Isotropy is presumed to keep the model simple and to prevent the introduction of pre-patterns that might predetermine the orientation of our patterns. Since we are interested in *"de novo"* pattern formation in this thesis, anisotropic models are postponed to future works. Obviously, assuming isotropy is a strong idealization and the tissue, e.g. in the blastula stage, is not always isotropic (cf. Lynch [93]). For instance, we neglect the cytoskeleton of biological cells, which is a complex network of proteins that gives the cell its shape and is responsible for its mechanical resistance to deformation. In contrast, assuming isothermal behavior is a common assumption in developmental biology, since temperature does not change significantly during biological processes such as pattern formation. In summary, we obtain relations of the form

$$\mathbf{P} = \frac{\partial \Psi(\mathbf{F})}{\partial \mathbf{F}}, \quad \boldsymbol{\Sigma} = \frac{\partial \Psi(\mathbf{E})}{\partial \mathbf{E}}. \tag{2.22}$$

Now, our premises of choosing the stored-energy function are the following: Firstly, we want a simple material model with a small number of modeling parameters, which are in general difficult to measure experimentally, see Labouesse [83]. For our prototypical systems of PDEs we will even argue that changes in the two Lamé constants do not significantly change the final results (cf. Subsection 5.3.3). Also, extensive numerical simulations will show that our mechanochemical patterns are robust with regard to the (material) parameters (cf. Subsection 5.3.4). In particular, we will argue that the principles involved in our positive feedback loops are valid regardless of the material model involved. Secondly, we rule out incompressible material models such as the Neo-Hookean model or the more advanced Mooney-Rivlin model, since the assumption of incompressibility is questionable (as discussed above). Also, these models introduce an additional equation for the pressure inside the tissue which not only considerably increases the numerical effort but also requires stabilization that results in another source of numerical errors.

For these reasons, we use the simple nonlinear *Saint-Venant-Kirchhoff model* for compressible, hyperelastic materials to model the biological tissue. The stored-energy function for the Saint-Venant-Kirchhoff model is based on *Hooke's law*, which states a linear relation between stress and strain. The stored-energy function is given by

$$\Psi(\mathbf{E}) = \frac{\lambda}{2} \operatorname{tr}(\mathbf{E})^2 + \mu \operatorname{tr}(\mathbf{E}^2).$$

Derivation with respect to $\mathbf{E}$ results in a material law which relates the second Piola-Kirchhoff stress tensor $\boldsymbol{\Sigma}$ to the Green-Lagrangian strain tensor $\mathbf{E}$, namely

$$\boldsymbol{\Sigma} = \frac{\partial \Psi(\mathbf{E})}{\partial \mathbf{E}} = \lambda \operatorname{tr}(\mathbf{E})\mathbf{I} + 2\mu\mathbf{E}. \tag{2.23}$$

Here, μ and λ are the Lamé constants. Values of the Lamé constants are usually given in terms of the Young's modulus E, which is a measure of the stiffness (relation of stress to strain along an axis) of a solid material, and Poisson's ratio ν, which is the first order approximation of

the signed ratio of transverse to axial strain. Both measures can be obtained by the conversion formulas

$$\mu = \frac{E}{2(1+\nu)} \text{ and } \lambda = \frac{E\nu}{(1+\nu)(1-2\nu)}. \tag{2.24}$$

Poisson's ratio for isotropic and compressible materials typically has a value of $0.2 < \nu < 0.5$. The upper limit case $\nu = 0.5$ holds for isotropic, incompressible materials. For a derivation of these conversion formulas and the physical interpretation of all constants as well as their typical values we refer to the detailed presentation in Ciarlet [27] (Chapter 3).

Also, we are aware of the fact that the Saint-Venant-Kirchhoff material is modeled to be accurate for small strains $\mathbf{E}$ only. Still, "any behavior [of an actual material] for large strains (understood in its mathematical sense) is essentially a mathematical assumption", (Ciarlet [27, p. 159]). In our opinion, this approach is to be preferred since we are interested in the principles involved in pattern formation as opposed to predicting the exact material response for one specific animal. Also, measuring the necessary material parameters required (e.g., for the Mooney-Rivlin material model) might be difficult, as previously discussed (cf. Labouesse [83]).

2.2 Active deformations (growth)

In this section, we introduce the concept of *active deformations* (or *"growth"*) to continuum mechanics. We follow the work of Rodriguez *et al.* [128] and employ a multiplicative decomposition of the deformation gradient into a prescribed, active part that models the active deformations of the biological cells and an elastic response which ensures continuity of the overall deformation. We see that the overall deformation is unique whereas the decomposition itself is only unique up to a rigid body rotation. Since the active deformations of cells are generally volume-preserving, we mostly refrain from the term "growth", which is often associated with approaches where volume is added or removed. The key assumption in decomposing the deformation gradient is that the intermediate configuration obtained by the active deformations alone is stress-free, and any stress is generated by the elastic response. Notably, this implies that the material law depends on the elastic response alone.

In Subsection 2.2.3, we introduce the implementation of growth in our structural equation, where we focus on the implications of active deformations on the material law. Also, we highlight Subsection 2.2.5, where we discuss the most important works on active deformations with respect to the approach presented in this thesis. Namely, we present the original work by Rodriguez *et al.* [128] and related successful adaptations of the deformation gradient decomposition. Examples are the contributions of Lubarda and Hoger [92] and Himpel *et al.* [63], who model biological materials (solids) with changing mass. Further, we shortly review the works by Taber and Perucchio [144] on modeling heart development and by Ambrosi and Mollica [4] on the mechanics of a growing tumor. In this work, we mainly consider active deformations of individual, biological cells by apical/basal constriction (wedging) or apico-basal shortening (thinning). In this context, we present the works by Conte *et al.* [29] as well as Muñoz *et al.* [106], where similar active deformations have been prescribed. In particular, we discuss all

these works with respect to the approach presented in this thesis and highlight the key conceptual differences. Most importantly, we are interested in spontaneous (*"de novo"*), robust pattern formation based on mechanical feedback on morphogen dynamics via tensor invariants rather than using active deformations alone to reproduce experimentally observed deformations.

For an overview of modeling approaches to active growth in biological tissue we refer to the contribution by Jones and Chapman [74].

2.2.1 Deformation gradient decomposition

Local deformation processes are incorporated using the *multiplicative deformation gradient decomposition*, which was firstly introduced to this kind of applications by Rodriguez *et al.* [128]. The idea is to split the deformation gradient into two parts, namely

$$\mathbf{F} = \mathbf{F}_e \mathbf{F}_a, \tag{2.25}$$

where $\mathbf{F}_a = \mathbf{F}_a(t, C_1 \cdots C_n)$ is a prescribed active deformation tensor. This tensor might simply depend on time t or on concentrations C_i, $i = 1, \cdots, n$ of signaling molecules (morphogens). $\mathbf{F}_a \colon \Omega \to \Omega_a(t)$ maps the reference domain to an intermediate configuration $\Omega_a(t)$, which is in general not a (connected) domain, since $\mathbf{F}_a$ may lead to superpositions or gaps in between biological cells. The elastic response $\mathbf{F}_e \colon \Omega_a(t) \to \Omega(t)$ ensures the continuity of the overall deformation such that $\mathbf{u}$ is always smooth. The key assumption is that the intermediate configuration is stress-free, and that any stress is solely generated by the elastic response. This implies that the material law depends on the elastic response alone. In literature, the stress generated by the elastic response is usually referred as *residual stress*, which is the stress that remains if all external forces are removed.

We have illustrated the deformation gradient decomposition for different active deformations in Fig. 2.1 and Fig. 2.2 to demonstrate how piecewise active cell-shape modifications lead to changes in the curvature of the biological tissue.

Non-uniqueness of the deformation gradient decomposition

The deformation gradient decomposition (2.25) is not uniquely defined [92, 128]. Following the presentation in Lubarda [92], this is easily shown by

$$\mathbf{F} = \mathbf{F}_e \mathbf{F}_a = \mathbf{F}_e^Q \mathbf{F}_a^Q,$$

where

$$\mathbf{F}_e^Q = \mathbf{F}_e \mathbf{Q}^T, \quad \mathbf{F}_a^Q = \mathbf{Q}\mathbf{F}_a,$$

with an arbitrary, local rotation which is given by the orthogonal tensor $\mathbf{Q}$ with $\mathbf{Q}^T = \mathbf{Q}^{-1}$. On the other hand, it is rather simple to obtain a unique decomposition by using Cauchy's polar decomposition theorem, which guarantees the existence of a unique left polar decomposition of the elastic response $\mathbf{F}_e$ by

$$\mathbf{F}_e = \mathbf{V}_e \mathbf{R}_e,$$

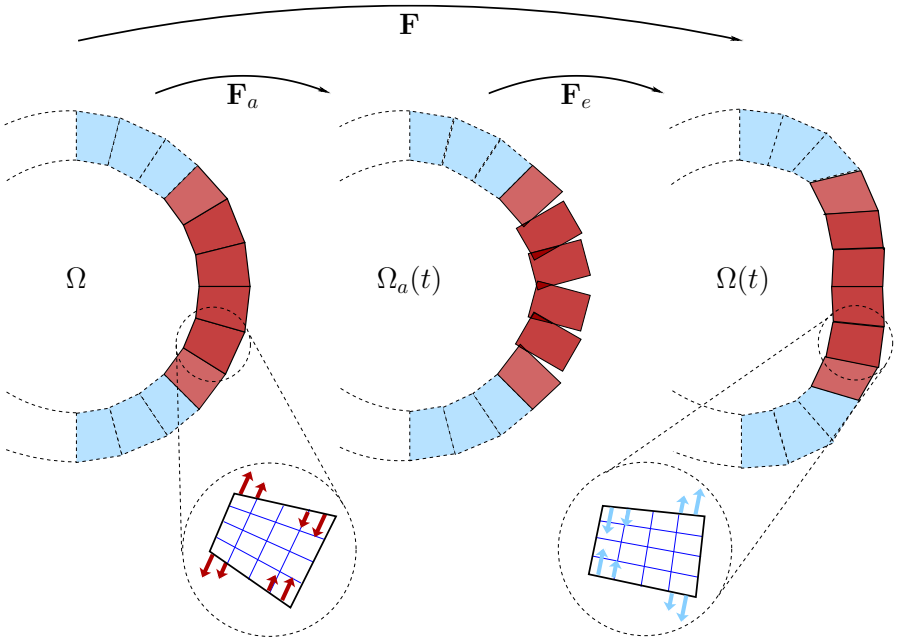

Figure 2.1: Example 1: Schematic illustration of the deformation gradient decomposition for basal constriction in 2D. Active biological cells (red, black boundary) resolved by numerical ones (blue grid) become thinner (red arrows) depending on morphogen concentrations C_i. Basal constriction results in superpositions or overlap (dark red) in $\Omega_a(t)$, and the elastic material response $\mathbf{F}_e$ (blue arrows) ensures continuity.

into a positive-definite symmetric tensor $\mathbf{V}_e$ and an orthogonal tensor $\mathbf{R}_e$, see Eq. (2.8) or Truesdell [148] for more details. This decomposition implies

$$\mathbf{F}_e^Q = \mathbf{V}_e \mathbf{R}_e \mathbf{Q}^T.$$

Thus, we simply set $\mathbf{R}_e = \mathbf{I}$ and $\mathbf{F}_e = \mathbf{V}_e$ and obtain a unique decomposition for theoretical purposes, if our isotropic material remains isotropic during the growth process.

The non-uniqueness of the deformation gradient decomposition does not have to be considered in practice. More precisely, we observe that the structural equations including growth are still stated in the reference domain Ω (cf. Subsection 2.2.3). Here, the transformation to the current domain $\Omega(t)$ is unique and rigid body rotations between time steps are not observed in our numerical simulations. The intermediate configuration however might only be unique up to rotations, is never physically attained and is not even a (connected) domain due to rupture or overlap.

2.2.2 Piecewise description of the active deformation gradient

In this work, the active deformation gradient $\mathbf{F}_a$ is usually piecewise-defined and prescribes active deformations of discrete, biological cells and the active deformation gradient $\mathbf{F}_a$ is not

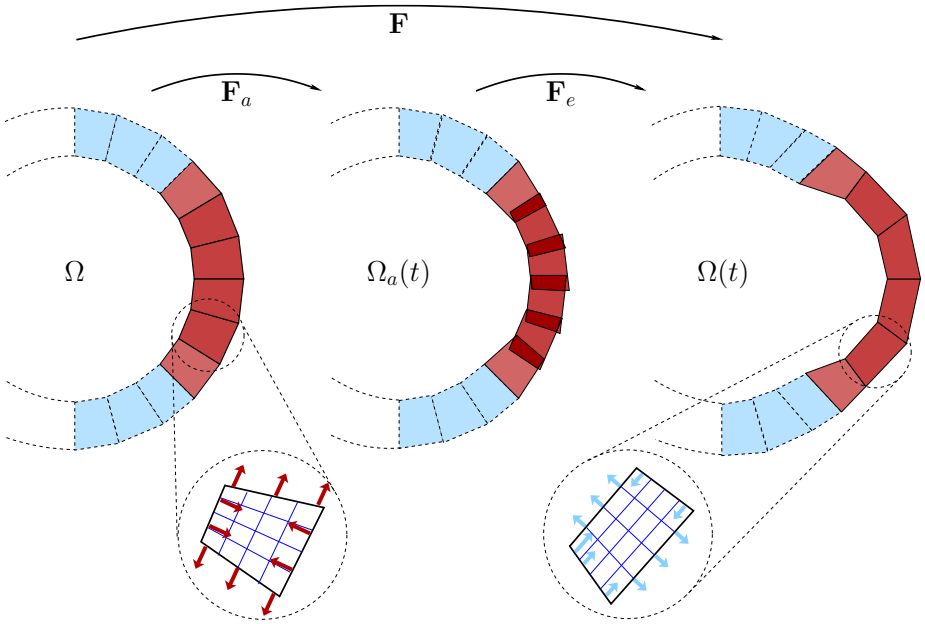

Figure 2.2: Example 2: Schematic illustration of the deformation gradient decomposition for apico-basal shortening in 2D. Active biological cells (red, black boundary) resolved by numerical ones (blue grid) become thinner (red arrows) depending on morphogen concentrations C_i. Shortening results in superpositions or overlap (dark red) in $\Omega_a(t)$, and the elastic material response $\mathbf{F}_e$ (blue arrows) ensures continuity.

injective in general. Even smoothly-defined active deformation gradients can result in overlap or rupture in the intermediate configuration. In both cases, the continuity of the overall deformation is preserved by the elastic response $\mathbf{F}_e$. In the following, we thus take a closer look at the definitions and the well-posedness of $\mathbf{F}_a$ and, more importantly, of its inverse $\mathbf{F}_a^{-1}$.

In general, we consider piecewise-defined active deformation gradients $\mathbf{F}_a$. Restricted to a biological cell K_i, these gradients are bijective mappings from this cell in the reference domain $K_i \subset \Omega$ to an actively deformed one $K_{a,i} \subset \Omega_a(t)$ in the intermediate configuration. In particular, $\mathbf{F}_a(\mathbf{X},t)|_{K_i}$ is invertible and we define for the global, active deformation gradient $\mathbf{F}_a$ and its inverse $\mathbf{F}_a^{-1}$:

$$\begin{aligned} \mathbf{F}_a(\mathbf{X},t)|_{K_i} &=: \mathbf{F}_{a,K_i}(\mathbf{X},t) && \text{for } \mathbf{X} \in K_i, \\ \mathbf{F}_a^{-1}(\mathbf{X}_a,t)\big|_{K_{a,i}} &=: \mathbf{F}_{a,K_{a,i}}^{-1}(\mathbf{X}_a,t) && \text{for } \mathbf{X}_a \in K_{a,i}, \end{aligned} \tag{2.26}$$

where $K_i \subset \Omega$ is the i-th biological cell. Note that the definition of the global inverse $\mathbf{F}_a^{-1}$ is not well-posed since the biological cells $K_{a,i}$ in the intermediate configuration $\Omega_a(t)$ usually overlap ($\mathbf{F}_a$ is globally not injective). Formally, this definition becomes well-posed if we regard $\mathbf{F}_a^{-1}$ to be meant biologically cell-wise in the structural equation (cf. Eq. (2.33)). In practice, our system of PDEs is transformed to the reference configuration such that the biological cell K_i

with $\mathbf{X} \in K_i$ is always known for a point $\mathbf{X} \in \Omega$. Hence, the local inverse $\mathbf{F}_{a,K_{a,i}}^{-1}$ is uniquely defined.

The precise, piecewise definition of $\mathbf{F}_a$ depends on the application at hand. For instance, the reader is referred to the cell-wise apical/basal constriction employed for mechanochemical pattern formation in embryogenesis, see Subsection 5.3.2.

Incompatible growth

As discussed above, we usually prescribe piecewise-defined active deformation tensors to model active deformations of individual, biological cells. In general, these tensors result in gaps and superpositions in between these cells in the intermediate configuration, and the elastic material response ensures the continuity of the overall deformation. It might yet be desirable to determine by simple analysis of the active deformation gradient if it will result in a continuous intermediate configuration or not. In the latter case, the active deformation is called *incompatible*. In linear elasticity, i.e. for small deformations, necessary and sufficient compatibility conditions are well-established in literature, both for simply- and multiply-connected regions (such as our spherical tissue shell). For the sake of brevity, we refer to the overview in Skalak *et al.* [138] or the original works by Fung [39] and Gurtin [56]. On multiply-connected domains, even smooth growth tensors that are locally injective (compatible) can lead to a geometric incompatibility of the body shape if the deformation as a whole results in superpositions or gaps. These (global) incompatibilities are called *Volterra dislocations* and are enumerated in Ref. [138]. An example of Volterra dislocations is circumferential growth/resorption in arterial segments, which lead to an overlap/gap in the intermediate configuration. These incompatibilities are examined in Rodriguez *et al.* [128] (cf. Fig. 2.3 and Subsection 2.2.5).

In finite strain theory, i.e. for large deformations, the derivation of compatibility conditions is considerably more complex. In Skalak *et al.* [138], conditions analogous to those for linear elasticity are summarized for simply-connected domains and individual cases for multiply-connected domains are studied, since "no generalizations [to finite elasticity] in terms of Volterra dislocations are available". (Skalak *et al.* [138, p. 889])

We omit the formal introduction of compatibility conditions since the active deformation gradients $\mathbf{F}_a$ defined in this work result in superpositions and gaps between biological cells by their very (piecewise-continuous) definitions (cf. Eq. 2.26). Further, these incompatibilities pose no numerical difficulties or other practical implications. Thus, we see no additional benefit in analyzing our continuously-defined active deformation tensors that we prescribe in the application to growth processes in tips of colonial hydroids (cf. Section 5.2). Examples for the incompatibility of our tensors are basal/apical constriction in embryonic development and apico-basal shortening in symmetry breaking in *Hydra*. We have illustrated the incompatibilities of these tensors in Fig. 2.1 and Fig. 2.2. The precise definitions of the corresponding active deformation tensors are given in Sections 5.3 and 5.4.

2.2.3 Material laws for active deformations

At this point, we consider how the deformation gradient decomposition approach from Subsection 2.2.1 can be incorporated in the Saint-Venant-Kirchhoff model for compressible hyperelastic

materials, which is presented in Eq. (2.23).

The key assumption behind the deformation gradient decomposition is that the intermediate state $\Omega_a(t)$ is stress-free. Hence, any stress in the material body is generated by the elastic part $\mathbf{F}_e$ of the deformation gradient, and the stored-energy function $\Psi(\mathbf{E}_e) = \frac{\lambda}{2}\operatorname{tr}(\mathbf{E}_e)^2 + \mu\operatorname{tr}(\mathbf{E}_e^2)$ with $\mathbf{E}_e = 0.5(\mathbf{F}_e\mathbf{F}_e - \mathbf{I})$ now depends on depend on $\mathbf{F}_e$ only. Next, we define stress tensors in the intermediate configuration, analog to the first and second Piola-Kirchhoff stress tensors defined in the reference domain (cf. Eq. (2.22)) by

$$\begin{aligned} \mathbf{P}_e &= \frac{d\Psi}{d\mathbf{F}_e}:\ \Omega_a(t) \to \Omega(t), \\ \mathbf{\Sigma}_e &= \frac{d\Psi}{d\mathbf{E}_e}:\ \Omega_a(t) \to \Omega_a(t). \end{aligned} \tag{2.27}$$

Then, derivation of the elastic, stored energy function yields the material law

$$\mathbf{\Sigma}_e = \lambda\operatorname{tr}(\mathbf{E}_e)\mathbf{I} + 2\mu\mathbf{E}_e, \quad \mathbf{E}_e = \frac{1}{2}(\mathbf{F}_e^T\mathbf{F}_e - \mathbf{I}), \tag{2.28}$$

analog to the usual material law given in Eq. (2.23). Note that $\mathbf{P}_e\mathbf{n}_a$ is defined as the force in the current configuration $\Omega(t)$ per unit surface area in the intermediate one $\Omega_a(t)$. Similarly, $\mathbf{\Sigma}_e\mathbf{n}_a$ is the force defined in $\Omega_a(t)$ per unit surface area also in $\Omega_a(t)$. These definitions come with the caveat that the intermediate configuration is not a real domain, and the surface area in $\Omega_a(t)$ and the normal direction $\mathbf{n}_a$ might not be uniquely defined. Hence, we transform our equations to the intermediate configuration where we insert the elastic material law (2.28). Subsequently, we express the stress in the Lagrangian framework by transformation to the reference configuration.

2.2.4 Active deformations in the structural equation

Since $\mathbf{\Sigma}_e$ is defined on the intermediate configuration, we cannot insert it directly into our structural equation that we expressed in the Eulerian or Lagrangian framework, compare Eq. (2.17) and Eq. (2.18). Instead, we take the integral containing the stress tensor in the Eulerian coordinate system (2.17) and proceed as follows: First of all, we transform this integral to the intermediate configuration. Therefor, we define the *elastic deformation* $\boldsymbol{\chi}_e(t)\colon \Omega_a(t) \to \Omega(t)$ by $\boldsymbol{\chi}_e(\mathbf{x}_a, t) \coloneqq \mathbf{x}$, analog to the definition of the deformation (2.1). Further, we use the notation

$$\mathbf{F}_e(\mathbf{x}_a, t) = \nabla\boldsymbol{\chi}_e(\mathbf{x}_a, t), \quad J_e \coloneqq \det(\mathbf{F}_e).$$

With these definitions at hand, we can formulate the transformation of an integral and the gradient from the Eulerian configuration to the intermediate one, analog to the transformation of Eq. (2.4) in Eulerian coordinates to Eq. (2.5) in the reference framework: The integral that expresses the surface forces from Cauchy's equation of motion (2.17) is transformed to the intermediate configuration by

$$\int_{\Omega(t)} \boldsymbol{\sigma}(\mathbf{x}, t)\nabla\boldsymbol{\varphi}\,\mathrm{d}\mathbf{x} = \int_{\Omega_a(t)} J_e(\mathbf{x}_a, t)\boldsymbol{\sigma}(\boldsymbol{\chi}_e(\mathbf{x}_a, t), t)\mathbf{F}_e^{-T}(\boldsymbol{\chi}_e(\mathbf{x}_a, t), t)\nabla\boldsymbol{\varphi}_a\,\mathrm{d}\mathbf{x}_a, \tag{2.29}$$

for all test functions $\boldsymbol{\varphi}(\mathbf{x}) \in V^d_{\Omega(t)}$ and $\boldsymbol{\varphi}_a(\mathbf{x}_a) \in V^d_{\Omega_a(t)}$. This gives us the following relations for the“ elastic” stress tensors in the intermediate configuration:

$$\mathbf{P}_e = J_e \boldsymbol{\sigma} \mathbf{F}_e^{-T}, \quad \mathbf{F}_e \boldsymbol{\Sigma}_e = \mathbf{P}_e, \tag{2.30}$$

which are analog to the usual relations (2.13) between the first and second Piola-Kirchhoff stress tensors that measure stress in the current and in the reference system, respectively. Next, we insert Eq. (2.30) into Eq. (2.29) and transform the resulting integral from the intermediate to the reference configuration. This yields

$$\begin{aligned}
&\int_{\Omega_a(t)} J_e(\mathbf{x}_a, t) \boldsymbol{\sigma}(\boldsymbol{\chi}_e(\mathbf{x}_a, t), t) \mathbf{F}_e^{-T}(\boldsymbol{\chi}_e(\mathbf{x}_a, t), t) \nabla \boldsymbol{\varphi}_a \, \mathrm{d}\mathbf{x}_a \\
&= \int_{\Omega_a(t)} \mathbf{F}_e(\mathbf{x}_a, t) \boldsymbol{\Sigma}_e(\mathbf{x}_a, t) \nabla \boldsymbol{\varphi}_a \, \mathrm{d}\mathbf{x}_a \\
&= \int_{\Omega} J_a(\mathbf{X}, t) \mathbf{F}_e(\boldsymbol{\chi}_a(\mathbf{X}, t), t) \boldsymbol{\Sigma}_e(\boldsymbol{\chi}_a(\mathbf{X}, t), t) \mathbf{F}_a(\mathbf{X}, t)^{-T} \nabla \boldsymbol{\Phi} \, \mathrm{d}\mathbf{X},
\end{aligned}$$

where we define the *active deformation* $\boldsymbol{\chi}_a(t) \colon \Omega \to \Omega_a(t)$ by $\boldsymbol{\chi}_a(\mathbf{X}, t) \coloneqq \mathbf{x}_a$ with $J_a \coloneqq \det(\mathbf{F}_a)$ such that the transformation between the last two integrals is analogous to the usual transformations (2.4) and (2.5) between the reference and the current coordinate system.

Finally, we insert the deformation gradient decomposition $\mathbf{F} = \mathbf{F}_e \mathbf{F}_a$ itself for $\mathbf{F}_e$ and compare the result to the usual structural equation (2.19) in the reference configuration. This comparison yields the following, important relation between the second Piola-Kirchhoff stress tensor $\boldsymbol{\Sigma}$ in the reference configuration and its elastic equivalent in the intermediate one:

$$\boldsymbol{\Sigma} = J_a \mathbf{F}_a^{-1} \boldsymbol{\Sigma}_e \mathbf{F}_a^{-T}, \tag{2.31}$$

analogous to the usual relation $\boldsymbol{\Sigma} = J \mathbf{F}^{-1} \boldsymbol{\sigma} \mathbf{F}^{-T}$ (cf. Eq. (2.13) that relates the second Piola-Kirchhoff stress tensor in the reference configuration with the Cauchy stress tensor given in Eulerian coordinates. Different derivations of this relation based on tensor algebra can be found in literature, for instance in Lubarda and Hoger [92] or in Himpel *et al.* [63]. At this point, we can insert the elastic material law $\boldsymbol{\Sigma}_e = \lambda \operatorname{tr}(\mathbf{E}_e)\mathbf{I} + 2\mu \mathbf{E}_e$, that we derived earlier in Eq. (2.28).

So far, we have prescribed homogeneous Neumann boundary conditions on the entire boundary $\partial\Omega$ for the sake of a simple derivation. To cover a wider range of applications as well as predictive, numerical experiments, we consider Dirichlet, Neumann and Robin boundary conditions on the three disjoint parts $\partial\Omega = \Gamma_D \cup \Gamma_N \cup \Gamma_R$. Finally, Cauchy's first equation of motion including active deformations in the reference configuration is given as the combination of Eq. 2.19 and Eq. 2.31 and reads:

Find displacement $\mathbf{u} \in V^d$ for a given body-force density $\mathbf{f} \in L^2(\Omega)^d$ and initial material density $\rho^0 \in L^2(\Omega)$, such that it holds $\mathbf{u}(\mathbf{X}, 0) = 0$ and

$$\int_{\Omega} \rho^0 \partial_{tt} \mathbf{u} \cdot \boldsymbol{\Phi} + \mathbf{F}\boldsymbol{\Sigma} \nabla \boldsymbol{\Phi} \, \mathrm{d}\mathbf{X} + \int_{\Gamma_N} \mathbf{G} \cdot \boldsymbol{\Phi} \, \mathrm{d}S + \int_{\Gamma_R} \mathbf{F}\boldsymbol{\Sigma}\mathbf{N} \cdot \boldsymbol{\Phi} \, \mathrm{d}S = \int_{\Omega} \rho^0 \mathbf{f} \cdot \boldsymbol{\Phi} \, \mathrm{d}\mathbf{X} \tag{2.32}$$

for all $\boldsymbol{\Phi} \in V^d$, where

$$\boldsymbol{\Sigma} = J_a \mathbf{F}_a^{-1} \boldsymbol{\Sigma}_e \mathbf{F}_a^{-T}, \quad \boldsymbol{\Sigma}_e = \lambda \operatorname{tr}(\mathbf{E}_e)\mathbf{I} + 2\mu \mathbf{E}_e,$$

and where $\mathbf{G}$ accounts for surface forces on the Neumann boundary Γ_N. Robin conditions are prescribed on Γ_R. Sufficient regularity provided, we can integrate by parts and obtain our structural equation in the Lagrangian framework, which reads:

Find displacement $\mathbf{u}$ for homogeneous initial conditions $\mathbf{u}(\mathbf{X}, 0) = 0$, such that

$$\begin{aligned} \rho^0 \partial_{tt}\mathbf{u} - \nabla \cdot (\mathbf{F}\boldsymbol{\Sigma}) &= \rho^0 \mathbf{f} && \text{in } \Omega, \\ \mathbf{u} &= 0 && \text{on } \Gamma_D, \\ \mathbf{F}\boldsymbol{\Sigma}\mathbf{N} &= \mathbf{G} && \text{on } \Gamma_N \text{ and} \\ \mathbf{r}(\mathbf{u}, \nabla\mathbf{u}, \mathbf{N}) &= 0 && \text{on } \Gamma_R \end{aligned} \tag{2.33}$$

holds, where

$$\boldsymbol{\Sigma} = J_a \mathbf{F}_a^{-1} \boldsymbol{\Sigma}_e \mathbf{F}_a^{-T}, \quad \boldsymbol{\Sigma}_e = \lambda \operatorname{tr}(\mathbf{E}_e)\mathbf{I} + 2\mu \mathbf{E}_e, \quad \mathbf{E}_e = \frac{1}{2}(\mathbf{F}_e^T \mathbf{F}_e - \mathbf{I}),$$
$$\mathbf{F}_e = \mathbf{F}\mathbf{F}_a^{-1}, \quad \mathbf{F} = \nabla\mathbf{u} + \mathbf{I}, \quad J = \det(\mathbf{F}) \text{ and } J_a = \det(\mathbf{F}_a).$$

Note that the divergence above is meant in a row-wise sense. Next, $\mathbf{G}$ account for possible surface forces acting on Γ_N and $\mathbf{r}(\mathbf{u}, \nabla\mathbf{u}, \mathbf{N})$ represents mixed Robin boundary conditions which might be prescribed, e.g. it incorporates the glass body of a pipette in our predictive, numerical experiments. In practice, splitting the deformation gradient hence means to replace the unknown elastic response $\mathbf{F}_e$ by $\mathbf{F}\mathbf{F}_a^{-1}$ with the prescribed, active deformation $\mathbf{F}_a$ and to subsequently solve for the overall deformation $\mathbf{u}$.

Finally, we point out that the elastic Green-Lagrangian strain tensor $\mathbf{E}_e$ remains symmetric, since

$$\mathbf{E}_e^T = \frac{1}{2}(\mathbf{F}_a^{-T}\mathbf{F}^T\mathbf{F}\mathbf{F}_a^{-1} - \mathbf{I})^T = \frac{1}{2}((\mathbf{F}_a^{-T}\mathbf{F}^T\mathbf{F}\mathbf{F}_a^{-1}) - \mathbf{I}) = \mathbf{E}_e$$

holds. Consequently, the Cauchy stress tensor σ and the second Piola-Kirchhoff tensor $\boldsymbol{\Sigma}$ also remain symmetric (see Eq. (2.31) and the definition of $\boldsymbol{\Sigma}_e$ in Eq. (2.28)).

Before we introduce the reaction-diffusion equations describing morphogen dynamics and model mechanochemical interactions, we complete the presentation by giving an overview of the literature that influenced the implementation of active deformations presented in this work.

2.2.5 Related works on growth and active deformations

In the recent decades, the mathematical description of active deformations (and growth) in the development of biological tissue has become an area of great interest. In the following, we give an overview of the most important works that influenced the mathematical modeling of active deformations in our approach. In particular, we discuss these works with respect to the key differences in the conception and the objectives of this thesis.

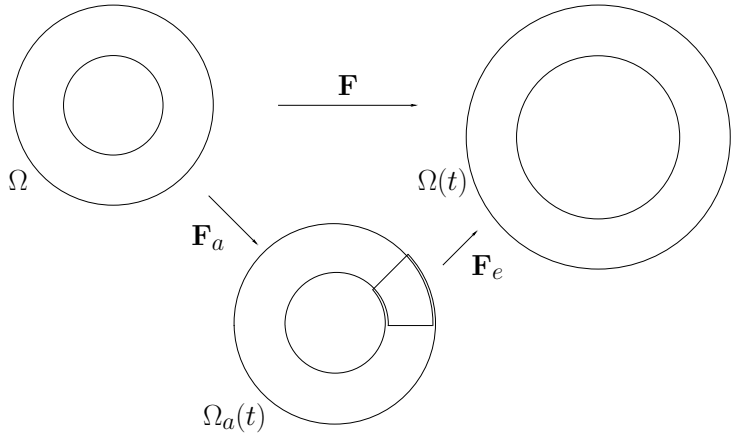

Figure 2.3: Schematic illustration of the deformation gradient decomposition as adapted from the original work by Rodriguez and coworkers [128]. Circumferential growth leads to superposition in $\Omega_a(t)$ and the elastic response ensures continuity of the overall deformation. Note that the radius of the cylinder does not change during growth, the reduced radius in $\Omega_a(t)$ merely illustrates the overlap of the tissue.

As shown above, the description of active deformations in this work is based on the idea of multiplicatively decomposing the deformation gradient into an active, prescribed part and an elastic response. Rodriguez *et al.* [128] were the first who applied this approach to growth and remodeling in biological tissue. Namely, they examine ventricular hypertrophy, that is the thickening of the heart muscle as a pathological reaction to overload, e.g., by high blood pressure, and stress-dependent growth in bone. We illustrate the concept of the deformation gradient decomposition by looking at the first of these applications: There, Rodriguez *et al.* consider a hollow cylindrical tube of incompressible and isotropic elastic material. They illustrate how circumferential growth/resorption leads to superposition/gaps in the intermediate configuration as sketched in Fig. 2.3. The elastic material response ensures the continuity of the overall deformation and results in residual stress. Thus, if the deformed cylinder $\Omega(t)$ was cut, the residual stress would produce shape changes such as a shift or an opening of the blood vessel (the latter for circumferential resorption that is not shown here). These changes are experimentally observed, see e.g. Chuong and Fung [26].

Example 1 In the following, we take a closer look at this application with regard to the active deformations, the elastic response and the compatibility of the deformation as a whole. With cylindrical reference coordinates (R, Θ, Z) in Ω, coordinates (r_a, θ_a, z_a) in the intermediate configuration and coordinates (r, θ, z) in the current configuration $\Omega(t)$, circumferential growth is expressed by the displacement field

$$r_a = R, \quad \theta_a = k\Theta, \quad z_a = Z,$$

with a constant k that results in growth for $k > 1$ and in resorption for $k < 1$. Next, the elastic response is given by the displacement field

$$r = r(r_a), \quad \theta = \eta\theta_a, \quad z = z_a,$$

which maps the intermediate to the deformed configuration Ω, where deformation in z-direction is not considered for simplicity. The active circumferential deformation and the elastic response result in the active and the elastic deformation gradients in Cartesian coordinates given by

$$\mathbf{F}_a = \begin{pmatrix} 1 & 0 & 0 \\ 0 & \frac{r_a}{R}k & 0 \\ 0 & 0 & 1 \end{pmatrix}, \text{ and } \mathbf{F}_e = \begin{pmatrix} \frac{dr(r_a)}{dr_a} & 0 & 0 \\ 0 & \frac{r}{r_a}\eta & 0 \\ 0 & 0 & 1 \end{pmatrix}.$$

We have illustrated this active deformation and the elastic response in Fig. 2.3, which we adapted from the original work by Rodriguez and coworkers [128]. Here, we observe how circumferential growth leads to a global incompatibility of the tissue geometry in the intermediate configuration $\Omega_a(t)$. This incompatibility is an example of a Volterra dislocation that we discussed in Subsection 2.2.2. The overall deformation $\mathbf{F}_a\mathbf{F}_e$ is continuous (i.e. compatible) for the choice $\eta = \frac{1}{k}$. From this elastic response, Rodriguez *et al.* then calculate the residual stress in the tissue cylinder by using a constitutive material law (one could also use our elastic material law as in Eq. (2.28)). Indeed, residual stress may not only be a mere consequence of growth but can also affect the growth itself. For instance, stress changes as a response to increased blood pressure can lead to normal or pathological cardiac growth, see Grossman [54]. Rodriguez *et al.* thus proceed to stress-dependent growth in bone due to external loading, which is not discussed in this thesis for the sake of brevity.

Related approaches adapting the deformation gradient decomposition The deformation gradient decomposition was successfully adapted in many subsequent works. For instance, we mention the contribution by Lubarda and Hoger [92], who present a general, constitutive theory of stress-modulated growth and discuss the uniqueness of the deformation gradient decomposition (cf. Subsection 2.2.1). In their work, they consider isotropic, transversely isotropic and orthotropic biomaterials, the latter two containing fibers in one or more directions. They prescribe simple, isotropic growth or growth along the eigendirections of these fibers. Thereby, these active deformations depend on the isotropic stretch ratio, which results from volumetric mass growth. To prevent unlimited growth, they propose an evolution law modeling a linear relation between the stretch ratio and the stress. Besides, this evolution law contains a nonlinear factor to limit a maximal stretch ratio.

This evolution law was adapted by Himpel *et al.* [63], who present a description of growth on the kinematic level to implement both, a change in density and a change in volume. Besides, they derive the transformations of the Piola-Kirchhoff stresses in the material, the intermediate and the current configuration using tensor algebra and commutative diagrams. In particular, they present an alternative derivation of the important relation (2.31).

Further contributions including the deformation gradient decomposition stem from Taber and coworkers, see e.g. Taber and Eggers [143] on stress-modulated growth in the aorta and Taber and Perucchio [144] on modeling heart development. Also, Ambrosi and Mollica [4] use this

approach for considering the mechanics of a growing tumor. Another mentionable, more general approach to the deformation gradient decomposition stems from Chen and Hoger [25], who take the current Eulerian configuration as the reference configuration and thereby provide the theoretical foundation to the (so far arbitrary) decomposition of the deformation gradient and the assertion that the material response should only depend on the elastic part of the deformation gradient. Note that this assertion was the key assumption in the derivation of our elastic material law (2.28). All these contributions have in common that they investigate simple isotropic growth or diagonal stress-dependent active deformation tensors on simple model geometries such as cylinders, where the problem can be reduced to two-dimensional spherical shells by symmetry arguments.

In this work, we rather consider piecewise-defined apical/basal constriction (wedging) or apico-basal shortening (thinning) of individual, biological cells, depending on the application at hand (cf. Subsection 2.2.2). Similar active deformations have been prescribed by Conte *et al.* [29] for a 3D model geometry and by Muñoz *et al.* [106] in 2D, who consider ventral furrow invagination in the *Drosophila melanogaster* embryo, i.e. an orthogonal inwards folding of the cells along the ventral center line of the embryo. Before we give details on these works, we emphasize that the intention of these two works differs significantly from the objective of this thesis: Although we consider similar active deformations in the following, the aim of Conte [29], Muñoz [106] and their respective coworkers is the exact mechanical reproduction of the invagination process in *Drosophila*. Thus, they seek suitable combinations of apical constriction and apico-basal elongation of biological cells in conjunction with boundary conditions that account for the fluid (yolk) inside the embryo and a slip condition to model the hard vitelline membrane around the tissue ellipsoid. The location of the invagination is predetermined by introducing the mesoderm zone, where the invagination occurs and where combinations of both active deformations are prescribed, and an endoderm zone, where only apico-basal shortening is considered. And yet, "the causes of the active deformations are not specified [but] are considered here as an internal (genetically or chemomechanically transduced) contribution that produces different combinations of the two active shape changes" ([29, p. 190], similar in [106, p. 1373]).

On the other hand, the main contribution of this thesis is the development of coupled systems of PDEs modeling simple, positive interaction rules ("feedback loops") that lead to *de novo* and robust mechanochemical patterns. In other words, we investigate how and why patterns form. The key component of this interaction process is the coupling of tensor invariants expressing stretch, strain and compression on the dynamics of signaling molecules which in turn lead to active deformations. Also, we do not introduce any pre-patterns to our model, e.g. by the prescription of zones as in [29, 106]. Instead, our feedback loops lead to spontaneous and robust patterns within the biological tissue.

Example 2 Here, we provide details on the description of active deformations in Conte *et al.* and Muñoz *et al.* ([29, 106]). They look at a *Drosophila* embryo, which started as a single cell and has developed into a stretched ellipsoid consisting of one layer of biological cells. It is filled with a viscous fluid (yolk) and surrounded by a semi-hard shell (vitelline layer). They use a hyperelastic neo-Hookean material law to model the biological tissue. Further, they pre-

scribe combinations of apical constriction and apico-basal elongation to qualitatively reproduce the deformations observed in the gastrulation of the *Drosophila* embryo to the greatest extent possible.

In this thesis, we express piecewise-defined active deformation tensors by introducing local coordinate systems $\hat{\mathbf{X}} = (\hat{X}_0, \hat{X}_1, \hat{X}_2)$ in the origin of every biological cell. These coordinate systems are oriented such that $\hat{X}_2$ points in the radial direction, with the obvious analogon in two dimensions. In contrast, Conte *et al.* define these tensors on the numerical reference elements. Hence, biological and numerical cells either coincide, or one biological cell is resolved by individually constricting numerical cells in tangential direction, thereby changing the nature of the biological system. Also, no mesh refinement could be "employed along the radial thickness of the embryo" (Conte *et al.* [29, p. 193]). The latter either results in very coarse meshes or highly unisotropic numerical cells, which might both lead to numerical difficulties. If no mesh refinement is employed and biological and numerical cells coincide, Conte *et al.* cannot even expect convergence, as our analysis in Section 3.5 will reveal.

We circumvent this obstacle by introducing local coordinate systems in the centroid of each biological cell. Here, local active deformation tensors are defined. The actual deformation tensor is then obtained by a transformations from these parametric systems to the reference configuration, see Subsection 5.3.2. In practice, we keep track of the biological cells by using material IDs during the entire process of discretization and parallelization. That way, we can always compute the transformation to the coordinate system of the current biological cell which can then be resolved by 64 numerical cells (hexahedra in 3D). In particular, we demonstrate that convergence of our methods is always ensured in a thorough convergence analysis (cf. Section 3.5).

We can express the active deformation gradients in our local coordinate systems $\hat{\mathbf{X}}$ and keep the notation of the tensors from Ref. [29, 106]. There, these tensors are yet defined on the numerical reference elements with the negative implications on numerical mesh refinement discussed above.

Conte et. al [29] prescribe active deformations $\mathbf{F}_a = \mathbf{F}_{el}\mathbf{F}_{ac}$ as combination of active apical constriction $\mathbf{F}_{ac}$ and active elongation $\mathbf{F}_{el}$ (the subscripts "ac" and "el" are adopted from the notation in [29, 106] and are only used in this example). In our local coordinates, these tensors are defined as

$$\hat{\mathbf{F}}_{ac}(\hat{\mathbf{X}}, \tau) \coloneqq \begin{pmatrix} 1 + \omega_{ac}\tau\hat{X}_1 & \omega_{ac}\tau\hat{X}_0 & 0 \\ 0 & 1 & 0 \\ 0 & 0 & 1 \end{pmatrix} \text{ and}$$

$$\hat{\mathbf{F}}_{el}(\tau) \coloneqq \begin{pmatrix} 1 + \omega_{el}\tau & 0 & 0 \\ 0 & (1 + \omega_{el}\tau)^{-1} & 0 \\ 0 & 0 & 1 \end{pmatrix},$$

where τ is a pseudo-time. These tensors are presented in both articles with the obvious reduction to 2D. In this thesis, we prescribe related active deformations. However, we consider active apical/basal constriction (cf. Eq. 5.5) and apico-basal shortening (cf. Eq. 5.13) in both tangential directions in the 3D case.

In Conte et. al [29] and Muñoz et. al [106], combinations of these deformations $\hat{\mathbf{F}}_a = \hat{\mathbf{F}}_{el}\hat{\mathbf{F}}_{ac}$ with $\omega_{ac}, \omega_{el} > 0$ are only prescribed in the mesoderm zone of the embryo, which consists of a circular sector that comprises one sixth of the tissue cross section. In the remaining tissue, the endoderm, apico-basal shortening $\mathbf{F}_{el}$ with $\omega_{el} < 0$ is assumed. That way, the deformation is predetermined and the invagination process is restricted to the mesoderm. This is the essential difference to this thesis where we are interested in spontaneous, robust pattern formation.

In their framework, Conte and Muñoz [29] show that certain combinations of active deformations reproduce the basic features of ventral furrow invagination. Namely, suitable values for $\alpha := \frac{\omega_{ac}}{\omega_{el}}$ range between $3 \leq \alpha \leq 6$ in 3D and $4 \leq \alpha \leq 5$ in the 2D case. They conclude that the ventral furrow invagination in 3D seems to be more robust with regard to α. Since the considered tissue is an almost cylindrical ellipsoid, the results in 3D and 2D are very similar due to this symmetry. Global, elastic compression and expansion effects in the domain (due to the fluid that has an additional degree of freedom in 3D) are the exception.

Finally, we remark that numerical simulations by Conte *et al.* and Muñoz *et al.* [29, 106] show that the slip conditions modeling the vitelline membrane seem to be essential in a precise reproduction of ventral furrow invagination. In contrast, an internal volume constraint seems to be negligible. In the context of this thesis, an internal pressure is introduced for the purpose of stopping the gastrulation process instead (cf. Subsection 5.3.5). For specific model organism such as *Drosophila*, our results might indeed be improved by considering the vitelline membrane. We have already implemented similar boundary conditions for modeling the glass body of a pipette in the context of our predictive, numerical experiments (cf. Subsection 5.4.2).

Example 3 Allena *et al.* [1] were the first to propose the dependence of active deformations on morphogen concentrations that are modeled by a reaction diffusion equation. More precisely, the rate of the strength of the active deformations linearly depends on the morphogen concentration via a simple evolution equation. In this method, the active deformation process is the result of an initially prescribed, diffusing morphogen gradient. These chemical pre-patterns "in fact correspond to the final conditions of other processes which have not been modeled" (Allena *et al.* [1, p. 28]). On the contrary, we are interested in both the process of robust *de novo* pattern formation and the final, stationary results such as gastrulation. The essential difference in this thesis compared to Ref. [1] is that we propose interaction rules ("feedback loops") that close the mechanochemical circle: Here, we also consider mechanical feedback expressed by tensor invariants describing stress, strain or stretch on morphogen dynamics. In turn, the latter lead to active deformations. To illustrate these differences further, we take a closer look at the methods and the application to ventral furrow invagination in *Drosophila* presented in Ref. [1].

In their application, Allena *et al.* [1] consider the full 3D geometry of the *Drosophila* embryo, similar to the previous example by Conte *et al.* [29]. Using Heaviside functions, they prescribe active deformations of individual material cells. The strength of the active deformations $\mathbf{F}_a = \mathbf{F}_a(\alpha)$ depends on an "intensity factor" α. The rate of this factor linearly depends on the morphogen concentration via the simple evolution law $\frac{d}{dt}\alpha = \beta C$, where $\beta = 0.1$ is a constant. Allena *et al.* [1] derive the precise form of the active deformation gradient as follows: They introduce a harmonic parameterization of the embryo geometry by local, curvilinear coordinate

systems that are the solution of two Laplace problems. In the intermediate configuration, they prescribe a deformation that resembles an invagination due to apical constriction. Then, differentiation of these active deformations yields the desired active deformation gradient (that result is not shown).

On the other hand, the purpose of the additional evolution equation used in Ref. [1] is to obtain stationary solutions once the morphogen concentration vanishes due to degradation and diffusion. Yet the authors remark that they limit their "attention and conclusion to a subinterval of this whole period, where [the evolution equation] seems better justified and better reproduces the experimental observations" (Allena *et al.* [1, p. 13]). Note that both having morphogen concentrations that dissolve over time and increasing concentrations of signaling molecules that eventually saturate are observed in practice. Whereas Allena *et al.* [1] consider the former using an additional evolution law, we prefer the latter mechanism. That way, we dispense with a third equation in our approach, which saves huge computational costs. Besides, we use the Michaelis-Menten kinetics (cf. Eq. (2.40)), which result in a saturation of the morphogen concentrations and ultimately yield stationary solutions.

Analog to this thesis, Allena *et al.* [1] model elastic, biological tissue by Hooke's material law and express morphogen dynamics by a simple reaction-diffusion equation, which reads in Lagrangian coordinates

$$\frac{d}{dt}(JC) = \nabla \cdot (Jk_D \mathbf{F}^T \mathbf{F} \nabla C) + Jk_R C,$$

where k_D is the diffusion coefficient and k_R is the morphogen degradation rate. For details on reaction-diffusion equations we refer to Subsection 2.3.1. Simple reformulation shows that the whole reaction term in their work is given by $C(Jk_R - \frac{d}{dt}(J)$, where J stems from the transformation of the reaction-diffusion equation to the reference domain. This (implicit) coupling reflects the fact that the morphogen concentration increases/decreases if the tissue is compressed/stretched. Hence, this coupling is not a modeling assumption, in contrast to our mechanical feedback on the morphogen dynamics based on tensor invariants that we propose in this thesis. In particular, this implies that Allena *et al.* [1] do not expect spontaneous mechanochemical pattern formation due to this mechanochemical coupling.

Example 4 Next, we shortly present the work by Frei *et al.* [38] who investigate mechanochemical fluid-structure interaction (FSI), namely the interaction of a growing solid with an incompressible fluid. The considered application is the formation and growth of plaque in blood vessels. The focus of their work is design of a "robust numerical framework for the coupled long-term dynamics of fluid structure interaction with active growth processes and large deformation" (Frei *et al.* [38, p. 876]). Before we go into details, we point out that in Ref. [38] growth of stress-dependent intensity is prescribed in a center around the middle part of the blood vessel. This is the key difference to the presented thesis where we consider spontaneous pattern formation (anywhere) in biological tissue.

Many difficulties in their application are similar to the difficulties that we face in the context of this work: The main challenges are the large system of equations, the huge deformations due to growth of plaque in the vessel (or of the tissue in the context of this thesis) and the different timescales of growth τ and the pulsating heart flow t (or of growth and elasticity in case of this thesis).

On the other hand, the mechanochemical feedback loops proposed in this thesis lead to a strongly coupled system of equations that requires a monolithic solution approach that is we implicitly solve the system of PDEs as a whole. In contrast, Frei *et al.* [38] propose a partitioning of the temporal scale: They consider a two-way coupled system of equations, where the initial stationary fluid flow is computed on the long-term growth scale. From there, they compute fluid velocity and pressure on the short scale (assuming that growth is constant here), which lead to stress on the vessel wall. This stress is averaged over the entire interface (between fluid and tissue) and leads to an increase of foam cell concentrations, described by a simplified ODE model. This mechanochemical dynamic is due to monocytes inside the blood that migrate into the tissue where the migration rate depends on the wall stress and the damage of the wall, see [38] and the references therein. In the vessel wall, these monocytes transform into foam cells which lead to isotropic growth by the active deformation tensor $\mathbf{F}_a = g\mathbf{I}$, where $g = g(\mathbf{X}, C(\tau))$ prescribes growth in the center of the blood vessel and linearly depends on the concentration of foam cells $C(\tau)$. This growth of the vessel wall (on the long-time scale τ) results in an update of the vessel width after solving for the next velocity and pressure of the long-scale problem. In turn, this new geometry leads to large wall stress. This process is iterated until the channel is clogged for a fully Eulerian ansatz or computations break down in a classical ALE approach.

All the works summarized above have in common that they consider growth as a mere consequence of mechanical or chemical pre-patterns: Either, active deformations that depend on time are prescribed or predefined local morphogen gradients are considered. In this thesis, we propose simple, positive feedback loops instead that are based on a novel mechanical feedback of tensor invariants describing stress, strain or stretch on morphogen dynamics. Indeed, many recent studies emphasize the active involvement of mechanics in pattern formation, (cf. [13, 24, 35, 105, 117]). Correspondingly, our numerous numerical simulations confirm that these positive feedback loops are vital to robustly produce spontaneous (*"de novo"*) mechanochemical patterns. Ultimately, the objective of this thesis hence substantially differs from the goals of the examples above: We want to help to unravel one of the big mysteries in biology: The mechanisms of self-organized pattern formation during embryogenesis. Ultimately, "it is not birth, marriage, or death, but gastrulation which is truly the most important time in your life" (Wolpert [156, p. 12]).

Example 5 One exception are the recent works by Mercker *et al.* [104, 105], who describe the tissue as an infinitely thin deforming surface. Similar to our work, they propose simple, positive feedback loops where morphogen concentration leads to active tissue curvature, which in turn induces morphogen production. These mechanochemical interactions lead to co-localized, local morphogen levels and increased, positive tissue curvature (i.e. an increased outward bending in parts of the domain). In Mercker *et al.* [104, 105], the biological tissue is described by the Helfich energy [61], which is often used to describe the mechanics of membranes and additionally depends on the morphogen concentrations. In contrast, the tissue mechanics in this thesis are described by a very different mechanical model, in particular, we include the deformation gradient decomposition ansatz and use tensor invariants to describe the mechanical tissue response. Yet, many numerical observations within this work and Mercker *et al.* [104] coincide,

namely that increased diffusion rates result in larger morphogen patches or that increasing the mechanochemical coupling leads to more patterns (cf. Fig. A.8 (b),(c)). Yet, the discussions in Brinkmann *et al.* [20] and this thesis show that it is essential to include the full 3D tissue geometry. For instance, symmetry breaking such as gastrulation events cannot be observed with lower-dimensional approaches [104, 105, 103].

Finally, we remark that we have already published parts of this thesis in Brinkmann *et al.* [20] and, restricted to 2D cross-sections, in Mercker *et al.* [103]. In this thesis, many novel aspects are added such as local, adaptive mesh refinement, a convergence and stability analysis, stress-mediated feedback loops and the application to symmetry breaking in *Hydra* aggregates including predictive, numerical experiments.

2.3 Mechanochemical interaction

In this section, we finally present our coupled system of prototypical PDEs to simulate mechanochemical pattern formation in biological tissue (Subsection 2.3.2). Beforehand, we introduce reaction-diffusion equations to model the dynamics of signaling molecules. The key aspect of our prototypical system is the coupling of these equations to our structural equation that includes active deformations. The idea of this coupling is to create self-energizing feedback loops which lead to spontaneous and robust mechanochemical patterns.

In Subsection 2.3.3, we present a novel coupling of mechanical cues on morphogen production via invariants of stretch, strain and stress tensors. Vice versa, morphogens results in active cell-shape changes via the active deformation gradient. In particular, we illustrate how these simple interaction rules lead to mechanochemical patterns and present a selection of suitable tensor invariants to describe the mechanical tissue response. Finding suitable combinations of active deformation tensors and mechanical invariants is vital and usually depends on the application at hand.

In the last Subsection 2.3.4, we discuss modified feedback loops where we integrate the mechanical feedback over biological cells and neglect diffusion. This approach is more accurate on a cellular level since not only active deformations but also uniform morphogen production is implemented for each biological cell. On the downside, integration of the feedback on every cell and neglecting diffusion increases the numerical costs.

2.3.1 Reaction-diffusion equations modeling morphogen dynamics

Now, we derive one-dimensional PDEs to model the dynamics of signaling molecules (morphogens). We describe conservation of mass for diffusing morphogens by *Fick's second law* and include a coupling (or reaction) term. This coupling incorporates the feedback of mechanical cues on the dynamics of signaling molecules as well as a degradation of the molecule species. More precisely, we use invariants of stress, strain or deformation tensors to trigger the production of morphogens as discussed in Subsection 2.3.3.

Initially, we have to specify the right function spaces to state the variational formulation of our reaction-diffusion equations. So let us consider concentrations of signaling molecules c_i and a test function ψ with $c_i, \psi \in V_{\Omega(t)}$, where $V_{\Omega(t)}$ was the Sobolev space of functions with first, generalized derivatives in $L^2(\Omega(t))$ that we defined in Eq. (2.16). Further, let us assume that the concentrations $c_i(\mathbf{x}, t)$ are differentiable in time for $t \in [0, T]$ to derive a variational formulation that is weak in space and strong in time. We prefer this formulation since it is more convenient when discretizing our reaction-diffusion equations with the implicit Euler method. More details are given in Chapter 3. Then, our prototypical reaction-diffusion equations in variational, Eulerian formulation read:

Find concentrations of signaling molecules $c_i(\mathbf{x}, t) \in V_{\Omega(t)}$ with initial conditions $c_i(\mathbf{x}, 0) = c_i^0(\mathbf{x})$ such that it holds

$$\int_{\Omega(t)} \partial_t c_i(\mathbf{x}, t)\psi + (\mathbf{v}(\mathbf{x}, t) \cdot \nabla)c_i(\mathbf{x}, t)\psi + \mathbf{D}\nabla c_i(\mathbf{x}, t) \cdot \nabla\psi - R_i(c_i(\mathbf{x}, t))\psi \, \mathrm{d}\mathbf{x} = 0, \tag{2.34}$$

for all test function $\psi \in V_{\Omega(t)}$. Here, $\mathbf{v}(\mathbf{x}, t) \in V^d_{\Omega(t)}$ with $\partial\mathbf{v} \in (H^{-1}(\Omega(t))^d$ is the velocity of the moving domain. Next, $\mathbf{D} \in \mathbb{R}^{d\times d}$, $d = 2, 3$ is the diffusion coefficient tensor, which is specified below. The coupling term $R_i(c_i)$ contains the degradation and the production of signaling molecules, the latter depending on mechanical cues such as stress, strain or stretch, and is introduced in Subsection 2.3.3.

The Lagrangian coordinate system is the natural framework for structural mechanics and the system of choice when using the deformation gradient decomposition to implement growth. This was a key observation in including active deformations, see Section 2.2. Thus, we transform Eq. (2.34) from the Eulerian to the reference framework using the transformation (2.4), the transformation for the time-derivative (2.7) and the transformation of the gradient (2.5), which yields

$$\int_{\Omega} J\partial_t c_i(\boldsymbol{\chi}(\mathbf{X}, t), t)\Psi + J\mathbf{D}\mathbf{F}^{-T}\nabla c_i(\boldsymbol{\chi}(\mathbf{X}, t), t) \cdot \mathbf{F}^{-T}\nabla\Psi - JR_i(c_i(\boldsymbol{\chi}(\mathbf{X}, t), t))\Psi \, \mathrm{d}\mathbf{X} = 0,$$

for all test functions $\Psi \in V$. Note that we skip the index of the function spaces if we state the equations in the reference configuration Ω. Then, we simplify the notation by $C_i(\mathbf{X}, t) = c_i(\boldsymbol{\chi}(\mathbf{X}, t), t)$, drop the arguments and replace $\mathbf{F}^{-T}$ by its adjoint operator $\mathbf{F}^{-1}$ such that our prototypical reaction-diffusion equations in Lagrangian coordinates read: Find morphogen concentration $C_i \in V_\Omega$ with initial conditions $C_i(\mathbf{X}, 0) = C_i^0(\mathbf{X})$ such that it holds

$$\int_{\Omega} J\partial_t C_i\Psi + J\mathbf{F}^{-1}\mathbf{D}\mathbf{F}^{-T}\nabla C_i \cdot \nabla\Psi - JR_i\Psi \, \mathrm{d}\mathbf{X} = 0 \quad \forall\Psi \in V. \tag{2.35}$$

Sufficient regularity provided, we can integrate by parts and use the fundamental lemma of calculus of variations (cf. Gelfand [44, p. 9] (Lemma 1)), which yields that Eq. (2.35) is almost everywhere equivalent to the reaction-diffusion equation in the strong formulation, which reads:

Find concentrations C_i of signaling molecules with initial conditions $C_i(\mathbf{X}, 0) = C_i^0(\mathbf{X})$ such that it holds

$$J\partial_t C_i - \nabla \cdot (J\mathbf{F}^{-1}\mathbf{D}\mathbf{F}^{-T}\nabla C_i) - JR_i(C_i) = 0 \quad \text{in } \Omega. \tag{2.36}$$

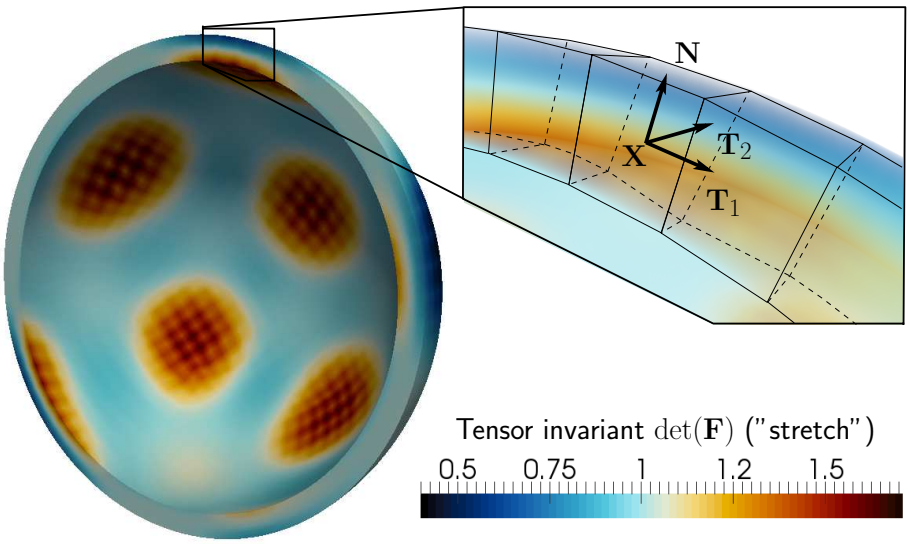

Figure 2.4: Simulation snapshot of the tensor invariant det(**F**) in the reference configuration for pattern formation by a feedback loop including basal constriction (wedging) of the tissue cells and stretch (yellow to red) as the tissue response.

The diffusion coefficient tensor

In our approach, we use the diffusion coefficient tensor $\mathbf{D} \in \mathbb{R}^{d\times d}$ to prescribe a large diffusion coefficient in normal (or radial) direction and a small one in the direction tangential to the tissue sphere. This choice is motivated biologically to ensure free diffusion in radial direction inside our biological cells, whereas a small diffusion coefficient in tangential directions limits diffusion between cells, where the cell-membrane and the intra-cellular space often act as a (selective) diffusion barrier. Mathematically speaking, morphogen is only produced in those parts of the biological cells where stress, strain or stretch modulate its production through the coupling term $R_i = R_i(\boldsymbol{\Sigma}, \mathbf{E}, \mathbf{F}, C_i)$. Here, large radial diffusion helps to reduce local concentration gradients. On the other hand, comparably small tangential diffusion rates ensure that patterns remain localized and are not blurred. This is essential in the three-dimensional regime, since patterns are either strongly localized or vanish for simple, isotropic diffusion ($\mathbf{D} = k_D\mathbf{I}$ with $k_D > 0$).

As an example, let us consider pattern formation based on the active constriction of the basal (outer) side of the tissue cells and stretch modulated morphogen production: Regarding Fig. 2.4, morphogen is produced in the apical (inner) stretched parts (orange) of the biological cells only. Then, our diffusion coefficient tensor ensures free diffusion in radial direction **N** inside the biological cells. On the one hand, this leads to a realistic diffusion behavior in radial direction, on the other hand uniform, radial morphogen concentration results in a realistic apical/basal constriction of the biological cell along the radial axis. We compare the stretch and the resulting morphogen concentrations in the deformed Eulerian configuration in Fig. 2.6.

We are aware of the fact that this approach is inexact on the cellular scale: In tangential direction, diffusion spreads at the same speed inside a cell as across cell boundaries. Yet, this is not a critical simplification to obtain patterns since we demonstrate that pattern formation is stable with regard to significant changes in the diffusion rate, e.g. see Fig. A.5. Notably, our results are confirmed by an enhanced approach where we integrate the mechanical feedback over each biological cell where we locally prescribe uniform morphogen production, see Subsection 2.3.4: This approach is more accurate on the cellular level since we have (almost) instant diffusion inside biological cells togehter with small diffusion rates to account for inter-cellular diffusion. Nonetheless, the final stationary results strongly resemble those obtained in this simpler modeling approach which requires less numerical effort, since we do not have to evaluate integrals over each biological cell in every time-step, which is numerically costly in 3D. Finally, we point out that we are primarily interested in results on the tissue scale, although we find it fruitful to consider the cellular level in the description of active deformations.

So let us consider the reference configuration where we prescribe individual diffusion rates $D_{\mathbf{N}}$ in normal (or radial) Lagrangian direction $\mathbf{N} = |\mathbf{X}|^{-1}\mathbf{X}$ of the tissue sphere and $D_{\mathbf{T}}$ in tangential Lagrangian directions $\mathbf{T}_1$ and $\mathbf{T}_2$, see again Fig. 2.4. This yields the diffusion coefficient tensor

$$\mathbf{D} = \mathbf{Q}^T \operatorname{diag}(D_{\mathbf{N}}, D_{\mathbf{T}}, D_{\mathbf{T}})\mathbf{Q}, \tag{2.37}$$

where $\operatorname{diag}(D_{\mathbf{N}}, D_{\mathbf{T}}, D_{\mathbf{T}})$ is expressed in the point-specific coordinate systems given by the unit vectors $\{\mathbf{N}(\mathbf{X}), \mathbf{T}_1(\mathbf{X}), \mathbf{T}_2(\mathbf{X})\}$. The tensor $\mathbf{Q}(\mathbf{X})$ is the transformation of the Cartesian coordinates to these systems. In matrix notation, they read

$$\operatorname{diag}(D_{\mathbf{N}}, D_{\mathbf{T}}, D_{\mathbf{T}}) = \begin{pmatrix} D_{\mathbf{N}} & 0 & 0 \\ 0 & D_{\mathbf{T}} & 0 \\ 0 & 0 & D_{\mathbf{T}} \end{pmatrix} \text{ and } \quad \mathbf{Q}(\mathbf{x}) = \begin{pmatrix} N_1 & N_2 & N_3 \\ T_{1,1} & T_{1,2} & T_{1,3} \\ T_{2,1} & T_{2,2} & T_{2,3} \end{pmatrix}.$$

Indeed, the tensor $\mathbf{D}$ results in the desired diffusion if it is included in Eq. (2.35) (we neglect J here to simplify the presentation). This can be seen as follows:

$$\begin{aligned} &\int_\Omega D_{\mathbf{N}}\partial_{\mathbf{N}}C_i\partial_{\mathbf{N}}\Psi + D_{\mathbf{T}}\partial_{\mathbf{T}_1}C_i\partial_{\mathbf{T}_1}\Psi \,\mathrm{d}\mathbf{X} + D_{\mathbf{T}}\partial_{\mathbf{T}_2}C_i\partial_{\mathbf{T}_2}\Psi \,\mathrm{d}\mathbf{X} \\ &= \int_\Omega D_{\mathbf{N}}(\mathbf{N}\cdot\nabla)C_i(\mathbf{N}\cdot\nabla)\Psi + D_{\mathbf{T}}(\mathbf{T}_1\cdot\nabla)C_i(\mathbf{T}_1\cdot\nabla)\Psi + D_{\mathbf{T}}(\mathbf{T}_2\cdot\nabla)C_i(\mathbf{T}_2\cdot\nabla)\Psi \,\mathrm{d}\mathbf{X} \\ &= \int_\Omega \operatorname{diag}(D_{\mathbf{N}}, D_{\mathbf{T}}, D_{\mathbf{T}})\mathbf{Q}\nabla C_i \cdot \mathbf{Q}\nabla\Psi \,\mathrm{d}\mathbf{X}, \end{aligned}$$

where simple reformulations and the definition of $\mathbf{Q}$ are used. Using the adjoint matrix $\mathbf{Q}^T$ yields the proposed diffusion coefficient tensor.

In two dimensions, we analogously prescribe different diffusion rates $D_{\mathbf{N}}$ in normal (or radial) Lagrangian direction $\mathbf{N} = |\mathbf{X}|^{-1}\mathbf{X}$ and $D_{\mathbf{T}}$ in tangential Lagrangian direction $\mathbf{T} = |\mathbf{X}|^{-1}(-X_2, X_1)$. This yields the diffusion coefficient tensor

$$\mathbf{D} = \mathbf{Q}^T \operatorname{diag}(D_{\mathbf{N}}, D_{\mathbf{T}})\mathbf{Q},$$

where

$$\operatorname{diag}(D_{\mathbf{N}}, D_{\mathbf{T}}) = \begin{pmatrix} D_{\mathbf{N}} & 0 \\ 0 & D_{\mathbf{T}} \end{pmatrix} \text{ and } \quad \mathbf{Q}(\mathbf{x}) = \begin{pmatrix} N_1 & N_2 \\ T_1 & T_2 \end{pmatrix} = \frac{1}{|\mathbf{X}|}\begin{pmatrix} X_1 & X_2 \\ -X_2 & X_1 \end{pmatrix}.$$

2.3.2 Coupled system of prototypical equations

Eventually, we can assemble our system of prototypical equations, which we use to model mechanochemical pattern formation in biological tissue. For this purpose, we combine our structural equation (2.33) including active deformations (growth) with our reaction-diffusion equations (2.36) that model the dynamics of mobile molecule species.

Quasi-stationary system

So far, we have neglected an important consequence of the deformation gradient decomposition as introduced in Subsection 2.2.1: Implicitly, once we combine our equations, the timescale of growth and the timescale of elasticity are also separated. In our biological setting, growth takes place over a timescale of several days whereas the elastic material response occurs within seconds. That is, the timescale of active deformations t_a is significantly larger than the elastic timescale t_e. Note, that the timescale of active deformation coincides with the timescale of morphogen dynamics by construction, since the active deformation gradient $\mathbf{F}_a(t, C_1, \cdots, C_n)$ (linearly) depends on the concentrations C_i, $i = 1, \cdots, n$. Ultimately, there are thus two different timescales with

$$t_e \ll t_a.$$

Obviously, we are interested in long-term active deformations (growth) rather than in (comparably high frequent) oscillations on the elastic timescale t_e. If we were interested in the elastic behavior of our tissue, we would have to resolve this timescale by very short time steps, which significantly increases the computational costs. The alternative of performing large time steps, however, would be numerically unstable. Moreover, the structural equation and the reaction-diffusion equations are strongly coupled, which adds to the difficulty and rules out splitting approaches, i.e. of solving the equations independently.

We propose a monolithic approach: Instead, our idea is to neglect the second time derivative in the structural equation to the greatest possible extend by regarding it as a stabilization term $\epsilon(k)\rho^0\partial_{tt}\mathbf{u}$, with $\epsilon(k) \ll 1$ depending on the discretization parameter k in time, and to solve the system as a whole. This modification is significant, since we change the character of our system from purely parabolic equations to a system of differential algebraic equations (DAE) with an elliptic structural equation. The numerical instability is thus a product of the different timescales in conjunction with the strong coupling of the equations. In particular, this instability requires numerical stabilization as discussed in Section 3.3.

In summary, we obtain a quasi-stationary system, where the structural, elastic equation is stationary and immediately adjusts to growth induced by changes of concentrations C_i. Thereby, neglecting the elastic timescale ensures that we do not observe unrealistic oscillations of the biological tissue.

System of prototypical equations

Let $\Omega \subset \mathbb{R}^d$, $d = 2, 3$ be a (bounded) domain. Further, let the boundary $\partial\Omega$ of our domain be split into three non-overlapping, i.e. disjoint parts $\partial\Omega = \Gamma_D \cup \Gamma_N \cup \Gamma_R$, where Dirichlet, Neumann

and Robin boundary conditions are imposed, respectively. Then, our prototypical coupled system of the structural equation (2.33) including active deformations and of the reaction-diffusion equations (2.36) reads:

Find displacement $\mathbf{u}$ and concentrations of signaling molecules C_i, $i = 1, \cdots, n$ with initial conditions $\mathbf{u}(\mathbf{X}, 0) = 0$, $C_i(\mathbf{X}, 0) = C_i^0(\mathbf{X})$ such that

$$\begin{aligned} -\nabla \cdot (\mathbf{F}\boldsymbol{\Sigma}) &= 0 && \text{in } \Omega, \\ J\partial_t C_i - \nabla \cdot (J\mathbf{F}^{-1}\mathbf{D}\mathbf{F}^{-T}\nabla C_i) - JR_i &= 0 && \text{in } \Omega,\ i = 1, \cdots, n \\ \mathbf{u} &= 0 && \text{on } \Gamma_D, \\ \mathbf{F}\boldsymbol{\Sigma}\,\mathbf{N} &= \mathbf{G} && \text{on } \Gamma_N \text{ and} \\ \mathbf{r}(\mathbf{u}, \nabla\mathbf{u}, \mathbf{N}) &= 0 && \text{on } \Gamma_R \end{aligned} \tag{2.38}$$

holds, where

$$\boldsymbol{\Sigma} = J_a \mathbf{F}_a^{-1} \boldsymbol{\Sigma}_e \mathbf{F}_a^{-T}, \quad \boldsymbol{\Sigma}_e = \lambda \operatorname{tr}(\mathbf{E}_e)\mathbf{I} + 2\mu\mathbf{E}_e, \quad \mathbf{E}_e = \frac{1}{2}(\mathbf{F}_e^T\mathbf{F}_e - \mathbf{I}),$$
$$\mathbf{F}_e = \mathbf{F}\mathbf{F}_a^{-1}, \quad \mathbf{F} = \nabla\mathbf{u} + \mathbf{I}, \quad J = \det(\mathbf{F}), \quad J_a = \det(\mathbf{F}_a)$$

and where μ, λ are the Lamé constants as introduced above. Further, R_i are the coupling terms which incorporate the feedback of mechanical tensor invariants on morphogen concentrations C_i via $R_i = R_i(I(\boldsymbol{\Sigma}), I(\mathbf{E}), I(\mathbf{F}), C_1, \cdots, C_n)$. Vice versa, $\boldsymbol{\Sigma}(\mathbf{F}_a(t, C_1, \cdots, C_n))$ allows for a reverse coupling of morphogen concentrations C_i on the active deformation process such as local tissue growth or active cell-shape changes. The precise form of the coupling is discussed in the next section.

In general, homogeneous Neumann boundary values are prescribed on the entire boundary $\partial\Omega$. In some applications, it is also useful to implement surface forces $\mathbf{G}$ as Neumann boundary conditions on Γ_N or Robin (slip) conditions $\mathbf{r}(\mathbf{u}, \nabla\mathbf{u}, \mathbf{N})$ on Γ_R. One example for the latter is modeling a pipette in predictive numerical experiments for the symmetry breaking in *Hydra*, where the pulling force by the pipette is specified on Γ_N and the glass body of the pipette is incorporated by a Robin condition (cf. Subsection 5.4.2). In the applications presented in this thesis, external volume forces are not considered and we set $\mathbf{f} = 0$ in Eq. (2.33).

Finally, $\mathbf{D} \in \mathbb{R}^{d\times d}$ is the diffusion coefficient tensor that is expressed in matrix notation by

$$\begin{aligned} \mathbf{D} &:= \mathbf{Q}(\mathbf{X})^T \operatorname{diag}(D_\mathbf{N}, D_\mathbf{T})\mathbf{Q}(\mathbf{X}) && \text{for } d = 2 \text{ and} \\ \mathbf{D} &:= \mathbf{Q}(\mathbf{X})^T \operatorname{diag}(D_\mathbf{N}, D_\mathbf{T}, D_\mathbf{T})\mathbf{Q}(\mathbf{X}) && \text{for } d = 3, \end{aligned}$$

with a diagonal matrix containing the diffusion coefficient $D_\mathbf{N}$ in normal (or radial) Lagrangian direction $\mathbf{N} = |\mathbf{X}|^{-1}\mathbf{X}$ and the diffusion coefficient $D_\mathbf{T}$ in the tangential directions $\mathbf{T}_1$ and $\mathbf{T}_2$ (or just one direction $\mathbf{T}$ in 2D). The rotation matrix $\mathbf{Q}^T$ transforms the diagonal matrix $\operatorname{diag}(D_\mathbf{N}, D_\mathbf{T}, D_\mathbf{T})$, which is defined in the point-specific coordinate systems given by the orthogonal unit vectors $\mathbf{N}(\mathbf{X})$, $\mathbf{T}_1(\mathbf{X})$ and $\mathbf{T}_2(\mathbf{X})$, to Euclidean coordinates. This choice is biologically motivated, as a large coefficient $D_\mathbf{N}$ in radial direction ensures free diffusion inside the biological cells, whereas a small coefficient $D_\mathbf{T}$ limits diffusion between biological cells (at least on the tissue scale), see Subsection 2.3.1 for details.

Note that in practice, the initial conditions $\mathbf{u}(\mathbf{X}, 0) = 0$, $C_i(\mathbf{X}, 0) = C_i^0(\mathbf{X})$ are incompatible, since the initial displacement $\mathbf{u}(\mathbf{X}, 0)$ corresponding to the prescribed initial concentrations $C_i^0(\mathbf{X})$ is usually unknown and set to zero. Hence, it takes a few time steps for the deformation and the concentrations to adjust. The compatibility of initial conditions and the setup of the parameters above are discussed in detail for each application, namely growth processes in tips of colonial hydroids, embryonic development, and symmetry breaking in *Hydra*, see Sections 5.2, 5.3 and 5.4, respectively.

2.3.3 Coupling

We designed our prototypical, coupled system of equations (2.38) to be a framework for investigating mechanochemical pattern formation in a wide range of model organisms. The centerpiece of the mechanochemical interactions in this framework is the coupling between structural mechanics and morphogen dynamics. Based on recent experimental data, we present simple positive feedback loops: Firstly, we show how morphogen leads to active cell shape changes via the active deformation gradient $\mathbf{F}_a = \mathbf{F}_a(t, C_1, \cdots, C_n)$. Secondly, we propose a novel coupling based on the invariants of stress, strain and stretch tensors on the morphogen production. In this context, we give an overview of tensor invariants that are well-suited as mechanical feedback and we obtain coupling terms of the form $R_i(I_j(\boldsymbol{\Sigma}))$, $R_i(I_j(\mathbf{E}))$, $R_i(I_j(\mathbf{F}))$ for invariants $I_j(\cdot)$, $j = 1, \cdots, d$. Finally, we illustrate how these mechanochemical couplings form positive, self-energizing feedback loops which lead to pattern formation.

In this thesis, we mainly consider morphogen-induced active apical/basal constriction (wedging) or active apico-basal shortening (thinning) of biological cells in conjunction with stretch-, strain- and compression-based feedback on the morphogen production. Finding such combinations of active deformation tensors and mechanical invariants is vital to obtain mechanochemical patterns. Clearly, the choice of the active deformations and the mechanical feedback depends on the application at hand: On the one hand, only certain active deformations might be observed in (parts of) the organism under consideration. On the other hand, the elastic response due to these active deformations dictates the shape of the tensor invariants. This shape of the mechanical tensor invariants is crucial to find suitable feedback loops. Further implications of these choices and how feedback loops for a model organism are found are discussed in the context of this subsection.

Eventually, we have implicit couplings in both the structural and the reaction-diffusion equations. In the latter, they appear in the transformation from Eulerian to Lagrangian coordinates in terms of $\mathbf{F}$ and its determinant (compare Eq. (2.35) and Eq. (2.34)). In the structural equation, implicit couplings in terms of $\mathbf{F}_a(t, C_1, \cdots, C_n)$ also stem from transformations, namely from those transformations between the Eulerian, the intermediate and the reference configuration (cf. Eq. (2.31)).

The following paragraphs are strongly related to the derivation of the coupling in our publications Brinkmann *et al.* [20] and Mercker *et al.* [103]. Yet the models and calculations were restricted to 2D cross sections in the latter work. Here, the discussion is extended to a more general setting including strain- and stress-based mechanical feedback, a larger set of suitable

tensor invariants and active deformations such as apico-basal shortening (thinning) of biological cells.

Coupling of morphogen on active deformations of (discrete) biological cells

In experiments, signaling molecules have been shown to influence the mechanics of biological cells in various ways, namely by local tissue growth, modifications of stiffness properties or active cell-shape changes [12, 17, 32, 58]. These processes can be anisotropic or can be restricted to just one of several cell layers. In our applications, we mainly consider morphogen-induced basal/apical constriction (wedging) and apico-basal shortening (thinning) of biological cells, since these are commonly observed deformations during morphogenesis, see [89, 98, 115, 118] and [31, 123, 139].

Clearly, the choice of the active deformation gradient depends on the application. In short, we prescribe basal/apical constriction for embryogenesis and apico-basal shortening for symmetry breaking in *Hydra*. The former results in a change of the tissue curvature by a constriction of the outer/inner sides of the biological cells. Apico-basal shortening results in a local thinning of the tissue. Our approach is flexible and simple isotropic or anisotropic growth as well as growth in just one (of several) cell layers to obtain curvature via a "bimetal effect" are also shown to lead to pattern formation (cf. Chapter 5). To complete the presentation, we also discuss combinations of active deformation tensors such as basal constriction with apico-basal shortening. The latter combination of deformation processes can actually be observed in nature, e.g. in the fish *Brachydanio rerio*, see Davies [31] (Chapter 18).

In morphogenesis, it is a common assumption that morphogen concentrations lead to local remodeling of the cytoskeleton and thus to local, active cell-shape changes [1, 104, 120]. Mathematically, this implies the direct coupling of morphogen concentrations with the active deformation gradient, namely we prescribe morphogen-induced active deformations via

$$\mathbf{F}_a = \mathbf{F}_a(t, C_1, \cdots, C_n).$$

In general, we consider active cell-shape changes of individual, biological cells, which results in a piecewise definition of the active deformation gradient (see Eq. 2.26). We believe that a piecewise description of active deformations is more precise on the cellular scale and numerical simulations reveal that larger deformations on the tissue scale (such as gastrulation events) are only obtained for piecewise-defined, active deformation gradients. Yet, mechanochemical pattern formation based on continuously defined active deformation tensors is also possible in the presented framework. Since we are interested in pattern formation on the tissue level, we do not resolve any sub-cellular structures. Apart from piecewise-defined active deformations, our approach remains continuous in general. One exception is an enhanced approach where we integrate the mechanical feedback over each biological cell separately and prescribe constant morphogen production (essentially free diffusion) inside these cells. This approach is more accurate on the cellular level and presented at the end of this chapter. The precise form of the implemented active deformation tensors depends on the application at hand and is specified in Chapter 5.

Notably, the overall deformation is then determined by the elastic material response $\mathbf{F}_e$, which ensures the continuity of the overall deformation.

Overall, we consider the following direct coupling of morphogen concentrations C_i on the elastic material law

$$\boldsymbol{\Sigma}_e = \boldsymbol{\Sigma}_e(\mathbf{F}_e) = \boldsymbol{\Sigma}_e(\mathbf{F}\mathbf{F}_a^{-1}(t, C_1, \cdots, C_n))$$

and thereby on tissue mechanics via

$$\boldsymbol{\Sigma} = J_a \mathbf{F}_a^{-1} \boldsymbol{\Sigma}_e(\mathbf{F}\mathbf{F}_a^{-1}(t, C_1, \cdots, C_n))\mathbf{F}_a^{-T}.$$

These interconnections are implemented in our prototypical system of PDEs (cf. Eq. (2.38)).

Mechanical feedback on the morphogen production

A main accomplishment of this work is the development of positive feedback loops that are based on a novel coupling of mechanics tensor invariants on the production of morphogens via the coupling terms R_i. Mechanosensitive mechanisms controlling chemical cellular processes have been extensively studied in biological experiments within the last decade, see e.g. [37, 95]. Indeed, many recent studies emphasize the active involvement of mechanics in pattern formation [13, 24, 35, 105, 117]. Namely, stress [90, 116, 117], strain [94, 153] and stretch/compression [20, 24, 79, 105] have been shown to influence morphogen dynamics.

Clearly the mechanical tissue response (to active deformations) on morphogen dynamics has to be objective (frame-indifferent). In particular, this means that the response should not depend on the choice of an observer and should not change under rotations of the coordinate system. In Subsection 2.1.4 we saw that the second Piola-Kirchhoff stress tensor $\boldsymbol{\Sigma}$, the deformation gradient $\mathbf{F}$ and the Green-Lagrange strain tensor $\mathbf{E}$ are objective. We choose the second Piola-Kirchhoff stress tensor $\boldsymbol{\Sigma}$ from the available, objective stress measures since it is given in the reference configuration just as our prototypical equations. Importantly, invariants of these frame-indifferent tensors are also objective: They are scalar measures of stress, strain and stretch and have the same value regardless of the choice of an observer. Thus, invariants of these tensors are well-suited for a mechanochemical feedback on the production of signaling molecules. Overall, our coupling term takes the form

$$R_i(I_j(\boldsymbol{\Sigma}), I_j(\mathbf{E}), I_j(\mathbf{F}), C_1, \cdots, C_n), \quad j = 1, \cdots, d. \tag{2.39}$$

It is objective for invariants I_j of the objective tensors $\boldsymbol{\Sigma}, \mathbf{F}$ and $\mathbf{E}$. Suitable feedback loops based on these tensor invariants are presented in the next subsection. Details on tensor invariants and objectivity are given in Subsection 2.1.4 or in literature, see e.g. Ciarlet [27] (Section 3.5) or Holzapfel [66] (Section 1.4).

In practice, the tensor invariants are included in the reaction-diffusion equations using the Michaelis-Menten kinetics (cf. Murray [109] (Chapter 6) or Brockmann [22]), which yields

$$R_i(I_j(\cdot), C_i) = k_2 \frac{\max\{I_j(\cdot), 0\}}{k_m + \max\{I_j(\cdot), 0\}} - k_1 C_i, \qquad j = 1, \cdots, d, \tag{2.40}$$

with positive constants $k_1, k_2, k_m > 0$. Here, k_1 represents a constant degradation rate of the morphogens in the entire tissue and the Michaelis constant k_m describes the value of $I_j(\cdot)$ where

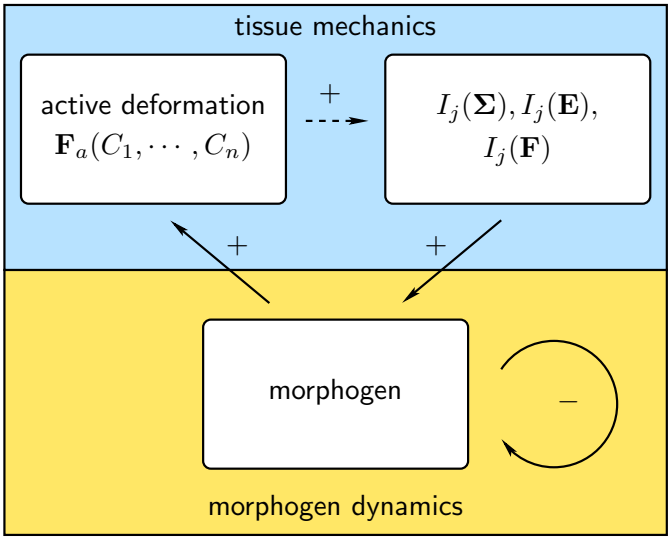

Figure 2.5: Schematic view of our positive feedback loops (similar to our publication [103]). Continuous arrows indicate explicit model assumptions, dotted arrows depict the passive material response to the active deformations.

half of the maximal production rate k_2 is reached. The nonlinear form of the production term results in convergence towards the maximal morphogen production rate k_2 for large values of the employed tensor invariant $I_j(\cdot)$. This saturation effect of $I(\cdot)$-induced morphogen production is a common, biochemical modeling assumption due to existence of maximal production and translation rates for gene products, see again Murray [109] or Brockmann [22]. Correspondingly, numerical tests show that the Michaelis-Menten kinetics are essential to bound the concentrations of signaling molecules in our positive feedback loops (cf. Fig 2.5) and thus to control the deformations. In summary, the Michaelis-Menten kinetics balance production and degradation rates such that stationary, mechanochemical patterns are obtained and prevent the system from developing non-biological singularities.

Note that in a more general setting, there can be further coupling terms in R_i. For instance, we might consider reactions with other morphogen species of concentrations C_k for $k \in \{1, \cdots, n\}$ as well.

Positive, mechanochemical feedback loops

In our coupled system of equations, mechanochemical patterns are formed by positive feedback loops as sketched in Fig. 2.5. We published suitable feedback loops in Brinkmann *et al.* [20] and in Mercker *et al.* [103], with the restrictions to stretch-based loops and to 2D cross-sections of the tissue sphere, respectively. Here, these works are extended by feedback loops based on strain and stress in combination with active, apical/basal constriction or apico-basal shortening of biological cells in three dimensions.

Our feedback loops are based on two experimentally motivated assumptions:

- Local morphogen levels lead to active, apical/basal constriction (or elongation) of individual, biological cells [98] (which again leads to local stretch/compression, strain and stress due to the elastic response of the biological tissue); and
- Local stretch/compression [79, 116], strain [94, 153] or stress [90, 117] induce local morphogen production.

By construction, these feedback loops are self-energizing, which we have indicated by the "+" signs in Fig. 2.5. The Michaelis-Menten kinetics (cf. Eq. (2.40)) ensure that the morphogen production becomes constant for large deformations, which slows down pattern formation. In conjunction with the concentration-dependent morphogen degradation (indicated by "−") we eventually obtain global, stationary solutions. The only exception are gastrulation events which involve significant geometry changes of the tissue sphere and, at first, do not result in stationary solutions. In these cases, we show that an internal pressure modeling the fluid that is contained inside the tissue sphere stops the invagination process and leads to stationary solutions once again. Details and results on an internal pressure are presented in Subsection 5.3.5.

In the following, we give a short overview of suitable, positive feedback loops that we consider in this work. These feedback loops lead to *de novo* pattern formation and were obtained by extensive numerical simulations. As previously discussed in this section, the choice of the active deformation tensor depends on the application at hand.

(A) In our application to embryogenesis we prescribe apical/basal constriction. This active process leads to spontaneous and robust mechanochemical pattern formation in conjunction with mechanical feedbacks (as implemented in Eq. (2.40)), if they are based on the following invariants:

  (1) The trace of the Green-Lagrangian strain tensor $I_1(\mathbf{E}) = \mathrm{tr}(\mathbf{E})$, which represents the hydrostatic strain;

  (2) The determinant of the deformation gradient $I_3(\mathbf{F}) = \det(\mathbf{F})$, which has the physical interpretation of compression or stretch. More precisely, $\det(\mathbf{F}) = \frac{dv(t)}{dV}$ is the ratio of the deformed volume element $dv(t)$ to the initial one dV;

  (3) The determinant of the elastic second Piola-Kirchhoff stress tensor $I_3(\mathbf{\Sigma}) = \det(\mathbf{\Sigma})$, which has no direct physical interpretation; and

  (4) The second, deviatoric tensor invariant of the second Piola-Kirchhoff stress tensor $I_2(\mathbf{\Sigma})$, which is often used to predict yielding of materials under loading (von Mises yield criterion).

  In the following, we term these four feedback loops based on the mechanical feedback they involve as "stretch-/compression-mediated feedback" (1.), "strain-mediated feedback" (2.) and "stress-mediated feedback" (3.), (4.), respectively. In Chapter 5 we demonstrate that these simple, positive feedback loops indeed lead to spontaneous (*de novo*) and robust mechanochemical pattern formation.

Alternatively, positive feedback loops based on active deformations such as isotropic growth in just one cell layer ("bimetal effect") or continuously defined active deformations also lead to pattern formation (in combination with stretch- or strain-based mechanical feedback). For the sake of a clear and brief presentation, these active processes are not considered in this thesis. Interestingly, large deformations such as gastrulation could not be observed for continuously defined active deformation tensors in our numerical tests.

(B) In the application to symmetry breaking in *Hydra* we prescribe apico-basal shortening of the biological cells. Due to this active deformation, the biological cell shortens in radial direction and enlarges in the tangential ones. These relative length changes are well-described by the concept of strain. Thus, it is not surprising that this active process leads to spontaneous and robust mechanochemical pattern formation in conjunction with strain-based mechanical feedback (2.40), where we use the trace of the Green-Lagrangian strain tensor $I_1(\mathbf{E}) = \mathrm{tr}(\mathbf{E})$. Physically, this invariant measures the hydrostatic part (i.e. the diagonal) of the strain tensor.

Illustration: How positive feedback loops lead to pattern formation

The mechanochemical feedback loops presented above have the capacity to spontaneously create mechanochemical patterns. As an example, let us consider a stretch-mediated feedback loop based on active basal constriction as illustrated in Fig. 2.6. Here, mechanochemical patterns develop for the following reason:

Once morphogen concentrations or the tissue stretch is locally inhomogeneous (e.g. due to the initial conditions) both morphogen and tissue curvature locally amplify each other. On the one hand, local morphogen levels lead to basal constriction of the biological cells (illustrated by red arrows in the top left Fig. 2.6). On the other hand, the elastic tissue response to these active deformations has to ensure the continuity of the overall deformation. In particular, this introduces stretch/compression in the lower/upper halves of the cells (cf. the stretched/compressed parts (orange/blue) in the top right of Fig. 2.6). In turn, this stretch results in morphogen production which completes the circle of our mechanochemical feedback loops. In developmental biology, the latter process is known as "short range activation". As a result of these interactions, patterns of co-localized mechanical stretch and morphogen concentrations emerge. Eventually, the morphogen concentrations saturates due to the Michaelis-Menten kinetics which leads to stationary solutions.

The "long-range" inhibition, i.e. the inhibition of pattern formation in the proximity of active patterns, is mainly constituted by tissue mechanics: As soon as the tissue is locally curved, in oder to maintain continuity, the surroundings of the curved patch have to be passively bent into the opposing direction. In the transition zone, however, this results in little curvature and prevents active deformations from inducing stretch here. Hence, a significantly smaller, continuous elastic response is necessary here in comparison to actively deformed regions. Consequently, there is little morphogen production, which is consumed by the degradation rate, in the (light-blue) passively bent areas. In the regions of activity, however, large and possibly discontinuous

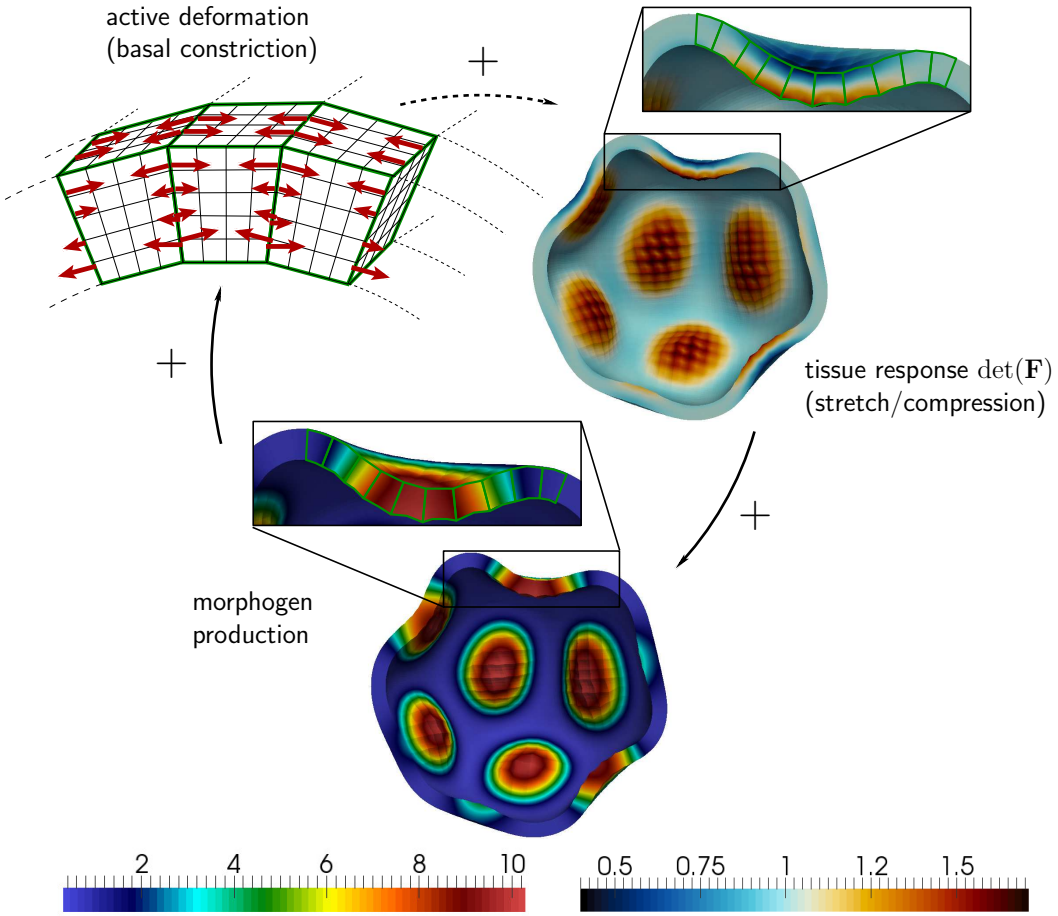

(a) Morphogen concentration C (b) Tensor invariant $\det(\mathbf{F})$

Figure 2.6: Schematic view of our positive stretch-mediated feedback loop, similar to Fig. 1 in our publication [20]). Local accumulation of morphogen leads to active constriction (red arrows) in biological cells (green), which leads to stretch ($\det(\mathbf{F}) > 1$) due to the elastic material response, which in turn leads to morphogen production.

active deformations require a strong elastic response that results in stretch and triggers our feedback loop (compare the light-blue areas and the red/orange ones in Fig. 2.6).

By the same mechanism of mechanical long-range inhibition, strong patterns or well-located combinations of weak patterns can dissolve smaller ones.

Suitable combinations of feedback loops can be found by numerical tests: Initially, we prescribed an active deformation that is commonly observed in the model organism under consideration, e.g. apical/basal constriction observed in embryogenesis. Next, we analyze the mechanical feedback to these active deformations by visualizing all tensor invariants listed above. Usually, we pick mechanical cues that are perfectly co-localized with the morphogen patches and test the full feedback loop on 2D cross-sections. By design of our implementation, we can simply switch with any promising model to the full 3D geometry (which is numerically costly) to conduct further numerical studies.

Remark: As described above, we use different diffusion rates to distribute local morphogen levels inside the biological cells. We are aware that this diffusion mechanism is inexact on the cellular level since concentrations gradients in tangential directions can remain inside biological cells and diffusion across cells boundaries can be as fast as inside cells (cf. Fig. 2.6). Yet, we point out that we are rather interested in pattern formation on the tissue scale and resolve the cellular level only when necessary (namely in modeling active deformations) to reduce computational costs. Nevertheless, we present an enhanced approach that is more accurate on the cellular level since we integrate the mechanical feedback over the biological cells in the next subsection. At the same time we stress that this enhanced model is not essential to obtain patterns. On the contrary, we observe that our usual approach is robust to large changes in the diffusion rates and that both models produce (almost) identical results.

2.3.4 Enhanced model: Integrate mechanical feedback over biological cells

Finally, we present an enhanced model where we integrate the tissue response over each biological cell. Here, we prescribe a constant morphogen production rate on each biological cell that depends on the average mechanical feedback integrated over this cell. In practice, we integrate the mechanical cues that we compute from the previous time-steps. This approach is more accurate on the cellular level: On the one hand, we have free (almost instant) diffusion inside the biological cells. On the other hand, diffusion is no longer required to distribute morphogen inside the biological cells and we can freely choose inter-cellular diffusion rates to influence the size and the number of biological patterns. The latter property reflects the influence of the cell-membranes and the intra-cellular space which often act as a (selective) diffusion barrier.

An alternative approach that might result in similar observations are discontinuous Galerkin methods, which allow us to model one concentration variable for each biological cell. This interesting approach is more precise on a cellular level as well. However, it requires significant changes in our implementation and is thus postponed to future research.

In our enhanced approach, we assume that morphogen is only expressed if the mechanical feedback exceeds a given threshold: First numerical tests revealed that integrating the mechanical feedback over biological cells alone is not practical, since tiny mechanical feedback in parts

of a cell is transported to the whole cell via integration. That way, any pattern spreads over the whole tissue sphere. We circumvent this obstacle by introducing thresholds for the expression of morphogen: Indeed, target genes in a biological cell are only expressed if morphogen concentrations in this cell are above a certain threshold, or, vice versa, "morphogens are able to induce or maintain the expression of different target genes at distinct concentration thresholds." (Gregor *et al.* [51]).

Mathematically, we proceed as follows: On each biological cell K_i, we integrate one of the suitable tensor invariants $I_j(\mathbf{X})$, $j = 1, \cdots, n$ describing stretch, strain or stress that we listed for our usual approach, see Subsection 2.3.3. Then, the mechanical feedback $\mathcal{I}_{|K_i}$ integrated over the biological cell K_i is given by

$$\mathcal{I}_{\mathcal{K}_i} = \int_{K_i} I(\mathbf{X}) \, \mathrm{d}\mathbf{X}$$

As explained above, we include our mechanical feedback using the Michaelis-Menten kinetics (cf. Murray [109] or Brockmann [22]). Further, we assume that morphogen is produced if a threshold $THRES$ of target genes is exceeded. In our implementation, we do not model gene activity explicitly but rather imply that genes (and morphogens) are expressed due to mechanical stretch, strain or compression. In our modeling framework, the coupling term in the reaction-diffusion equation hence takes the form

$$R(\mathcal{I}, C) = \begin{cases} k_2 \dfrac{\mathcal{I}}{k_m + \mathcal{I}} - k_1 C & \text{for } \mathcal{I} > THRES \\ -k_1 C & \text{else,} \end{cases} \tag{2.41}$$

with the positive constants $k_1, k_2, k_m > 0$ that were introduced above (cf. Eq. (2.40) for details).

Originally, we developed the idea of integrating the mechanical feedback for the stress-mediated feedback loop. Here, the feedback is expressed in terms of the discontinuous first Piola-Kirchhoff stress tensor $\mathbf{\Sigma}$ and is strongest in singular points in the corners of the active biological cells. Integration smoothes this feedback and hence large diffusion rates to distribute morphogens are obsolete in this enhanced approach.

Numerical simulations based on this enhanced model are presented in Subsection 5.3.6.

3 Discretization

In this chapter, we present the finite element discretization of our coupled system of prototypic equations (2.38) that we introduced in Chapter 2. These equations are discretized by Rothe's method: Firstly, we discretize in time by suitable implicit time-stepping schemes which results in a sequence of quasi-stationary PDEs. Secondly, these problems are discretized in space by finite element methods (FE methods). The choice of Rothe's method offers the practical advantage that we can adopt the spatial discretization in between time-steps by local mesh refinement. Finally, we present an extensive numerical convergence and stability analysis.

This chapter is subdivided into the following parts: In Section 3.1, we present the variational formulation (Galerkin formulation) of our prototypical system of PDEs modeling mechanochemical long-term problems. Then, in Section 3.2, we introduce the discretization in time by finite difference methods: We employ the implicit Euler scheme for the discretization of the reaction-diffusion equations modeling morphogen dynamics, whereas the second time derivative in the structural equation is discretized by a two-step method. The latter temporal derivative in the structural equation is considered as a stabilization term.

This stabilization is presented in Section 3.3 and tackles the instabilities, which stem from the strong coupling of our system of equations, the different timescales of growth and elasticity involved as well as the sole description of homogeneous Neumann values.

In Section 3.4, the discretization in space is in focus. The spatial discretization is based on linear and quadratic finite elements (Q_1- and Q_2-FE) and a triangulation by quadrilaterals and hexahedra in 2D and 3D, respectively.

Ultimately, in Section 3.5, we conduct a comprehensive convergence analysis and define a quantity of interest to measure discretization and stabilization errors. As quantity of interest we choose the coupling term based on mechanical tensor invariants of tissue mechanics on morphogen dynamics. In 2D, we observe optimal quadratic and cubic convergence rates for linear and quadratic (Q_1- and Q_2-) finite elements, respectively. In 3D, fewer mesh levels are available due to the huge computational effort involved and Q_2-FE are essential to efficiently reduce the error in our quantity of interest.

Furthermore, we perform a stabilization analysis where we develop a guideline for choosing the stabilization parameter. Following this guideline, we verify that the stabilization as well as the temporal discretization error are well below the discretization error in space.

Lastly, we propose a local mesh refinement strategy to numerically resolve the discontinuous material response in case of a stress-mediated feedback loop. Here, we demonstrate that adaptive mesh refinement significantly improves the convergence of our solution approach.

3.1 Galerkin Formulation

The Galerkin formulation of our system of prototypic equations is given by combining the structural equation (2.32) and reaction-diffusion equation (2.35), which were both derived in the weak formulation. The mechanochemical coupling of these equations was discussed in Section 2.3 and is specified for each application at hand.

In the following, we derive the Galerkin formulation for our framework of prototypical systems of PDEs on the (bounded) domain $\Omega \subset \mathbb{R}^d$, $d = 2, 3$. The boundary $\partial\Omega$ of this domain is split into three disjoint parts $\partial\Omega = \Gamma_D \cup \Gamma_N \cup \Gamma_R$, where Dirichlet, Neumann and Robin boundary conditions are imposed, respectively. Next, let $V \coloneqq H^1(\Omega)$ be the Sobolev space of first, generalized derivatives in $L^2(\Omega)$, where the latter space denotes the Lebesgue space of measurable, square-integrable functions on Ω. $L^2(\Omega)$ is even a Hilbert space with the scalar product and the induced norm

$$(\mathbf{u}, \mathbf{v})_{L^2(\Omega)} = \int_\Omega \mathbf{u}\mathbf{v}\,\mathrm{d}\mathbf{X}, \quad \|\mathbf{u}\|_{L^2(\Omega)} = (\mathbf{u}, \mathbf{u})^{\frac{1}{2}}_{L^2(\Omega)}.$$

Details on these spaces are given in literature, see e.g. Alt [2] or Rannacher [125].

In the following, the L^2-scalar product and its norm are used to simplify our notation, e.g. in the definition of a quantity of interest to measure convergence. If the context is clear, we simply denote the L^2-scalar product by $(\cdot, \cdot)_\Omega$.

With these preparations, the Galerkin formulation of our prototypical system of PDEs for test functions $\boldsymbol{\Phi} \in V^d$ and $\Psi \in V$ reads:

Find the displacement $\mathbf{u} \in V_0^d \coloneqq \{\mathbf{v} \in V^d \colon \mathbf{v}|_{\Gamma_D} = 0\}$ and the concentrations of signaling molecules $C_i \in V$ for $i = 0, 1, \cdots, n$ with initial conditions $\mathbf{u}(\mathbf{X}, 0) = 0$, $C_i(\mathbf{X}, 0) = C_i^0(\mathbf{X})$ such that

$$\begin{aligned} (\rho^0 \partial_{tt}\mathbf{u}, \boldsymbol{\Phi})_\Omega + (\mathbf{F}\boldsymbol{\Sigma}, \nabla\boldsymbol{\Phi})_\Omega - (\mathbf{G}, \boldsymbol{\Phi})_{\Gamma_N} - (\mathbf{F}\boldsymbol{\Sigma}\,\mathbf{N}, \boldsymbol{\Phi})_{\Gamma_R} = 0 \qquad & \forall \boldsymbol{\Phi} \in V^d \\ (J\partial_t C_i, \Psi)_\Omega + (J\mathbf{F}^{-1}\mathbf{D}\mathbf{F}^{-T}\nabla C_i, \nabla\Psi)_\Omega - (JR_i, \Psi)_\Omega = 0 \qquad & \forall \Psi \in V \text{ and} \end{aligned} \tag{3.1}$$

for $i = 1, \cdots, n$ holds, where

$$\boldsymbol{\Sigma} = J_a \mathbf{F}_a^{-1} \boldsymbol{\Sigma}_e \mathbf{F}_a^{-T}, \quad \boldsymbol{\Sigma}_e = \lambda \operatorname{tr}(\mathbf{E}_e)\mathbf{I} + 2\mu\mathbf{E}_e, \quad \mathbf{E}_e = \frac{1}{2}(\mathbf{F}_e^T\mathbf{F}_e - \mathbf{I}),$$
$$\mathbf{F}_e = \mathbf{F}\mathbf{F}_a(t, C_1, \cdots, C_n)^{-1}, \quad \mathbf{F} = \nabla\mathbf{u} + \mathbf{I}, \quad J = \det(\mathbf{F}), \quad J_a = \det(\mathbf{F}_a),$$

and where μ, λ are the Lamé constants. These tensors and constants were introduced above in the derivation of the structural equation (cf. Eq. (2.32)). Next, R_i are the coupling terms that incorporate the mechanical feedback on morphogen dynamics. Vice versa, $\mathbf{F}_a(t, C_1, \cdots, C_n)$ prescribes morphogen-induced, active deformations such as active cell-shape changes. The precise form of the coupling usually depends on the application at hand (e.g. see Fig. 2.6). Finally, $\mathbf{D} \in \mathbb{R}^{d\times d}$ is the diffusion coefficient tensor.

In general, homogeneous Neumann values are prescribed on the entire boundary $\partial\Omega$. In some applications, it is also useful to implement surface forces $\mathbf{G}$ as Neumann boundary conditions on

Γ_N or Robin (slip) conditions $\mathbf{r}(\mathbf{u}, \nabla\mathbf{u}, \mathbf{N})$ on Γ_R. For instance, we employ the latter conditions in predictive numerical experiments modeling micropipette aspiration of biological tissue. In this thesis, we do not consider external volume forces, so we set the right hand side in the structural equation to $\mathbf{f} = 0$.

To simplify the notation, we introduce the semi-linear elliptic differential operator $\mathbf{a}(\mathbf{u}, C_i)(\boldsymbol{\Phi})$, which is nonlinear in $\mathbf{u}$ and C_i (due to the nonlinear dependency of $\boldsymbol{\Sigma}(C_i)$ on C_i) and linear in its second argument and the semi-linear operator $b(\mathbf{u})(C_i, \Psi)$ that are defined as

$$\begin{aligned} \mathbf{a}(\mathbf{u}, C_i)(\boldsymbol{\Phi}) &\coloneqq (\mathbf{F}\boldsymbol{\Sigma}(C_i), \nabla\boldsymbol{\Phi})_\Omega - (\mathbf{G}, \boldsymbol{\Phi})_{\Gamma_N} - (\mathbf{F}\boldsymbol{\Sigma}\,\mathbf{N}, \boldsymbol{\Phi})_{\Gamma_R} \\ b(\mathbf{u})(C_i, \Psi) &\coloneqq (J\mathbf{F}^{-1}\mathbf{D}\mathbf{F}^{-T}\nabla C_i, \nabla\Psi)_\Omega - (JR_i, \Psi)_\Omega, \quad i = 1, \cdots, n. \end{aligned} \tag{3.2}$$

These differential operators are particularly useful in the definition of the Newton residuals and in the temporal discretization.

Note that this is a prototypical framework. We specify the equations, the active deformations, the mechanical feedback and computational domain Ω for each application at hand. Namely, we consider applications to growth pulsations in hydroid tips, embryogenesis and symmetry breaking in *Hydra* (cf. Sections 5.2, 5.3 and 5.4, respectively).

3.1.1 (Dirichlet) boundary values

The main intention of this thesis is the modeling and derivation of efficient numerical methods to solve prototypical systems of PDEs modeling mechanochemical long-term problems. In this framework, we also consider the implementation of Dirichlet boundary values. In general, however, the location of mechanochemical pattern formation is *a priori* unknown, for instance in the applications to embryogenesis or symmetry breaking in *Hydra*. Besides, numerical tests confirm that the prescription of Dirichlet values substantially influences pattern formation in these applications: Either, the organism cannot produce patterns or the entire organism aligns symmetrically to the Dirichlet boundary if Dirichlet values are implemented. Furthermore, convergence of our methods is only mildly improved by imposing Dirichlet values.

Nonetheless, Dirichlet values are well suited to model mechanical properties of an organism in our application to growth pulsations in hydroids tips, where the computational domain covers the tip of the growing hydroid stolon. Here, homogeneous Dirichlet values are prescribed on the cutting surface towards the remaining body of the organism. More precisely, the soft tissue layers (coenosarc) in colonial hydroids are surrounded by a rigid, organic skeleton (perisarc), where the latter is assumed to be immobile in the cross-section to the remaining organism during growth pulsations. The hydroid tip geometry including the boundary parts is illustrated in Fig. 5.3 (b).

3.2 Discretization in time

We use Rothe's method for the discretization of our coupled systems of PDEs. Rothe's method is based on discretizing first in time and then in space. Here, we focus on the temporal discretization of our prototypical system of PDEs in variational formulation (3.1). The reaction-diffusion equations modeling the dynamics of morphogen species are discretized in time via a one-step θ-scheme. Strictly speaking, we employ the backward Euler time-stepping scheme (i.e. $\theta = 1$), which is an implicit and A-stable method. This discretization results in a sequence of quasi-stationary, elliptic PDEs. In general, the implicit Euler method has convergence order one [124]. Regarding the structural equation, we use a two-step method to discretize the second derivative in time.

So let us assume that we solve our systems of parabolic PDEs over the time-interval $[0, T]$, such that a stationary state is attained for $t = T$. Then, we introduce discrete points in time $t_0, t_1, t_2, \cdots, t_M$ with

$$0 = t_0 < t_1 < t_2 < \cdots < t_M = T, \quad k_m := t_m - t_{m-1}, \quad k := \max_{0 \leq m \leq M} k_m$$

as well as the notation

$$\mathbf{u}^m = \mathbf{u}(\cdot, t_m), \quad C_i^m = C_i(\cdot, t_m),$$

for $i = 0, 1, \cdots, n$.

With this notation at hand, our prototypical system of PDEs discretized in time by a two-step method for the structural equation and by the implicit Euler scheme for the reaction-diffusion equations reads: Find the displacement $\mathbf{u}^m \in V_0^d := \{\mathbf{v} \in V^d : \ \mathbf{v}|_{\Gamma_D} = 0\}$ and the concentrations of signaling molecules $C_i^m \in V$ for $i = 0, 1, \cdots, n$ with initial conditions $\mathbf{u}^0(\mathbf{X}) = 0$ and $C_i^0(\mathbf{X})$ such that

$$\begin{aligned} \rho^0(\mathbf{u}^m - 2\mathbf{u}^{m-1} + \mathbf{u}^{m-2}, \boldsymbol{\Phi})_\Omega + k^2\, \mathbf{a}(\mathbf{u}^m, C_i^m)(\boldsymbol{\Phi}) = 0 \quad & \forall \boldsymbol{\Phi} \in V^d \\ J(t_m)(C_i^m - C_i^{m-1}, \Psi)_\Omega + k\, b(\mathbf{u}^m)(C_i^m, \Psi) = 0 \quad & \forall \Psi \in V,\ i = 1, \cdots, n, \end{aligned} \tag{3.3}$$

with the elliptic, differential operators introduced above. This discretization results in a semi-discretized system that is equivalent to a dG(0) approach. A formal derivation of this equivalency reveals, that evaluating the determinant of the deformation gradient $J = \det(\mathbf{F})$ at the current time-step, i.e. at $J(t_m)$, is a reasonable choice (cf. Richter [126]).

3.3 Stabilization by the time derivative

We face two main sources of numerical instabilities regarding our prototypical systems of PDEs describing mechanochemical long-term problems:

Firstly, we are primarily interested in the timescale of growth (days) on the tissue level rather than the timescale of the elastic material response (seconds), see also Subsection 2.3.2. The idea is to perform large time-step on the scale of growth on the one hand and to suppress non-physical oscillations of the tissue on the elastic timescale on the other. Regarding the variational formulation of our system of PDEs in Eq. (3.1), it is hence desirable to neglect the second temporal

derivative in our structural equation, which results in a differential algebraic equation (DAE) of an elliptic structural equation and parabolic reaction-diffusion equations (cf. Eq. (2.38). Yet, this changes the nature of our system of PDEs which results in numerical instabilities due to the strong coupling of our equations in conjunction with considering nonlinear elasticity. Indeed, the strong coupling of our prototypical system of PDEs seems to be the main source of instability in our numerical tests.

Unfortunately, the objectives of performing large time-steps while neglecting the elastic time scale to prevent oscillations on the elastic timescale are incompatible.

Secondly, we highlighted another source of instability, namely the prescription of homogeneous Neumann values on the entire boundary, which introduces additional degrees of freedom: By changing the nature of the structural equation to an elliptic one, our solution is only unique up to rigid body translations and rotations. Assuming homogeneous Neumann values on the entire boundary, however, is an indispensable prerequisite to obtain spontaneous pattern formation in the applications to embryogenesis and symmetry breaking in *Hydra* as discussed in the previous section.

As a compromise, we keep the second derivative as a stabilization term and pick a small stabilization parameter to prevent unrealistic elastic oscillation. Hence, we regard the time derivative in the semi-discrete system of equations (3.3) as a stabilization term only. In the following, we hence consider a stabilized structural equation given by

$$\epsilon(k)\rho^0 \left(\mathbf{u}^m - 2\mathbf{u}^{m-1} + \mathbf{u}^{m-2}, \boldsymbol{\Phi}\right)_\Omega + k^2\, \mathbf{a}(\mathbf{u}^m, C_i^m)(\boldsymbol{\Phi}) = 0 \quad \forall \boldsymbol{\Phi} \in V^d, \tag{3.4}$$

with the semi-linear differential operator $\mathbf{a}(\mathbf{u}^m, C_i^m)(\boldsymbol{\Phi})$ defined above. Notice, that a stabilization based on the time derivative implies a coupling of the time-step size and the stabilization parameter. For instance, the size of the stabilization term is quartered if we halve the time-step size in the two-step method discretizing the second derivative in Eq. (3.4). Accordingly, we propose to quadratically scale the stabilization parameter with the time-step size by $\epsilon(k) = k^2\epsilon_0$.

In the course of this chapter, we assess the impact of this stabilization in a comprehensive stability analysis. In particular, we demonstrate that the stabilization error is indeed of the same size as the discretization error in time for the choice $\epsilon(k) = 0.1k^2$.

3.4 Discretization in space

The spatial discretization of our prototypical systems of PDEs is based on finite element methods. In the standard theory, the finite element discretization relies on discrete subspaces $V_h \subset V$ of bilinear and biquadratic finite elements (Q_1- and Q_2-finite elements), where the solution to our system of PDEs is approximated. For details on the finite element method and the discrete spaces involved, we refer to literature (cf. Brenner & Scott [18], Ciarlet [28] or Wloka [154]).

In general, our tissue sphere Ω has a smooth but curved boundary, which cannot be matched by the finite element mesh, i.e. $\Omega_h \approx \Omega$. In particular, this implies $V_h \not\subset V$ and our finite element

space is hence not conforming. Here, we do not go into details on non-conforming finite element methods and the approximation of curved boundaries but refer to Braess [14] instead.

We partition our domain into a triangulation (or mesh) based on quadrilaterals in 2D and hexahedra in 3D. In all our discretizations, these cells are disjoint and of similar size and shape. The index h is used to identify discrete functions, function spaces and domains. Since an adaptive, local mesh refinement strategy will be proposed, we explicitly allow hanging nodes, i.e. nodes that are not shared by all surrounding cells. These properties are denoted as size, shape and structural regularity of the mesh, see e.g. Ciarlet [28] or Rannacher [125].

With these preparations, we formulate the finite element discretization of the prototypical system discretized in time in Galerkin formulation (3.3). This algebraic system includes the stabilization (cf. Eq. (3.4)) reads for suitable test functions $\boldsymbol{\Phi}_h \in V_h^d$ and $\Psi_h \in V_h$:

Find the displacements $\mathbf{u}_h^m \in V_{0,h}^{d,m} = \{\mathbf{v}_h \in V_h^{d,m} \colon \mathbf{v}|_{\Gamma_{D,h}} = 0\}$ and the concentrations of signaling molecules $C_{i,h} \in V^m$, $i = 0, 1, \cdots, n$ with initial conditions $\mathbf{u}_h^0(\mathbf{X}) = 0$, $C_{i,h}(\mathbf{X}, 0) = C_{i,h}^0$ such that

$$\begin{aligned} \epsilon(k)\rho^0(\mathbf{u}_h^m - 2\mathbf{u}_h^{m-1} + \mathbf{u}_h^{m-2}, \boldsymbol{\Phi}_h)_{\Omega_h} + k^2\, \mathbf{a}_h(\mathbf{u}_h^m, C_{i,h}^m)(\boldsymbol{\Phi}_h) = 0 \qquad & \forall \boldsymbol{\Phi}_h \in V_h^d \\ J_h^m(C_{i,h}^m - C_{i,h}^{m-1}, \Psi_h) + k\, b_h(\mathbf{u}_h^m)(C_{i,h}^m, \Psi_h) = 0 \qquad & \forall \Psi_h \in V_h,\ i = 1, \cdots, n, \end{aligned} \tag{3.5}$$

where the the semi-linear forms $\mathbf{a}_h(\cdot,\cdot)(\cdot)$ and $b_h(\cdot)(\cdot,\cdot)$ are nonlinear in the arguments in the first and linear in those in the second brackets and read

$$\begin{aligned} \mathbf{a}_h(\mathbf{u}_h^m, C_{i,h}^m)(\boldsymbol{\Phi}_h) &= (\mathbf{F}_h^m \boldsymbol{\Sigma}_h^m(\mathbf{u}_h^m, C_{i,h}^m), \nabla \boldsymbol{\Phi}_h)_{\Omega_h} - (\mathbf{G}, \boldsymbol{\Phi}_h)_{\Gamma_{N,h}} - (\mathbf{F}_h^m \boldsymbol{\Sigma}_h^m \mathbf{N}_h, \boldsymbol{\Phi}_h)_{\Gamma_{R,h}} \\ b_h(\mathbf{u}_h^m)(C_{i,h}^m, \Psi_h) &= (J_h^m(\mathbf{F}_h^m)^{-1}\mathbf{D}(\mathbf{F}_h^m)^{-T}\nabla C_{i,h}^m, \nabla \Psi_h)_{\Omega_h} - (J_h^m R_{i,h}^m, \Psi_h)_{\Omega_h}, \end{aligned} \tag{3.6}$$

where

$$\begin{gathered} \boldsymbol{\Sigma}_h = J_{a,h}^m(\mathbf{F}_{a,h}^m)^{-1}\boldsymbol{\Sigma}_{e,h}^m(\mathbf{F}_{a,h}^m)^{-T}, \quad \boldsymbol{\Sigma}_{e,h}^m = \lambda\, \mathrm{tr}(\mathbf{E}_{e,h}^m)\mathbf{I} + 2\mu \mathbf{E}_{e,h}^m, \quad \mathbf{E}_{e,h}^m = \frac{1}{2}((\mathbf{F}_{e,h}^m)^T\mathbf{F}_{e,h}^m - \mathbf{I}), \\ \mathbf{F}_{e,h}^m = \mathbf{F}_h^m(\mathbf{F}_{a,h}^m)^{-1}, \quad \mathbf{F}_h^m = \nabla \mathbf{u}_h^m + \mathbf{I}, \quad J_h^m = \det(\mathbf{F}_h^m), \quad J_{a,h}^m = \det(\mathbf{F}_{a,h}^m), \end{gathered}$$

and where μ, λ are the Lamé constants. Here, $R_{i,h}(I(\mathbf{E}^m, \mathbf{F}^m, \boldsymbol{\Sigma}^m), C_i^m)$ are the coupling terms that incorporate mechanical feedback on morphogen dynamics. Vice versa, $\mathbf{F}_a^m = \mathbf{F}_a(t, C_{1,h}^m, \cdots, C_{n,h}^m)$ prescribes morphogen-induced active deformations such as active cell shape changes. The precise form of the coupling usually depends on the application at hand (e.g. see Fig. 2.6). Finally, $\mathbf{D} \in \mathbb{R}^{d\times d}$ is the diffusion coefficient tensor.

3.5 Convergence and stability

In our applications, we mainly focus on the three-dimensional setting that is crucial to obtain realistic mechanochemical tissue behavior such as gastrulation. Yet, considering the full 3D geometry implies substantial numerical effort in order to guarantee a sufficient numerical resolution of the biological cells in space. To assess the accuracy of our FE-approach, we hence rely on an extensive convergence analysis in two dimensions.

In the following, we demonstrate that convergence in space and time is assured, both in 2D and in 3D. Further, we show that the stabilization error and the temporal discretization error are well below the dominating discretization error in space, if the stabilization parameter scales depending on the time-step size by $\epsilon(k) = k^2\epsilon_0$ (as proposed above). For our parameter setup, the spatial discretization error dominates since employing additional mesh refinement requires huge numerical effort and is only feasible for calculating a reference solution. Regarding stress-based mechanical feedback loops, an efficient local mesh refinement strategy is proposed.

As a model problem, we consider the application to embryogenesis (cf. Section 5.3), where we reduce the Galerkin problem (3.1) to a single reaction-diffusion equation and the structural one and prescribe homogeneous Neumann conditions on the entire boundary.

Quantity of interest

To evaluate the convergence and the stability of our approach, we first need to define a quantity of interest to measure the discretization and the stabilization errors. In our model problem on embryogenesis, we mainly focus on stress- and stretch-based mechanochemical feedback loops. Hence, we pick the L^2-Norm of the mechanical coupling term $R(I(\boldsymbol{\Sigma}), I(\mathbf{F}), C)$ in the reaction-diffusion equation as our quantity of interest to measure convergence and stability of solving our coupled systems. On the one hand, this term is the main driver of morphogen dynamics and well suited to measure convergence in the reaction-diffusion equation. On the other hand, it is composed of tensor invariants of the deformation gradient and the first Piola-Kirchhoff stress tensor, which captures the elastic material response.

In the case of the stretch-mediated feedback loop, the mechanical response is based on the determinant of the deformation gradient and the quantity of interest reads

$$\mathcal{J}_{\mathbf{F}}(\mathbf{u}_h) := \|R(I_d(\mathbf{F}_h))\|_{L^2(\Omega)} = \left\| \frac{\max\{\det(\mathbf{F}_h) - 1, 0\}}{k_m + \max\{\det(\mathbf{F}_h) - 1, 0\}} \right\|_{L^2(\Omega)}, \tag{3.7}$$

where $\mathbf{F}_h = \nabla \mathbf{u}_h + \mathbf{I}$ is the deformation gradient.

In case of the stress-mediated feedback loop, we evaluate the quantity of interest given by

$$\mathcal{J}_{\boldsymbol{\Sigma}}(\mathbf{u}_h) := \|R(I_d(\boldsymbol{\Sigma}_h))\|_{L^2(\Omega)} = \left\| \frac{\max\{\det(\boldsymbol{\Sigma}_h), 0\}}{k_m + \max\{(\boldsymbol{\Sigma}_h), 0\}} \right\|_{L^2(\Omega)}, \tag{3.8}$$

where we refer to Section 2.1for the derivation of the second Piola-Kirchhoff stress tensor $\boldsymbol{\Sigma}$ in terms of the displacement $\mathbf{u}$. To increase readability, we also express convergence by the *relative error in the quantity of interest* $|\mathcal{J}(\mathbf{u}_h) - \mathcal{J}(\mathbf{u}_{ref})|\,\mathcal{J}(\mathbf{u}_{ref})^{-1}$.

Stationary solutions

To evaluate the discretization errors and the convergence rates, we compare our quantities of interest in the stationary solutions obtained for different spatial and temporal discretizations. A

stationary solution is attained if the largest component of the Newton residual of our discretized system of PDEs is smaller or equal to a given threshold, i.e. if

$$\max_{k=0,\dots,d} | - \mathbf{A}(\cdot)(\cdot)_k| \coloneqq \begin{pmatrix} \epsilon(k)\rho^0(\mathbf{u}_h^m - 2\mathbf{u}_h^{m-1} + \mathbf{u}_h^{m-2}, \boldsymbol{\Phi}_h)_{\Omega_h} + k^2\, \mathbf{a}_h(\mathbf{u}_h^m, C_h^m)(\boldsymbol{\Phi}_h) \\ J_h^m(C_h^m - C_h^{m-1}, \Psi_h)_{\Omega_h} + k\, b_h(\mathbf{u}_h^m)(C_h^m, \Psi_h) \end{pmatrix}_{l^\infty} \leq THRES$$

for $d = 2, 3$, where the Newton residual is the right hand side in Newton's method (cf. Eq. (4.1)) and the threshold is chosen as $THRES = 10^{-8}$.

3D reference solution based on Richardson extrapolation

When considering the full 3D geometry, it is only practical to compute solutions on three mesh levels due to the huge computational costs. An additional reference value in our quantity of interest is computed by Richardson extrapolation [124]: Assuming that we computed values in our quantity of interest $\mathcal{J}(\mathbf{u}_{h_i})$ (cf. Eq. 3.7) for spatial discretizations $h_0 > h_1 > \cdots > h_L$, an approximation of the limit $\mathcal{J}(\mathbf{u}_{0,ref}) = \lim_{h\to 0} \mathcal{J}(\mathbf{u}_h)$ for a finite element method of order q is given by

$$\mathcal{J}(\mathbf{u}_{0,ref}) = \frac{\mathcal{J}(\mathbf{u}_{h_i}) - \mathcal{J}(\mathbf{u}_{h_j})\left(\frac{h_i}{h_j}\right)^q}{1 - \left(\frac{h_i}{h_j}\right)^q}.$$

For the moment, let us assume cubic convergence for Q_2 finite elements, which will be confirmed by our numerical results in the two-dimensional setting. Further, we halve the mesh size h_i to obtain the finer mesh level h_{i+1}. In practice, this yields for the Richardson extrapolation

$$\mathcal{J}(\mathbf{u}_{0,ref}) = \frac{\mathcal{J}(\mathbf{u}_h) - \mathcal{J}(\mathbf{u}_{\frac{h}{2}})(0.5)^3}{1 - (0.5)^3} \tag{3.9}$$

3.5.1 Convergence in time

In our applications to pattern formation in biological tissue, we are interested in stationary solutions to our strongly coupled system of prototypical equations. The temporal discretization error is computed by comparing the stationary solutions obtained for different discretizations in time, i.e. for different time-step sizes. Here, we focus on the stretch-mediated feedback loop, where the discretization errors are measured in the quantity of interest based on the determinant of the deformation gradient (cf. Eq. (3.7)).

In a stationary state, we expect only small errors in our quantity of interest for different discretizations in time. This hypothesis is confirmed by our numerical results: The discretization error in time is well below the discretization error in space for the chosen time-step sizes as shown in the context of our stability analysis in Table 3.3 and Fig 3.3. In this table, we observe a convergence order in our quantity of interest for the discretization in time of only about 0.5. It is indeed not at all obvious, which convergence order we can expect in our nonlinear quantity of interest for a coupled system with a two-step method for the stabilization term in the structural equation and an implicit Euler scheme discretizing the reaction-diffusion equation. Besides,

the derivation of *a priori* error estimates for dynamic processes based on strongly coupled systems of PDEs including growth is immensely difficult and theoretical results are not available in literature.

Regarding Table 3.3, time-step sizes of 2.5s in 2D (and 20s in 3D, result not shown) seem a reasonable choice to balance the desire to perform large time-steps with the need of a small time-step size. As discussed, small time-steps increase the stabilization and ensures a small discretization error in time.

The huge number of time steps to obtain a stationary solution remains as a bottleneck. We perform adaptive time-stepping only in the first 10 to 50 Newton steps, where the initial distribution of morphogen leads to large and quick deformations in the initially undeformed domain. Once co-localized morphogen/curvature patterns evolve, constant and larger time steps are performed.

3.5.2 Convergence in space for Q_1 and Q_2 finite elements

We analyze convergence in space for our model problem introduced above, which is based on a stretch-mediated feedback loop including apical/basal constriction. The discretization error in space is hence evaluated in the stretch-based quantity of interest (cf. Eq. 3.7). At this point, we focus on uniform mesh refinement for Q_1 and Q_2 finite elements. An adaptive local mesh refinement strategy is introduced for the stress-mediated feedback loop and is presented at the end of this chapter.

We discretize a 3D tissue sphere or a 2D cross-section of this sphere that are composed of 1 536 and 128 circumferentially arranged biological cells of size H by quadrilaterals and hexahedra of size h with $h < H$ and $\Omega_h \approx \Omega$. In each *nodal point* of the d-dimensional discrete domain Ω_h, we have d degrees of freedom for the displacement $\mathbf{u}$ one degree of freedom for the morphogen concentration C.

In Table 3.1, we present the 2D discretization error and the convergence rates in our quantity of interest. Further, in Fig. 3.1, we plot the convergence results in our quantity of interested over the number of nodal points in a double-logarithmic plot. In particular, we observe quadratic and cubic convergence rates (illustrated by the two black lines) for linear (Q_1-) and quadratic (Q_2-) finite elements. This results confirms the strength of our solution approach, since these convergence orders are the best we can anticipate on domains with smooth boundaries. Besides, theoretical convergence results for our strongly coupled system including active deformations are extremely difficult to derive and not available in literature.

Regarding Table 3.1, we observe that quadratic finite elements are very efficient: Comparing the third line for Q_2-FE with the fourth line for Q_1-FE, we observe that quadratic finite elements require one mesh level less to result in a similar discretization error in the quantity of interest. Notably, the relative spatial discretization error for Q_2-finite elements is even well below 1% on all mesh levels.

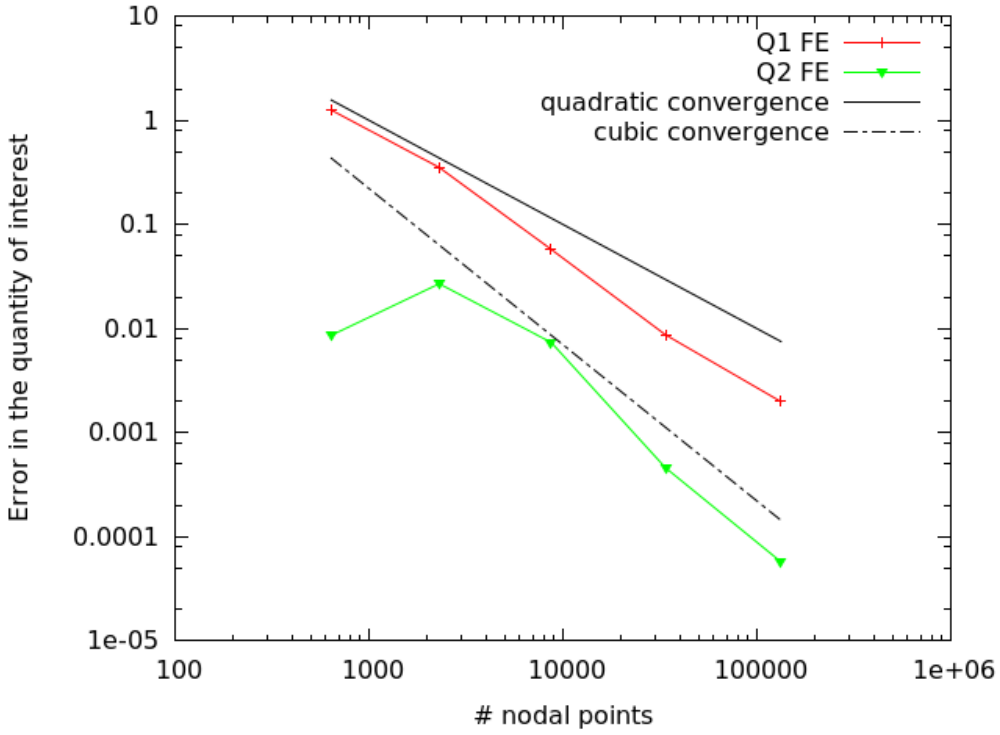

Figure 3.1: 2D: Plot of the error in the quantity of interest over the number of nodal points.

	#cells	#points	Q_1-FE		Q_2-FE	
			$\lvert\Delta\mathcal{J}(\mathbf{u}_h) - \mathcal{J}(\mathbf{u}_{ref})\rvert$	conv.	$\lvert\mathcal{J}(\mathbf{u}_h) - \mathcal{J}(\mathbf{u}_{ref})\rvert$	conv.
1	512	640	1.25e0 (15.11%)		8.60e-3 (0.1039%)	
2	2 048	2 304	3.51e-1 (4.24%)	1.8	2.69e-2 (0.3251%)	-1.6
3	8 192	8 704	5.47e-2 (0.69%)	2.6	7.35e-3 (0.0888%)	1.9
4	32 768	33 792	8.69e-3 (0.11%)	2.7	4.60e-4 (0.0056%)	4.0
5	131 072	133 120	1.98e-3 (0.02%)	2.1	5.75e-5 (0.0007%)	3.0

Table 3.1: 2D: Error, relative error in % and convergence rate in the quantity of interest for uniform mesh refinement. The reference solution was computed using Q_2-finite elements and a mesh of 528 384 nodal points.

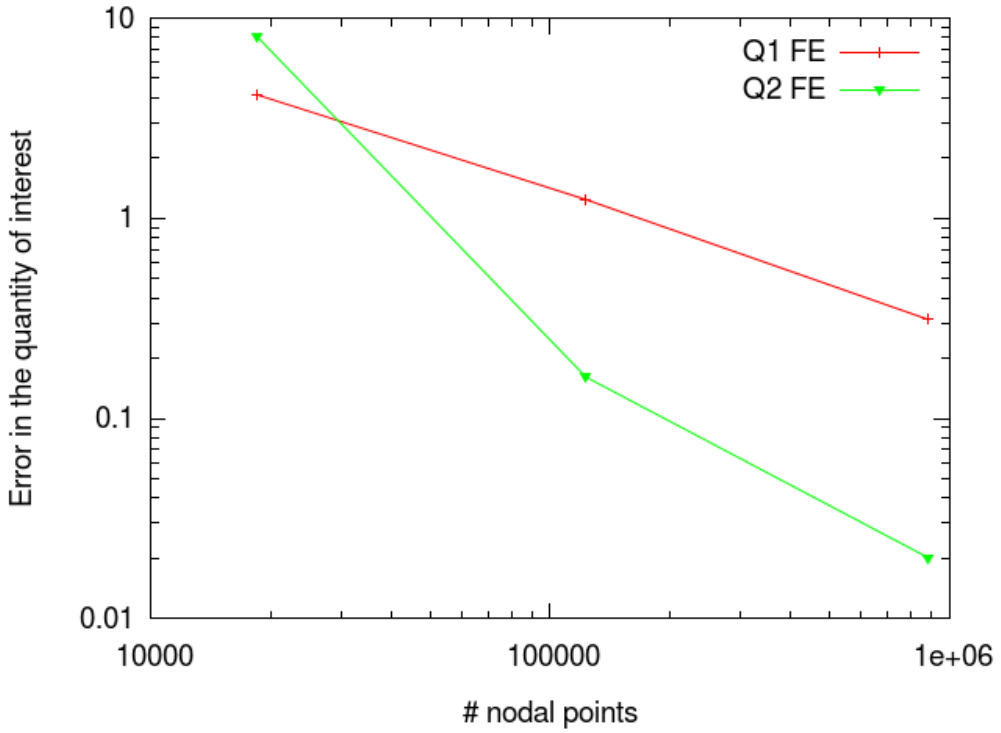

Figure 3.2: 3D: Plot of the error in the quantity of interest over the number of nodal points.

	#cells	#points	Q_1-FE			Q_2-FE		
			$\lvert\Delta\mathcal{J}\mathbf{u}_h) - \mathcal{J}(\mathbf{u}_{ref})\rvert$	conv.	$\bar{t}$	$\lvert\mathcal{J}(\mathbf{u}_h) - \mathcal{J}(\mathbf{u}_{ref})\rvert$	conv.	$\bar{t}$
1	12 288	18 438	4.14e0 (23.1%)		0.7 s	8.11e0 (45.2%)		1.2 s
2	98 304	122 890	1.24e0 (6.90%)	1.7	4.9 s	1.61e-1 (0.90%)	5.7	7.4 s
3	786 432	884 754	3.12e-1 (1.74%)	2.1	72.1s	2.01e-2 (0.11%)	3.0	78.1 s

Table 3.2: 3D: Error, relative error in % and convergence rate in the quantity of interest for uniform mesh refinement. Further, $\bar{t}$ is the average computation time per time-step. The reference solution was obtained by extrapolation of the two finest Q_2-approximations.

In Table 3.2 we show the spatial discretization error for Q_1- and Q_2-finite elements for the available spatial discretizations in 3D. Next, in Fig. 3.2, we plot the convergence results in our quantity of interested over the number of nodal points in form of a double-logarithmic plot. Clearly, we observe convergence in our quantity of interest for linear and quadratic finite elements. Yet, it is difficult to make conclusions regarding the convergence rates in our full 3D solution approach, since only three mesh levels are available. In the light of our previous results in 2D, it is reasonable to assume that we have cubic convergence for Q_2 finite elements since we simply transfer our model to the full smooth 3D tissue sphere. With this convergence order at hand, a reference solutions can be obtained by Richardson extrapolation, see Eq. (3.9).

In Table 3.2, we see that a relative error in our quantity of interest is below 1% for quadratic finite elements only. In particular, we observe that the spatial discretization error for quadratic finite elements is one magnitude below the error for linear finite elements in the last two lines. At the same time, the computational costs only increase by factor 1.5 if Q_2- instead of Q_1-finite elements are considered (cf. the second last line in Table 3.2). On the other hand, solving on finer meshes significantly increase the numerical effort, particularly in 3D: For instance, the computation times increase almost by factor 15, if we solve our systems of PDEs for Q_1-FE on the finest mesh level instead of the second finest one, see Table 3.2.

In summary, our convergence analysis shows that quadratic finite elements are our discretization of choice if the full 3D geometry is considered. The presented approach is efficient and we observe fast, quadratic and cubic convergence for linear and quadratic finite elements.

3.5.3 Stabilization error

In Section 3.3, we introduced a stabilization of the structural equation to improve the conditioning of our system matrix and the convergence of our solution approach. Here, we do not only determine the size of the stabilization error but also give guidance on how to choose the intensity of the stabilization term, i.e. how to pick the factor $\epsilon(k)$ based on time-step size k in the structural equation. Due to the huge computational effort in three dimension, we restrict ourselves to the discretization by Q_2-finite elements for our model problem in two-dimensions. Corresponding calculations in 3D confirm that the stabilization and the temporal discretization error are three, respectively two scales below the dominating spatial discretization error for our standard parameter setup.

In Table 3.3, we list the stabilization error measured in our quantity of interest for decreasing the stabilization parameter and for a fixed discretization by Q_2-finite elements such that the spatial discretization error does not change. As a reference, we compute a stationary solution $\mathbf{u}^{\epsilon}_{ref}$ for a very small stabilization term with $\epsilon = 10^{-4}$. Regarding tissue development, we hence focus on the timescale of growth and neglect the timescale of tissue elasticity to the greatest possible extend. In Fig. 3.3, we see that $\epsilon = \epsilon_0 = 0.1$ is indeed a reasonable choice, which ensures that the discretization error in space remains the dominating error term for all three time-step sizes $k \in \{2.5\text{s}, 1.25\text{s}, 0.625\text{s}\}$ and a fixed discretization in space (cf. Table 3.3).

Notice however, that a stabilization term based on the time derivative implies a coupling of the stabilization parameter to the time-step size. For instance, the size of the stabilization term is quadrupled if we halve the time-step size in the two-step method which discretizes the second

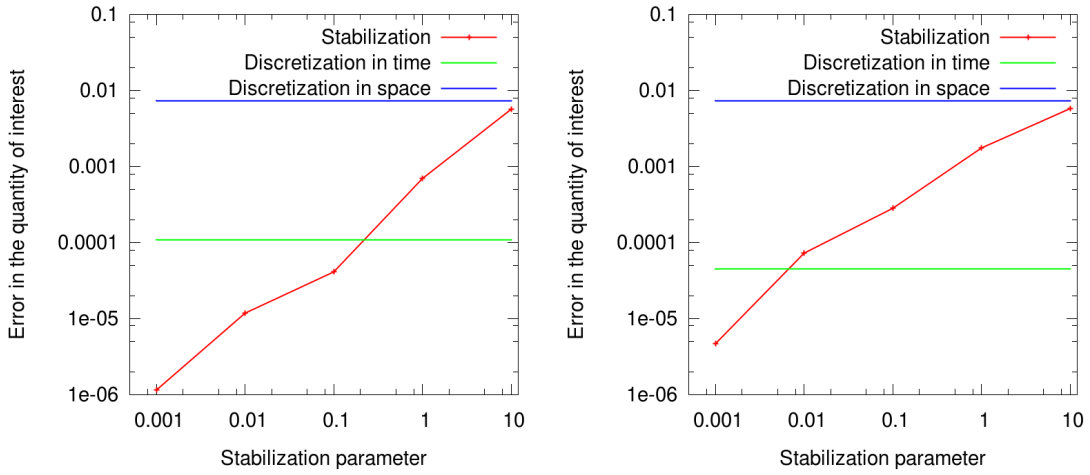

(a) For time-step size $k = 2.5$s

(b) For time-step size $k = 0.625$s

Figure 3.3: 2D: Plot of the stabilization error over the stabilization parameter ϵ for two different time-step sizes and a fixed discretization by Q_2-finite elements in space.

$\epsilon(k) = \epsilon_0$	#nodal points	Error in $\lvert\mathcal{J}(\mathbf{u}_h^\epsilon) - \mathcal{J}(\mathbf{u}_{ref}^\epsilon)\rvert$		
		$k = 2.5$s	$k = 1.25$s	$k = 0.625$s
10	8 704	5.66e-3	5.82e-3	5.77e-3
1	8 704	6.96e-4	1.25e-3	1.75e-3
0.1	8 704	4.11e-5	8.78e-5	2.81e-4
0.01	8 704	1.18e-5	1.00e-5	7.24e-5
0.001	8 704	1.15e-6	2.48e-5	4.66e-6
Disc. error in time		1.09e-4	7.09e-5	4.47e-5
Disc. error in space		7.35e-3	7.35e-3	7.35e-3

Table 3.3: Error in the quantity of interest for decreasing stabilization parameter, two different time-step sizes k and Q_2-finite elements. The reference solution was obtained for choosing the stabilization parameter as $\epsilon_0 = 10^{-4}$.

derivative in the structural equation (cf. Eq. (3.4)). Hence, we propose to quadratically scale the stabilization parameter with the time-step size by $\epsilon(k) = k^2\epsilon_0$ to ensure that the stabilization error is of equal size or below the discretization error in time.

In Fig. 3.3, we plot all three sources of errors, the stabilization error as well as the temporal and spatial discretization errors in form of a double-logarithmic plot. We observe that the error in time as well as the stabilization error are about two scales below the discretization error in space for $\epsilon(k) = 0.1$ and the chosen time-step sizes. Regarding Fig. 3.3 (b), we see that the discretization error in time decreases for a quartered time-step size. This confirms, that the stabilization parameter should indeed be scaled by the quadratic time-step size.

In summary, we have shown that the error introduced by the stabilization term is always well below the dominating spatial discretization error. This agrees well with the fact that the stabilization term based on the time derivative vanishes in the stationary state. Also, various numerical tests confirm the robustness of our stationary solutions with regard to changes in the initial conditions, the tissue geometry or the parameters (cf. Section 5.3.4). It is a fascinating observation that we eventually obtain stable stationary solutions to a dynamic (but robust) process including large deformations, stresses and strains. From a mathematical point of view, it hence seems immensely difficult to derive a comprehensive stability analysis or even *a priori* estimates for our strongly coupled systems of PDEs and literature on the stability of nonlinear elasticity including growth is still sparse.

Remark: Regarding our numerical simulations, we also followed the idea of implementing translation- and rotation-free ansatz and test spaces to stabilize our elliptic structural equation. The objective was to reduce the degrees of freedom in case of prescribing homogeneous Neumann values on the entire boundary. Yet, this approach was not fruitful and the convergence of our methods was not improved in our numerical tests even though translations and rotations were clearly removed from the solution space.

3.6 Adaptivity and local refinement

In this section, we propose a simple adaptive mesh refinement strategy to accurately resolve stress-based mechanical feedback, which is expressed by invariants of the second Piola-Kirchhoff stress tensor $\mathbf{\Sigma}$ (cf. Eq.(2.31)). In our modeling approach including active deformations, the Piola-Kirchhoff tensor depends on the piecewise-defined active deformations and is discontinuous in general. In particular, it depends on the elastic response to piecewise-defined active deformations that are discontinuous in between biological cells.

Since we consider a stress-mediated feedback loop, we measure the spatial discretization error in the stress-based quantity of interest, which was presented in Eq. (3.8). We recapitulate that strain- and stretch-mediated feedback loops do not require local mesh refinement, since they employ mechanical feedback based on the continuous Green-Lagrange strain tensor and the continuous deformation gradient, respectively.

Algorithm 1 Local refinement strategy

```
Initial, uniform mesh refinement
for i ← 1 to niter do                                          ▷ Iterations in time
    if i + 1 mod f = 0 then          ▷ Frequency of mesh refinement, usually f = 100
        for CELL in CELLS do
            if C(EDGE) > THRES for all EDGES of CELL then      ▷ For concentration C
                refine(CELL)
            end if
        end for
    end if
    Solve system of PDEs
end for
```

In algorithm 1, we present a simple local mesh refinement strategy, where a numerical cell ("CELL", for Q_1-FE) or a patch of cells (for Q_2-FE) is refined, if the morphogen concentration C is above a given threshold ("$THRES$") in all edges of this cell or patch. In the finite element library GASCOIGNE3D [9], each quadratic test and ansatz function is defined on patches of four cells in 2D and eight cells in 3D. If all cells in a patch are marked to be refined, the entire patch is refined at once. In alternative finite element approaches, additional degrees of freedom are introduced inside each cell if Q_2-FE are used. By construction, each biological cell in the 3D tissue sphere is resolved by eight patches due to the initial refinement but a patch is never distributed among biological cells.

In our numerical simulations, an update of the meshes in every hundredth time-step seems sufficient. In practice, we use the stress-induced morphogen concentration rather than the stress itself as a criterion for local mesh refinement. The main reason is the modeling of intercellular diffusion, which smoothes the morphogen distribution as well as the adaptive mesh refinement.

This algorithm can be generalized by coarsening of the mesh, which is necessary if weak patterns move or dissolve. In the following convergence analysis, we abstain from this complication for the sake of a clearer presentation.

In this section, we focus on the stress-mediated feedback loops including basal constriction with a single initial morphogen spot, which leads to gastrulation events (cf. simulation snapshots in Fig. 5.16 (d) and Fig. A.7 for 2D in the appendix). Further, in Fig. 3.4, we show simulation snapshots for the stress-mediated feedback loop in two and three dimensions, where the adaptively refined meshes in the final, stationary states are visualized (black grids). In particular, we highlight two morphogen/curvature patches which are resolved by our adaptive, local mesh refinement strategy.

Finally, we discuss the spatial discretization errors for the stress-mediated feedback loop in the stress-based quantity of interest (cf. Eq. (3.8)). All errors are evaluated in the stationary solution obtained on a 2D tissue cross-section as shown in the left half of Fig. 3.4.

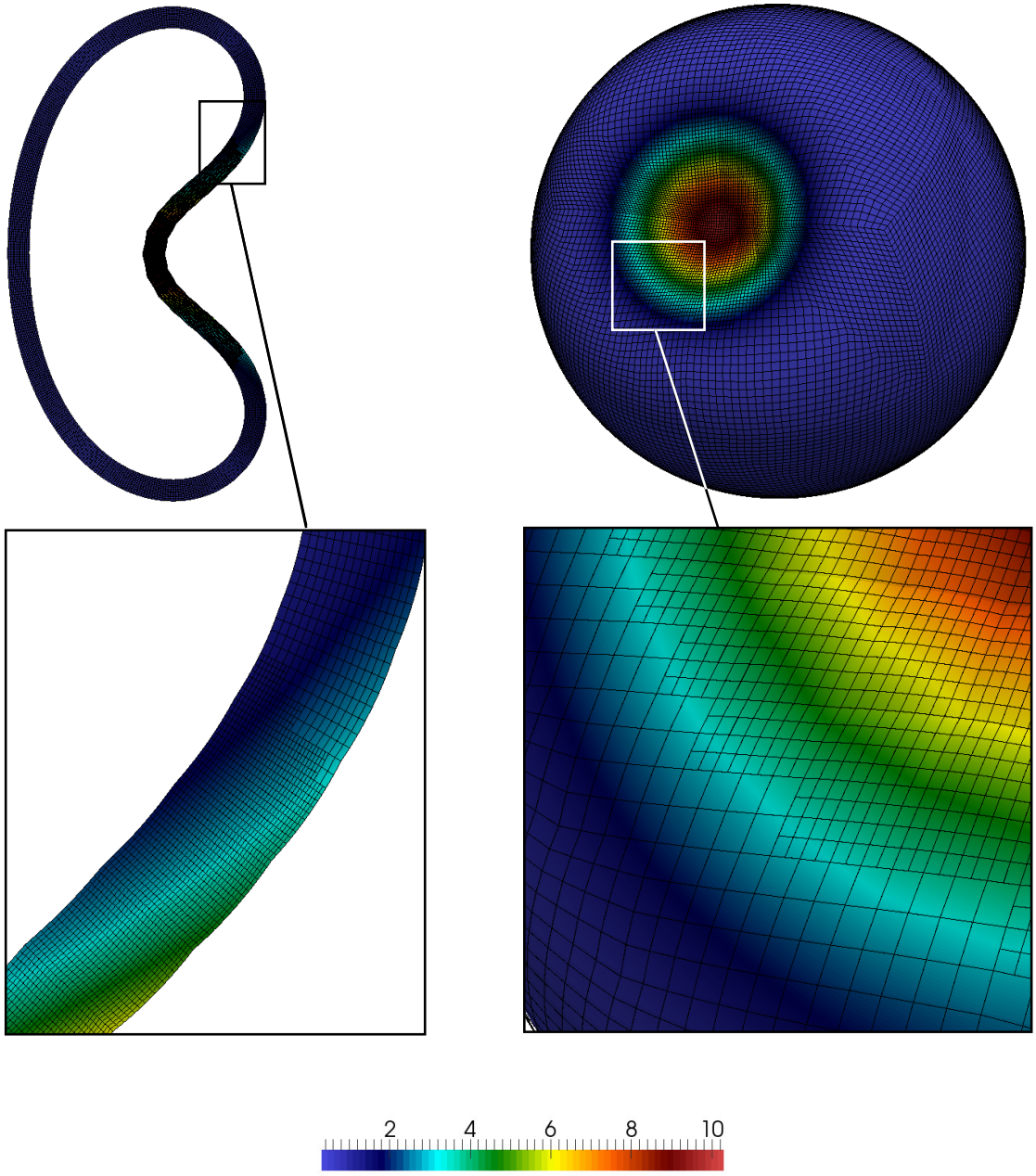

Figure 3.4: Simulation snapshots with locally refined meshes based on refinement strategy 1 for the stress-mediated feedback loop including basal constriction.
Left: Snapshot for pattern formation on a 2D cross-section for 14 336 nodal points.
Right: Snapshot for pattern formation on the full 3D tissue sphere for 146 722 nodal points. Highlighted: Regions of local adaptive mesh refinement.

mesh level	#cells	#nodal points	$\lvert\mathcal{J}(\mathbf{u}_h) - \mathcal{J}(\mathbf{u}_{ref})\rvert$ (rel. err.)		conv.
1	512	640	18.12e0	(44.77%)	
2	2 048	2 304	1.75e0	(4.32%)	3.4
3	8 192	8 704	1.49e0	(3.70%)	0.2
4	32 768	33 792	2.29e-1	(0.57%)	2,7
5	131 072	133 120	2.86e-2	(0.07%)	3.0

Table 3.4: 2D: Error, relative error in % and convergence rate in the quantity of interest for the stress-mediated feedback loop and uniform mesh refinement.

#cells	#nodal points	$\lvert\mathcal{J}(\mathbf{u}_h) - \mathcal{J}(\mathbf{u}_{ref})\rvert$ (rel. err.)		conv.
872	1 036	9.68e0	(23.921%)	
3 440	3 764	2.93e-1	(0.724%)	5.0
13 688	14 336	2.10e-2	(0.052%)	3.8
54 464	55 760	1.88e-3	(0.004%)	3.4

Table 3.5: 2D Error, relative error in % and convergence rate in the quantity of interest for the stress-mediated feedback loop and the local, adaptive mesh refinement strategy 1.

In Table 3.4 we list the discretization errors in space for uniform mesh refinement. For comparison, the spatial error resulting from our adaptive, local mesh refinement strategy 1 is presented in Table 3.5. A reference solution was computed for 524 288 Q_2 finite elements on a uniformly refined mesh. We highlight the error in the last line of Table 3.4 compared to the error in the second line of Table 3.5, which are of the same size (10^{-2}): Our adaptive mesh refinement strategy requires an impressive factor 10 fewer mesh points (or degrees of freedom) to achieve the same spatial accuracy.

In Fig. 3.5, we show a double-logarithmic plot of the spatial discretization error over the number of nodal points for uniform mesh refinement (red line) as well as for local adaptive mesh refinement based on strategy 1 (green line). Interestingly, we also observe cubic convergence for Q_2 finite elements in case of a stress-mediated feedback loop based on the discontinuous Piola-Kirchhoff stress tensor. The same convergence order was observed for the stretch-mediated feedback loop based on the continuous deformation gradient, see Fig. 3.1. Apparently, the discontinuous form of the Piola-Kirchhoff stress does not seem to influence the convergence order of our method. Regarding uniform mesh refinement, we discover that convergence for the stress-mediated feedback loop can only be observed for significantly finer meshes compared to the stretch-mediated one (cf. Fig. 3.1 (green line) and Fig. 3.5 (red line)). In fact, our refinements strategy is efficient and considerably improves the convergence of our method as the discontinuous mechanical feedback is resolved: Our adaptive approach gives a better constant for the cubic convergence rate, which is a common observation for adaptive local mesh refinement.

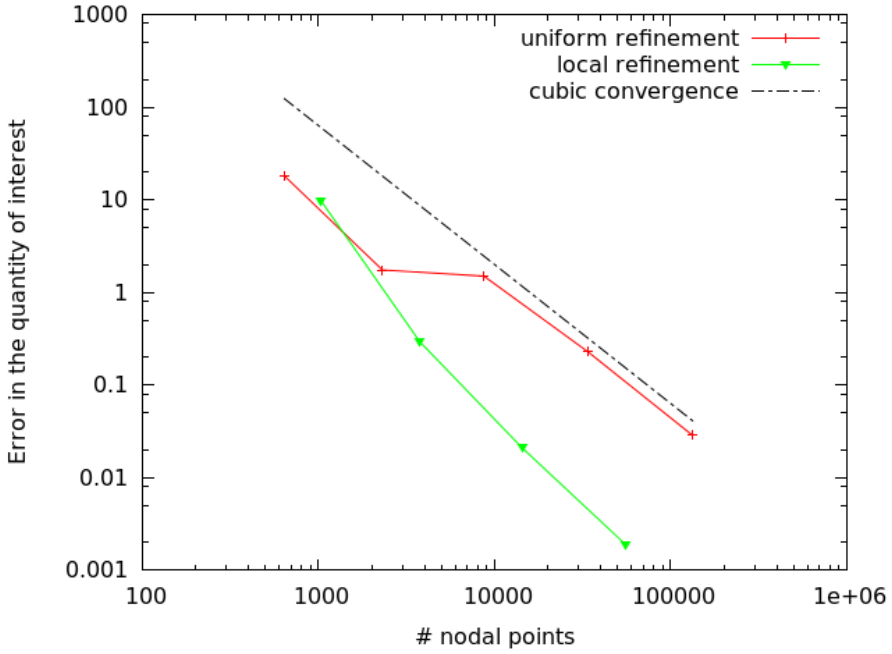

Figure 3.5: 2D: Plot of the error in the quantity of interest for the stress-mediated feedback loop and different refinement strategies over the number of nodal points.

At least in two dimensions, it is not efficient to employ an adaptive mesh refinement strategy where the mesh is locally resolved by two additional refinement levels. Regarding this strategy, numerical tests revealed similar error reduction as in the case of uniform mesh refinement. Also, we point out that imposing an internal volume constraint stabilizes the invagination process and is highly recommended to ensure convergence towards a stationary solution, which is crucial to conduct an accurate convergence analysis.

In summary, our adaptive mesh refinement strategy is successful: We observe fast cubic convergence rates for Q_2-FE since we refine exactly where the discontinuous stress-based feedback requires a high numerical resolution. Besides, coarser meshes levels seem sufficient to accurately capture the elastic deformation of the passively bent remaining tissue. This highlights the accuracy of our (parallelized) solution approach regarding the spatial discretization.

4 Solver

In this chapter, we discuss the numerical methods employed in solving the nonlinear algebraic system obtained by the finite element discretization of our prototypical system in Galerkin formulation (cf. Eq. (3.5)).

In Section 4.1, Newton's method is introduced which linearizes the nonlinear algebraic system obtained in each time-step. Next, in Section 4.2, we present the *iterative Generalized Minimal Residual Method* (GMRES) [132], which is used to solve the linear systems resulting from Newton's method. The GMRES method is preconditioned by a parallelized *geometric Multigrid Method* (MG) [57], where the high frequent error contributions on each mesh level are smoothened by a *Incomplete LU Factorization* (ILU). This parallel solution approach stems from the state-of-the-art finite element library GASCOIGNE3D [9]. The parallel multigrid solver is based on the idea of applying the computationally expensive ILU decomposition in parallel on each part of the decomposed computational domain as discussed in Section 4.4.

Lastly, in Section 4.5, we asses the speedup and the efficiency of this parallel solution approach for solving our strongly coupled systems of PDEs modeling mechanochemical long-term problems. In particular, we show that an impressive speedup of the computational time by a factor 12 is possible by solving the algebraic system in parallel on 14 CPU cores instead of solving sequentially on just one core.

4.1 Newton's method

As a first step in solving our algebraic system (3.5), the system is linearized by Newton's method. The algebraic system was obtained based on Rothe's method, i.e. from a discretization in time by implicit time-stepping schemes and a subsequent finite element discretization.

Initially, we state a compact formulation of our prototypical system (3.5) for the sake of a readable presentation. Therefor, we define a semi-linear operator $\mathbf{A}(\cdot)(\cdot)$ in the time interval $T^m := [t^{m-1}, t^m]$, $m = 1, \cdots, M$ by

$$\begin{aligned}&\mathbf{A}(\mathbf{u}_h^m, C_h^m)(\mathbf{u}_h^{m-1}, \mathbf{u}_h^{m-2}, \boldsymbol{\Phi}_h, C_h^{m-1}, \Psi_h) := \\ &\begin{pmatrix} \epsilon(k)\rho^0(\mathbf{u}_h^m - 2\mathbf{u}_h^{m-1} + \mathbf{u}_h^{m-2}, \boldsymbol{\Phi}_h)_{\Omega_h} + k^2\, \mathbf{a}_h(\mathbf{u}_h^m, C_h^m)(\boldsymbol{\Phi}_h) \\ J_h^m(C_h^m - C_h^{m-1}, \Psi_h)_{\Omega_h} + k\, b_h(\mathbf{u}_h^m)(C_h^m, \Psi_h) \end{pmatrix},\end{aligned}$$

where $\mathbf{u}_h^{m-1}, \mathbf{u}_h^{m-2}$ and C_h^{m-1} are solutions from previous time-steps. Here, we further simplified the discrete Galerkin formulation of our prototypical systems of PDEs (cf. Eq. 3.5) by considering one species of signaling molecules only. Nonetheless, the solution methods discussed in this chapter also apply to the more general setting considering several species.

With this definition at hand the discrete formulation of our prototypical system of PDEs in compact form in the time interval T^m is given by:

$$\mathbf{A}(\mathbf{u}_h^m, C_h^m)(\mathbf{u}_h^{m-1}, \mathbf{u}_h^{m-2}, \boldsymbol{\Phi}_h, C_h^{m-1}, \Psi_h) = 0 \qquad \forall \boldsymbol{\Phi}_h \in V_h^d,\ \forall \Psi_h \in V_h,$$

To keep the notation simple, we drop the solutions $\mathbf{u}_h^{m-1}, \mathbf{u}_h^{m-2}$ and C_h^{m-1} from previous time-steps as arguments of the semi-linear operator $\mathbf{A}(\cdot)(\cdot)$.

With this compact notation of our algebraic system, the l-th Newton iteration in form of a defect correction step with initial guesses $\mathbf{u}_h^{m,0} \in V_h^d$ and $C_h^{m,0} \in V_h$, reads:

$$\begin{aligned} \mathbf{A}'(\mathbf{u}_h^{m,l}, C_h^{m,l})(\delta\mathbf{u}_h^{m,l}, \boldsymbol{\Phi}_h, \delta C_h^{m,l}, \Psi_h) &= -\mathbf{A}(\mathbf{u}_h^{m,l}, C_h^{m,l})(\mathbf{u}_h^{m-1,l}, \mathbf{u}_h^{m-2,l}, \boldsymbol{\Phi}_h, C_h^{m-1,l}, \Psi_h) \\ \mathbf{u}_h^{m,l+1} &= \mathbf{u}_h^{m,l} + \delta\mathbf{u}_h^{m,l} \\ C_h^{m,l+1} &= C_h^{m,l} + \delta C_h^{m,l}, \end{aligned} \tag{4.1}$$

where $-\mathbf{A}(\cdot)(\cdot)$ is the Newton residual for a zero right hand side. Further, we take a look at the Newton matrix, which can be expressed on high-level by

$$\begin{aligned} &\mathbf{A}'(\mathbf{u}_h^{m,l}, C_h^{m,l})(\delta\mathbf{u}_h^{m,l}, \boldsymbol{\Phi}_h, \delta C_h^{m,l}, \Psi_h) = \\ &\begin{pmatrix} \left(\epsilon(k)\rho^0(\boldsymbol{\Phi}_h^i, \boldsymbol{\Phi}_h^j)_{\Omega_h} + k^2 \mathbf{a}'_{\mathbf{u}}(\mathbf{u}_h^{m,l}, C_h^{m,l})(\boldsymbol{\Phi}_h^i, \boldsymbol{\Phi}_h^j)\right)_{i,j=0}^{3N,3N} & \left(k^2 \mathbf{a}'_C(\mathbf{u}_h^{m,l}, C_h^{m,l})(\boldsymbol{\Phi}_h^i, \boldsymbol{\Phi}_h^j)\right)_{i,j=0}^{3N,N} \\ \left(J'^{,m}_{h,u}(C_h^{m,l} - C_h^{m-1,l}) + k\, b'_{\mathbf{u}}(\mathbf{u}_h^{m,l})(C_h^{m,l}, \Phi_h^i, \Phi_h^j)\right)_{i,j=0}^{N,3N} & \left(J_h^m C_h^{m,l} k\, b'_C(\mathbf{u}_h)(\Phi_h^i, \Phi_h^j)\right)_{i,j=0}^{N,N} \end{pmatrix} \begin{pmatrix} \delta\mathbf{u}_h \\ \delta C_h \end{pmatrix}, \end{aligned}$$

using the abbreviations $(\delta\mathbf{u}_h, \delta C_h)^T = (\delta\mathbf{u}_h^0, \cdots, \delta\mathbf{u}_h^{3N}, \delta C_h^0, \cdots, \delta C_h^N)^T$ and expressing discrete quantities by the ansatz

$$\delta u_h^k = \sum_{i=0}^{N} \delta u_h^{k,i} \Phi_h^i,\ k = 1, \cdots, d, \quad \delta C_h = \sum_{i=0}^{N} \delta C_h^i \Phi_h^i.$$

Here, $\{\Phi_h^i, i = 1, \cdots, N\}$ is the nodal basis of the finite element space V_h and $N = \dim V_h$ is the number of nodal points. Further, the Jacobi matrix consists of the Gâteaux derivatives, which are exemplarily given by

$$\mathbf{a}'_{\mathbf{u}}(\mathbf{u}_h^m, C_h^m)(\delta\mathbf{u}_h^m, \boldsymbol{\Phi}_h) = \frac{d}{ds}\mathbf{a}(\mathbf{u}_h^m + s\,\delta\mathbf{u}_h^m, C_h^m)(\boldsymbol{\Phi}_h)\Big|_{s=0}.$$

The Newton matrix is presented to stress two main observations: Firstly, we observe that the strong coupling between morphogen dynamics and structural mechanics leads to a strongly coupled Newton matrix. In particular, we point out that every entry depends on the deformation $\mathbf{u}$ and the morphogen concentrations C, in the first row even in nonlinear matter. Secondly, we observe that the d diagonal components (related to the first equation for the displacement $\mathbf{u}$) of the matrix are strengthened if the time-step size k is small or if the stabilization factor $\epsilon(k)$ is large. In the first case, this actually results in good convergence of the linear solvers, i.e. of the GMRES and the multigrid methods at the expense of performing many time-steps. In the second case, the stabilization error is increased and mechanical oscillations might be observed.

Obviously, it is desirable to balance these two requirements, which was discussed in Section 3.3. For the chosen combinations of time-step size and stabilization parameter an analysis of the stabilization error revealed that the stabilization as well as the discretization error in time are well below the dominating spatial discretization error, see Subsection 3.5.3.

As indicated above, it is essential that we strengthen/stabilize the diagonal of the Newton matrix by a stabilization term to improve the convergence rate and to reduce the number of necessary iterations of the linear solvers (GMRES preconditioned with parallel multigrid method). For instance, if we had a strictly diagonal dominant matrix, this matrix would be positive semi-definite with non-negative eigenvalues. In particular, the eigenvalues might be of similar size such that the conditioning of the non-symmetric Newton matrix A', i.e. the quotient of the square roots of maximal over minimal eigenvalue of $(A')^T A'$ is small. Indeed, a small condition number is a strong criterion for good convergence of the GMRES method.

In general, there are about 2-3 Newton steps necessary in each time-step. In each step of the Newton iteration, the resulting linear system is then solved by 8-10 GMRES iterations, which are preconditioned by a geometric multigrid method. The latter methods are discussed in the following section.

Note that initially, stochastically distributed morphogen levels in each biological cell or a single morphogen spot are prescribed whereas corresponding deformations are not known. Hence, we usually observe that more Newton and GMRES steps are necessary in the first five to 20 time-steps until the calculated displacement corresponds to the current morphogen distribution.

4.2 GMRES and Multigrid method

To solve our strongly coupled prototypical systems modeling mechanochemical long-term problems we rely on the solution techniques from the state-of-the-art finite element library GASCOIGNE3D [9]. Here, the solution of the linearized system (4.1) in each Newton iteration is based on the iterative generalized minimal residual method (GMRES method) [132], which is preconditioned by a parallelized geometric multigrid method [57] with ILU factorization as a smoother.

Before we go into details, note that the geometric multigrid method alone is not capable of solving the linearized system of equations, since suitable smoothers are not known. This is confirmed in our numerical tests, where the multigrid method preconditioned with an ILU or Jacobi smoother does not converge. As an alternative, the GMRES method preconditioned with the ILU factorization converges in our numerical simulations. This approach was less efficient since considerably more GMRES iterations on the finest mesh level are necessary in this configuration. Hence, these results are not shown.

The geometrical multigrid method is motivated by the observation that - generally slowly converging - Jacobi or Gauss-Seidel methods quickly smoothen high-frequent contributions of the error. Then, the solution process is carried to a nested coarser mesh level where low-frequent solution parts are approximated. The geometric multigrid method has an optimal complexity of

requiring only $O(N)$ arithmetic operations to solve our linear system of equations with a system matrix of size $4N \times 4N$.

In the finite element library GASCOIGNE3D [9] smoothers for the algebraic multigrid method based on the Jacobi method or the ILU factorization are available. In our numerical simulations, the parallelized ILU factorization is the smoother of choice, since the MG method does not converge for a simple smoother such as a Vanka-type block Jacobi method. Regarding the ILU factorization, we employ the Cuthill-McKee algorithm [30] for sorting the system matrix of the linearized algebraic system. This algorithm permutes a sparse matrix into a band matrix with small bandwidth which is the desired structure of the system matrix for multigrid methods.

4.3 Parameter setup

Due to initial uniform mesh refinement, three different FE mesh levels are available for the standard settings in our solution approach. A finer mesh is obtained by splitting each numerical cell in a coarse mesh into four, respectively eight cells in two and three dimensions. This also applies to adaptive local mesh refinement where the multigrid method is based on these three hierarchical meshes and optional further local refinement.

The parameters for the solvers taken from the finite element (FE) library GASCOIGNE3D [9] are chosen as follows: The global tolerance for the Newton residual (cf. Eq.(3.5)) is set to 10^{-8} and the tolerance for the GMRES method is set to 10^{-6}. The time step size is given by 20 s in 3D and 2.5 s in 2D. With these settings, a stationary solution is attained after around 50 000 time-steps were performed.

4.4 Parallelization

The finite element library GASCOIGNE3D [9] features parallelized solution techniques which are based on the parallelization of the adaptive multigrid method. In the latter method, the computationally costly smoothing steps by the ILU factorization are applied in parallel on each part of the decomposed computational domain. Yet, the ILU method is an inherently global method and its parallelization is not straightforward. In practice, the domain is split into parts with minimal overlap where homogeneous Dirichlet values are prescribed such that the local subproblems on each part can be interpreted as Dirichlet problems. The mesh decomposition is handled by the library metis [77], which represents the mesh by a partitioned graph.

The idea of parallelized multigrid solvers based on domain decomposition is not new and was proposed by Brandt [16] as early as 1981. Another, major contribution was the development of completely parallel multilevel preconditioners that are suited for local mesh refinement by Bramble *et al.* [15] and were parallelized by Bastian [7]. This small overview of the literature was adapted from Richter [127, p. 54], where a broader presentation is available.

In the FE library GASCOIGNE3D, the focus lies on the accuracy of the numerical algorithms rather than parallel efficiency. Regarding the efficiency, it is important to uniformly distribute the computational load among the CPUs and to minimize the communication via the standardized Message Passing Interface (MPI) in between the parallel processes. In multigrid methods with

adaptive mesh refinement, the uniform distribution of load is particularly delicate. For instance, on coarse meshes in the multigrid hierarchy, less processors are required such that CPUs are idle. These challenges are resolved, since the largest computational effort accumulates on the finest meshes such that the multigrid hierarchy is usually attained by from there by global coarsening, see Ref. [78, 127].

In this thesis, we consider large prototypical systems of PDEs such that a parallelized solution approach is deemed to be necessary. To assess the speedup due to parallelization and its efficiency, we summarize the most important definitions used in our isoefficiency analysis. Essentially, analyzing the isoefficiency addresses the question if we can increase "the number of CPUs according [to] the problem size and preserve the efficiency of the parallel algorithm" (Richter [127, p. 54]). The definitions given in the following were originally taken from Grama *et al.* [50, p. 221] and were adopted by Richter [127].

Firstly, let us introduce the term of the *best sequential algorithm* to solve an algebraic problem that is applicable in practice. Its computation time on a single CPU depends on the problem of size N. Secondly, we define:

> The **sequential time** is the computation time $T_s(N)$ of the best available sequential algorithm necessary for solving a problem of size N;
>
> The **parallel time** is the computation time $T_P(N, P)$ for the parallel algorithm on P processors for the problem of size N;
>
> The **speedup** is the quotient of the sequential time and the parallel time for P processors for the problem of size N and is given by
>
> $$S(N, P) \coloneqq \frac{T_s(N)}{T_P(N, P)};$$
>
> The **efficiency** is the speedup per number of CPUs P for the problem of size N and is given by
>
> $$S(N, P) \coloneqq \frac{T_s(N)}{P\, T_P(N, P)};$$

Note that the speedup has to be smaller than the number of CPUs P that are employed in the parallel solver, i.e. $S(N, P) \leq P$. Otherwise, we could sequentially execute the parallel algorithm P times and obtain a new, fastest sequential algorithm in contradiction to the original sequential algorithm being the fastest one. Hence, a speedup that is equal to the number of processors involved is the optimum that we can hope for.

4.4.1 Mesh partitioning

The parallelization of the multigrid solver is based on the decomposition of the mesh into subdomains with minimal overlap, where our prototypical equations are solved in parallel. The partitioning of the mesh is handled by the library metis [77], where the finite element mesh is represented by a graph. The graph is partitioned by a minimal number of cuts into subgraphs

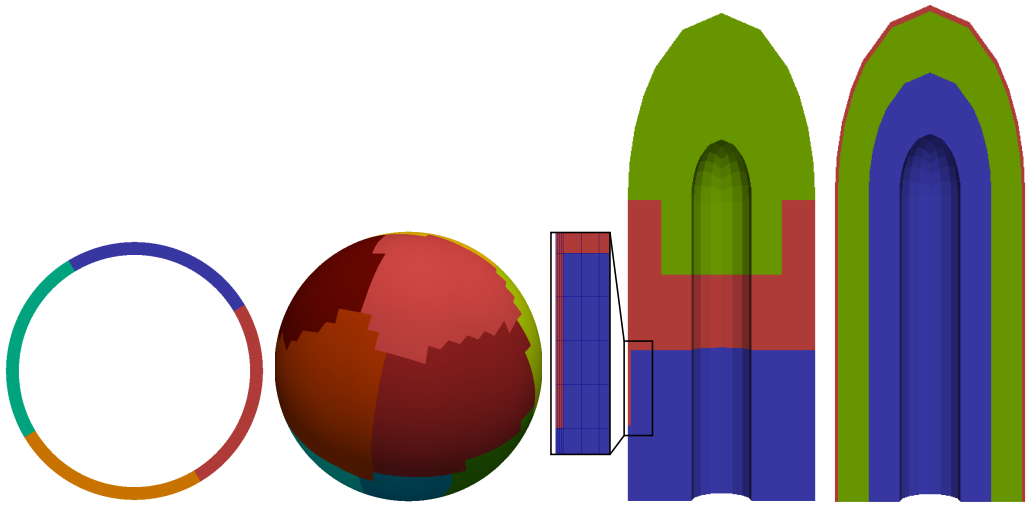

(a) 2D sphere, four parts (metis) (b) 3D sphere, 14 parts (metis) (c) Hydroid, three parts (metis) (d) Hydroid, three parts (own partitioning)

Figure 4.1: Partitioning of the computational domain for parallelization: (a)-(b) Uniform distribution by metis; (c) uneven distribution by metis; (d) Our own partitioning into three layers of biological cells (with evenly distributed numerical cells).

with - ideally - uniformly distributed numbers of cells in each part. A detailed description of this process is presented in Richter [127]. We describe the uniformity of a partitioning by evaluating the quotient of the maximal and the minimal number of cells in a part, i.e., for sub-domains of cells T_k, we define $NI := \max_k(T_k) \min_k(T_k)^{-1}$.

In this thesis, we mainly focus on the applications to embryogenesis and to symmetry breaking in *Hydra*, where we discretize a hollow tissue sphere. In Fig. 4.1 (a)-(b), we visualize the partitioning of the tissue sphere in two and three dimensions. In the first, the 2D setting, 8 192 numerical cells are uniformly distributed into four parts of 2 048 cells. Similarly, metis achieves an almost optimal distribution of cells into 14 parts in three dimensions, where the quotient of maximal over minimal number of cells in a part is $NI = 0.95$.

Regarding Fig. 4.1 (c), we highlight an uneven distribution of numerical cells by metis in the application to growth pulsations in tips of colonial hydroids. Here, the maximal number of cells in a part can be almost twice the minimal number of cells, namely $NI = 0.52$. Hence, we modified the partitioning process, where we take the structure of the organism (and the computational domain) into account: Hydroids consist of two soft tissue layers which are surrounded by a thin but rigid organic skeleton (cf. Section 5.2). Here, each of these three layers is discretized by the same number of cells. We take advantage of this structure during parallelization by splitting the domain into three parts corresponding to these three layers, see Fig. 4.1 (d). Naturally, these three parts might be further partitioned themselves such that each layer is distributed among the same number of CPUs. With this modification of the partitioning process, we indeed obtain a uniform partitioning of the mesh (with $NI = 1$).

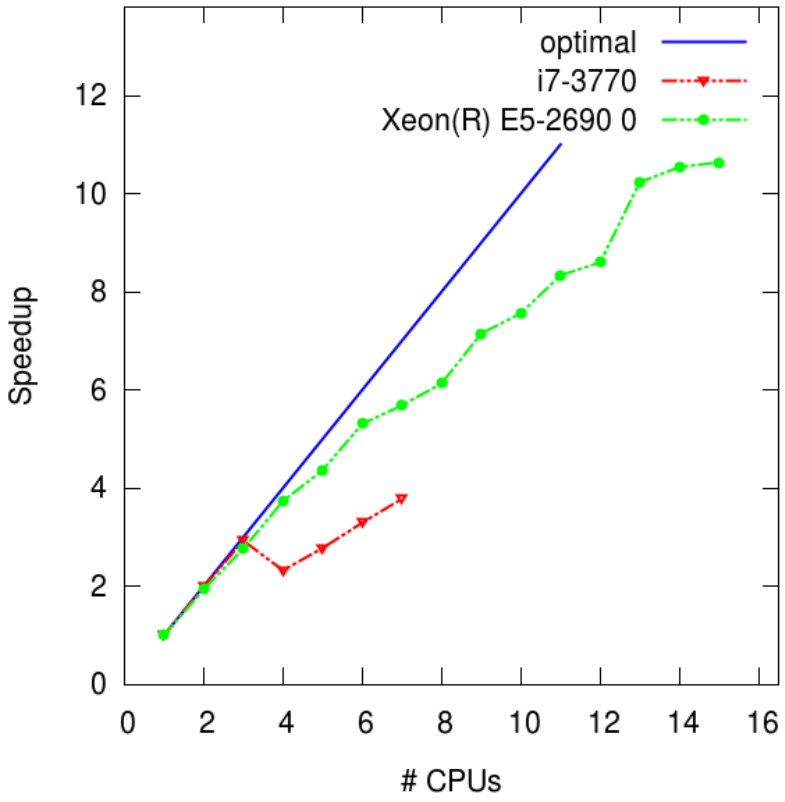

Figure 4.2: Speedup due to parallel multigrid solvers for our numerical simulations in 3D on a personal computer (red) with 4 cores and a computing server (green) with 16 cores.

4.5 Numerical results and discussion

Eventually, we assess the speedup and the efficiency of the parallel multigrid solvers for simulating our systems of PDEs modeling mechanochemical long-term problems. Due to the intense mechanochemical interactions involved, the highly coupled systems of PDEs (cf. Section 4.1 are solved by a monolithic parallelized solution approach. As a model problem, we consider our system of PDEs applied to embryogenesis, i.e. a stretch-mediated feedback loop including basal constriction (cf. Eq.(5.4)). Corresponding simulation snapshots are shown in Fig. 5.9.

To evaluate the speedup and the efficiency of our parallel solution approach, we measure the average computation time per time-step for performing 100 time-steps of 20 second each for a discretization of the full 3D tissue geometry by Q_2-finite elements and 98 304 numerical cells (i.e. for a system with almost 400 000 unknowns). This measurement was repeated ten times on an otherwise unoccupied machine such that the average computation time per time-step was computed for 1 000 time-steps. All our numerical simulations were performed on several personal computers (PCs) as well as on a computing server with the following specifications:

- Intel(R) Core(TM) i7 − 3770 CPU @ 3.40GHz, 4 physical cores (8 by Hyper-Threading) and 16 GB DDR3 RAM;

- Intel(R) Xeon(R) CPU E5 − 2690 0 @ 2.90, 16 physical cores (32 by Hyper-Threading) and 256 GB RAM.

Intel's Hyper-Threading is a realization of the simultaneous multithreading technology, which is based on the idea of presenting two virtual or logical cores to the operating system for each physical core. Internally, two processes are scheduled to be executed on one physical core such that, while one process might be waiting for data from memory or other CPUs, the other process is continued.

In a nutshell, the sequential time was calculated on both types of machines by averaging the time per time-step over 1 000 steps. To assess the speedup and the efficiency of our parallel solution approach, these measurements were repeated for simulations on $1-7$ and $1-15$ CPU cores, depending on the machine listed above. Here, a decomposition of the domain in the multigrid method into P parts corresponds to numerical simulations on P CPU cores. Also, we always kept at least one physically present processor core for the operating system and the master process which handles the communication between the CPUs. Communication between the ILU smoothing operations is indispensable for the exchange of values on interface between parts of the decomposed mesh or for the initial distributing of the mesh, see Richter [127].

In Fig. 4.2 we plot the speedup gained by the parallel multigrid solvers over the number of CPU cores used in the parallelization. The optimal scenario, i.e. employing P CPUs leading to a speedup of factor P, is depicted by the blue line. Yet, in practice, the necessary communication between the processes of the parallelized ILU factorization significantly increases with the size of the interface between the parts of the decomposed mesh, i.e. with the number of CPU cores that are employed. Nonetheless, the computation time per time-step is almost halved on two CPU cores and divided in thirds on three cores for both, the PC and the compute server.

Amazingly, the speedup due to the parallel multigrid solver on the Intel(R) Xeon(R) compute server remains close to the optimum (cf. green and blue line in Fig. 4.2) when even more CPU cores are used: An impressive speedup of the computational time by a factor 11 is possible by solving the algebraic system in parallel on 15 CPU cores compared to the sequential use of the multigrid solver.

Regarding the personal computer with an Intel(R) Core(TM) i7 − 3770, we observe a speedup of close to factor three on $P = 3$ CPU cores but a subsequent drop of the speedup on four cores. Afterwards, the speedup increases again when more CPU cores are employed, e.g. the computation time is reduced by a factor four on seven CPU cores (cf. Fig. 4.2 (red line)). The reason for the drop in the speedup is the design of the i7 processor which has only four physical cores but appears as 8 logical cores to the operating system via Hyper-Threading (see the explanations above). Since one core is reserved for the operating system and the master process which handles the communication between the distributed smoothing steps, Hyper-Threading is employed for a mesh decomposition into four parts. Clearly, Hyper-Threading is less efficient and the speedup initially drops for solving on four CPU cores (cf. Fig. 4.2 (red line)).

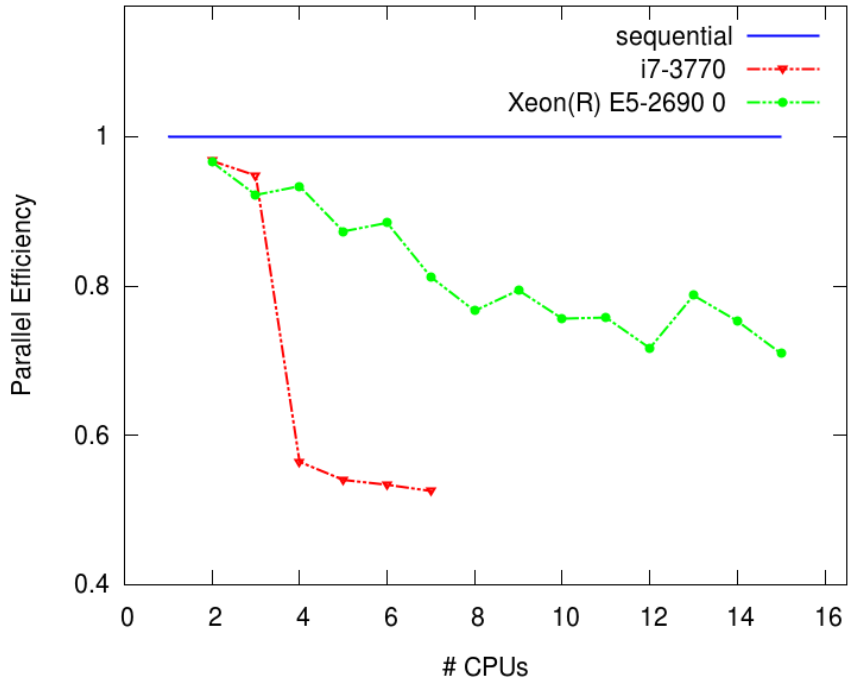

Figure 4.3: Parallel efficiency over the number of CPU cores for solving the algebraic systems in 3D on a personal computer (red) with 4 cores and a computing server (green) with 16 cores.

By definition, the sequential algorithm has an efficiency one, which is "optimal". During parallelization, increasing the number of CPUs also increases the size of the interfaces between the parts of the decomposed mesh and, accordingly, the communication between the CPU cores accumulates. Hence, we cannot expect an optimal efficiency with an increasing usage of CPU cores.

In Fig. 4.3, we plot the efficiency of our parallel solution approach over the number of CPU cores used in the numerical simulation. Regarding the compute server with an Intel(R) Xeon(R) E5 – 2690 0 processor, we correspondingly observe that the efficiency is decreasing. Yet overall, we acknowledge at the same time that the efficiency of the parallel multigrid solver on this compute server remains well above 0.7 for an increasing number of CPU cores, as shown by the green line in Fig. 4.3. Here, we believe that the zig-zag pattern in the decreasing efficiency stems from the internal load distribution among the CPUs, e.g. via Hyper-Threading. Further, despite averaging over a large number of time-steps that were performed over different days and times of day, we cannot fully exclude that the compute server was always entirely empty as it was shared among the members of our working group and also served as a file server.

In case of a personal computer with an Intel(R) Core(TM) i7 – 3770 processor, Fig. 4.3 clearly shows the good efficency of the parallel multigrid solver for distributing the mesh among two and three CPUs (red line). Once Hyper-Threading is necessary for simulations on more than

three cores, a severe drop in the efficiency is observed. This behavior was anticipated, since only four physical CPU cores are available where one is reserved for the master process and the operating system, as discussed in the context of the speedup analysis above.

Note that all our numerical simulations to asses the speedup and the efficiency of our solution approach were carried out on an otherwise unused compute server. Hence, the standard deviation in the measured computation time per time-step was usually small and did not exceed five percent. If other calculations however conflicted with these runtime tests, we observe that the speedup is influenced less if the parallelization distributes the computational load over more CPU cores. Presumably, the computational effort can be distributed better among the CPUs in this case due to the architecture of the Intel(R) Xeon(R) E5 − 2690 0 processor.

As the bottleneck in our approach the sheer number of time-steps required to obtain a stationary solution remains: In practice, we need to partly resolve the elastic timescale of seconds for the sake of a stable solution approach, which requires small time-steps (cf. Section 3.3). In general, we hence perform between 50 000 and 100 000 time-steps which results in a computing time of two to four days on 15 CPU cores for solving systems of PDEs on the full 3D geometry.

In summary, we present a highly efficient solution approach to solve the algebraic systems obtained in each Newton step. In particular, the parallelization of the multigrid solver is crucial to obtain a reasonably fast solution approach for the strongly coupled huge systems of PDEs considered in this thesis. With these techniques at hand, a decisive reduction of the computational costs is demonstrated: For instance, an impressive speedup of the computational time per time-step by a factor 11 is possible when solving the algebraic systems in 3D on 15 CPU cores compared to using the sequential solver.

5 Applications

In this chapter, we apply our prototypical coupled system of PDEs to different model organisms and demonstrate that our simple positive interaction rules ("feedback loops") lead to spontaneous and robust mechanochemical pattern formation.

Firstly, in Section 5.1, we provide the background to self-organization and pattern formation in biological tissue and discuss preceeding works in this field of developmental biology, see Section 5.1. Secondly, in Section 5.2, we reduce the model to the structural equation only and investigate growth processes during the development of tips in colonial hydroids. In this application, we explore how two active deformation tensors that prescribe rotations and shearings of biological cells lead to distinctly different growth processes in the tip of this organism. Subsequently, we compare these deformations to the experimental data shared by my colleague Igor Kosevich [81].

Thirdly, in Section 5.3, the main numerical results on mechanochemical pattern formation during embryogenesis are presented. In particular, we examine stress- and stretch-mediated feedback loops in conjunction with active apical/basal constriction (wedging) of individual biological cells. Further, we focus on the robustness of our approach with regard to the model size and geometry, diffusion, active deformations, parameters and initial conditions.

Lastly, in Section 5.4, we apply our system to symmetry breaking in *Hydra* aggregates where we propose a strain-mediated feedback loop including apico-basal shortening (thinning) of the biological cells. Also here, we observe spontaneous pattern formation, namely spontaneous head development after growth oscillations. Moreover, we highlight Subsection 5.4.5 where we present predictive numerical experiments of head formation triggered by a micropipette aspiration of the regenerated *Hydra* aggregate. In particular, we directly compare our results to the experimental observations for micropipette aspiration by Sander [133].

We point out that the biological motivation in Section 5.1 and our application to embryogenesis in Section 5.3 are closely related to the introduction and the results in our publication Brinkmann *et al.* [20]. In particular, Moritz Mercker has drafted substantial parts of the biological motivation as well as the discussion and the summary of the numerical results (cf. the acknowledgments). Regarding my side, the methodology and the underlying prototypical model equations, the investigation and numerical computations, the implementation, the programming in the FE library GASCOIGNE3D [9] and writing the texts are the main contributions to our publication Brinkmann *et al.* [20] as well as to this thesis (see the roles of the authors described in Ref. [20]).

In this thesis, our research is extended by numerical simulations on the robustness of pattern formation with regard to diffusion and the model geometry, particularly for active apical constriction, as well as stress-mediated feedback loops. Further, we introduce an inner volume constraint/internal pressure that accounts for the fluid contained inside our tissue sphere. That

way, the invagination process during gastrulation is stabilized and we obtain stationary solutions. Finally, we present a novel enhanced model which is more accurate on the cellular level: We prescribe uniform morphogen production rates on each biological cell by (biological) cell-wise integration of the mechanical feedback, which leads to a single gastrulation event, see Subsection 5.3.6.

Finally, we emphasize that all results regarding growth processes in tips of colonial hydroids (cf. Section 5.2) and symmetry breaking in *Hydra* aggregates (cf. Section 5.4) are exclusive to this thesis. In particular, this includes our comparison to experimental data in case of the former and the predictive numerical experiments in case of the latter application.

5.1 Biological Motivation

During embryogenesis or tissue development, various chemical and mechanical patterns emerge in a self-organized way based on relatively simple structures, such as a tissue sphere [47]. During the last decades, a main focus in developmental biology was the experimental identification of signaling molecules ("morphogens") being spatio-temporally associated with certain developmental steps in various model organisms [21, 47]. However, the knowledge about *how* chemical patterns are produced, controlled, and how they interact with mechanical patterns is still very unsatisfactory.

A frequent obstacle to the research on mechanochemical pattern formation is the mechanical aspect, since mechanical tissue modification tools, molecular markers for mechanical cues and mechanochemical modeling are still in its infancy [103]. Especially, it appears that often the full 3D nature of tissue mechanics has to be considered in experiments and models for obtaining results which can be related to *in vivo* processes [3, 5, 49, 52, 86, 130, 147] making the situation even more challenging. Thus, although correlations between biological forms and mechanical phenomena were already pointed out in the seminal work of D'Arcy Thompson [146], mainly pure chemical theories have been predominated hereof during the last century of research in order to explain tissue pattern formation during development.

The first one of these theories assumes that embryogenesis is a sequence of successive chemical patterns, where each chemical pattern relies (in other words, depends sensitively) on the previous pattern [155]. A model organism partially fitting this theory is the fruit fly *Drosophila*, in which the orientation of the initial body axis sensitively depends on the maternally inherited Bicoid RNA [34], and later stages are defined by distinct chemical patterns ("gap genes" [69]). However, experimental studies show that embryonic patterns are often robust to removal, addition or redistribution of embryo parts during the preceding patterning stages [11, 47, 135]. Moreover, for an increasing number of biological systems it even appears that patterning does not rely on any pre-pattern, but it may develop in a self-organized way from dissociated and re-aggregated cells [19, 45, 67, 75, 150]. This capacity of self-organization during pattern formation is called "*de novo*" or "spontaneous" or "self-organized" pattern formation and strongly disagrees with the above mentioned theory.

Due to these difficulties, a second, more robust theory of pattern formation has received increasing attention, namely a theory which assumes that pattern formation occurs spontaneously and robustly just by specific interactions among diffusing chemicals ("morphogens") with possible involvement of the chemical environment. This theory was based on the pioneering work of Alan Turing [151] and its extensions by Gierer, Meinhardt, and Murray [46, 99, 110], and others. In contrast to previous studies on biological patterning [146, 155], these new approaches were not restricted to the pure description of patterns, but offered the possibility to explain their genesis by *de novo* mechanisms [6]. Originally, such "Turing patterns" are assumed to be driven by the mutual interaction of a slowly-diffusing activator morphogen interacting with a fast-diffusing inhibitor morphogen in a specific nonlinear manner ("short range activation and long range inhibition") [110]. Later works showed that the long-range inhibition does not necessarily require a diffusing inhibitor, but can also result from the depletion of a substrate that is recruited as a result of self-enhancement of the activator ("activator-depleted substrate mechanism" [46, 85]). However, beside these Turing models, other chemical *de novo* models for pattern formation have been proposed, such as the Swift-Hohenberg equation which requires only one diffusing and reacting chemical in order to spontaneously produce patterns [142]. A variety of non-Turing patterns arising in systems coupling one diffusing component with a non-diffusing subsystem has been recently shown in Refs. [59, 60, 97].

These purely chemical theories (including the Turing models) still remain among the central concepts of developmental biology. However, this theory is not devoid of serious difficulties, such as the following ones:

- After more than 60 years of research, the experimental verification of classical Turing-type morphogens (activator/inhibitor) showing properties proposed by the theory is still very rare: E.g. an appropriate candidate for the long-range inhibitor is still missing in many cases [64, 80];
- Turing patterns are common but not robust and usually only stable over narrow parameter ranges [136];
- Diffusion rates as required for Turing-type long-range inhibitors are often at or beyond the limit of measured diffusion rates in biological tissues, especially for patterns appearing on larger tissue scale [68];
- Experimental evidence for the Swift-Hohenberg models as well as for the activator-depleted substrate mechanism is sparse; for the latter there exist candidates for subcellular patterns [70, 91] but not for patterns on tissue scale;
- In many developmental processes, dynamic and complex tissue geometries are likely to prevent the establishment of long range inhibitor gradients [33]; and finally,
- The Turing-theory requires highly nonlinear interactions among different types of morphogens in order to produce *de novo* patterns, which makes the underlying assumptions regarding molecular interactions relatively complex [100].

Finally, the two chemical theories we discussed usually assume that mechanical patterns are ”blind” end-results of chemical pre-patterns. In contrast, various recent studies show that mechanical patterns are not only passive results of chemical pre-patterns, but can play instead a central role by being actively involved in tissue pattern formation (Ref. [13, 24, 35, 105, 117], beyond many others). This agrees well with the observation that mechanical cues can be translated in various ways in order to influence and control chemical patterns, leading to the rapidly evolving research area of mechanotransduction in cell biology [37, 71, 95, 121, 122].

Hence, due the experimental observations and disagreements listed above, tissue mechanics is increasingly moving into focus to explain features of pattern formation which have been previously ascribed to diffusing molecules according to the Turing theory. Notably, forces and flows generated by motor proteins or advection have been proposed to significantly increase diffusion rates for long-range inhibition [68]; and tissue mechanics/geometry (via different mechanical cues such as stretch, stress and strain or tissue curvature) has been theoretically shown to successfully work as long-range inhibitors in spontaneous pattern formation [20, 103, 104]. Importantly, there is also an increasing experimental support for mechanochemical interactions as an important driving force in biological patterning. Examples describing, among other, coupling between diffusing morphogens and tissue bending are summarized in Ref.[64, 112]. Finally, also the Swift-Hohenberg equation has been recently linked to mechanical processes, leading to a possible explanation of different biological patterns such as finger prints [141]. However, a general mechanochemical theory for robust pattern formation is still missing.

Although the need for new modeling approaches integrating chemical (morphogen) and mechanical processes during development has been recently stressed [152], models investigating mechanochemical pattern formation are still rare. One of the first seminal works considering the richness and self-organization of biological growth and forms was the book ”On Growth and form” by D’Arcy Thompson in 1917 [146]. However, even its second edition was written before computers made it possible to develop and study more sophisticated models of biological patterning [6]. One of the first attempts to integrate tissue mechanics in pattern formation models have been the papers by Murray and Oster [107, 111]. In their works, the interplay between migrating and contracting cells and a deformable elastic surrounding medium, for instance an extracellular matrix, can lead to a variety of patterns. The model has been successfully applied to the process of vasculogenesis [108]. A mechanistically related model in which epithelium cells represent the elastic part and actomyosin cross-bridges depict the contractile units has been proposed by Odell *et al.* [119]. Using finite element simulations, they showed that a simple interplay between stretch-induced active contractility and passive propagation of cell stretch can lead to spontaneous gastrulation in tissue spheres. Indeed, recent simulation studies of different mechanochemical models compared to experimental data indicate that the interplay between tissue stretch and morphogens may trigger spontaneous pattern formation in the *Hydra* polyp [105]. Finally, simulation studies demonstrated that mechanical cues other than stretch such as curvature, strain, or stress [103, 104], may drive *de novo* mechanochemical pattern formation.

However, one of the chief simplifications of the above-mentioned approaches is the representation of the 3D tissue body by a 1D curve or a 2D surface. This simplification may cause bias or unrealistic behavior in both chemical and mechanical processes. On one hand, the neglect of one or more dimensions may lead to appearance of nonexistent diffusion barriers, since additional dimensions may allow the molecules to move around obstacles, which is not possible if these dimensions are not present in the model. On the other hand, tissue deformations and mechanical cues propagate via direct interactions of cells or molecules. These processes are altered if dimensions are neglected. For example, describing the tissue as an infinitely thin deforming surface [104, 105] neglects apico-basal chemical and mechanical gradients (i.e. gradients in stretch, strain or stress in normal direction of the tissue sphere) which often accompany deformations. Representing the tissue as a 2D cross-section [103, 119] ignores the 2D nature of circumferential chemistry and mechanics. For instance, saddle surfaces with negative Gaussian curvature promote invaginations and cannot be described adequately if dimensions are neglected, although they may play a critical role for tissue growth and deformations [49, 130]. Several recent experimental works highlight the importance of considering full 3D tissues in order to obtain realistic tissue behavior [5, 52, 86, 147]. In summary, transferring of the above-cited mechanochemical modeling results to reality is possible only to a limited extent.

In his seminal paper, Turing proposed the integration of mechanical aspects in pattern formation, but restricted his own studies to purely chemical processes, since *"...the interdependence of the chemical and mechanical data adds enormously to the difficulty"* [151]. During the last decades, however, modeling and computation approaches integrating mechanical aspects of morphogenesis have reached a sophisticated level (for reviews, cf. Ref. [129, 157]).

In the present study, we thus generalize and extend the existing modeling approaches by introducing a mechanochemical tissue model with the following features:

- Tissue is represented by a time-dependent deformable 3D body formulated in the framework of continuum-mechanics;
- The continuous formulation is blended with an explicit description of cell boundaries, the latter among other representing active forces exerting and possibly showing discontinuities at the plasma membrane ("actomyosin cortex");
- Model equations allow an arbitrary coupling between morphogen dynamics and different mechanical cues, such as curvature, strain, or compression and stretch;
- Simulations are based on the state-of-the-art finite element library GASCOIGNE3D [9] in conjunction with the possibility of local mesh control, multigrid methods as well as parallelization to ensure optimal stability and minimal simulation times.

Since recent experimental efforts to visualize and study tissue mechanics are promising [55, 101, 102, 159], the proposed modeling approach may offer a future basis to verify new experimental hypotheses and to motivate experiments, respectively. Close interplay between experimental manipulations and computer simulations will help to further unravel mechanochemical processes leading to robust patterns during tissue development.

To demonstrate the capacity of mechanochemical interactions in *de novo* pattern formation, in the following, we use the modeling approach as presented within Section 2.3 to simulate feedback loops between morphogen dynamics and tissue mechanics. Especially, we show how different, simple interaction rules based on mechanical feedback by tensor invariants describing stretch, strain and stress lead to spontaneous and robust mechanochemical pattern formation.

5.2 Growth processes in the development of tips in colonial hydroids

Morphogenesis is the fascinating process of organisms developing their structure and their shape, which "remains one of the largest and so far unsolved problems of current biology" (Kosevich [81, p. 90]). In particular, the mechanisms involved during morphogenesis are a topic of special interest in developmental biology. Yet, the underlying organizational and mechanochemical processes remain unknown in most interesting cases. In the course of this application, we asses by numerical simulations how active shearing and rotating cell movements might drive the extensions in growing tips of colonial hydroids (*Hydrozoa, Cnidaria*). In a second step, we compare these deformations to the experimental data provided by Igor Kosevich.

A hydroid colony is a system of branched tubes (shoots) and the stolon that roots the colony on a substrate. Either growing tips or feeding zooids are located at the end of these tubes. The growing tips are solely responsible for the expansion of the hydroid colony and are the center of morphogenesis, see Kosevich [82]. Growing tips in hydroids are ideal subjects to study, as their shape is relatively simple and the cells are uniformly distributed in two soft tissue layers (see e.g. Beloussov [10]). Further, their complexity increases "only through changes in the local curvature" (Kosevich [81, p. 90]), which perfectly fits our modeling approach.

The elongation in hydroid tips is characterized by *growth pulsations*, i.e. by cycles of consecutive extensions, resting and retraction into a single direction. In this dynamic process, six successive phases were first identified by Wyttenbach [158]:

1. Phase A: Extension to the initial peak and resting;
2. Phase B: Retraction;
3. Phase C: Retraction and resting at a (local) minimal length;
4. Phase D: Re-extension to the length in phase A;
5. Phase E: Resting;
6. Phase F: Further extension to the next peak.

We have illustrated these consecutive phases in Fig. 5.1 for experimental data on six successive growth pulsations that was kindly provided by Igor Kosevich [81]. Here, growth pulsations in a hydroid tip were registered under a microscope and are measured in three selected points: In the tip apex (point 1), at the apical part of the basal membrane vault (point 2) and on the

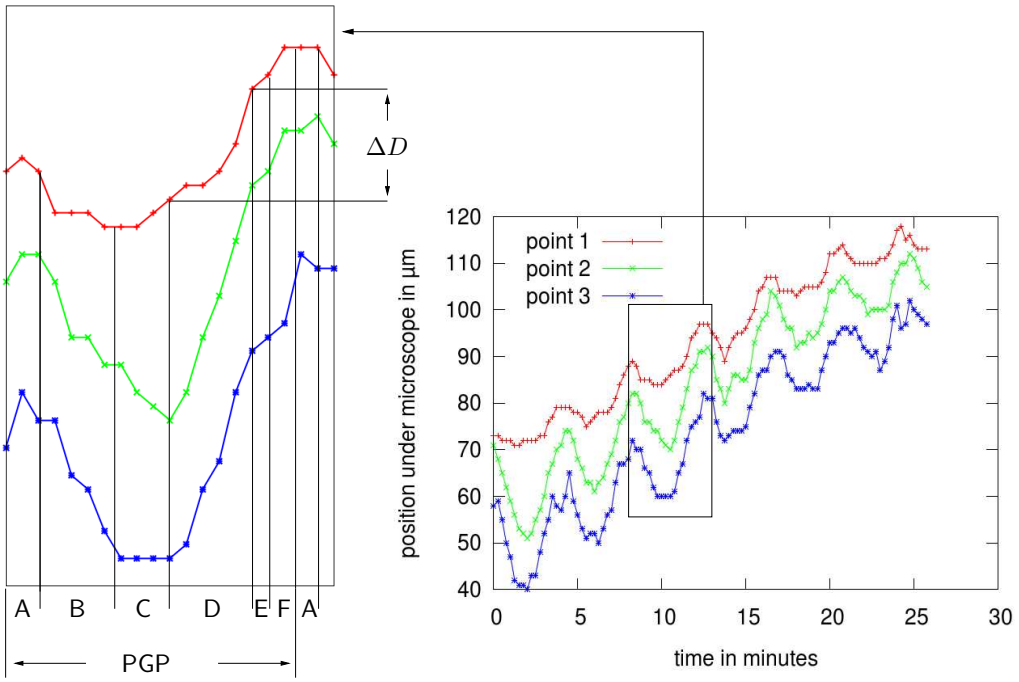

Figure 5.1: Plot of growth pulsations in hydroid tips for three selected points 1,2,3 over time. One period of growth pulsation (PGP) is divided into six successive phases A-F (Wyttenbach [158]). ΔD is the amplitude of tip deformation at point 1 in phase D. Both plots are based on experimental data kindly provided by Igor Kosevich [81].

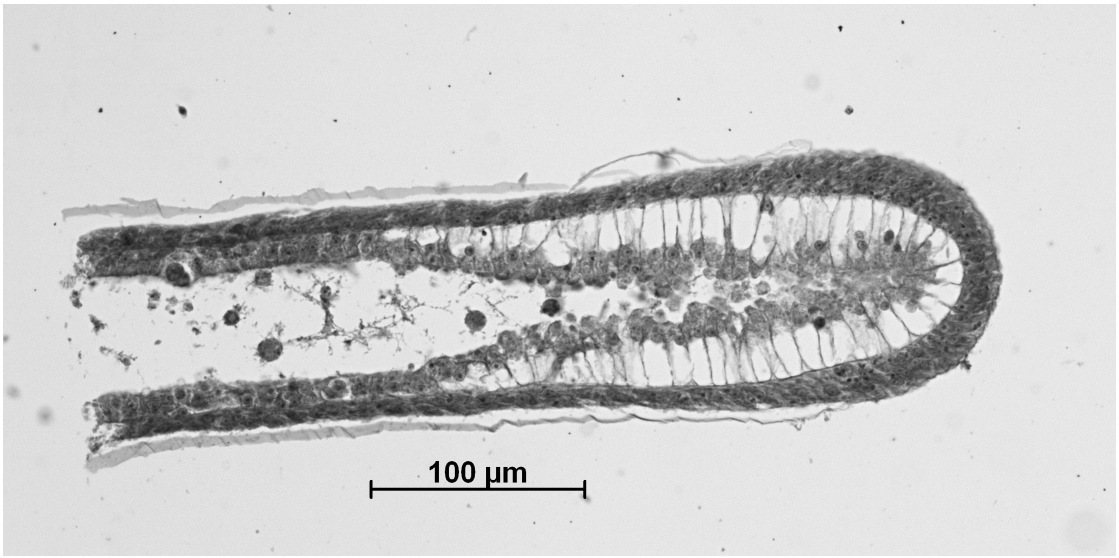

Figure 5.2: Stolon tip in resting phase E after growth in phase D: Longitudinal section through the middle of the stolon and parallel to the substrate . The microscopic picture was kindly provided by Igor Kosevich.

inner surface of the endoderm (point 3) that are located in the distal side of the hydroid tip. The location of these points is illustrated in Fig. 5.3 (b).

The soft hydroid tissue (coenosarc) consists of an inner layer (endodermal cells "END") and an outer one (ectodermal cells "ECT"), which are separated by a membrane (mesoglea). Growing tips differ from the rest of the hydroid body: Here, the soft tissue layers are in close contact with a stiff organic skeleton made of sclerotized chitin "P" (perisarc), that becomes relatively thin, transparent and soft towards the apex of the hydroid tip, see Fig. 5.2 and our illustration of the layers in Fig. 5.3 (a). The three selected points are thus visible through the perisarc which allows a registration of the growth itself as well as of changes in the thickness of each layer.

Based on these six phases of growth pulsations shown above, Kosevich was the first to propose a scheme for the periodic growth processes in hydroids, where the roles of all cell layers are fully considered. With these descriptions at hand, its is now possible to test different mathematical models of the underlying active deformations.

In this thesis, we focus on the re-extension of the hydroid tip (phase D). This phase is characterized by a re-orientation of the ectodermal cells that spreads from the bottom (proximal part) of the hydroid tip to the top, i.e. in distal direction. From the numerical perspective, this phase is the most interesting as it yields the largest deformation of the tip. Besides, the nature of these active deformation is difficult to asses in biological experiments. Here, we try to answer this question from a numerical point of view: First, we propose active deformation tensors that describe shearing and rotational cell movements. In a second step, we can verify our numerical results obtained for these two hypothesized movements by comparing the resulting extensions to the microscope images and findings in Kosevich [81] as well as by comparing the deformations in the three selected points to the experimental data.

Throughout this section, we use the denomination of terms regarding growth pulsations from Igor Kosevich [81]. That way, our presentation is consistent with the nomenclature in the cited literature.

5.2.1 Model geometry

From a mathematical standpoint, we parameterize a hollow cylinder with finite thickness, where all cell layers are in direct contact. The top of the hydroid tip is modeled by a hollow semi-ellipsoid. This initial configuration corresponds to the resting phase C (where no cell movements are registered) prior to the extension phase D and is depicted as the domain above the dashed line in Fig. 5.3 (a).

We prescribe homogeneous Dirichlet values on a small circular cross-section Γ_D of the perisarc, which is a rigid organic skeleton and does not move during growth pulsations by assumption (cf. Fig. 5.3 (b)). Indeed, cutting the domain at this level is justified since we are primarily interested in growth processes in the top of the hydroid tip rather than in its bottom. Further, from a biological perspective, experimental observation indicate that the growth in the hydroid tip functions independently from the rest of the hydroid [10, 81, 158]. On the remaining boundary $\Gamma_N = \partial\Omega \backslash \Gamma_D$, homogeneous Neumann conditions are prescribed.

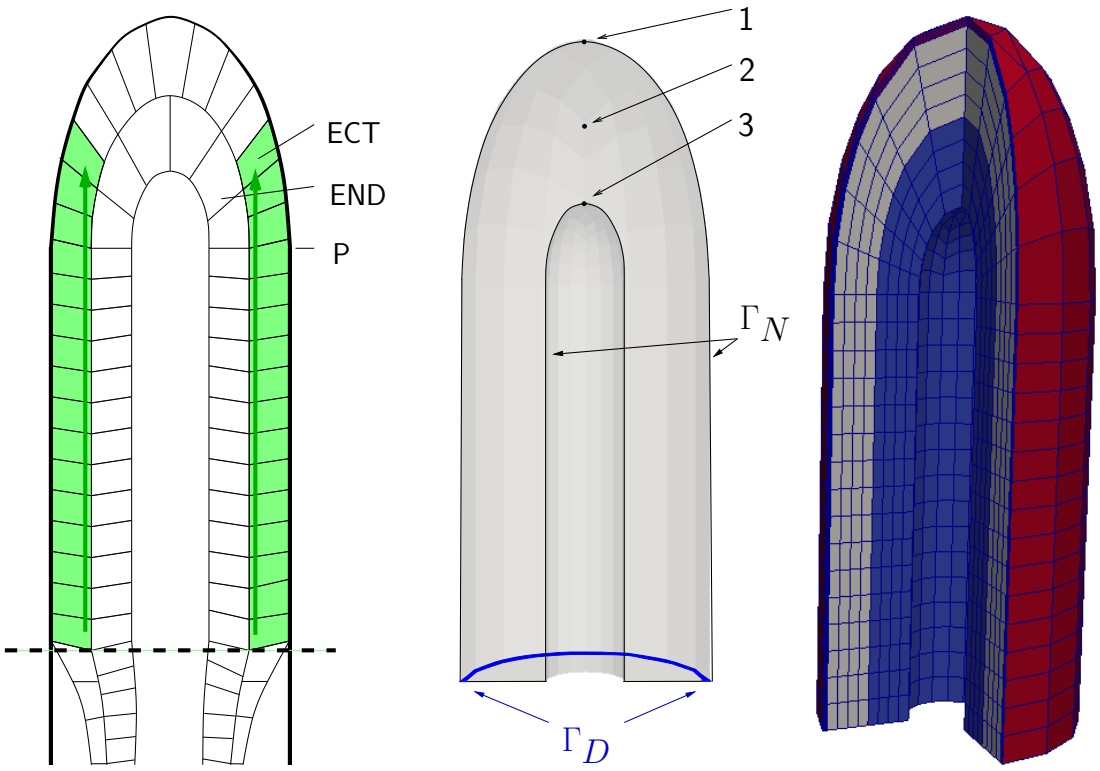

(a) Schema of active extension in phase D in a growing tip of a hydroid colony, adapted from Kosevich [81].

(b) Disjoint boundary parts in a sliced hydroid and selected points of interest.

(c) 3D model geometry and grid of numerical cells (dark blue).

Figure 5.3: Model geometry of a growing tip in a colonial hydroid stolon. (a) Ectodermal (ECT), endodermal (END) cells and the perisarc (P). Actively deforming cells are marked in green. To form the computational domain, we only consider the tip part of the hydroid that is above the dashed line. (b) Dirichlet boundary Γ_D and Neumann boundary Γ_N as well as points $1, 2, 3$ of interest. (c) Numerical cells (blue grid) and biological cell layers (color). Individual, biological cells are not resolved in this application. The hydroid tip has been sliced for the sole purpose of a better visualization

The body of the hydroid tip is composed of 4 032 numerical cells (dark blue grid) that are equally distributed among three material layers forming the endodermal (blue) and ectodermal (grey) cell layers as well as the perisarc (red), as shown in Fig. 5.3 (c). Note that individual, biological cells are not resolved in this application. Rather, the material layers help to distinguish actively deforming cells from passively moving ones and from the perisarc. Further, the material layers are used in the mesh decomposition employed during parallelization of the multigrid solver (cf. Fig. 4.1 (a)). A reference solution necessary to ensure convergence of our solvers was computed for 32 256 numerical cells.

In this thesis, the hydroid tip is initially assumed to be 320µm long, which is the hight above the dotted line in Fig. 5.3 (a). Further, the length (hight) of the endodermal layer is 280µm and the tissue cylinder has an outer diameter of 125µm. The outer radius of the ectodermal tube is assumed to be $R_0 = 60\mu m$ and is important in the description of active deformations. These values were picked consistent with the geometrical description of a growing hydroid tip in Kosevich [81].

5.2.2 Model equations

In the following, we specify our prototypic equations in variational form (3.1) to investigate growth processes in the development of tips in colonial hydroid. Therefor, we reduce our model to the structural equation only and investigate how different active deformations lead to qualitatively different extensions of hydroid tips. In the hydroid tip, the actively deforming tissue layers are surrounded by a rigid skeleton (perisarc) that is only soft towards the growing tip but can be regarded as fixed on its cross-section towards the main body of the hydroid colony as discussed above.

Hence let $\Omega \subset \mathbb{R}^d$, $d = 2, 3$ be a (bounded) domain. Let the boundary $\partial\Omega$ of our domain be split into two disjoint parts $\partial\Omega = \Gamma_D \cup \Gamma_N$ where homogeneous Dirichlet and Neumann conditions are prescribed, respectively. Further, we define the Hilbert space V_0^d with $V_0 := \{\mathbf{v} \in H^1(\Omega) : \mathbf{v}|_D = 0\}$ for $d = 2, 3$. Then, our reduced model applied to growth processes in hydroids reads in variational form:

Find displacement $\mathbf{u} \in V_0^d$ for initial conditions $\mathbf{u}(\mathbf{X}, 0) = 0$, $C(\mathbf{X}, 0) = C^0(\mathbf{X})$ such that

$$(\rho^0 \partial_t \mathbf{u}, \boldsymbol{\Phi})_\Omega + (\mathbf{F}\boldsymbol{\Sigma}, \nabla\boldsymbol{\Phi})_\Omega = 0 \qquad \forall \boldsymbol{\Phi} \in V^d$$

holds, where

$$\boldsymbol{\Sigma} = J_a \mathbf{F}_a^{-1} \boldsymbol{\Sigma}_e \mathbf{F}_a^{-T}, \quad \boldsymbol{\Sigma}_e = \lambda \operatorname{tr}(\mathbf{E}_e)\mathbf{I} + 2\mu\mathbf{E}_e, \quad \mathbf{E}_e = \frac{1}{2}(\mathbf{F}_e^T \mathbf{F}_e - \mathbf{I}),$$
$$\mathbf{F}_e = \mathbf{F}\mathbf{F}_a^{-1}, \quad \mathbf{F} = \nabla\mathbf{u} + \mathbf{I}, \quad J = \det(\mathbf{F}), \quad J_a = \det(\mathbf{F}_a),$$

and μ, λ are the Lamé constants that we introduced in Subsection 2.1.5.

In these model equations, we replaced the second derivative in time by the first derivative: That way, we can discretize the first derivative by the implicit Euler method, which proved to be the straightforward way to damp oscillations of the tissue during growth in our numerical

tests. Also, enhanced numerical damping methods still lack. Oscillations are damped since, on the one hand, we are interested in the growth processes itself rather than the exact elastic material behavior. On the other hand, we have so far neglected the water surrounding *Hydra* colonies which takes the role of damping in the actual natural setting. Yet, numerical tests with a fluid surrounding the hydroid do not provide further insights but proved to be computationally expensive and required significant, additional model assumptions.

Active deformation gradients

In this application, we focus on the mechanical mechanisms involved in the morphogenesis of hydroid tips. In particular, we are interested in the active deformations that lead to the active extensions observed in phase D of each growth pulsation. In this phase, the ectodermal cells (green) change their orientation towards the apex (distal direction), see Fig. 5.3 (a). The side towards the basal membrane experiences the largest deformation whereas the side towards the rigid perisarc remains immobile. Further, this active deformation is located in the growing tip only and does not involve the endodermal cells (cf. Kosevich [81]). Based on these experimental observations, we propose two different active deformation tensors to describe this motion:

On the one hand, we prescribe an active shearing where the ectodermal cells move towards the top of the hydroid tip only. Whereas this seems to be efficient at first sight, we also observe that this process involves a thinning of the ectodermal layer. Hence, the endodermal tube inside the tissue widens due to the elastic response that ensures the continuity of the overall deformation, i.e., it closes the "gap" between both layers that the active shearing causes in the intermediate configuration, as shown in the middle of Fig. 5.4.

On the other hand, we prescribe an active rotation of the ectodermal cells as shown in the right of Fig. 5.4. This rotation of a point in the ectodermal layer is prescribed around an axis, which is orthogonal to the cylindrical radius of this point and located in at the membrane towards the stiff perisarc surrounding the growing tip. Further, we observe that this rotating motion does not necessarily, by definition, result in rupture in the intermediate configuration and does not widen the endodermal tube inside the hydroid. For the sake of a crisp presentation, we have moved the geometrical details of this rotation to the appendix, see Section A.1.

For the moment, we assume that both active deformations depend on time in a linear manner. This is a reasonable assumption since we merely intend to asses the quality of the active deformations, i.e., whether a shearing or a rotating active deformation describes the observed growth process more accurately. Furthermore, this simplification reduces our system of equations to the structural one only, see Eq. 5.2.2. Correspondingly, experimentally observed growth processes suggest that growth rates in phase D are almost constant (cf. Kosevich [81]) in a single organism. The magnitude of stolon growth however depends on various parameters that are difficult to account for such as stolon age, the nutrition state, the genetic makeup and the temperature. Hence, anticipating the magnitude of the extension in advance is not possible (Wyttenbach [158]). In summary, a linear dependency of growth on time seems reasonable whereas it is not constructive to overfit our parameters to attain a certain magnitude of the elongation.

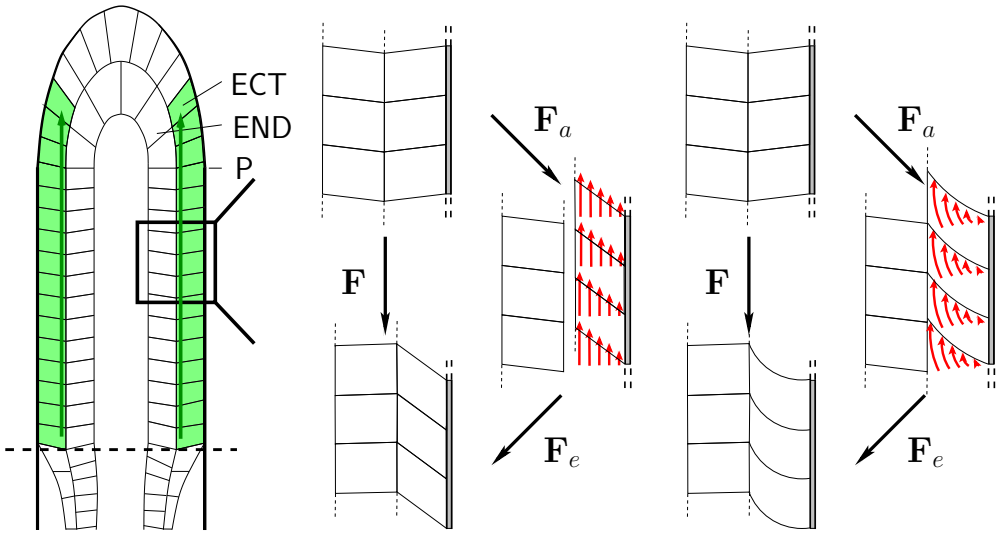

Growing hydroid tip, adapted from Kosevich [81].

Shearing active deformation

Rotating active deformation

Figure 5.4: Schematic illustration of the deformation gradient decomposition: Active extension of the hydroid tip due to shearing and rotation for a selected part of the tissue (left). Both active deformation gradients are continuous within the ectodermal layer (ECT).

For a shearing active motion of the biological cells in the ectoderm layer (ECT), the active deformation tensor is given by

$$\mathbf{F}_a(\mathbf{X}, t) := \begin{pmatrix} 1 & 0 & 0 \\ 0 & 1 & 0 \\ -X_0 r^{-1} k(t) & -X_1 r^{-1} k(t) & 1 \end{pmatrix}. \tag{5.1}$$

Further, the active deformation tensor for a rotating motion of the biological cells in the ectodermal layer (ECT) is given by

$$\mathbf{F}_a(\mathbf{X}, t) := \begin{pmatrix} X_1^2 r^{-3} A(\alpha) + \cos(\alpha(t)) & X_0 X_1 r^{-1} A(\alpha) & 0 \\ X_0 X_1 r^{-3} A(\alpha) & X_0^2 r^{-3} A(\alpha) + \cos(\alpha(t)) & 0 \\ -\sin(\alpha(t)) X_0 r^{-1} & -\sin(\alpha(t)) X_1 r^{-1} & 1 \end{pmatrix}, \tag{5.2}$$

with

$$\begin{aligned} A(\alpha) &= R_0 - R_0 \cos(\alpha(t)) - K \sin(\alpha(t)), \\ \alpha(t) &= \pi(r_0 - r) k(t). \end{aligned}$$

In both definitions, $r = \sqrt{X_0^2 + X_1^2}$ is the cylindrical radius of $\mathbf{X}$ in the hydroid body. Next, R_0 is the cylindrical radius of the border between ectodermal cells and perisarc and K the offset in X_2-direction between the rotation axis and $\mathbf{X}$. Whereas the shearing tensor takes a simple form and it is straightforward to visualize the rotation tensor (cf. Fig. 5.4), the geometrical derivation

of the latter is rather complex. For the sake of readability, the reader will find the derivation of these active deformation tensor in Section A.1 of the appendix.

Both tensors depend on time in a linear manner:

$$k(t) = \begin{cases} t - X_2 T_{next} & \text{if } X_2 T_{next} < t < X_2 T_{next} + T \text{ and } \mathbf{X} \text{ in } ECT \\ T & \text{if } t \geq X_2 T_{next} + T \text{ and } \mathbf{X} \text{ in } ECT \\ 0 & \text{else.} \end{cases} \tag{5.3}$$

Hence, both tensors prescribe an active deformation in $\mathbf{X}$ if this point belongs to an ectodermal cell in the hydroid cylinder (colored green in Fig. 5.3 (a)) and of the current time exceeds $X_2 T_{next}$. That way, the deformation propagates from the bottom to the top of the hydroid tip. After time $t \geq X_2 T_{next} + T$ we prescribe a constant deformation. The latter is crucial since we neither update the reference configuration nor consider a viscoelastic material model. Instead, the tissue will return to its initial state if the active deformation is removed. For all other cells in the tip, the endodermal layer (END) or the perisarc (P) we set $\mathbf{F}_a = \mathbf{I}$ by $k(t) = 0$.

Here, we introduced two constants, namely T_{next} and T. The former describes the speed of the propagation of the active deformation towards the hydroids tip, i.e. this is essentially the time one biological cell needs to deform before the next one commences - although we stress that we do not model biological cells explicitly in this setting. The latter constant is the absolute time/angle until which the point shears/rotates. Since the active deformation depends linearly on time, T effectively scales the maximal deformation rate. Note that, in case of a rotation, T is essentially the maximal deformation angle. We misused the notation here for the sake of a consistent definition of $k(t)$ covering both active deformation tensors.

For a shearing motion, the active deformation gradient is volume-preserving: This is simple to spot, since $J_a = \det(\mathbf{F}_a) = 1$ which gives for any deformed volume $\hat{V}_a$ and its corresponding volume $\hat{V}$ in the reference configuration

$$|V_a| = \int_{V_a} \mathrm{d}X_2 \mathrm{d}X_1 \mathrm{d}X_0 = \int_V |\det(\mathbf{F}_a)| \, \mathrm{d}X_2 \mathrm{d}X_1 \mathrm{d}X_0 = \int_V \mathrm{d}X_2 \mathrm{d}X_1 \mathrm{d}X_0 = |V|.$$

Next, the determinant of our active deformation tensor describing a rotating motion is given by $J_a = \det \mathbf{F}_a = \cos(\alpha)(\cos(\alpha) + A(\alpha) r^{-1})$, which is not equal to one in general so that we scale the active rotations by its determinant. Alternatively, we could simply leave the volume-preservation to the elastic material model, which is successfully tested in the next application to embryogenesis in case of one specific active deformation gradient.

5.2.3 Parameter setup

Firstly, the time needed for the propagating deformation to effect one cell is set to $T_{next} = 12$s. Secondly, the maximal deformation time/ deformation angle is given by $T = 30$s for a shearing and by $T = 0.25$rad in case of rotating cell movement (the angle is given in terms of radians rather than degrees, minutes and seconds). With these settings, we obtain a timescale of 120s for phase D of a growth pulsation. Although this value varies in contrast to the invariance of a whole pulsation period, this is the value generally proposed in literature [81, 158].

The choice of the Lamé constants is not important (cf. Subsection 5.3.3). In fact, it is only essential to reflect the different stiffness properties of the tissue layers: The soft coenosarc composed of the endodermal and ectodermal cell layers and the stiff outer skeleton (perisarc). The Lamé constants are usually expressed in terms of Young's modulus E and Poisson's ratio ν, which can be obtained by the conversion formulas given in Eq. (2.24). For the soft tissue, we used $E = 100\,\text{Pa}$ and $\nu = 0.4$ similar to the assumptions made in Ref. [1] in the context of ventral furrow invagination in *Drosophila*. In the perisarc, we assume $E = 200\text{Pa}$ and $\nu = 0.4$ in its rigid cylindrical part (fat black line in Fig. 5.3) and a quadratic drop of E (over the range of one biological cell) to 100 Pa in its soft and transparent semi-ellipsoidal top. We postpone the implementation of viscoelastic behavior of the tip apex to future research.

Finally, we point out that the router radius of the ectodermal tube depends on the geometry of the growing hydroid tip under consideration. In the description of the model geometry above, we chose $R_0 = 60\,\mu\text{m}$.

5.2.4 Numerical results and discussion

In this first application, we reduced our prototypical system of PDEs to the structural equation only to investigate growth processes in colonial hydroids. These processes occur in cycles, called growth pulsations, where we focus on phase D that comprises active deformations of the ectodermal cells (cf. Fig. 5.3 (a) (green)) and results in an extension of the stolon tip. In the previous section, we proposed active deformation tensors describing shearing and rotating movements of the ectodermal cells to model this motion.

Simulation snapshots showing the extension in the tip of a colonial hydroid for both active deformations are shown in Fig. 5.5. We observe how the deformation propagates from the bottom to the top of the hydroid tip over time. For a rotating motion of the ectodermal cells in the top row, we register a larger extension of the tip compared to a shearing one. Interestingly, the deformation of the ectodermal cells in the cylindric part of the tip is larger for a shearing deformation which results in a smaller extension of the tip nonetheless. Additionally, snapshots of a shearing motion indicate that the endodermal tube is widened for this kind of active deformation. This deformation would hence mean a huge effort to be summoned by the ectodermal cells that does not translate into a large extention of the growing tip. Moreover, a widening of the endodermal tube is not experimentally observed in phase D (see Kosevich [81]).

In the next step, we want to compare the tip extensions that we witnessed in our numerical simulations to experimental data collected by Igor Kosevich. These observations were made under a Biolam microscope (Russia), where $5 - 12$ successive cycles with a total duration of $1 - 1.5$h were captured every twelve seconds (cf. Kosevich [81]). Regarding the dynamics of stolon elongation in hydroid, Wyttenbach [158] established that the duration of each cycle is highly reproducible if the temperature and the organic contamination of the sea water are constant. In particular, it is invariant to the colony age (i.e. the mass due to growth over time), the location of the stolon inside the colony and the nutrition state. The successive phases in a cycle are even negatively correlated which ensures the constancy of the pulsation period (cf. Kosevich [81]).

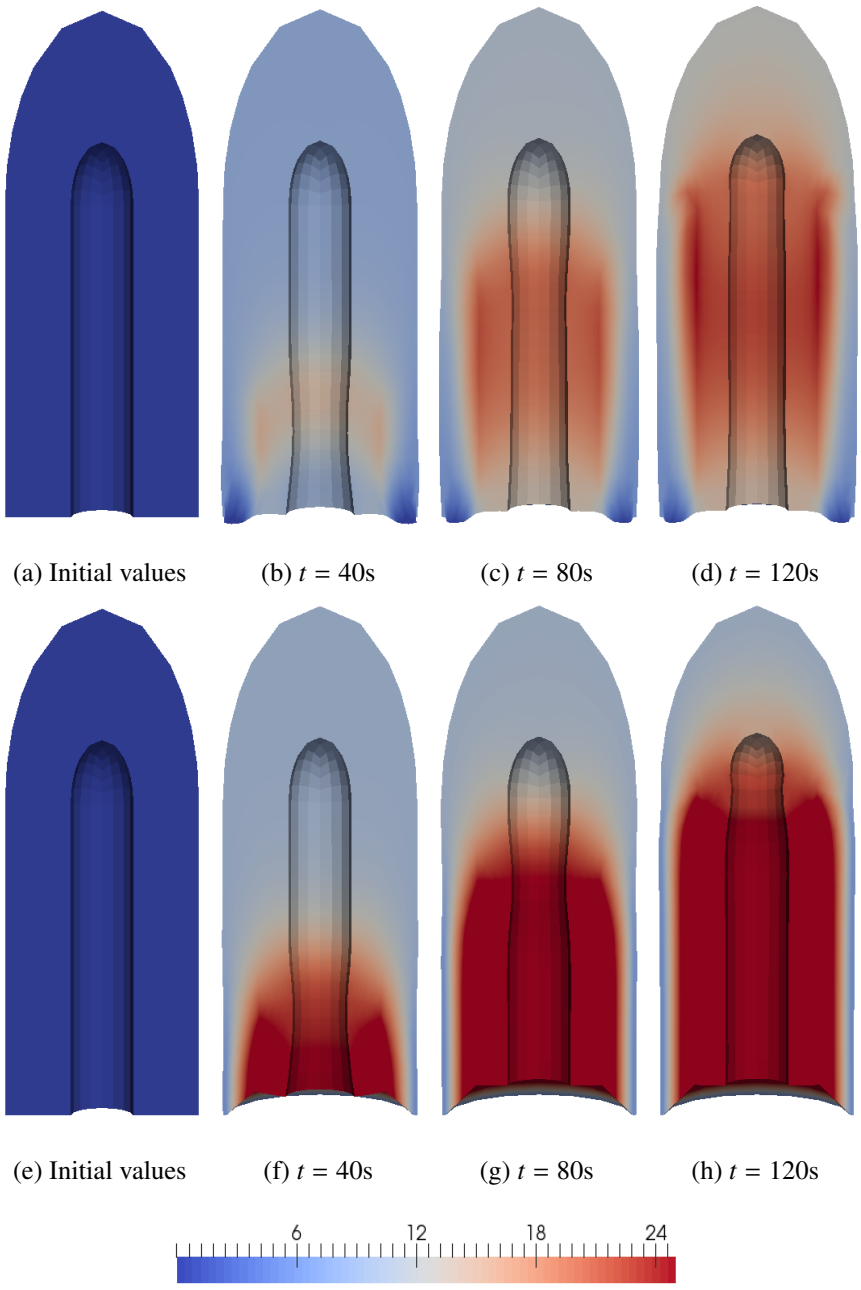

(a) Initial values (b) t = 40s (c) t = 80s (d) t = 120s

(e) Initial values (f) t = 40s (g) t = 80s (h) t = 120s

Growth of the tip in distal direction (X_2) in μm

Figure 5.5: Simulation snapshots showing an extension in the tip of a colonial hydroid due to active deformations of the ectodermal cells (phase D of growth pulsations). (a)-(d) active rotation, (e)-(h) active shearing.

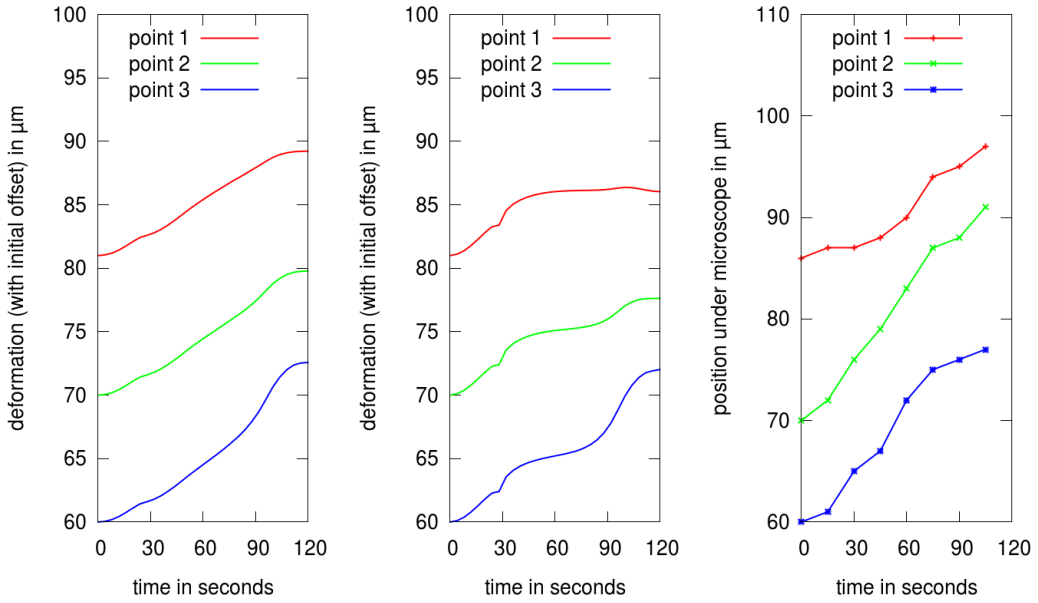

(a) Active rotation (b) Active shearing (c) Experiment, cf. Fig. 5.1

Figure 5.6: Plots of the deformations during the extension phase D in the three selected points (cf. Fig 5.3). (a)-(b): Deformation during our numerical simulations. (c): Deformation registered during phase D of growth pulsations, extracted from the experimental data shown in Fig. 5.1 (provided by Igor Kosevich [81]).

Yet, a quantitative comparison of our results to the experimental data is not feasible, since the magnitude of the extension varies significantly and depends on the stolon age, the nutrition state, the genetic makeup and the temperature: Anticipating the magnitude of the extension in advance is thus not possible (Wyttenbach [158]) and a “considerable variability in the rates of movements of ectodermal cells has been demonstrated” Beloussov *et al.* [10, p. 317].

For a qualitative assessment, we pick phase D from the highlighted pulsation in Fig. 5.1 to compare our numerical results with the experimental data. This comparison is carried out in the previously selected points in the tip apex (point 1), at the apical part of the basal membrane vault (point 2) and on the inner surface of the endoderm (point 3).

In Fig. 5.6 we have plotted the extension in distal direction in the three selected points based on an active rotation (a), active shearing (b) and for the experimental data (c). One the one hand, we observe that the plots for the active deformation describing a rotation of the ectodermal cells strongly resembles the experimental one shown on the right. In particular, we observe an almost constant extention of the hydroid tip. On the other hand, an active shearing results in a comparably smaller extension of the hydroid tip. Also, we find saddle points in the growth over time plotted for a shearing that are not registered in the actual organism under the microscope.

In summary, a rotational active deformation of the ectodermal cell better explains the elongation process during phase D of growth pulsations for the following reasons:

- Our simulation snapshots of rotating active motions strongly resemble phase D in experimentally observed growth pulsations. In contrast, we observe saddle points in the shearing motion over time which are not registered in the experimental observations. Correspondingly, Kosevich [81] states that the "rate of tip movement at phases B,D and F is constant";
- The shearing deformation results in a larger deformation in the cylindrical hydroid part but yields a smaller elongation of the hydroid tip (cf. Fig. 5.5 (a)-(d) to (e)-(h)). This is a strong indication that a shearing deformation does not model a biological process which is usually driven by minimizing the energy that is required for a motion;
- Ultimately, a shearing motion of the ectodermal cells leads to a widening of the endodermal tube (cf. Fig. 5.5 (e)-(h)) and yet to a smaller elongation of the tip. In phase D, such a widening is not observed experimentally and is also absent for a rotating cell movement.

This first example allowed to verify the implementation of growth and gave a glimpse into the importance of choosing an active deformation gradient. In the following section, we apply the whole prototypical coupled system of PDEs to the more complex situation of *de novo* mechanochemical pattern formation in embryogenesis.

5.3 Mechanochemical pattern formation in embryonic development

One of the most fascinating processes in developmental biology is the self-organization and the self-complexation of biological tissue. One prominent example is embryogenesis where a fertilized cell develops step by step into a complex organism. Here, we focus on the blastula stage, where various mechanical and chemical patterns emerge on relatively simple structures, namely a tissue sphere of biological cells [47]. As discussed in the biological motivation of this chapter (cf. Section 5.1), pattern formation in biological tissue requires a modeling approaches that combines tissue mechanics and morphogen dynamics.

In this section, we apply our prototypical system of PDEs (3.1) including mechanochemical feedback loops to embryogenesis leading to spontaneous (*de novo*) and robust pattern formation.

The results presented in this section were recently published in Brinkmann *et al.* [20]. In the course of this work, those results were supplemented by further simulations, e.g. by novel results for the stress-mediated feedback loop including mesh adaptivity and an enhanced model, where we integrate the mechanical feedback over biological cells. Further, the robustness with regard to the model geometry, diffusion rates and material properties are investigated. In particular, two invaginations are observed for quadrupled diffusion rates and stretch-mediated mechanical feedback in conjunction with active apical constriction (wedging) of biological cells. Finally, we implemented a novel internal pressure to account for the fluid contained inside the tissue sphere, which leads to stationary mechanochemical patterns during gastrulation events.

In two dimension, we published first results in Mercker et al [103]. In this work, the interplay between stiffness and diffusion was further investigated and is interpreted in the light of our new findings in three dimensions. For the sake of brevity, we postpone the presentation of these results to the appendix.

This section is split into the following parts: Firstly, we illustrate the model geometry and present our system of prototypic PDEs applied to mechanochemical pattern formation. Thereafter, the piecewise-defined active deformation gradient modeling apical/basal constriction of individual biological cells is derived. Also, we specify the stretch- and strain-based mechanical feedback on the morphogen production.

Secondly, we present simulation snapshots of our numerical results where we focus on gastrulation events and the robustness of our modeling approach, e.g. with regard to initial conditions, diffusion rates or model geometry.

Finally, we present the inner volume constraint (pressure) which accounts for the fluid contained inside the tissue sphere and leads to stationary solutions for gastrulation as well as a novel enhanced modeling approach where we integrate the mechanical feedback over biological cells.

5.3.1 Model geometry

We investigate a system representing developmental stages following the blastula stage of an embryo.

In two dimensions, we parameterize over a 2D cross-section through the blastula that is a tissue loop with a finite thickness which is confined to the 2D plane. This loop represents one cell layer which is composed of 128 biological cells that are circumferentially arranged in two layers. Each biological cell is resolved by $64 = 8^2$ numerical ones such that 8 192 numerical cells are required overall (cf. Fig. 5.7 (a)-(b)). In two dimensions, results were verified by resolving each biological cell by $4096 = 64^2$ numerical ones, which results in 528 384 numerical cells overall. In detail, convergence is analyzed in Section 3.5.

In 3D, we parameterize a deforming tissue body over a hollow tissue sphere (cf. Fig. 5.7 (c)-(d)). The sphere is composed of 1 536 biological cells which are arranged circumferentially in one layer. Each biological cell contains $64 = 4^3$ numerical ones, which implies that we have 98 304 numerical cells overall. Simulation results have been exemplarily verified using $512 = 8^4$ numerical cells for each biological one, i.e. for a total of 786 432 numerical cells. A thorough convergence analysis in two and three dimensions including an adaptive local mesh refinement strategy for stress-based mechanical feedback is presented in Section 3.5.

If not stated otherwise, the outer radius of this tissue sphere is 150µm and the inner radius is 135µm which results in a tissue thickness of 15µm in the two- and three-dimensional settings.

5.3.2 Coupled system of model equations

In the following, we specify our prototypic equations in variational form (3.1) for the application to mechanochemical pattern formation in embryonic development. Especially, we only consider one species of signaling molecules of concentration C and consequently consider only

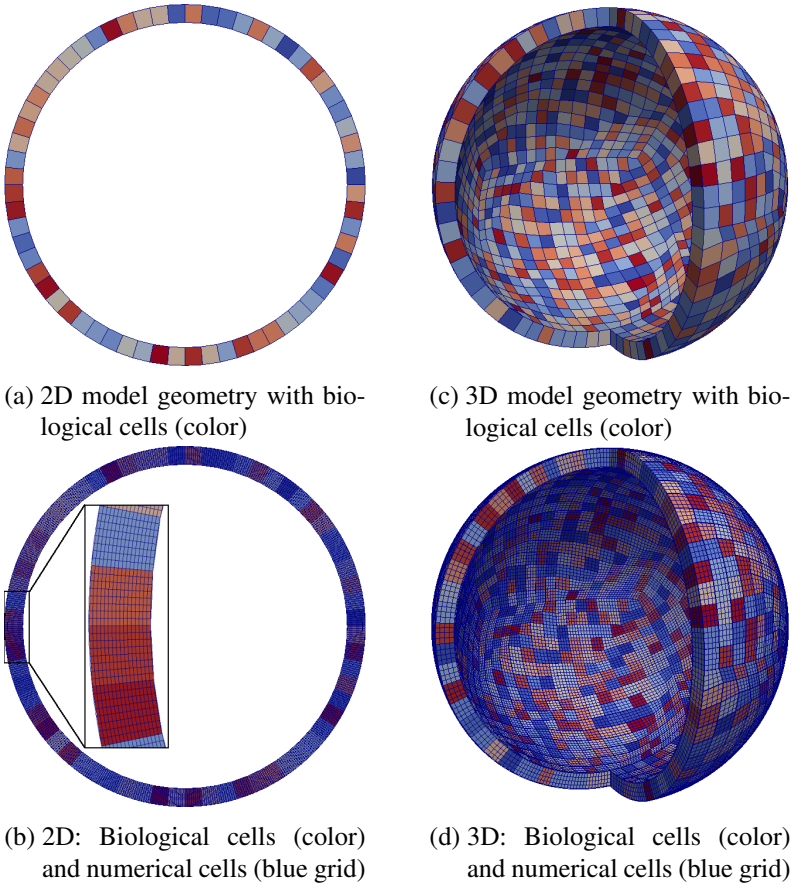

(a) 2D model geometry with biological cells (color)

(c) 3D model geometry with biological cells (color)

(b) 2D: Biological cells (color) and numerical cells (blue grid)

(d) 3D: Biological cells (color) and numerical cells (blue grid)

Figure 5.7: Model geometries: (a)-(b) 2D tissue cross-section, (c)-(d) 3D tissue sphere, which was sliced for the sole purpose of a better visualization.

one reaction-diffusion equation coupled to the structural one. Typically in embryonic development, it is *a priori* not known where deformation will take place and Dirichlet boundary values cannot be prescribed. In general, we thus employ homogeneous Neumann boundary values on the entire boundary, which requires to include a stabilization term as discussed in Section 3.3.

We consider $\Omega \subset \mathbb{R}^d$, $d = 2, 3$ to be a (bounded) domain in two or three dimensions. Next, let the boundary $\partial\Omega$ of our domain be split into two disjoint parts $\partial\Omega = \Gamma_{in} \cup \Gamma_{out}$ that denote the inside and the outside of the tissue sphere. Then, for suitable Hilbert spaces V^d and $V := H^1(\Omega)$ for $d = 2, 3$, our prototypic equations in variational form (3.1) applied to embryonic development reads:

Find displacement $\mathbf{u} \in V^d$ and concentration of signaling molecules $C \in V$ with initial conditions $\mathbf{u}(\mathbf{X}, 0) = 0$, $C(\mathbf{X}, 0) = C^0(\mathbf{X})$ such that

$$\begin{aligned} (\epsilon\rho^0 \partial_{tt}\mathbf{u}, \boldsymbol{\Phi})_\Omega + (\mathbf{F}\boldsymbol{\Sigma}, \nabla\boldsymbol{\Phi})_\Omega - (\mathbf{g}, \boldsymbol{\Phi})_{\Gamma_{in}} = 0 \qquad & \forall \boldsymbol{\Phi} \in V^d \\ (J\partial_t C, \Psi)_\Omega + (J\mathbf{F}^{-1}\mathbf{D}\mathbf{F}^{-T}\nabla C, \nabla\Psi)_\Omega - (JR, \Psi)_\Omega = 0 \qquad & \forall \Psi \in V \end{aligned} \tag{5.4}$$

holds, where

$$\boldsymbol{\Sigma} = J_a \mathbf{F}_a^{-1} \boldsymbol{\Sigma}_e \mathbf{F}_a^{-T}, \quad \boldsymbol{\Sigma}_e = \lambda \operatorname{tr}(\mathbf{E}_e)\mathbf{I} + 2\mu\mathbf{E}_e, \quad \mathbf{E}_e = \frac{1}{2}(\mathbf{F}_e^T\mathbf{F}_e - \mathbf{I}),$$
$$\mathbf{F}_e = \mathbf{F}\mathbf{F}_a^{-1}, \quad \mathbf{F} = \nabla\mathbf{u} + \mathbf{I}, \quad J = \det(\mathbf{F}), \quad J_a = \det(\mathbf{F}_a),$$

and where μ, λ are the Lamé constants. Further, the parameter $\epsilon \sim 0.1$ prescribes the strength of the stabilization. Next, R is the coupling term incorporating the feedback of mechanical tensor invariants on the morphogen concentration C via $R = R(I(\boldsymbol{\Sigma}), I(\mathbf{E}), I(\mathbf{F}), C)$ and will be specified in the following. Vice versa, $\boldsymbol{\Sigma}(\mathbf{F}_a(t, C))$ allows for a coupling of the morphogen concentration C on the active deformation process such as local tissue growth or cell-shape changes. The active deformation will be specified in the next subsection. The coupling results in a positive, self-inducing feedback loop which is presented in Subsection 2.3.3 and illustrated in Fig. 2.5.

The change in the geometry observed in a gastrulation event speeds up the deformation process. To obtain stationary solutions in that process, an inner pressure is implemented. This pressure accounts for the fluid contained inside the hollow sphere. We implement a surface force $\mathbf{g}$ to model the inner pressure which acts on the inner boundary of the tissue sphere. This surface force depends on the change of the inner volume of the tissue sphere and is introduced in Subsection 5.3.5.

Finally, $\mathbf{D} \in \mathbb{R}^{d\times d}$ is the diffusion coefficient tensor, which reads in matrix notation

$$\begin{aligned} \mathbf{D} &:= \mathbf{Q}(\mathbf{X})^T \operatorname{diag}(D_\mathbf{N}, D_\mathbf{T})\mathbf{Q}(\mathbf{X}) && \text{for } d = 2 \\ \mathbf{D} &:= \mathbf{Q}(\mathbf{X})^T \operatorname{diag}(D_\mathbf{N}, D_\mathbf{T}, D_\mathbf{T})\mathbf{Q}(\mathbf{X}) && \text{for } d = 3, \end{aligned}$$

with a diagonal matrix containing the diffusion coefficient $D_\mathbf{N}$ in normal (or radial) Lagrangian direction $\mathbf{N} = |\mathbf{X}|^{-1}\mathbf{X}$ and the diffusion coefficient $D_\mathbf{T}$ in the tangential directions $\mathbf{T}_1$ and $\mathbf{T}_2$ (or just one direction $\mathbf{T}$ in 2D). The rotation matrix $\mathbf{Q}^T$ transforms the diagonal matrix $\operatorname{diag}(D_\mathbf{N}, D_\mathbf{T}, D_\mathbf{T})$ defined in the point-specific coordinate systems given by the orthogonal unit vectors $\mathbf{N}(\mathbf{X})$, $\mathbf{T}_1(\mathbf{X})$ and $\mathbf{T}_2(\mathbf{X})$ to Euclidean coordinates. This choice is biologically motivated: On the tissue scale, a large coefficient $D_\mathbf{N}$ in radial direction ensures free diffusion inside the biological cells whereas a small coefficient $D_\mathbf{T}$ limits diffusion between biological cells. On the cellular level, this approach is not exact as concentration gradients inside biological cells remain. Still, we believe that our modeling approach is sufficiently accurate: In particular, we are interested in pattern formation on the tissue scales and biological cells are not resolved except for the cell-wise description of active deformations. These matters are extensively discussed in Subsection 2.3.1.

Mechanical feedback

In this application, we mainly consider mechanical feedback on the morphogen production that is based on the determinant of the deformation gradient. This tensor invariant has the physical interpretation of compression ($\det(\mathbf{F}) < 1$) or stretch ($\det(\mathbf{F}) > 1$), i.e. $\det(\mathbf{F}) = \frac{dv(t)}{dV}$ is the ratio of the deformed volume element $dv(t)$ to the initial one dV. In the stretch-mediated feedback loop, the coupling term $R(I_3(\mathbf{F}), C)$ (cf. Eq. (2.40)) including $I_3(\mathbf{F}) = \det(\mathbf{F})$ takes the form

$$R(I_3(\mathbf{F}), C) = k_2 \frac{\max\{(I_3(\mathbf{F}) - 1), 0\}}{k_m + \max\{(I_3(\mathbf{F}) - 1), 0\}} - k_1 C.$$

Note that morphogen is produced if the biological cell is stretched. This choice is arbitrary as implementing morphogen production in case of compression produces identical results. The careful reader may have noticed that morphogen is thus only produced in parts of stretched biological cells and distributed by large radial diffusion rates. A complete discussion on the role of diffusion is given in Subsection 2.3.1.

We point out that qualitatively identical results were obtained for the strain-mediated feedback loop which relied on the first invariant of the Green-Lagrange strain tensor $I_1(\mathbf{E}) = \mathrm{tr}(\mathbf{E})$. These results are not shown.

In the following, we further present results for the stress-mediated feedback loop where the determinant of the second Piola-Kirchhoff stress tensor $I_3(\mathbf{\Sigma}) = \det(\mathbf{\Sigma})$ is used. For this tensor invariant, the coupling term given in Eq. (2.40) takes the form

$$R(I_3(\mathbf{\Sigma}), C) = k_2 \frac{\max\{I_3(\mathbf{\Sigma}), 0\}}{k_m + \max\{I_3(\mathbf{\Sigma}), 0\}} - k_1 C.$$

For details on the implications of this coupling we refer to Subsection 2.3.3.

Active deformation gradient

In experiments, signaling molecules have been shown to influence the mechanics of biological cells in various ways, such as growth, modifications of stiffness properties or active cell-shape changes [12, 17, 32, 58]. These processes can be anisotropic or can be restricted to just one of several cell layers. In this application, we mainly consider morphogen-induced (basal/apical) constriction in one layer of biological cells, since this is a commonly observed mechanism during morphogenesis [89, 98, 106, 115, 118, 134]. Here, apical constriction refers to the constriction (wedging) of the biological cells at the side pointing towards the blastula lumen (i.e. towards the inside of the tissue sphere), whereas basal constriction is the analogous constriction of the side pointing away from the blastula lumen (i.e. towards the outside of the tissue sphere). A schematic illustration of basal constriction is shown in Fig. 5.8.

In all our feedback loops, the influence of morphogens on local tissue mechanics is expressed via the active part $\mathbf{F}_a(\mathbf{X}, C)$ of the decomposed deformation gradient $\mathbf{F} = \mathbf{F}_e\mathbf{F}_a$ (cf. Eq.(2.25)). Thereby, it is a common assumption that the concentration of signaling molecules directly couples into the active deformation gradient [1, 20, 104, 120].

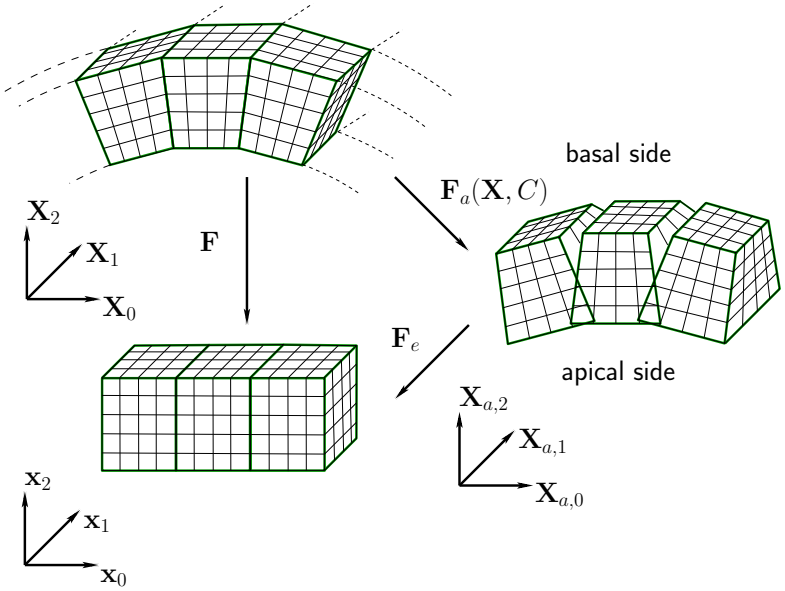

Figure 5.8: Schematic illustration of the multiplicative deformation gradient decomposition for basal constriction.

To define the active deformation tensor $\mathbf{F}_a$, we first introduce local coordinate systems $\hat{\mathbf{X}}$ in the origin of every biological cell. These coordinate systems are oriented such that $\hat{\mathbf{X}}_2$ points in the radial direction in the 3D setting. Further, let $\mathbf{Q}$ and $\mathbf{m}$ be the rotation matrix and the translation vector from the reference coordinates $\mathbf{X}$ to these parametric ones. We have depicted both coordinate systems and the transformation by $\mathbf{Q}$ in Section A.1 of the appendix.

In these local parametric coordinate systems $\hat{\mathbf{X}}$, the constriction tensor is given by

$$\hat{\mathbf{F}}_a(\hat{\mathbf{X}}, C) := \begin{pmatrix} 1 + kC\hat{X}_2 & 0 & kC\hat{X}_0 \\ 0 & 1 + kC\hat{X}_2 & kC\hat{X}_1 \\ 0 & 0 & 1 \end{pmatrix} \tag{5.5}$$

where k is a constant and $\hat{\mathbf{X}} = (\hat{X}_0, \hat{X}_1, \hat{X}_2)^T$ are the 3D coordinates in the local systems introduced in each biological cell. Positive values of k result in an apical constriction and negative values in a basal one. Observing $\mathbf{Q}\mathbf{Q}^T = \mathbf{Q}^T\mathbf{Q} = \mathbf{I}$, $\mathbf{F}_a$ in the reference system is now given as the transformation of the tensor $\hat{\mathbf{F}}_a(\hat{\mathbf{X}}, C)$ and its first argument by

$$\mathbf{F}_a(\mathbf{X}, c) = \mathbf{Q}^T \hat{\mathbf{F}}_a(\mathbf{Q}\mathbf{X} - \mathbf{Q}\mathbf{m}, C)\mathbf{Q}. \tag{5.6}$$

Note that $\mathbf{Q}$ depends on the biological cell under consideration whereas $\hat{\mathbf{F}}_a$ remains identical. In particular, this definition implies that $\mathbf{F}_a$ is a piecewise-defined tensor which results in a semi-discrete model whereas our system of equations (5.4) was entirely continuous up to this point. For the sake of a crisp presentation, we present a full derivation of this tensor and its two-dimensional equivalent in Section A.1 of the appendix.

Active constriction processes usually occur on one side of a biological cell by local contraction of correspondingly located acto-myosin networks, see Martin *et al.* [98]. Nevertheless, during these deformations, the local volume of the biological cells often appears to be conserved (cf. Gelbart *et al.* [43]). Similar as in Conte *et al.* [29] we thus want $\mathbf{F}_a$ to be volume-preserving. Indeed, this specific choice of $\hat{\mathbf{F}}_a$ and thus $\mathbf{F}_a$ (since $\det(\mathbf{Q}) = 1$) is volume-preserving since for the volume $\hat{V}_{i,a}$ deformed by $\hat{\mathbf{F}}_a$ and the initial volume $\hat{V}_i$ of any biological cells K_i it holds

$$\begin{aligned}\hat{V}_{i,a} &= \int_{K_{i,a}} \mathrm{d}\hat{X}_2\mathrm{d}\hat{X}_1\mathrm{d}\hat{X}_0 = \int_{K_i} |\det(\hat{\mathbf{F}}_a)|\mathrm{d}\hat{X}_2\mathrm{d}\hat{X}_1\mathrm{d}\hat{X}_0 \\ &= \int_{K_i} (1 + kC\hat{X}_2)^2\mathrm{d}\hat{X}_2\mathrm{d}\hat{X}_1\mathrm{d}\hat{X}_0 = \hat{V}_i + kC\int_{K_i} \hat{X}_2(2 + kc\hat{X}_2)\mathrm{d}\hat{X}_2\mathrm{d}\hat{X}_1\mathrm{d}\hat{X}_0 = \hat{V}_i,\end{aligned}$$

where the last integral vanishes since the centroid of K_i has been transformed to the origin and integration with respect to $\hat{X}_1$ and $\hat{X}_0$ cancels out.

We point out that we are interested in simulating pattern formation on the tissue scale. In particular, the numerical resolution of individual discrete biological cells is computationally expensive. Nonetheless, our numerical results clearly confirm that it is essential to prescribe piecewise-defined active deformations to observe realistic tissue development.

The robustness of pattern formation with regard to active deformations is a key aspect in Subsection 5.3.4. In particular, regular patterns persist if we redefine the active deformation tensors so that active constriction is limited to one side of the biological cells without actively expanding the other side. In this setup for basal constriction, the outer (basal) part of the cell is actively constricted and ensuring volume-preservation is left to the (almost) incompressible hyperelastic material model.

Continuous, active deformation tensors In principle, we can also base our mechanochemical feedback loops on continuously defined active deformation tensors or on growth in just some of several cell layers ("bimetal effect"). Two possible choices are presented in the following. However, extensive numerical tests reveal that only significantly smaller deformations can be obtained for these tensors. Similarly, combinations of apico-basal shortening and basal constriction did not improve our standard approach from above. Interestingly, such combinations of active deformations are observed in organisms such as the fish *Brachydanio rerio* (cf. Davies [31]).

The first alternative approach is based on considering two layers of biological cells where just the inner one is expanding. The corresponding active deformation tensor is defined by

$$\mathbf{F}_a(\mathbf{X}, C) := \begin{cases} kC\mathbf{I} & \text{if } |\mathbf{X}| < R_0 \\ \mathbf{I} & \text{else,} \end{cases}$$

where R_0 is the radius of the cell membrane between both tissue layers. By this definition, morphogen concentrations lead to an expansion of the inner layer and tissue curvature towards

the blastula lumen (the inside of the tissue sphere) via the "bimetal effect". Similarly, we prescribed isotropic growth in one layer and isotropic shrinking in the other, such that the volume is preserved.

An alternative, approach that leads to mechanochemical pattern formation is based on a continuously defined active deformation tensor given by

$$\mathbf{F}_a(\mathbf{X}, C) \coloneqq kC(R_0 - |\mathbf{X}|)\mathbf{I}.$$

5.3.3 Parameter setup

First, we focus on the essential parameters: Mathematically and biologically, it is vital to have a comparably small diffusion coefficient $D_{\mathbf{T}} \sim 10 \times 10^{-14}\mathrm{m}^2\,\mathrm{s}^{-1}$ in the tangential directions in relation to a large coefficient $D_{\mathbf{N}} \sim 10 \times 10^{-12}\mathrm{m}^2\,\mathrm{s}^{-1}$ in the outer normal direction of the tissue sphere. This is motivated and discussed in Subsection 2.3.1. Now, the crucial point in finding suitable parameters is to balance the choice of the diffusion coefficients with the maximal morphogen production rate $k_2 \sim 10 \times 10^{7}\mathrm{mol}\,\mathrm{m}^{-3}\,\mathrm{s}^{-1}$ which is also related to the Michaelis constant which was set to $k_m = 2.0$: Half of the production rate k_2 is attained, once the size of the tensor invariant $I(\cdot)$ describing the mechanical tissue response has reached k_m, e.g. once $\det(\mathbf{F}) = 2.0$. The two parameters k_2 and k_m depend on one another as they both influence the maximal morphogen concentration after saturation (in conjunction with the diffusion coefficients). Further, we set $k_1 \sim 10 \times 10^{-4}\mathrm{s}^{-1}$ for the degradation rate of the morphogen level in the entire domain.

Detailed numerical studies on the robustness of our approach with regard to changes in these parameters are presented in the following, e.g. see Fig. 5.12 (or Fig. A.8 in the appendix).

Values of the Lamé constants are usually given in terms of Young's modulus E and Poisson's ratio ν. They can be obtained by the conversion formulas given in Eq. (2.24). In particular, the Lamé constants linearly depend on E. Notably, the choice of the material constants is not essential: A dimensionless analysis shows that, in the absence of external forces, Young's modulus can be extracted from the structural equation and changes in E only alter the elastic timescale, which is not resolved since we are only interested in the comparably long timescale of active deformations (cf. Section 3.3). We have used $E = 100\,\mathrm{Pa}$ and $\nu = 0.4$ as in Allena *et al.* [1] for our computations. Also here, changing ν does not significantly alter our results, i.e. choosing $E = 1\,000\,\mathrm{Pa}$ and $\nu = 0.3$ as in Conte *et al.* [29] leads to qualitatively similar results.

The stabilization parameter was set to $\epsilon = 0.1$. This choice is based on our stability analysis and ensures that the stabilization error is always well below the dominating discretization error in space (cf. Subsection 3.5.3).

As initial conditions, uniformly distributed random concentrations for each biological cell or a morphogen gradient were used. In both cases, the morphogen concentration was prescribed in the interval $c \in [0, 10^9]\mathrm{mol}\,\mathrm{m}^{-3}$. For the visualization of our results, the initial morphogen concentrations were transformed to the interval $c \in [0, 1]\mathrm{mol}\,\mathrm{m}^{-3}$. In any case, the scale of the morphogen concentration is not crucial since only the constant k, which determines how strong the morphogen concentration couples into the active deformation gradient, simply has to scale in the same manner. It was set to $k \sim 10^{-6}\mathrm{mol}^{-1}\,\mathrm{m}$. We point out that the initial deformation is

set to $\mathbf{u}(\mathbf{X}, 0) = 0$, since the deformation corresponding to the initial concentration distribution in not known. Notably, this means that these initial conditions do not match which reduces the convergence rate of Newton's method in the first three to five time-steps until deformation and morphogen concentration correspond. Vice versa, we could also prescribe an initial deformation and a homogeneous initial concentration distribution to trigger mechanochemical pattern formation.

In some simulations, we include an internal pressure that accounts for the fluid contained inside the hollow tissue sphere. The intensity of this pressure is steered by changing the constant $k_p \approx 8 \times 10^{-10}$. Also, in our enhanced modeling approach, we employ a threshold for the expression of morphogen which is set to $THRES \approx 70$ in 3D and $THRES \approx 5 \times 10^{-3}$ in the 2D case.

All parameters specified above can be employed regardless if the full 3D geometry or 2D cross-sections are considered. This finding underlines the flexibility of our approach: Once a new hypothesis is tested and confirmed on the two-dimensional level (which is computationally simple), the newly designed model is subsequently leveraged to the full 3D sphere.

5.3.4 Numerical results and discussion

In our second application, we combine the most commonly observed interplays in embryogenesis between chemistry and tissue mechanics to create a simple feedback loop. Namely, we assume that there exists one morphogen species within the tissue, and that this morphogen locally induces active cell shape changes. In detail, these cell shape changes are assumed to be apical or a basal constrictions (i.e., deforming cells from symmetric to wedge-shaped), since these are frequently appearing deformations during tissue morphogenesis [89, 98, 115, 118]. Furthermore, we assume that tissue stretch induces production of the morphogen, which has also been experimentally observed [24, 79]. These two mechanisms lead to a simple positive feedback loop that we thoroughly described in Subsection 2.3.3. As an example, we have illustrated a stretch-mediated feedback loop based on basal constriction in Fig. 2.6.

In short, mechanochemical feedback loops of this type have the capacity to spontaneously create patterns for the following reason: As soon as the morphogen concentration or the stretch inside the tissue is locally inhomogeneous, both morphogen and tissue curvature locally amplify each other, since morphogen produces cell shape changes which lead to local stretch (due to the elastic material response), which again leads to morphogen production. Thus, a short range activation takes place. The long-range inhibition, in contrast, is mainly constituted by tissue mechanics: Once the tissue is locally curved, in oder to maintain continuity, the surroundings of the curved patch have to be bent into the opposing direction. This passive deformation prevent the introduction of stretch by active deformations and a continuous, elastic response that results in little stretch is sufficient. Morphogen produced here is consumed by the degradation rate (in the regions of activity, however, large and possibly discontinuous active deformations require a strong elastic response that results in stretch and triggers our feedback loop). An illustration of these processes is shown in Fig. 2.6.

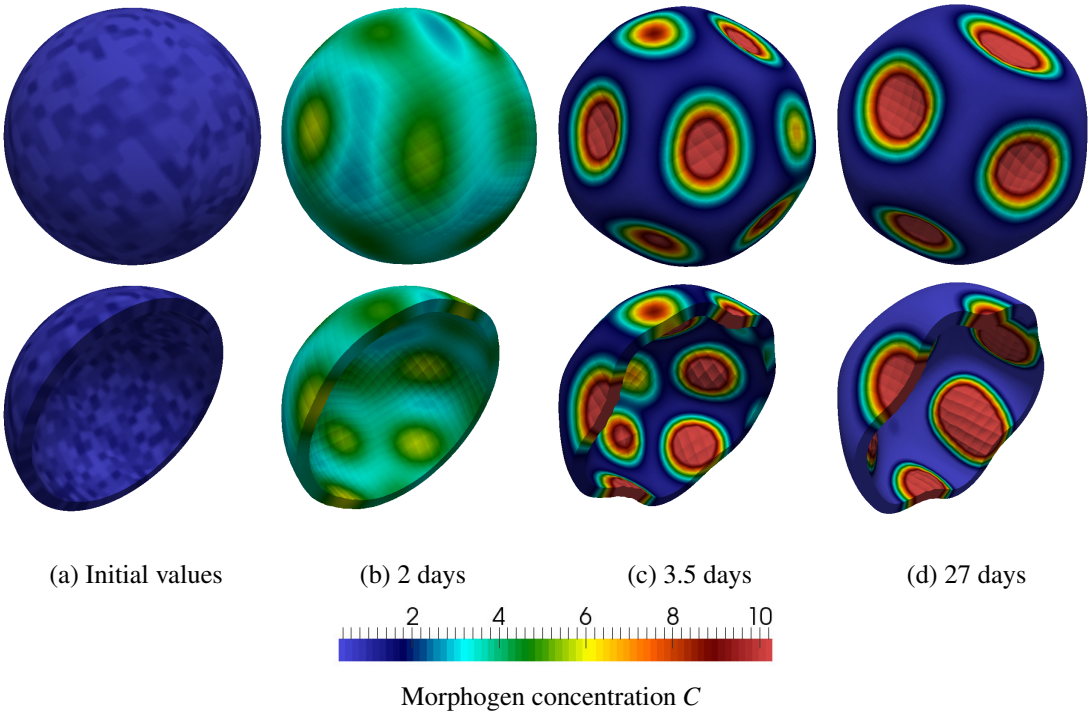

(a) Initial values (b) 2 days (c) 3.5 days (d) 27 days

Figure 5.9: Simulation snapshots that show spontaneous pattern formation for the stretch-mediated feedback loop including basal constriction. The tissue sphere has been sliced for the sole purpose of a better visualization. An experimental example showing co-localization of tissue curvature and morphogen concentration during *Hydra* development can be found in Hobmayer *et al.* [65].

Simulation snapshots for the stretch-mediated feedback loop including basal constriction (i.e., constriction at the end of the cell pointing away from the blastula lumen) are shown in Fig. 5.9. We observe that this simple mechanochemical interplay is sufficient to spontaneously produce regular mechanochemical patterns, where the equilibrium pattern consists of regular morphogen patches coinciding with patches of local tissue curvature. Results appeared to be numerically stationary after $t \approx 20$ days (referring to the model-time; corresponding to about 85 000 numerical time steps), which is a typical order of magnitude for developmental processes. Indeed, co-localization of high morphogen levels and local tissue curvatures have been described in many organisms and developmental steps, from head formation events in the freshwater polyp *Hydra* [145] through tooth outgrowth in vertebrates [137] and shoot-meristem growth in the plant *Arabidopsis* [84]. Interestingly, for all three processes mentioned above, there are experimental evidences that mechanochemical interactions play an indispensable role during pattern formation [17, 84, 96, 105, 139].

Furthermore, the simulated *de novo* equilibrium patterns appear to be very robust against the perturbation of preceding patterning stages, the latter represented by the choice of initial conditions: Regardless if we start with stochastically distributed morphogen levels in biological

cells (cf. Fig. 5.9), with only one morphogen spot (cf. Fig. A.3 in the appendix) or any different, non-homogeneous initial morphogen distribution, we always obtain approximately the same number and size of mechanical and biological patterns. This robustness agrees well with the experimental observation that embryonic patterns are robust to the perturbation of preceding patterning stages [11, 47, 135].

Keeping all parameters constant but considering apical constriction instead of a basal one (i.e., constriction at the end of the cell pointing to the blastula lumen) finally leads to a gastrulation event, with the highest morphogen concentration found in an annulus around the invagination (cf., Fig. 5.10). However, due to strong deformations, the material model eventually breaks down and Newton's method no longer converges, so that the final pattern in Fig. 5.10 does not represent a stationary result. This does not come as a surprise since, firstly, significant geometrical changes during gastrulation are witnessed which facilitate the invagination process. Secondly, the fluid contained inside the tissue sphere is not considered in our model. Indeed, we will demonstrate in Subsection 5.3.5 that imposing an inner volume constraint stabilizes the invagination process at an earlier stage and leads to stationary solutions.

Also here, the gastrulation appears to be insensitive to the initial conditions and thus appears to be very robust (Fig. A.4 in the appendix). Similar mechanochemical patterns have been observed experimentally during gastrulation, e.g. in *Xenopus* [113] and the freshwater polyp *Nematostella* [140]. Interestingly, the simulations first show regular (though transient and weak) mechanochemical patterns, comparable to those from basal constriction, before gastrulation occurs (compare Fig. 5.9 and Fig. 5.10). The role of transient morphogen patterns during tissue development has recently been further investigated e.g. by Ref. [8, 114]. If mechanochemical coupling is chosen as less intense, such as for a weaker coupling of stretch to the morphogen production, these transient patterns become stationary after $t \approx 6$ days (about 2 days before the snapshot shown in Fig. 5.10 (c)) and do not result in gastrulation. The results in Fig. 5.10 (c) for apical constriction are strongly related to the patterns obtained for basal constriction: In the former result, deformations are essentially the same but the morphogen is no longer co-located with the inwards-directed deformation but co-located with the now active outward-directed deformation around the invaginations, compare again 5.9 (d) with 5.10 (c) where one image is the negative of the other (morphogen-wise (color) and deformation-wise). In contrast, with a stronger coupling between morphogens and mechanics, i.e. a stronger impact of stretch on the morphogen production, the relative intensity of these transient patterns diminishes. Note that in both simulations result, one can spot checked patterns in the actively deformed parts which are the interfaces between the individually constricting biological cells (mathematically speaking we spot the discontinuities of the active deformation gradient here).

We point out that our simulations indicate that also with basal constriction, a gastrulation (one dominating wavelength) can be obtained when mechanochemical coupling is chosen as more intense. Corresponding results are presented for the stress-mediated feedback loop in conjunction with basal constriction that is presented in the following. Yet, numerical calculations for the stretch-mediated feedback loop break down at an earlier stage. More precisely, Newton's

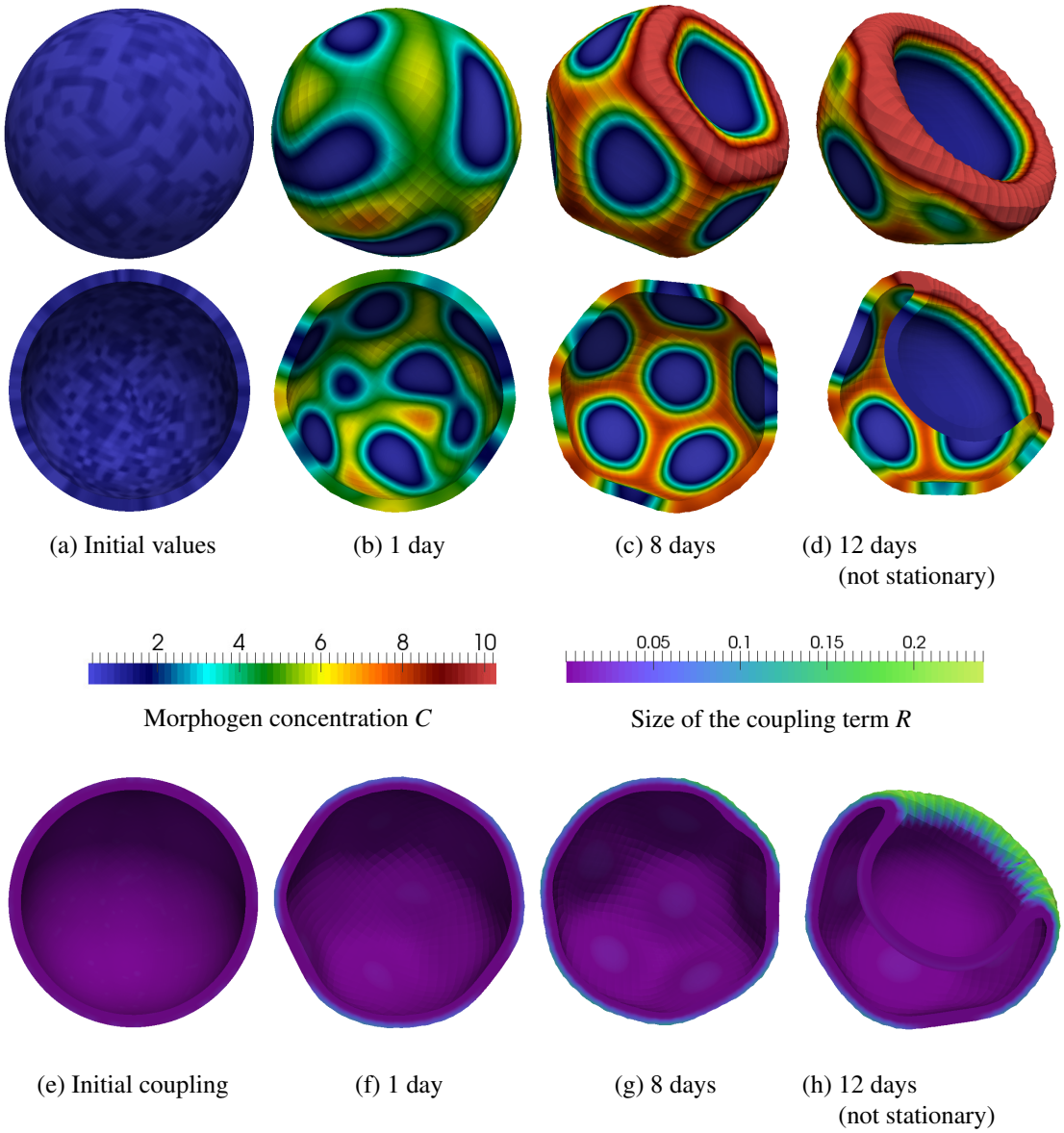

(a) Initial values (b) 1 day (c) 8 days (d) 12 days (not stationary)

Morphogen concentration C Size of the coupling term R

(e) Initial coupling (f) 1 day (g) 8 days (h) 12 days (not stationary)

Figure 5.10: Simulation snapshots that show spontaneous pattern formation for the stretch-mediated feedback loop including apical constriction. The tissue sphere has been sliced for the sole purpose of a better visualization. Microscopic pictures showing similar morphogen and curvature patterns can be found in Scrivastava *et al.* [140].

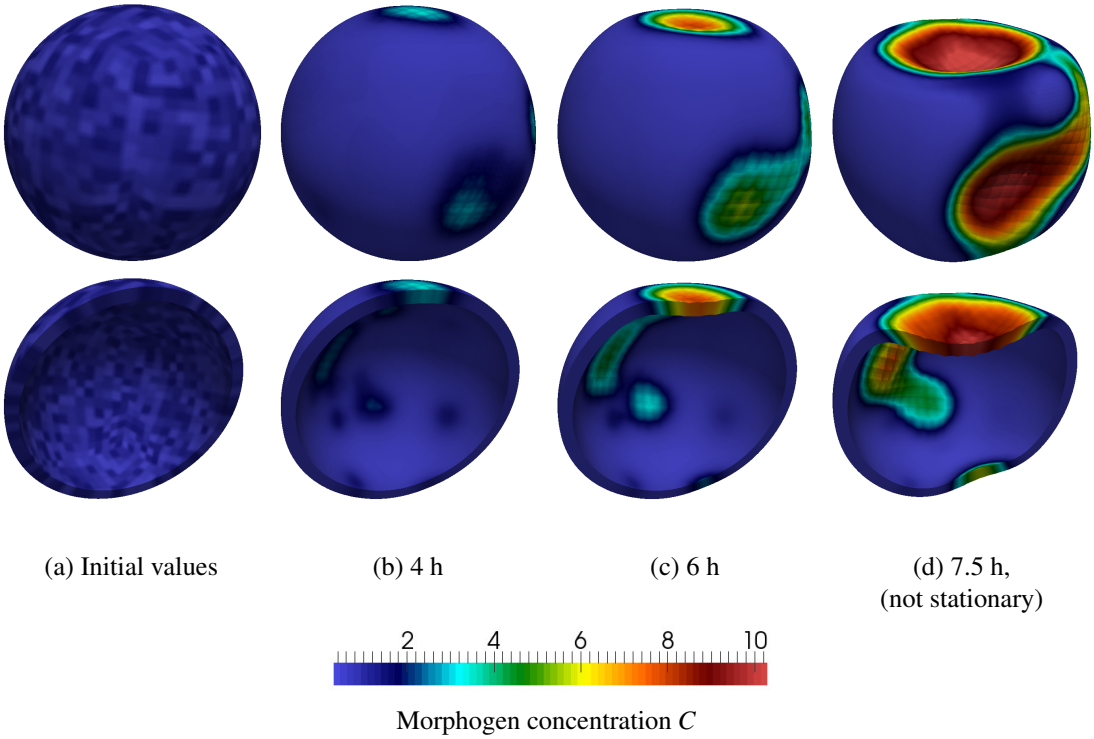

(a) Initial values (b) 4 h (c) 6 h (d) 7.5 h, (not stationary)

Figure 5.11: Simulation snapshots that show spontaneous pattern formation for the stress-mediated feedback loop including basal constriction. The tissue sphere has been sliced for the sole purpose of a better visualization.

method no longer converges if we increase the morphogen production to obtain larger deformations. In the subsequent paragraph on the robustness of our model, we will observe that changes in the parameters, in diffusion rates and the model geometry lead to stationary mechanochemical patterns of similar structure as in Fig. 5.9. Further, many combinations of active deformations, including continuously defined tensors, were tested. Ultimately, we could not fully settle the question of why the stretch-mediated feedback loop and basal constriction did not lead to invaginations. Yet, there are strong indications that the combination of active deformation and mechanical feedback is essential, e.g. we obtain a single invagination for the stress-mediated feedback loop.

Simulation snapshots for the stress-mediated feedback loop with basal constriction are presented in Fig. 5.11. Here, we observe large co-located patterns of morphogen patches. Notably, the active deformations extend to large invaginations due to the changing tissue geometry within this process. This topological change accelerates the invagination process and we do not obtain a stationary solution, similar to the gastrulation events for the stretch-mediated feedback loop (cf. Fig. 5.10). However, we demonstrate that imposing an internal volume constraint that models the fluid inside the tissue sphere leeds to a single, stationary invagination (cf. Fig. 5.16). These stationary results are again robust with regard to changes in the initial conditions, namely

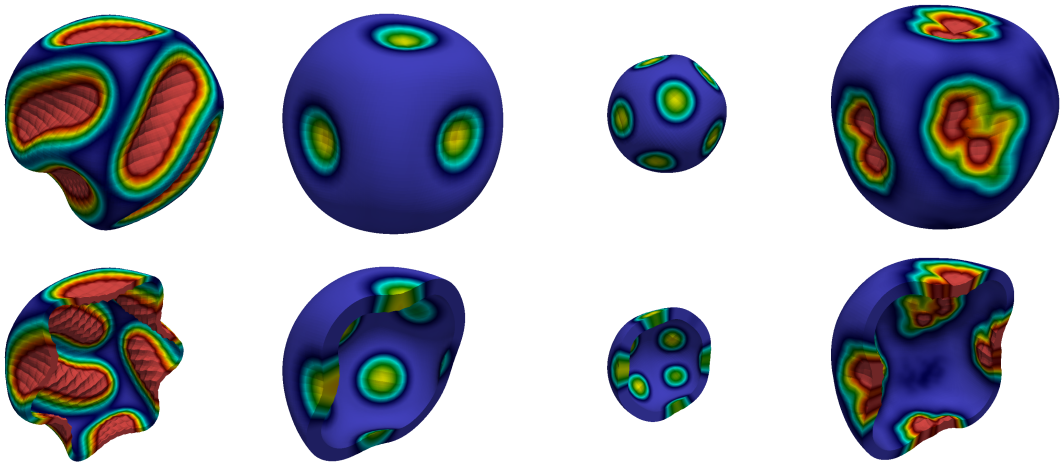

(a) Thinner tissue sphere, 16 days

(b) Thicker tissue sphere, 23 days

(c) Smaller sphere of 384 cells only, 6 days.

(d) Basal constriction in basal half of the biol. cells only, 24 days

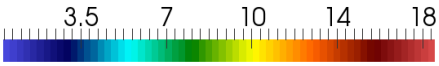

Morphogen concentration C

Figure 5.12: Simulation snapshots showing the robustness of pattern formation with regard to changes in the tissue thickness (a-b), the system size (c) and non-volume preserving active deformations (d). In the lower row, the tissue sphere has been sliced for the sole purpose of a better visualization.

stochastically distributed morphogen levels for each biological cell or a single initial morphogen spot (result not shown).

Robustness

Additional simulations were performed to further investigate the robustness of our mechano-chemical feedback loops: Firstly, we focused on the influence of model size and geometry on the resulting patterns for the stretch-mediated feedback loop including basal constriction, which we presented in Fig. 5.9. In particular, we varied the initial size of the system and the tissue thickness (relative to the radius). We observe that a thicker tissue layer leads to an increased distance between two neighboring tissue/curvature patches whereas a thinner tissue layer leads to a decrease in the distance (cf. Fig. 5.12 (a-b)). This observation was intuitively expected, since mechanics is responsible for a long-range inhibition as explained in the beginning of this subsection: The stiffer the material is, the larger is the range of propagation of the mechanical signal. And the thinner the tissue is, the weaker becomes the inhibition of patterns and the closer patterns will grow towards each other Fig. 5.12.

Also, the number of patches appears to scale with the system size: A smaller system of only

384 biological cells of the usual size exhibits fewer patches (Fig. 5.12 (c)). Most probably, this is a direct result of the smaller tissue surface. Nonetheless, the mechanochemical patterns themselves also shrink in comparison to pattern formation on the standard sphere with larger surface (cf. Fig. 5.9). Besides, the relative tissue thickness is increased which reduces the number of patterns by mechanical long-range inhibition, similar to the result observed in Fig. 5.12 (a).

Secondly, we show that we still obtain mechanochemical patterns if we change the nature of the active deformations. For example, regular patterns persist if we redefine the active deformation tensor from Eq. (5.5) so that it only prescribes constriction at one side of the cell (the outer one regarding basal constriction) without actively expanding the other side. By definition, this active deformation tensor is no longer volume-preserving and the preservation is ensured by the (almost) incompressible tissue material. This active deformation is interesting from a biological perspective since it might in some sense better reflect the underlying constriction mechanism in biological cells. Surprisingly, morphogen patches are frequently not spherical but rather develop to "double-patches", i.e., two superimposed patches constituting together a dumbbell-shape (Fig. 5.12 (d)).

Thirdly, we see that (tangential) diffusion rates are not a critical ingredient for obtaining mechanochemical patterns: Quartering the lateral diffusion for the stretch-mediated feedback loop based on basal constriction still leads to patterns (cf. Fig. A.5 in the appendix), although the reduced diffusion rate clearly diminishes the size of the initial morphogen/curvature patches. Also, diffusion accelerates morphogen transportation and hence the speed of initial pattern formation increases, compare Fig. 5.9 and Fig. A.5. The same influence of diffusion on the initial pattern formation can be observed for basal constriction (we have shown this result in Fig. 4 E in Brinkmann *et al.* [20]). Overall, tangential diffusion appears to influence the process of pattern formation by smoothing/regularizing morphogen patterns and by initially accelerating the information transport and hence the pattern formation. Ultimately, however, diffusion rates only have a marginal influence on the stationary solution: Quartering the diffusion leads to 13 (instead of 12), further localized and smaller morphogen/curvature patterns (diffusion smoothes patterns as observed before). Interestingly, both stationary solutions are attained after about 25 days, referring to the "biological model time". Most likely, this can be explained by the duration of the consolidation process of strong patterns inhibiting weaker ones: The duration of this process is increased if larger patterns develop earlier due to larger diffusion rates. These effects are even strengthened when tangential diffusion is completely inhibited (result is shown in Brinkmann *et al.* [20]). Also, we point out that changes in the material parameters do not significantly alter our numerical results (not shown). Mathematically speaking, Young's modulus merely scales the elastic timescale (which is not resolved) when extracted from the equation as discussed in Subsection 5.3.3.

Next, we highlight that mechanochemical pattern formation seems significantly more robust with regard to tangential diffusion rates, if the full 3D geometry of the tissue sphere is considered: Whereas we obtain almost identical stationary states in the 3D setting, the diffusion rates can considerably influence the number of patterns in 2D, e.g. see Fig. A.8.

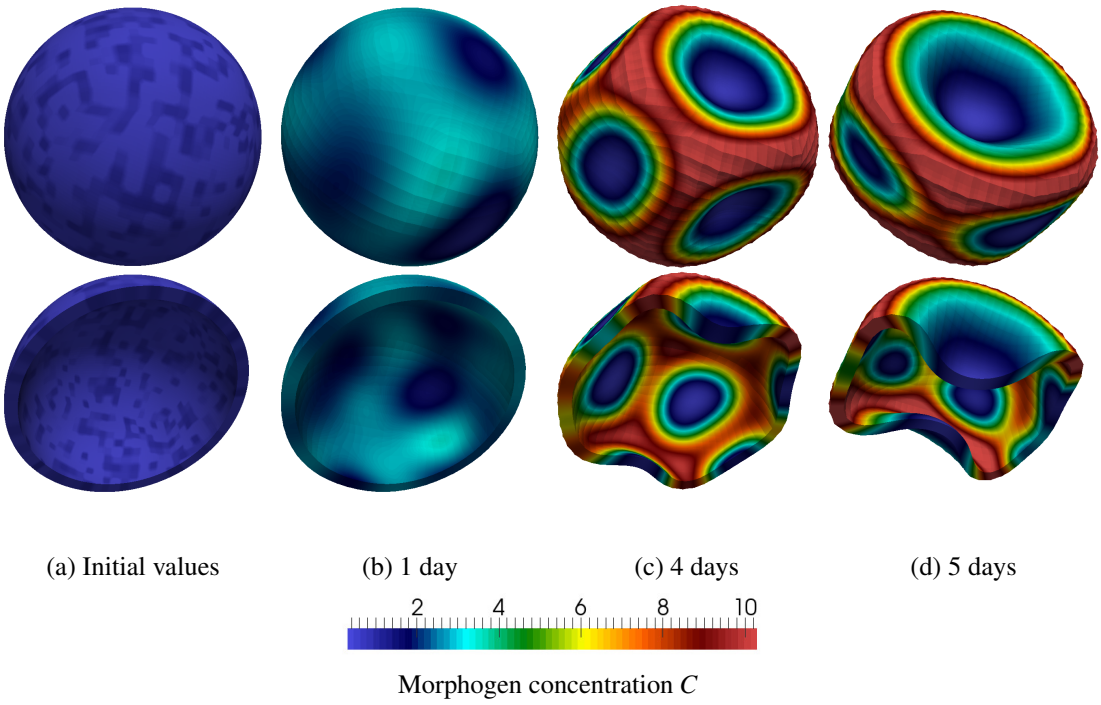

(a) Initial values (b) 1 day (c) 4 days (d) 5 days

Figure 5.13: Simulation snapshots that show spontaneous pattern formation for the stretch-mediated feedback loop including apical constriction with quadrupled, tangential diffusion rate. The tissue sphere is sliced for the purpose of a better visualization.

We observe, however, that the influence of (tangential) diffusion rates is astonishing with respect to the appearance of the final mechanochemical patterns for the stretch-mediated feedback loop based on apical constriction: A quadrupled diffusion rate leads to two dominating morphogen/curvature patches in annuli around the invaginations (Fig. 5.13 (d)). As above, higher diffusion rates seem to increase the "communication" between (local) patterns. This accelerates initial pattern formation and the global consolidation process of dominant patters absorbing or dissolving weaker ones. Regarding apical constriction, two patterns quickly dominate after just four days for quadrupled diffusion compared to a consolidation process of eight days in case of a single gastrulation, cf. Fig. 5.13 (b)-(c) and Fig. 5.10 (b)-(c)). This corresponds well with the previous observation regarding basal constriction, where transient patterns develop earlier if the diffusion rate is increased.

Notably, the significant geometrical changes during the invagination facilitates the deformation Fig. 5.13 (d) does not represent a stationary solution. Hence, we elaborate on this result and impose an internal pressure that accounts for the fluid contained inside the tissue sphere. This inner volume constraint stabilizes the invagination processes leads to stationary solutions which are robust with regard to changes in the diffusion rates (cf. Subsection 5.3.5).

Summary

Our numerical simulations indicate that it is important to consider a full 3D approach (rather than 2D simplifications), since the resulting patterns presented in this work cannot be obtained by lower-dimensional approaches (cf. Section A.3 in the appendix for our results on pattern formation in 2D cross-sections or Mercker *et al.* [103, 104]). In the three-dimensional setting discussed above, we show that gastrulation-like deformations can be obtained from a range of non-uniform or non-rotationally invariant types of initial conditions, for both basal and apical constriction, and for different feedback loops based on stretch or stress. In this application, results for the strain-mediated feedback loop are almost identical to those for the stretch-mediated one and were omitted for the sake of a shorter presentation. In 2D or pseudo 3D approaches, however, it was not possible to obtain gastrulation driven by *de novo* pattern formation [103, 104]. Hence, the full 3D approach most likely leads to more realistic simulation results, which is due to the fact that both chemical and mechanical behavior is strongly biased if dimensions are neglected.

Finally, the present study offers for the first time the possibility to explain gastrulation by robust *de novo* mechanochemical pattern formation, leading to simulation results similar to patterns observed in model organisms such as *Hydra*, *Nematostella* and *Xenopus*. However, until now, the experimental evidence for the specific feedback loops as presented in our work is still sparse. Possible reasons are: (1) visualization of mechanical measures in living biological tissues is still under development and connected with a high experimental effort [17, 117]; and (2) the ”pure chemical approach” to explain pattern formation is still very prominent in the field of developmental research.

Encouragingly, the number of mechanochemical feedback loops experimentally documented to be drivers of pattern formation increases [17, 87, 112] and new methods of the visualization of mechanical cues are currently under development [55, 101, 102, 159].

Thus, our simulation results show that even simple interactions between chemistry (morphogens) and tissue mechanics can lead to robust and spontaneous pattern formation. Especially, it is worth pointing out that

- mechanochemical pattern formation appears to be very robust against perturbation of preceding patterning stages, model parameters and a range of specific assumptions;
- experimental verification of long-range inhibitors is neither necessary nor possible, since long-range inhibition may be caused by mechanical cues;
- mechanical cues (such as compression) naturally propagate at an enormous speed due to the direct mechanical interaction of molecules or cells. Hence, the mechanochemical theory is not restricted to relatively small length scale due to maximum possible diffusion rates of morphogens;
- dynamic and complex tissue topologies do not prevent patterning but are rather actively involved in pattern formation. Thus, they provide a natural and robust feedback to ensure the success of mechanical pattern formation;

- On the contrary, the full 3D geometry appears to be essential to obtain many realistic numerical results such as gastrulation events;
- even simple linear relationships between chemistry and morphogens lead to spontaneous pattern formation, highly nonlinear interactions do not have to be assumed.

Hence, the presented mechanochemical mechanism fits well the recent experimental data and all main difficulties of purely chemical theories (listed in the introduction to this chapter) are naturally resolved.

5.3.5 Internal pressure to ensure stationary gastrulation events

In the previous discussion of our numerical results we have seen that the geometry of our tissue sphere changed significantly during gastrulation events. In particular, these shape changes facilitate the invagination process. For very large deformations, this ultimately results in a breakdown of the material model. This observation agrees well with the physical intuition that, after a certain point, the total potential energy is minimized if the sphere invaginates further (imagine a broken ping-pong ball that does not return to its spherical shape).

So far, we have neglected the water that is naturally contained inside the embryo and strongly influences the gastrulation process. Yet, it is difficult do asses the quality of this pressure: For instance, it is not experimentally settled if we can assume incompressible behavior of a fluid inside a tissue sphere or if an initial pressure precedes gastrulation, see Conte *et al.* [29, p. 191]. Apparently, the fluid is under pressure during gastrulation events as it squirts if the tissue is pierced.

On the one hand, the fluid itself is certainly (nearly) incompressible. On the other hand, integral membrane proteins, called aquaporins, form water channels trough the cell membranes. Aquaporins are highly selective: They significantly increase the in- and outflow of water compared to diffusion through the cell membranes but prevent ions from passing. Inside the *Hydra* embryo, ion pumps produce ions such that osmosis leads to an inflow of water. In deformation processes such as gastrulation, the geometry of the initial tissue sphere is significantly changed and the volume inside the tissue sphere is reduced. Consequently, the ion concentration increases which in turn results in osmotic pressure. Summarizing this discussion, assessing the quality of the osmotic pressure is highly speculative. Until this question is experimentally settled, we performed various numerical experiments with different internal volume constraints to collect further knowledge about this process.

Implementation of an internal pressure In this work, we accounted for this pressure by introducing a surface force $\mathbf{g}$ on the inner boundary of the tissue sphere, see Figure 5.14. The further the tissue is compressed, i.e. the smaller the volume contained in the tissue sphere becomes, the stronger has to be the surface force. This force is directed in the Eulerian, normal direction $\mathbf{n}$. Since our equations are given in the Lagrangian framework, this boundary force has to be expressed in terms of the Lagrangian, normal direction $\mathbf{N}$.

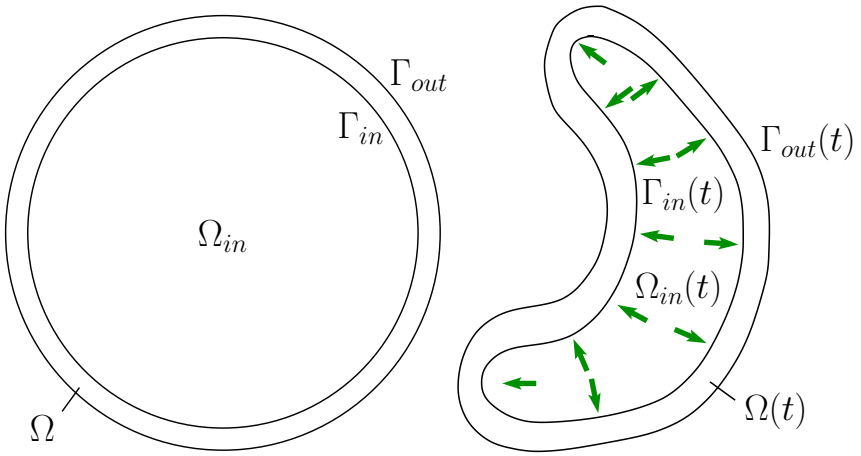

(a) Initial domains (b) Deformed domains

Figure 5.14: (a) Computational domain Ω for the tissue sphere and domain Ω_{in} with boundary Γ_{in} surrounded by the tissue without initial internal pressure (by assumption) (b) Outline of the deformed configurations taken from our numerical simulations with illustration of the internal pressure (green arrows).

So far, we prescribed homogeneous Neumann conditions on the entire boundary $\partial\Omega = \Gamma_N$. Now, we split the boundary into the inner and the outer boundary of the initial reference sphere and of the deformed configuration by

$$\partial\Omega = \Gamma_N = \Gamma_{in} \cup \Gamma_{out}, \quad \partial\Omega(t) = \Gamma_N(t) = \Gamma_{in}(t) \cup \Gamma_{out}(t)$$

as illustrated in Figure 5.14. As usual, homogeneous Neumann conditions are prescribed on Γ_{out}. On the inner boundary Γ_{in}, the surface force produced by the compressed fluid is given by

$$\int_{\Gamma_{in}(t)} \mathbf{g}(\mathbf{n}, t) \cdot \boldsymbol{\varphi} \, \mathrm{d}s = k_p \, e^{(V(t)-V_0)} \int_{\Gamma_{in}(t)} \mathbf{n} \cdot \boldsymbol{\varphi} \, \mathrm{d}s = k_p \, e^{(V(t)-V_0)} \int_{\Gamma_{in}} J\mathbf{F}^{-T}\mathbf{N} \cdot \boldsymbol{\Phi} \, \mathrm{d}S, \tag{5.7}$$

where k_p is a constant. By assumption, the force on the inner boundary depends exponentially on the difference of the current volume $V(t)$ and the initial volume V_0 of the fluid domain Ω_{in} contained inside the tissue sphere. This definition of the internal pressure agrees well with Boyle's law for ideal gasses, where an exponential increase in the pressure is observed if the volume occupied by the gas is reduced. For completion, we point out that we extensively tested forces depending on constant, linear, quadratic and cubic factors $(V(t) - V_0)^k$, $k = 0, 1, 2, 3$, as well, which were incapable of stopping the invagination process.

The transformation of the integral is obtained by using Gauss's divergence theorem to transform the boundary integrals into volume integrals. Next, the volume integral in the Eulerian configuration is transformed by substitution (cf. Eq. 2.4) and the transformation of the gradient (cf. Eq. 2.5), which produce the determinant of the Jacobian $J(\mathbf{X}, t) = \det(\mathbf{F}(\mathbf{X}, t))$ and $\mathbf{F}^{-T}(\boldsymbol{\chi}(\mathbf{X}, t), t)$, respectively.

Initially, there is no deformation i.e. $V(t) - V_0 = 0$ and thus no pressure acts on the inside of the tissue sphere. This is merely an assumption as an initial internal pressure might already exist at the blastula stage. To calculate the volume contained inside the tissue sphere, let $\mathbf{u}(\mathbf{X}, t)$, $\mathbf{X} \in \Omega \cup \Omega_{in}$ be the continuation of our displacement into Ω_{in}. Since $\mathbf{u} \in H^1(\Omega)$ is smooth, the existence of a continuation of $\mathbf{u}$ into $\Omega_{in}(t)$ is ensured by the theorem of Calderon-Zygmund (cf. Wloka [154, p. 100]). Thus, this continuation provides a deformation from Ω_{in} to $\Omega_{in}(t)$ for the domain contained inside the tissue sphere.

With these preparations, the current volume $V(t)$ of the deformed domain $\Omega_{in}(t)$ is given by:

$$\begin{aligned} V(t) = &\int_{\Omega_{in}(t)} 1 \, \mathrm{d}\mathbf{x} = \frac{1}{3} \int_{\Omega_{in}(t)} \nabla \cdot \mathbf{x} \, \mathrm{d}\mathbf{x} \\ =&\frac{1}{3} \int_{\Omega_{in}} J J^{-1} \nabla \cdot (J\mathbf{F}^{-1}(\mathbf{X} + \mathbf{u})) \, \mathrm{d}\mathbf{X} \\ =&\frac{1}{3} \int_{\Gamma_{in}} J\mathbf{F}^{-T}\mathbf{N} \cdot (\mathbf{X} + \mathbf{u}) \, \mathrm{d}S, \end{aligned} \tag{5.8}$$

where the transformation of the divergence to the reference configuration was used to obtain the second line (see Eq. (2.6)). Further Gauss's divergence theorem yields a surface integral over Γ_{in} such that we can calculate the current volume $V(t)$ contained inside Ω. Notably, we evaluate the integral over Ω_{in}, which is not part of actual computational domain Ω, on the inner boundary $\Gamma_{in} \subset \partial\Omega$ in the reference configuration.

In practice, we thus evaluate the functional (5.8) for the current time-step and use this value in the subsequent one. In our implementation, this is the only explicit calculation in an otherwise implicitly coupled system. We point out, that the different timescales in our strongly coupled system of equations require small time-steps in all our calculations. Thus, changes in the contained volume quickly effect the inner pressure and no unwanted behavior is observed.

Notice that the pressure observed in a real life tissue sphere is determined by three mutually interfering phenomena: Firstly, by the incompressible fluid contained in this sphere. Secondly, by the permeability of the biological cells, i.e. by the fluid leaving the sphere, and thirdly, by the stretching of the hyperelastic tissue sphere due to the decreasing inner volume for the incompressible fluid. Whereas the elasticity is incorporated in the structural equation modeling the tissue sphere, the first two items are left to be modeled. Here, we assume that the pressure is inversely proportional to the volume occupied by the liquid. This relation is known as Boyle's law which holds under the assumptions of constant temperature and an unchanged amount of gas. Correspondingly, in the case of an ideal gas, the pressure (5.7) exponentially depends on the volume dV occupied by the gas. Obviously, this is a strong simplification since it also neglects the viscous behavior of the fluid leaving the tissue sphere. Notably, including an incompressible fluid described by the Navier-Stokes equations was not successful as it lead to an immediate breakdown of convergence for Newton's method.

Finally, we point out that the pressure defined in Equation (5.7) is reasonable from a physical point of view. Especially, a pressure p should satisfy the property $\int_{\Gamma_{in}} p\,\mathbf{n}\mathrm{d}s = 0$, which is obviously fulfilled, see the Eulerian description of the pressure. Most importantly, this condition

ensures that the pressure produces the same forces in all directions. In particular, the domain does not move out of itself due to this pressure. In the Lagrangian description, this property is preserved by the transformation with the Jacobian $J = \det(\mathbf{F})$) which is e.g. large for strong deformations $\mathbf{u}$ that give a small term $\mathbf{F}^{-T}\mathbf{N}$.

Numerical results and discussion We apply our internal volume constraint to the stretch-mediated feedback loop including apical constriction which leads to two invaginations for quadrupled tangential diffusion rates (cf. Fig. 5.13).

In Fig. 5.15 (d) we plot the development of the maximal deformation measured by the maximum of the Euclidean norm $\max_{\mathbf{X}\in\Omega} \|\mathbf{u}(\mathbf{X})\|_2$ over time. The evolution of this deformation for the stretch-mediated feedback loop in conjunction with an internal pressure (green line) demonstrates that the invagination process is stopped. A stationary solution is attained after around 170h. In contrast, the invagination for the stretch mediated feedback loop alone accelerates and our simulation breaks down after around 125h (cf. red line in Fig. 5.15 (d)). Accordingly, Fig. 5.15 (a) for a stretch-mediated feedback loop including an internal pressure represents a stationary result whereas Fig. 5.15 (b) does not.

We highlight that the tissue in Fig. 5.15 (a) for a feedback loop including an internal volume constraint has a smoother spherical form compared to (b), since the pressure pushes smaller patterns to the outside. Indeed, the peak in the green line at around 130h in Fig. 5.15 (d) stems from a third large pattern (besides the two dominating invaginations) that was pushed away from the blastula lumen (outwards). Momentarily, this increases the volume inside the tissue sphere which diminishes the inner pressure and in turn leads to a larger invagination, i.e. a peak in the maximal deformation.

Analogously, a stationary solution is attained if we apply this constraint to a gastrulation event with a single invagination: Fig. 5.15 (c) represents a stationary result for the stretch-mediated feedback loop including an internal pressure whereas Newton's method no longer converges shortly after the simulation snapshot presented in Fig. 5.10 (d) is taken.

Our simulations further indicate that the stationary gastrulation result is robust with regard to changes in the intensity of the internal pressure. On the one hand, a smaller intensity simply stops the invagination at a later stage. On the other hand, the two invaginations in Fig. 5.15 (a) seem to be reduced to a single one, if a stronger pressure is prescribed. In short, a strong internal pressure seems to facilitate the stronger of two competing invaginations.

We point out that internal pressure should indeed increase exponentially with decreasing volume inside the tissue sphere: Our numerical simulations show that this pressure should initially be sufficiently small such that the gastrulation process itself is preserved. Moreover, the pressure needs to increase fast enough to ensure a stationary solution. In addition, numerical experiments showed that pressures depending constantly, linearly, quadratically or cubicly on $V(t) - V_0$ did not lead to stationary results: Either, the pressure did not increase sufficiently fast or the invagination itself was pushed back into its spherical form such that the stationary solution resembled the state presented in Fig. (5.10) (c).

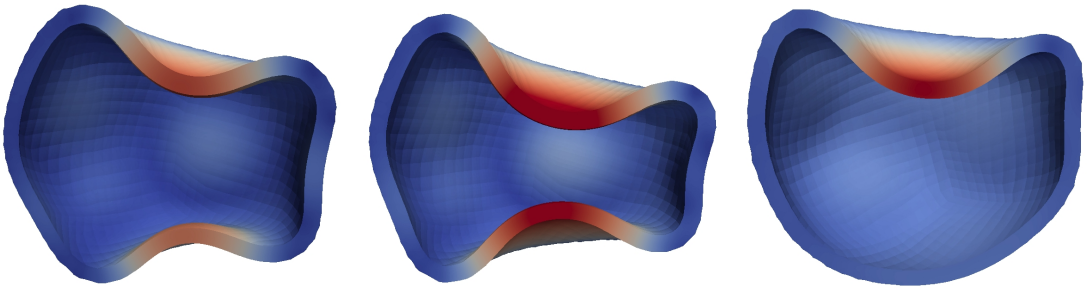

(a) Quadrupled diffusion, internal pressure (stationary solution)

(b) Quadrupled diffusion, no internal pressure, (not stationary)

(c) Normal diffusion rate, internal pressure (stationary solution)

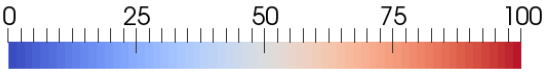

Maximal deformation $\max_{\mathbf{X}\in\Omega} \|\mathbf{u}(\mathbf{X})\|_2$ in µm

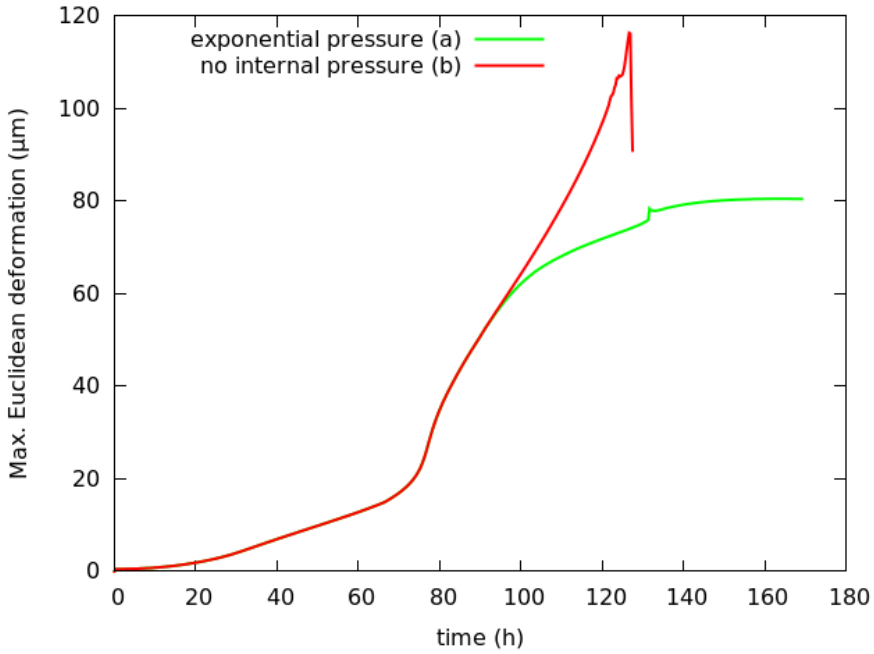

(d) Plot regarding the setup with quadrupled diffusion rates: Maximal deformation $\max_{\mathbf{X}\in\Omega} \|\mathbf{u}(\mathbf{X})\|_2$ in µm over time during gastrulation events.

Figure 5.15: Comparison of simulation snapshots showing gastrulation events for the stretch-mediated feedback loop including basal constriction: (a) Simulation snapshot in the stationary state ($t = 170$h) for an exponentially increasing internal pressure. (b) Snapshot for the feedback loop alone (without an internal pressure) taken at $t \approx 120$h shortly before the breakdown of our numerical simulations. (c) Snapshot in the stationary state for the stretch-mediated feedback loop for the usual diffusion rate and in conjunction with an internal pressure. (d) Maximal deformation over time during gastrulation.

In summary, we conclude that our model including an internal pressure is clearly more accurate from a biological perspective. We emphasize that, due to this pressure,

- the invagination process during gastrulation events is stopped and we obtain stationary mechanochemical patterns;
- the gastrulation becomes more robust, e.g. with regard to changes in the diffusion rates. Namely, an internal pressure seems to facilitate the formation of a single invagination that prevents a second one from emerging via increasing the pressure.

5.3.6 Enhanced model: Integrate mechanical feedback over biological cells

Finally, in the last part of this section, we apply our enhanced model to the stress-mediated feedback loop including basal constriction in 3D. This enhanced model was introduced in Subsection 2.3.4 and is based on the idea that we integrate the mechanical feedback over the biological cell and use this value to prescribe constant morphogen production rates in each of these cells. This approach is more accurate on the cellular level since it models fast (basically instant) diffusion inside biological cells and small diffusion rates between cells.

Notably, small stresses can be propagated through the entire domain due to the integration processes. Hence, we need to introduce a threshold which regulates the expression of morphogen. This is a reasonable assumption (cf. Gregor *et al.* [51]) which is also discussed in Subsection 2.3.4. In practice, the morphogen is produced via the coupling term $R(I, C)$ in the reaction-diffusion equation if the mechanical feedback exceeds a threshold, i.e. if $I > THRES$.

Simulation snapshots show that we eventually obtain a single stationary gastrulation (cf. Fig. 5.16) if we combine our enhanced model based on a stress-mediated feedback loop based on apical constriction with an inner volume constraint (cf. the preceding subsection). This single curvature/morphogen patch does not show distinct biological cells due to inter-cellular diffusion in contrast to the integrated feedback as shown in the second row. Here, the threshold for the expression of morphogen plays a crucial role in stopping the morphogen patches from expanding to adjacent biological cells: In absence of such a threshold, any stress-based feedback would be integrated over the entire biological cell which results in its constriction that in turn introduces stress in all adjacent cells.

Both, the internal pressure and a threshold for morphogen expression hence contribute to the inhibition of weaker morphogen/curvature patches, such that only one morphogen/curvature patch remains, compare to the results for the standard model shown in Fig.5.11. Consequently, this enhanced approach does not seem to be essential to obtain a single invagination but rather the combination of an internal pressure and the threshold for morphogen expression seem to be the dominating factor. As discussed previously, a larger invagination cannot be attained for a model including basal constriction (this is also true for all other active deformation gradients that we have tested so far).

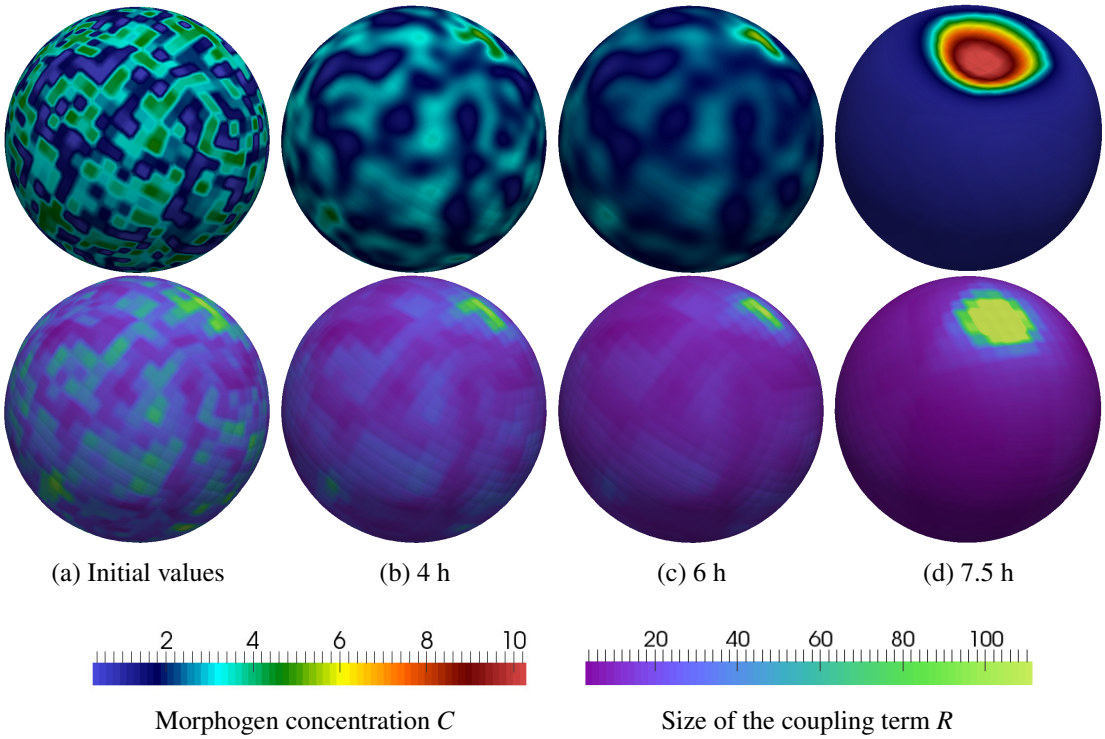

Figure 5.16: Simulation snapshots showing spontaneous pattern formation for a feedback loop based on integrated stress-mediated feedback in combination with basal constriction. The feedback is integrated over each biological cell, shown in the lower row.

Next, we consider the 2D setting to conduct further simulations for the enhanced approach based on stress- and stretch-mediated mechanical feedback. Also here, we asses the robustness with regard to diffusion. Firstly, let us consider the stretch-mediated feedback loop including basal constriction. In Fig. 5.17 (a)-(d), we show pattern formation for the stretch-mediated integrated feedback where diffusion is not essential to obtain mechanochemical patterns in this enhanced approach. Interestingly, these simulation snapshots strongly resemble our findings for the stretch-mediated feedback loop for one tenth of the usual diffusion rate in the standard approach (cf. Fig. A.8). If diffusion is considered we obtain a foot-sole/peanut shaped result (cf. Fig. 5.17 (e)-(h)) similar to our simulation snapshots for the standard approach in 2D presented in the appendix (cf. Fig. A.6.

Secondly, for the stress-mediated feedback loop, we obtain a single invagination for an initial morphogen spot. A clear distinction between actively constricting cells (green and red) and passive cells (blue) (cf. Fig. 5.18) compared to the usual model (cf. Fig. A.7) is possible.

In summary, a single active gastrulation was observed for the feedback loop based on integrated stress-mediated feedback including basal constriction, where a threshold for the expression of morphogen is crucial to stop the expansion of mechanochemical patterns into the entire domain. More importantly, the presented enhanced approach yields results that, at least on the

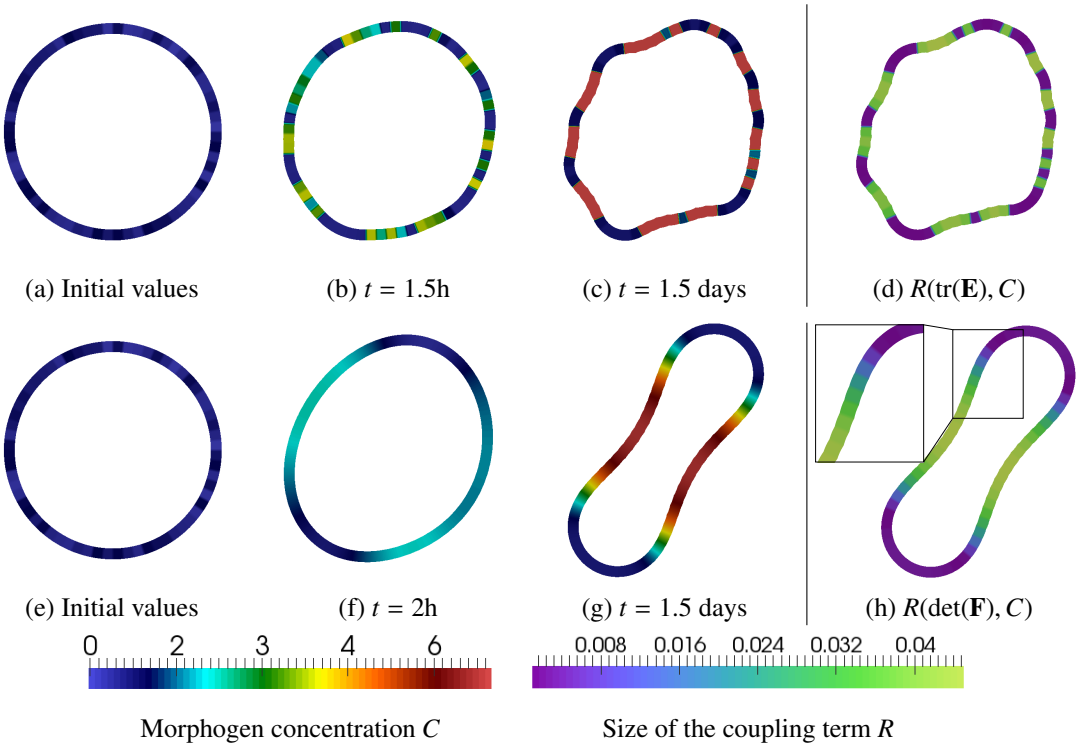

Figure 5.17: Simulation snapshots showing spontaneous pattern formation for a feedback loop based on integrated stretch-mediated feedback in combination with basal constriction. (a)-(d): No diffusion (f)-(j): Usual diffusion rates as in Fig. A.6. As initial conditions, we prescribe uniformly distributed, random morphogen concentrations for each biological cell.

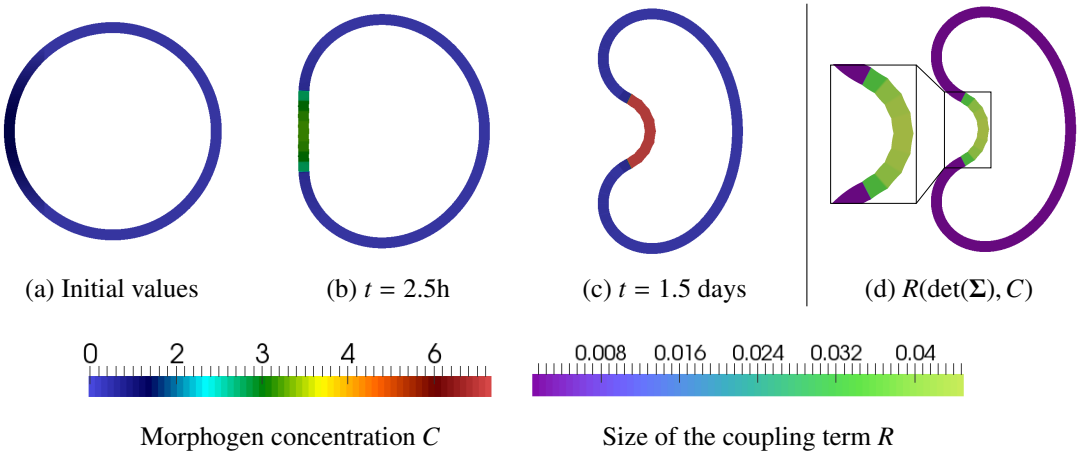

Figure 5.18: Simulation snapshots showing spontaneous pattern formation for a feedback loop based on integrated stress-mediated feedback in conjunction with basal constriction. Initially, morphogen is distributed with a spot at one side of the sphere.

tissue scale, closely resemble those from our usual feedback loops. This indicates that our standard approach is indeed suitable to describe mechanochemical pattern formation on the tissue level. In general, it hence seems that the additional effort of integrating the mechanical feedback is not required to gain meaningful results on the tissue scale with our standard approach that we presented in the beginning of this section.

5.4 Mechanochemical pattern formation for symmetry breaking in *Hydra* aggregates

Finally, we apply our prototypical systems of PDEs to symmetry breaking and subsequent head formation in aggregates of the fresh-water polyp *Hydra*. Clearly, the highlight of this section are our predictive numerical experiments, where we focus on the impact of mechanical stimuli, namely micropipette aspiration, on biological tissue. This research is based on simple mechanical manipulations which is particularly attractive since mechanical tissue modification tools, molecular markers and mechanochemical models are still in its infancy [103]. Besides, we have the opportunity to qualitatively compare our numerical results to the experiments by Heike Sanders [133]. This application further emphasizes the flexibility of our approach as we demonstrate how our simple mechanochemical feedback loops adapted to a new model organism robustly lead to pattern formation. These loops are based on morphogen induced apico-basal shortening (thinning) of biological cells which results in strain that in turn triggers morphogen production. The precise model organism under consideration is of less importance.

Here, we focus on the fresh-water polyp *Hydra*, which is a fascinating and frequently studied model organism where *de novo* mechanochemical pattern formation is witnessed. Besides, experiments by micropipette aspiration are conducted for *Hydra* regenerates and allow for a cross-reference with our numerical results, see Sander [133]. Gierer *et al.* [45] demonstrate the extraordinary regeneration capabilities of *Hydra*: Sufficiently many separated (gastric) cells of *Hydra* reaggregate into a tissue sphere and develop into a normal animal. Any positional information is lost during aggregation (cf. Ref. [45]) such that *de novo* mechanochemical pattern formation leading to symmetry breaking is vital, see Soriano *et al.* [139].

Further, studying *Hydra* aggregates is appealing from a modelers perspective [105]: It has a simple model geometry and a reduced complexity compared to the complete, original organism, e.g. we do not need sophisticated assumptions regarding the initial conditions. Thus, it is not surprising that *Hydra* aggregates are an established model organism in developmental biology [42, 53].

Spontaneous symmetry breaking and head formation in *Hydra* aggregates is characterized by the following steps: Initially, sufficiently many separated *Hydra* cells regenerate and form a hollow sphere where the cells are arranged in a bilayer. Then, the aggregate shows osmotically driven growth oscillations that eventually lead to a symmetry breaking: During growth pulsations, Fütterer *et al.* observe sawtooth-like oscillations of inflation due to the inflow of water followed by rapid contractions, where fluid and detached cells are released due to the rupture of the tissue (phase I). Next, smaller oscillations are registered and the symmetry is broken by

an elongation that subsequently leads to head formation (phase II). Interestingly, the location of head formation does not necessarily coincide with the points of rupture during phase I, see Sander [133]. Finally, the organism grows into a complete animal with a head, tentacles and a foot.

In the last decades, the Wnt pathway has become a well-established mechanism to explain the formation of the head organizer in *Hydra*, see Broun *et al.* [23], Hobmayer *et al.* [65] or Lengfeld *et al.* [88]. However, there "is no consensus about the exact mechanism how and why the wnt head organizing center is initially established at a specific location", Sander [133, p. 2].

Further, activator and inhibiter molecules required for classical Turing type models have not yet been identified [40, 139]. On the contrary, "experiments investigating *de novo* symmetry breaking in hydra shperoids suggest a mechanical basis of the self-organized symmetry breaking process ", Sander [133, p. iii]. Further, experiments by Henderson *et al* [62] or the use of magnetic tweezers and *in vivo* laser ablation by Desprat *et al* [33] stress the indispensable role of tissue mechanics (and the cytoskeleton [133]) in morphogenesis. In the introduction to this chapter, we further illuminated the central role of mechanics in pattern formation.

These findings further stress the need for new modeling approaches. A first approach by Soriano *et al.* [139] combines reaction-diffusion equations and mechanics by coupling morphogen transport to stress. Recently, Mercker *et al.* [105] proposed simple feedback loops between morphogen dynamics and mechanical stretch to explain many experimental observations by simulations on 2D surfaces: Osmotic pressure (phenologically modeled) leads to tissue stretch which produces morphogen. In turn, morphogen reduces the mechanical resistance to stretch such that mechanochemical patterns develop.

In this thesis, we apply our prototypical system of PDEs to spontaneous symmetry breaking in *Hydra* aggregates. We demonstrate how simple mechanochemical feedback loops robustly lead to pattern formation where the consideration of the full 3D geometry seems essential to obtain realistic results. The highlights of this section are our predictive numerical experiments which are validated against microscopic observations of micropipette aspiration.

5.4.1 Model geometry

In this application, we investigate a system representing so-called *Hydra* aggregates of the sweetwater polyp *Hydra*. One advantage of studying *Hydra* aggregates is their reduced complexity compared to the complete organism and their simple geometry [45]. Initially, its cells are ordered in form of a hollow tissue sphere, analogous to the model geometry in embryonic development that we showed in Fig. 5.7. Thus, we parameterize a deforming tissue body over a hollow tissue sphere. The sphere is composed of 1536 biological cells that are arranged circumferentially in one layer. Each biological cell contains $64 = 4^3$ numerical ones, i.e. we have 98 304 numerical cells overall (blue grid in Fig. 5.19 (b)).

If not stated otherwise, the outer radius of this tissue sphere is 150µm, and the inner radius is 135µm. Hence, we have a tissue thickness of 15µm.

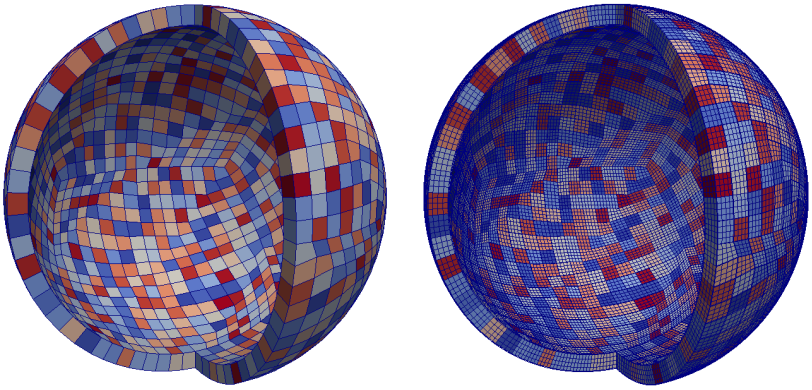

Biological cells (color and lines)

Resolution of biological by numerical cells (blue grid)

Figure 5.19: Model geometry for simulating symmetry breaking in *Hydra* aggregates. The 3D tissue sphere is sliced for the sole purpose of a better visualization.

5.4.2 Robin and Neumann boundary conditions for modeling the pipette

In general, we prescribe homogeneous Neumann conditions on the entire boundary since *Hydra* aggregates are usually surrounded by water. In biological experiments, head formation in regenerated *Hydra* aggregates can be triggered by aspiration with a micropipette, see Sander [133]. *Hydra* regenerates are sensitive to mechanical stimuli and even gravity: Hence, the regenerate is solely fixed by the micropipette itself during these experiments. Here, this translates to a prescription of homogeneous Neumann boundary conditions except for the part where we model the aspiration by the micropipette. Here, a Neumann boundary condition accounts for the force applied by the pipette, and a Robin condition models its glass body.

Hence, let $\Omega \subset \mathbb{R}^3$ be a (bounded) domain in three dimensions. In general, homogeneous Neumann conditions $\mathbf{F\Sigma N} = 0$ on $\partial\Omega$ are assumed, since *Hydra* aggregates are usually surrounded by water and it is *a priori* not obvious where deformations will occur. Also, Dirichlet conditions are not an option since numerical simulations confirm that they significantly alter our numerical results.

Additionally, we want to consider predictive numerical experiments as illustrated in Fig. 5.20: In this experiment, we prescribe homogeneous initial conditions such that pattern formation is solely triggered by a pipette that aspirates the *Hydra* tissue. This pipette acts as a surface force on the boundary of the biological tissue. Hence, we derive boundary integrals that model the pull by the pipette on the one hand and the constraints that are imposed by the glass body of the pipette on the other. This leads to three different boundary conditions on the three non-overlapping parts,

$$\partial\Omega = \Gamma_N \cup \Gamma_R, \quad \Gamma_N = \Gamma_{N0} \cup \Gamma_{NP},$$

of our boundary $\partial\Omega$, see Fig. 5.20. Note that the white pipette in this figure is solely included for the purpose of a better visualization and never part of the computational domain.

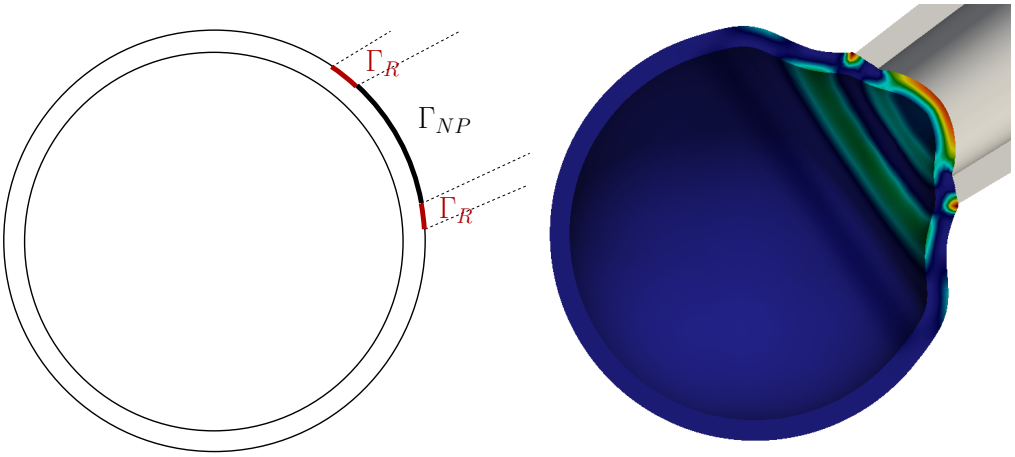

Figure 5.20: Setup in our predictive numerical experiment for pattern formation induced by the pull of a pipette. Left: Schematic illustration of the boundary parts on a 2D cross-section, where Robin and Neumann conditions are prescribed on Γ_R (red) and Γ_{NP}. Right: Simulation snapshot of our predictive, numerical experiment where morphogen (color) is induced by positive strain. The 3D tissue is sliced for the sole purpose of a better visualization

Firstly, we include a prescribed surface force modeling the pull by the pipette using a Neumann boundary condition on Γ_{NP}. Secondly, the glass edge in the tip of the pipette prevents the tissue from deformations in normal direction $\mathbf{n}$. We model the glass body by free slip and no penetration boundary conditions, i.e., the biological tissue can slide along the tip of the pipette but it cannot penetrate its glass body. Note that we neglect friction and that considering the glass body significantly changes the material response in comparison to simply pulling the *Hydra* tissue (cf. Subsection 5.4.5). Slip (with friction) and no penetration boundary conditions are also implemented in many applications of the Navier-Stokes equations. For instance, Galdi and Layton [41] propose to apply slip with friction and no penetration boundary conditions to compute the large eddies (vortices) of a turbulent flow.

In this application, we mainly follow the work of John [73], who describes the implementation of these conditions for finite element discretization. The practical realization of the no penetration condition $(\mathbf{u} \cdot \mathbf{n}) = 0$ that accounts for the glass body leads to a Robin boundary condition on Γ_R. Finally, we assume that no forces act on the rest of the boundary Γ_{N0}, where homogeneous Neumann conditions are prescribed.

We start from the structural equation in Eulerian coordinates (2.17), which reads

$$\int_{\Omega(t)} \rho(\mathbf{x},t)\partial_t \mathbf{v}(\mathbf{x},t)\boldsymbol{\varphi} + \rho(\mathbf{x},t)(\mathbf{v}(\mathbf{x},t)\cdot\nabla)\mathbf{v}(\mathbf{x},t)\boldsymbol{\varphi}\,\mathrm{d}\mathbf{x} + \int_{\Omega(t)} \boldsymbol{\sigma}(\mathbf{x},t)\nabla\boldsymbol{\varphi}\,\mathrm{d}\mathbf{x}$$
$$+ \int_{\partial\Omega(t)} \boldsymbol{\sigma}(\mathbf{x},t)\mathbf{n}\,\boldsymbol{\varphi}\,\mathrm{d}s = 0$$

if a body force $\mathbf{f}$ is not considered and if the boundary term no longer vanishes due to the inhomogeneous boundary conditions in this setting. Next, let the boundary in the deformed configuration be split in the disjoint Neumann and Robin parts $\partial\Omega(t) = \Gamma_N(t) \cup \Gamma_R(t)$, with $\Gamma_N(t) = \Gamma_{N0}(t) \cup \Gamma_{NP}(t)$. For the boundary term in the previous equation, this yields

$$\int_{\partial\Omega(t)} \boldsymbol{\sigma}(\mathbf{x}, t)\mathbf{n}\,\boldsymbol{\varphi}\,\mathrm{d}s = \int_{\Gamma_{NP}(t)} \mathbf{g}(\mathbf{x})\,\boldsymbol{\varphi}\,\mathrm{d}s + \int_{\Gamma_R(t)} \alpha^{-1}(\mathbf{u}\cdot\mathbf{n})\mathbf{n}\,\boldsymbol{\varphi}\,\mathrm{d}s, \tag{5.9}$$

where $\alpha = \alpha_0 h > 0$ is a considerably small and positive constant. It depends on the mesh size h and has to be picked smaller on finer grids (John [73]). On $\Gamma_{N0}(t)$, homogeneous Neumann values are prescribed and the boundary term vanishes. Further, we express the boundary force modeling micropipette aspiration in direction $(0, 0, x_2)^T$ by

$$\mathbf{g}(\mathbf{x}) = c_b \cos\left(0.5\sqrt{x_0^2 + x_1^2}\right)\mathbf{n}, \qquad \forall\, \mathbf{x} \in \Gamma_{NP}(t),$$

with a constant c_b that determines the strength of the pull in normal direction $\mathbf{n}$. In practice, we pick $\Gamma_{NP} = \{\mathbf{x} \in \partial\Omega \,|\, \sqrt{x_0^2 + x_1^2} < \pi,\ x_2 < 0\}$ such that $\mathbf{g}$ is zero on the boundary of Γ_{NP} and that the continuation by zero of $\mathbf{g}$ onto the entire boundary $\partial\Omega$ is continuous. The existence of such a continuation is shown in literature, e.g. we refer to the the continuation theorem by Calderon-Zygmund in Wloka [154, p. 100], and will be important for the upcoming transformation to the reference domain. Finally, regarding Eq. (5.9), we have introduced a Robin boundary condition

$$\alpha\boldsymbol{\sigma}(\mathbf{x}, t)\mathbf{n} = (\mathbf{u}\cdot\mathbf{n})\mathbf{n} \quad \text{on } \Gamma_R(t),$$

which accounts for the glass body of the pipette and was inspired by John [73], who applied this no penetration condition as boundary conditions for the Navier-Stokes equation. In the limit $\alpha \to 0$, we obtain $(\mathbf{u}\cdot\mathbf{n}) = 0$ such that the no penetration condition prevents any movement of the tissue in normal Eulerian direction towards the glass edge in the tip of the pipette.

Finally, we transform Eq. (5.9) to the reference configuration, where our structural equations are naturally given (cf. Eq. (2.33)). The idea is to use Gauss's divergence theorem to convert the surface into a volume integral, which we transform to the reference configuration. Then, we use Gauss's theorem in the opposed way to obtain the surface integral in the reference configuration.

(1) We begin by transforming the integral that describes the surface force on Γ_{NP}: To apply Gauss's theorem, we define the continuous continuation of $\mathbf{g}$ onto the entire boundary by

$$\tilde{\mathbf{g}}(\mathbf{x}) \coloneqq \begin{cases} \mathbf{g}(\mathbf{x}) & \text{if } \mathbf{x} \in \Gamma_{NP}(t), \\ 0 & \text{else.} \end{cases}$$

Next, we need the continuation of $\tilde{\mathbf{g}}$ into the entire domain such that $\tilde{\mathbf{g}} \in H^1(\Omega)$. The unique existence of this function is guaranteed by Riesz representation theorem, since there exists a unique solution to Laplace's equation with continuous boundary data $\tilde{\mathbf{g}}(\mathbf{x}, t)$. Obviously, this solution

is the desired continuation in $H^1(\Omega)$. With these preparations, we apply Gauss's divergence theorem and obtain

$$\begin{aligned}\int_{\Gamma_{NP}(t)} \mathbf{g}(\mathbf{x}) \cdot \boldsymbol{\varphi} \, \mathrm{d}s &= \int_{\partial\Omega(t)} |\tilde{\mathbf{g}}(\mathbf{x})| \mathbf{n} \cdot \boldsymbol{\varphi} \, \mathrm{d}s = \int_{\Omega(t)} \nabla_{\mathbf{x}} \cdot (|\tilde{\mathbf{g}}(\mathbf{x})| \, \boldsymbol{\varphi}) \, \mathrm{d}\mathbf{x} \\ &= \int_{\Omega(t)} \nabla_{\mathbf{x}} |\tilde{\mathbf{g}}(\mathbf{x})| \cdot \boldsymbol{\varphi} + |\tilde{\mathbf{g}}(\mathbf{x})| \nabla_{\mathbf{x}} \cdot \boldsymbol{\varphi} \, \mathrm{d}\mathbf{x}.\end{aligned}$$

Now, we can employ our transformations of the integral (2.4), the gradient (2.5) and the divergence (2.6) and obtain

$$\begin{aligned}&\int_{\Omega(t)} \nabla_{\mathbf{x}} |\tilde{\mathbf{g}}(\mathbf{x})| \cdot \boldsymbol{\varphi} + |\tilde{\mathbf{g}}(\mathbf{x})| \nabla_{\mathbf{x}} \cdot \boldsymbol{\varphi} \, \mathrm{d}\mathbf{x} \\ &= \int_{\Omega} J\mathbf{F}^{-T} \nabla_{\mathbf{X}} |\tilde{\mathbf{G}}(\mathbf{X})| \cdot \boldsymbol{\Phi} + |\tilde{\mathbf{G}}(\mathbf{X})| \nabla_{\mathbf{X}} \cdot (J\mathbf{F}^{-1}\boldsymbol{\Phi}) \, \mathrm{d}\mathbf{X} \\ &= \int_{\partial\Omega} |\tilde{\mathbf{G}}(\mathbf{X})| J\mathbf{F}^{-1}\boldsymbol{\Phi} \cdot \mathbf{N} \, \mathrm{d}S = \int_{\Gamma_{NP}} \mathbf{G}(\mathbf{X}) \cdot \boldsymbol{\Phi} \, \mathrm{d}S,\end{aligned} \tag{5.10}$$

where we employ our usual notation and define $\mathbf{G}(\mathbf{X}) \coloneqq \mathbf{g}(\boldsymbol{\chi}(\mathbf{X}))$, which has a (continuous) continuation $\tilde{\mathbf{G}}(\mathbf{X})$ onto the entire boundary. The unique existence of this continuation is again guaranteed by Riesz representation theorem using the same arguments as for the continuation $\tilde{\mathbf{g}}(\mathbf{x})$ in Eulerian coordinates.

(2) We transform the Robin condition on $\Gamma_R(t)$ analog to the derivation for the boundary force $\mathbf{G}(\mathbf{X})$. Firstly, we need a continuation of $\alpha^{-1}(\mathbf{u} \cdot \mathbf{n})$ on Γ_R onto the entire boundary. Here, finding a continuation is more complex, since the simple continuation by zero is not continuous. Instead, we take small strips $\Gamma_\epsilon \subset \Gamma_{N0}$ of measure ϵ between Γ_R and the rest of Γ_{N0}. Then, we define a continuous function $\beta(\mathbf{x})$ which attains α^{-1} on Γ_R, zero on Γ_{N0} and smoothly decreases between these values on Γ_ϵ. By this construction, we obtain a smooth continuation $\tilde{\beta}(\mathbf{x})\mathbf{u} \cdot \tilde{\mathbf{n}}$ of our robin condition onto the entire boundary. Since $\mathbf{u}, \boldsymbol{\varphi} \in H^1(\Omega(t))$ and $\mathbf{n} \in C^\infty(\partial\Omega(t))$, the existence of continuations for each of these function into the entire domain can be shown. Note that in this sense of a continuation, the normal directions $\mathbf{n}, \mathbf{N}$ will appear in volume integrals.

Secondly, we can proceed by using Gauss's divergence theorem followed by our transformations of the integral (2.4), the gradient (2.5) and the divergence (2.6). In detail, this gives:

$$\begin{aligned}&\int_{\Gamma_R(t)} \alpha^{-1}(\mathbf{u} \cdot \mathbf{n})\mathbf{n} \cdot \boldsymbol{\varphi} \, \mathrm{d}s + \int_{\Gamma_\epsilon(t)} \beta(\mathbf{x})(\mathbf{u} \cdot \mathbf{n})\mathbf{n} \cdot \boldsymbol{\varphi} \, \mathrm{d}s \\ &= \int_{\Omega(t)} \tilde{\beta}(\mathbf{x})(\mathbf{u} \cdot \tilde{\mathbf{n}}) \nabla_{\mathbf{x}} \cdot \boldsymbol{\varphi} + \tilde{\beta}(\mathbf{x}) \nabla_{\mathbf{x}} (\mathbf{u} \cdot \tilde{\mathbf{n}}) \cdot \boldsymbol{\varphi} \, \mathrm{d}\mathbf{x} \\ &= \int_{\Omega} \tilde{\beta}((\boldsymbol{\chi}(\mathbf{X})) \, (\mathbf{u} \cdot J\mathbf{F}^{-T}\tilde{\mathbf{N}}) \nabla_{\mathbf{X}} \cdot (J\mathbf{F}^{-1}\boldsymbol{\Phi}) + \tilde{\beta}((\boldsymbol{\chi}(\mathbf{X})) \, \nabla_{\mathbf{X}} (\mathbf{u} \cdot J\mathbf{F}^{-T}\tilde{\mathbf{N}}) \cdot J\mathbf{F}^{-T}\boldsymbol{\Phi} \, \mathrm{d}\mathbf{X} \\ &= \int_{\Gamma_R} \alpha^{-1} J^2 (\mathbf{u} \cdot \mathbf{F}^{-T}\mathbf{N})(\mathbf{F}^{-T}\mathbf{N} \cdot \boldsymbol{\Phi}) \, \mathrm{d}\mathbf{X} + \int_{\Gamma_\epsilon} \beta(\epsilon) J^2 (\mathbf{u} \cdot \mathbf{F}^{-T}\mathbf{N})(\mathbf{F}^{-T}\mathbf{N} \cdot \boldsymbol{\Phi}) \, \mathrm{d}\mathbf{X},\end{aligned}$$

where we use Gauss's divergence theorem in the last step. The normal direction transforms as $\mathbf{n} = J\mathbf{F}^{-T}\mathbf{N}$, which can be deduced from comparing the first and the last integral in the derivation of the Neumann boundary conditions derived in Eq. (5.10).

Finally, notice that $\|\beta(\mathbf{x})\| \leq \alpha^{-1}$ holds by the definition of β and that $\mathbf{u} \cdot \mathbf{n}$ and $\boldsymbol{\varphi}$ are bounded. Hence, we can estimate

$$\left| \int_{\Gamma_\epsilon(t)} \beta(\mathbf{x})(\mathbf{u} \cdot \mathbf{n})\mathbf{n} \cdot \boldsymbol{\varphi} \, \mathrm{d}s \right| \leq \int_{\Gamma_\epsilon(t)} \alpha^{-1} c \, \mathrm{d}s \to 0 \quad \text{for } \epsilon \to 0,$$

with a constant $c > 0$. Analogously, this estimate can be shown for the transformed integral on Γ_ϵ. Together, these transformations yield our boundary conditions in the reference configuration:

$$\int_{\partial\Omega} \mathbf{F}\boldsymbol{\Sigma}\mathbf{N} \cdot \boldsymbol{\Phi} \, \mathrm{d}S = \int_{\Gamma_{NP}} J\mathbf{F}^{-T}\mathbf{G}(\mathbf{X}) \cdot \boldsymbol{\Phi} \, \mathrm{d}S + \int_{\Gamma_R} \alpha^{-1} J^2 (\mathbf{u} \cdot \mathbf{F}^{-T}\mathbf{N})(\mathbf{F}^{-T}\mathbf{N} \cdot \boldsymbol{\Phi}) \, \mathrm{d}S,$$

where the surface force for the constant c_b and $\mathbf{X} = (X_0, X_1, X_2)^T \in \Gamma_{NP}$ is given by

$$\mathbf{G}(\mathbf{X}) = c_b \cos\left(0.5\sqrt{X_0^2 + X_1^2}\right)\mathbf{N}(\mathbf{X}), \qquad \forall\, \mathbf{X} \in \Gamma_{NP}.$$

In strong form, the Robin boundary condition for including our predictive numerical experiment in our prototypical system of equations (2.38) reads

$$\mathbf{r}(\mathbf{u}, \nabla\mathbf{u}, \mathbf{N}) = \alpha\mathbf{F}\boldsymbol{\Sigma}\,\mathbf{N} - J^2(\mathbf{u} \cdot \mathbf{F}^{-T}\mathbf{N})\mathbf{F}^{-T}\,\mathbf{N} = 0 \quad \text{on } \Gamma_R, \tag{5.11}$$

with the considerably small constant $\alpha = \alpha_0 h > 0$ from above. In the limit $\alpha \to 0$ we prescribe the no penetration condition $(\mathbf{u} \cdot \mathbf{F}^{-T}\mathbf{N}) = 0$, i.e., α_0 should be small. In this work, picking $\alpha_0 = 10^{-6}$ is sufficient.

5.4.3 Coupled system of model equations

Now, we apply our prototypic equations in variational form (3.1) to symmetry breaking in *Hydra*. As before in embryonic development, we only consider one species of signaling molecules of concentration C. Consequently, we couple just one reaction-diffusion equation to the structural one.

So let $\Omega \subset \mathbb{R}^3$ be a (bounded) domain in two or three dimensions. Further, let the boundary $\partial\Omega$ of our domain be split into two non-overlapping (i.e. disjoint) parts $\partial\Omega = \Gamma_N \cup \Gamma_R$, where Neumann and Robin boundary conditions are imposed, respectively. In general, homogeneous Neumann values are prescribed. In our predictive experiments, boundary forces and Robin conditions modeling a micropipette are also implemented. Details on these boundary conditions are given in the preceding section. Then, for suitable Hilbert spaces V^3 and $V := H^1(\Omega)$ our prototypic equations in variational form (3.1) applied to embryonic development reads:

Find the displacement $\mathbf{u} \in V^d$ and the morphogen concentration $C \in V$, with initial conditions $\mathbf{u}(\mathbf{X}, 0) = 0$, $C(\mathbf{X}, 0) = C^0(\mathbf{X})$ such that

$$\begin{aligned}(\epsilon\rho^0\partial_{tt}\mathbf{u}, \boldsymbol{\Phi})_\Omega + (\mathbf{F}\boldsymbol{\Sigma}, \nabla\boldsymbol{\Phi})_\Omega - (J\mathbf{F}^{-T}\mathbf{G}, \boldsymbol{\Phi})_{\Gamma_N} - (\alpha^{-1}J^2(\mathbf{u}\cdot\mathbf{F}^{-T}\mathbf{N})\mathbf{F}^{-T}\mathbf{N}, \boldsymbol{\Phi})_{\Gamma_R} = 0 \quad \forall\boldsymbol{\Phi} \in V^d \\ (J\partial_t C, \Psi)_\Omega + (J\mathbf{F}^{-1}\mathbf{D}\mathbf{F}^{-T}\nabla C, \nabla\Psi)_\Omega - (JR, \Psi)_\Omega = 0 \quad \forall\Psi \in V\end{aligned} \tag{5.12}$$

holds, where

$$\boldsymbol{\Sigma} = J_a\mathbf{F}_a^{-1}\boldsymbol{\Sigma}_e\mathbf{F}_a^{-T}, \quad \boldsymbol{\Sigma}_e = \lambda\,\mathrm{tr}(\mathbf{E}_e)\mathbf{I} + 2\mu\mathbf{E}_e, \quad \mathbf{E}_e = \frac{1}{2}(\mathbf{F}_e^T\mathbf{F}_e - \mathbf{I}),$$
$$\mathbf{F}_e = \mathbf{F}\mathbf{F}_a^{-1}, \quad \mathbf{F} = \nabla\mathbf{u} + \mathbf{I}, \quad J = \det(\mathbf{F}), \quad J_a = \det(\mathbf{F}_a),$$

and μ, λ are the Lamé constants. Further, $\epsilon \sim 0.1$ stems determines the intensity of the stabilization by the time derivative and introduced in Section 3.3. Next, R is the coupling term incorporating the feedback of mechanical cues on the morphogen concentration C via $R = R(\boldsymbol{\Sigma}, \mathbf{E}, \mathbf{F}, C)$, which will be specified in the following paragraph. Vice versa, $\boldsymbol{\Sigma}(\mathbf{F}_a(t, C))$ allows for a coupling of the morphogen concentration C on the active deformation process. More precisely, the active deformation gradient $\mathbf{F}_a$ prescribes an elongation or shortening for each individual biological cell and is specified in the next section. This mutual coupling of tissue mechanics and morphogen dynamics results in a positive self-inducing feedback loop, which was presented in Subsection 2.3.3 and illustrated in Fig. 2.5.

Further, $\mathbf{D} \in \mathbb{R}^{3\times3}$ is the diffusion coefficient tensor which reads in matrix notation

$$\mathbf{D} \coloneqq \mathbf{Q}(\mathbf{X})^T\,\mathrm{diag}(D_\mathbf{T}, D_\mathbf{T}, D_\mathbf{T})\mathbf{Q}(\mathbf{X})$$

with a diagonal matrix containing the diffusion coefficient $D_\mathbf{N}$ in normal (or radial) Lagrangian direction $\mathbf{N} = |\mathbf{X}|^{-1}\mathbf{X}$ and the diffusion coefficient $D_\mathbf{T}$ in the tangential directions $\mathbf{T}_1$ and $\mathbf{T}_2$. The rotation matrix $\mathbf{Q}^T$ transforms the diagonal matrix $\mathrm{diag}(D_\mathbf{N}, D_\mathbf{T}, D_\mathbf{T})$ defined in the point-specific coordinate systems given by the orthogonal unit vectors $\mathbf{N}(\mathbf{X})$, $\mathbf{T}_1(\mathbf{X})$ and $\mathbf{T}_2(\mathbf{X})$ to Euclidean coordinates.

This choice of the diffusion coefficient tensor is biologically motivated, as a large coefficient $D_\mathbf{N}$ in radial direction ensures free diffusion inside the biological cells whereas a small coefficient $D_\mathbf{T}$ limits diffusion between biological cells (at least on the tissue scale), see Subsection 2.3.1 for details.

In general, homogeneous Neumann values are assumed on the entire boundary $\partial\Omega$. Predictive, numerical experiments are an exception: There, homogeneous initial conditions $\mathbf{u}(\mathbf{X}, 0) = 0$ and $C(\mathbf{X}, 0) = 0$ are assumed. Growth is solely triggered by the boundary force that is applied by a pipette. This force results in deformation of the tissue which in turn stimulates our positive feedback loop. The force applied by the pipette is modeled by a surface force $\mathbf{G}$ on the Neumann boundary Γ_{NP} and a Robin condition $\alpha\mathbf{F}\boldsymbol{\Sigma}\,\mathbf{N} = J^2(\mathbf{u}\cdot\mathbf{F}^{-T}\mathbf{N})\mathbf{F}^{-T}\,\mathbf{N}$ on Γ_R accounts for the glass body of the pipette itself as introduced in Subsection 5.4.2.

Mechanical feedback

In this application, we consider a strain-mediated feedback loop including apico-basal shortening. Here, apico-basal shortening refers to the thinning of biological cells in radial direction and will be specified hereafter. We thus employ strain-mediated feedback which best captures the relative length changes (shortening in radial, stretching in tangential directions) that are induced by this active deformation. As a mechanical feedback on morphogen production, we use the hydrostatic strain expressed in terms of the first invariant of the Green-Lagrange strain tensor $I_1(\mathbf{E}) = \mathrm{tr}(\mathbf{E})$.

Firstly, we employ mechanical feedback based on positive strain. Then, the general coupling term presented in Eq. (2.40) takes the form

$$R(I_1(\mathbf{E}), C) = k_2 \frac{\max\{I_1(\mathbf{E}), 0\}}{k_m + \max\{I_1(\mathbf{E}), 0\}} - k_1 C.$$

Secondly, in our predictive numerical experiments, we also focus on mechanical feedback related to negative strain such that the coupling term is given by

$$R(I_1(\mathbf{E}), C) = -k_2 \frac{\min\{I_1(\mathbf{E}), 0\}}{k_m - \min\{I_1(\mathbf{E}), 0\}} - k_1 C.$$

Finally, another experimental setup is based on using the absolute value of all hydrostatic strain, which yields

$$R(I_1(\mathbf{E}), C) = k_2 \frac{|I_1(\mathbf{E})|}{k_m + |I_1(\mathbf{E})|} - k_1 C.$$

Active deformation gradient

In experiments, signaling molecules have been shown to modify the mechanics of biological cells in various was such as growth or active cell-shape changes [12, 17, 32, 58]. In the application to symmetry breaking in *Hydra*, we consider active cell shape changes by apico-basal shortening. This term refers to the shorting of biological cells in radial direction of the tissue sphere such that the tissue sphere becomes locally thinner but enlarges in the tangential directions, see Fig. 5.21. This active deformation is not only observed in *Hydra* aggregates [123, 139] but is also very common in tissue morphogenesis, see e.g. Davies [31]. Also, similar active deformations were prescribed in ventral furrow invagination in the *Drosophila melanogaster* embryo (cf. Conte *et al.* [29]). We assume a linear coupling of morphogen concentrations on active deformations, analog to our approach based on apical/basal constriction in embryogenesis (cf. Subsection 5.3.2). Mathematically, this is realized by coupling the concentration of signaling molecules C into the active part of the decomposed deformation gradient $\mathbf{F} = \mathbf{F}_e\mathbf{F}_a(C)$ [1, 20, 104, 120].

Similar to the active constriction in embryonic development, local coordinate systems $\hat{\mathbf{X}}$ are introduced in the origin of each biological cell, oriented such that $\hat{\mathbf{X}}_2$ points in radial direction.

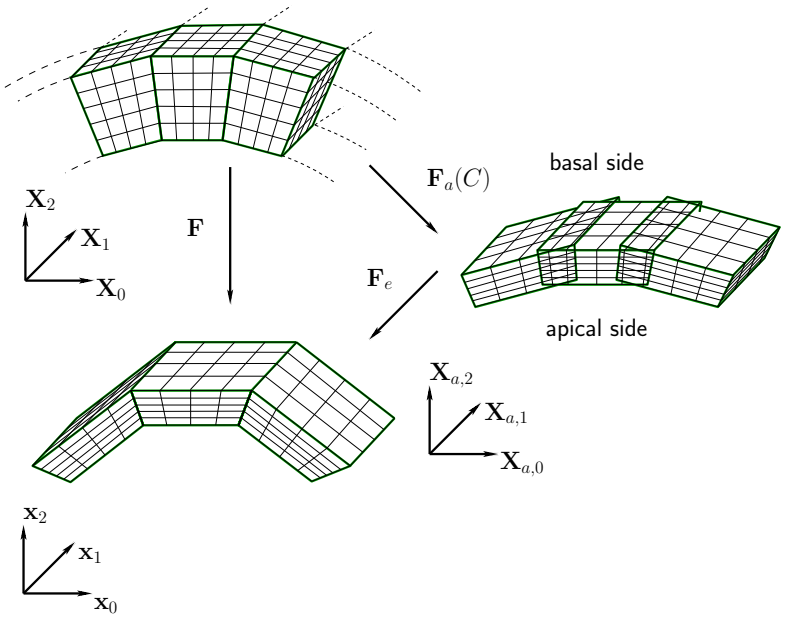

Figure 5.21: Deformation gradient decomposition $\mathbf{F} = \mathbf{F}_e\mathbf{F}_a$ with active deformation gradient $\mathbf{F}_a(c)$ on three arbitrary biological cells resulting in apico-basal shortening.

In these local coordinates, the active deformation gradient is defined as

$$\begin{aligned}\hat{\mathbf{F}}_a(C) &:= \begin{pmatrix}(1+kC)^{-1} & 0\\ 0 & 1+kC\end{pmatrix} && \text{in 2D,}\\ \hat{\mathbf{F}}_a(C) &:= \begin{pmatrix}(1+kC)^{-1} & 0 & 0\\ 0 & (1+kC)^{-1} & 0\\ 0 & 0 & (1+kC)^2\end{pmatrix} && \text{in 3D.}\end{aligned} \tag{5.13}$$

respectively, where k is a constant. Positive values of k result in an apico-basal shortening (thinning) of the biological cells and negative values in elongation. The derivation of the active deformation gradient is similar to the one for apical constriction in Eq. (5.6): $\hat{\mathbf{F}}_a$ is defined in parametric coordinates which are rotated by a matrix $\mathbf{Q}$ to the reference configuration such that the orientation of both coordinate systems coincide. Since the argument of this active deformation gradient is independent of $\mathbf{X}$, the active deformation gradients thus acts in the desired way.

Together, the active deformation tensor $\mathbf{F}_a(c)$ in the reference configuration can be expressed by

$$\mathbf{F}_a(\mathbf{X}, C) = \mathbf{Q}^T\hat{\mathbf{F}}_a(C)\mathbf{Q}, \tag{5.14}$$

where that $\hat{\mathbf{F}}_a$ is identical for each biological cell. The rotation matrix depends on the specific biological cell and has the property $\mathbf{Q}^T\mathbf{Q} = \mathbf{Q}\mathbf{Q}^T = \mathbf{I}$. Further, $\mathbf{Q}$ is globally defined (cf. Eq. (A.6) of the appendix) and is piecewise continuous on each biological cell K_i. The transforma-

tions involved are illustrated in Fig. A.2 in the context of apical/basal constriction. Clearly, this active deformation tensor is volume-preserving as $J = \det(\mathbf{F}_a(C)) = 1$.

In this application, all deformations are driven by this active deformation gradient, which includes growth pulsations. In particular, we did not explicitly account for the inner pressure by a surface force on the inner boundary as discussed in Subsection 5.3.5. Although this is fairly simple and an internal pressure is included in our modeling approach already, many additional assumptions are required to model growth oscillations by surface forces, and, most importantly, it is involved to model the rapid retraction due to rupture of the tissue. Whereas it is certainly possible to prescribe an internal pressure and its quick reduction [105], the actual rupture of the solid domain remains a huge numerical challenge.

Finally, we point out that the biological cells rip apart or overlap in the intermediate configuration, see Figure 5.21. Mathematically speaking, the active deformation gradient $\mathbf{F}_a$ is not injective. Especially, the local inverse $\mathbf{F}^{-1}_{a,K_{a,i}}$ is always well-defined but not injective, whereas its global representation $\mathbf{F}_a^{-1}$ is thus not a function and has to be interpreted as evaluating our coupled system of Equations (5.4) on each biological cell individually.

5.4.4 Parameter setup

In this application to symmetry breaking in *Hydra* aggregates, we employ a similar system of PDEs on the same model geometry as in the previous application to embryogenesis. Thus, most parameters and their values coincide with the choices made in Subsection 5.3.3.

Rather, we focus on two main differences: Firstly, in this applications, we are interested in growth oscillations that occur on the timescale of elasticity. To resolve this timescale, we consider the usual, parabolic structural equations which translates to setting our stabilization parameter to $\epsilon = 1$. Until here, we were rather interested in pattern development on the timescale of growth an regarded the second time derivative as a stabilization, see Subsection 3.5.3.

Secondly, we adjusted the interval of the initially described morphogen concentrations by tripling the maximum which are now prescribed in the interval $c \in [0, 3 \times 10^9]\mathrm{mol\,m^{-3}}$. This change was necessary since, in general, smaller initial conditions dissolved over time and no patterns were formed if all other parameters are kept as before. Initially, uniformly distributed random concentrations for each biological cells or a morphogen gradient were prescribed. Initial deformations are not assumed, since a deformation that corresponds to the initial concentration distribution is not known. In general, it hence takes a few time-steps for morphogen and tissue curvature to align.

In this application, we introduced a new parameter in the description of our predictive, numerical experiment. Here, the aspiration of a *Hydra* aggregate by a micropipette is modeled. The glass body of this pipette is accounted for by a Robing condition, where a small constant $\alpha_0 = 10^{-6}$ is necessary to prevent movement of the tissue sphere towards the glass body (cf. Subsection 5.4.2).

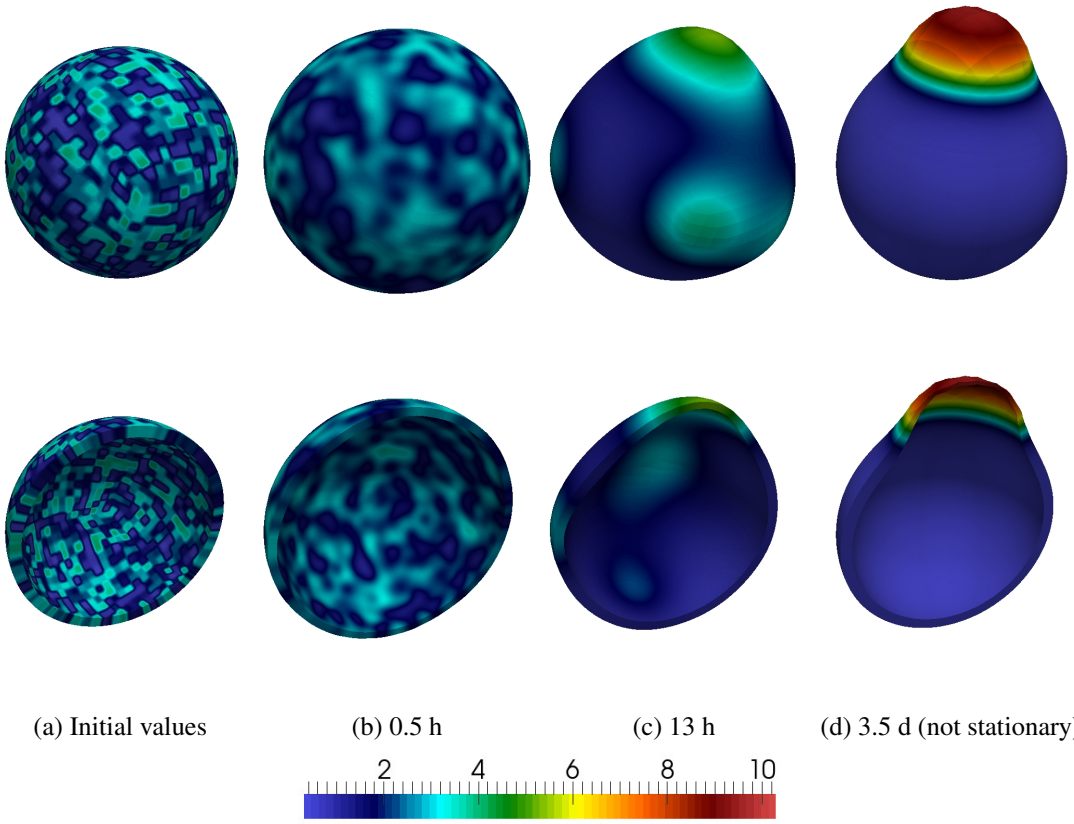

(a) Initial values (b) 0.5 h (c) 13 h (d) 3.5 d (not stationary)

Figure 5.22: Simulation snapshots that show spontaneous pattern formation in *Hydra* aggregates for the strain-mediated feedback loop including apico-basal shortening. The tissue sphere has been sliced for the sole purpose of a better visualization.

For the sake of a complete presentation, we shortly recapitulate the remaining parameters. Also here, we prescribe a comparably small diffusion coefficient $D_{\mathbf{T}} \sim 10^{-14}\mathrm{m}^2\,\mathrm{s}^{-1}$ in the tangential directions in relation to a large coefficient $D_{\mathbf{N}} \sim 10^{-12}\mathrm{m}^2\,\mathrm{s}^{-1}$ in the normal one.

The Lamé constants are usually given in terms of Young's modulus E and Poisson's ratio ν. They can be obtained by the conversion formulas given in Eq. (2.24). Again, we employ $E = 100\,\mathrm{Pa}$ and $\nu = 0.4$ as in Allena *et al.* [1]. The parameter for the mechanochemical coupling is set to $k \sim 10^{-6}\mathrm{mol}^{-1}\,\mathrm{m}$, the degradation rate is given by $k_1 \sim 10^{-4}\mathrm{s}^{-1}$ and the production rate is $k_2 \sim 10^{7}\mathrm{mol}\,\mathrm{m}^{-3}\,\mathrm{s}^{-1}$. Finally, the Michaelis constant is set to $k_m = 2.0$.

5.4.5 Numerical results and discussion

In this application, we focus on a strain-mediated feedback loop including active apico-basal shortening. Namely, apico-basal shortening refers to the thinning of biological cells in radial direction (and elongation in the tangential ones) which is commonly observed in *Hydra* aggre-

gates [123, 139]. These deformations are best described by strain that measures relative length changes and is our mechanical feedback of choice. Accordingly, Henderson and Carter [62] propose that local mechanical cues such as strain influence morphogenesis by deforming tissue and by influencing the direction of growth and its growth rates. Note that a stress-mediated feedback loop leads to promising results as well (not shown). Interestingly, the stretch-mediated feedback loop does not produce results similar to those of the strain mediated one, which was a key observation in our previous application to embryogenesis (cf. Section 5.3).

Simulation snapshots for the strain-mediated feedback loop based on apico-basal shortening are shown in Fig. 5.22. Initially, we prescribe uniformly distributed morphogen concentrations which lead to a thinning of the tissue layer and an expansion of the sphere. In this extention phase, the volume contained inside the tissue sphere increases by about 50% (cf. Fig. 5.22). The subsequent retraction of the sphere is driven by the elastic material response to the active elongation. Over time, several oscillation with decreasing amplitude can be observed. Ultimately, mechanochemical interactions lead to one dominating pattern that leads to head formation and prevents further growth oscillations (cf. Fig. 5.22 (c)-(d)).

A co-localization of high morphogen levels and local tissue curvature (cf. Fig. 5.22) has been described for head formation in the freshwater polyp *Hydra* by Takahashi *et al.* [145] and Hobmayer *et al.* [65]. In our simulations, head formation takes about three to four days, which is a typical order of magnitude: Depending on the origin of the cells (e.g. aggregates might contain only head cells), it usually takes two to seven days until head structures or tentacles are visible [45].

Although morphogen concentrations eventually saturate, Fig. 5.22 (d) does not represent a stationary results. Instead, the mechanochemical patch slowly spreads until it covers the entire domain and a uniformly expanded sphere is attained in the stationary state. For now, we simply assume that other processes such as the Wnt pathway (cf. [23, 65, 88]) to establish a head take over at some point.

Regarding Fig. 5.23, we notice that the simulated *de novo* patterns seem to be insensitive with regard to the initial conditions: If we start with only one initial morphogen spot, we again obtain a single mechanochemical pattern representing a newly formed head. This observation corresponds to the experimental observation that any positional information is lost during aggregation of *Hydra* cells [45]. For the sake of a crisp presentation, we do not repeat an evaluation regarding the robustness of mechanochemical pattern formation to changes in the model geometry or the diffusion rates. Instead, we refer to the robustness analysis in our application to embryogenesis, see Subsection 5.3.4.

Predictive numerical experiments

The highlight of this section are our predictive numerical experiments. Here, we want to enable researchers in developmental biology to investigate the role of mechanics during pattern formation and to inspire new experiments based on micropipette aspiration. In general, experiments with micropipettes are well established whereas mechanical tissue modification tools, molecular markers and mechanochemical models are still in its infancy [103].

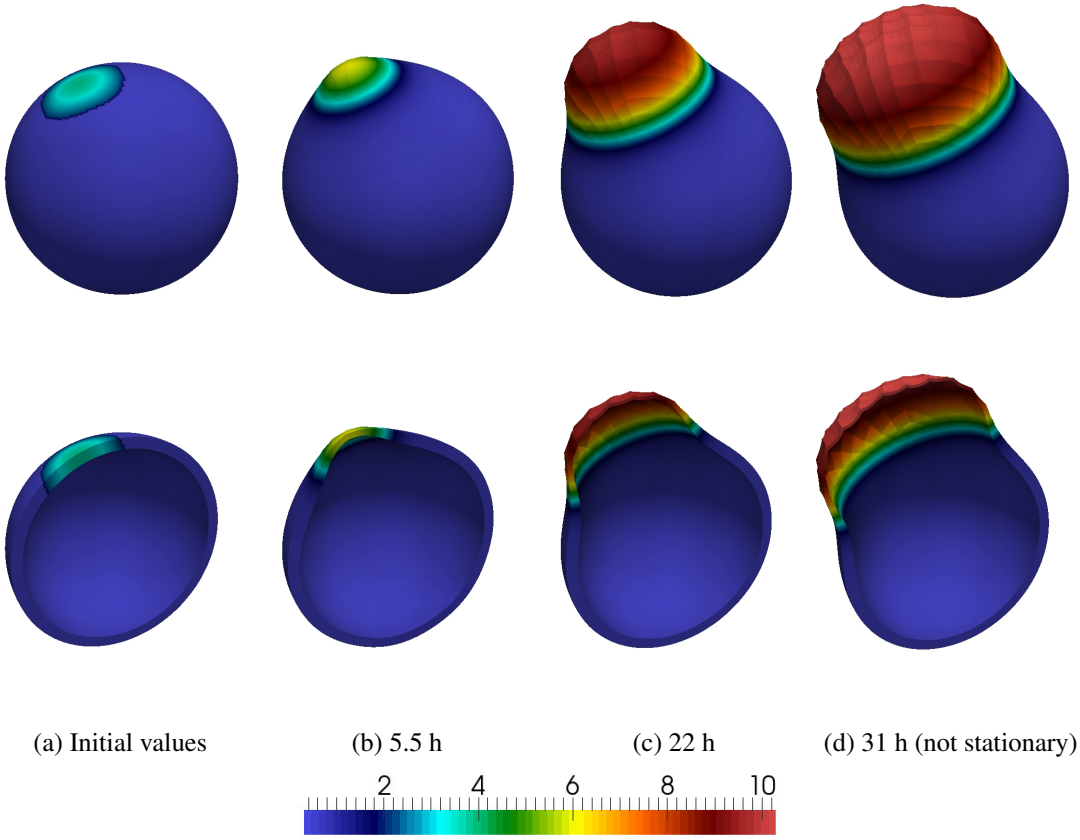

(a) Initial values (b) 5.5 h (c) 22 h (d) 31 h (not stationary)

Figure 5.23: Simulation snapshots that show spontaneous pattern formation in *Hydra* aggregates for the strain-mediated feedback loop including apico-basal shortening. As initial conditions, a morphogen gradient in a single spot was prescribed. The tissue sphere has been sliced for the sole purpose of a better visualization.

In our experiments, we focus on *Hydra* aggregates and a strain-mediated feedback loop. Our numerical simulations show that considering the glass body of the pipette significantly changes the strain inside the tissue sphere compared to implementing a surface force only. In particular, we observe inwards deformations of the tissue sphere in a circle around the glass body due to the elastic material response. This deformation implies negative hydrostatic strain (i.e. $\mathrm{tr}(\mathbf{E}) < 0$) in an annulus around the tip of the pipette, see Fig. 5.24 (b). In comparison, a simple aspiration, i.e. neglecting the glass body, leads to a dominating spot of positive strain whereas hardly any negative strain was observed, see Fig. 5.24 (a).

Finally, we emphasize that the Robin condition modeling the glass body prevents any movement of the tissue into the pipette as well as any motion of the entire domain. However, a homogeneous displacement of the entire computational domain is observed if only the surface force is applied (again neglecting the glass body of the pipette). This result was anticipated, since the tissue sphere is not fixed in space if Dirichlet or Robin values are not prescribed (cf.

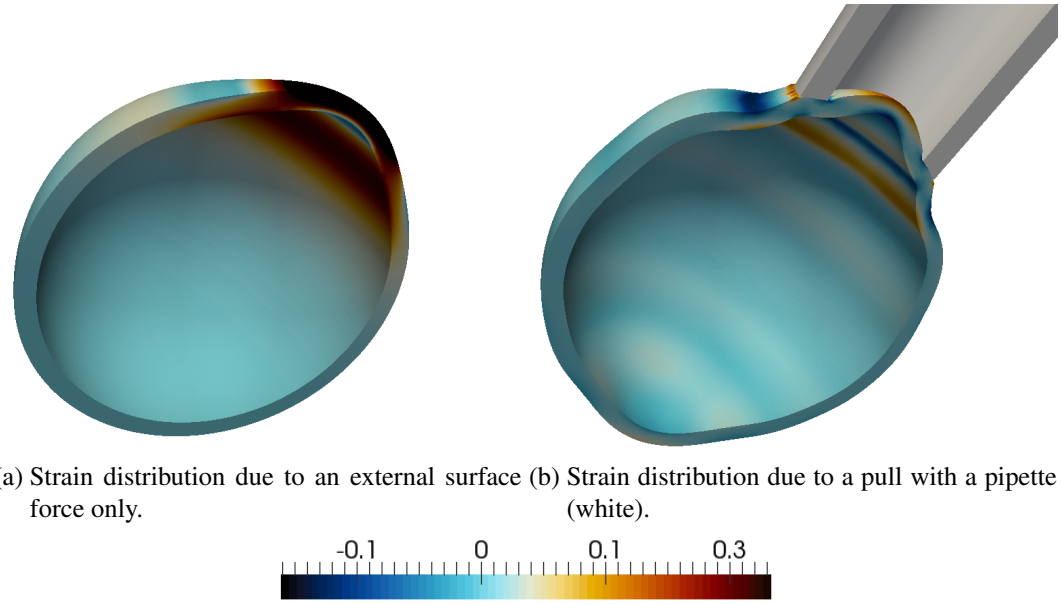

(a) Strain distribution due to an external surface force only.

(b) Strain distribution due to a pull with a pipette (white).

Figure 5.24: Simulation snapshot showing the strain caused by external surface forces. The tissue sphere has been sliced and a pipette has been added in (b) for the sole purpose of a better visualization.

Subsection 5.4.2). Dirichlet values are not an option since they significantly alter the numerical results. These findings further underline the importance of accounting for the glass body of the pipette by adequate boundary conditions.

Also, note that the pipette is solely modeled by surface integrals describing a surface force which leads to the aspiration and a Robin slip condition that allows the tissue to slip over the glass body of the pipette but prevents any movement into the glass itself (i.e. in normal direction). In particular, this implies that the visualized pipette is never part of the computational domain.

Simulation snapshot of our numerical experiments are presented in Fig. 5.25. In particular three different experimental setups regarding the mechanical feedback are proposed (cf. Subsection 5.4.3): Firstly, the coupling term is based on positive strain, secondly, on negative strain, and, finally, on the absolute value of all hydrostatic strain. Corresponding simulation results are depicted in the first, second and third row in Fig. 5.25, respectively. In all three experiments, we do not prescribe any initial conditions. Instead, our strain-mediated feedback loop is triggered by the micropipette aspiration itself. By assumption, the surface force modeling micropipette aspiration is applied for five minutes. Afterwards, the external forces and the Robin condition accounting for the glass body of the pipette are removed and free mechanochemical pattern formation is witnessed.

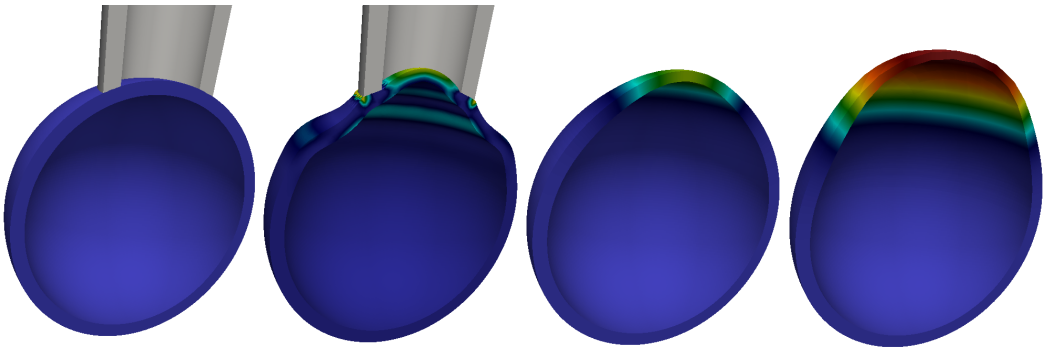

(A) Feedback loop based on positive strain

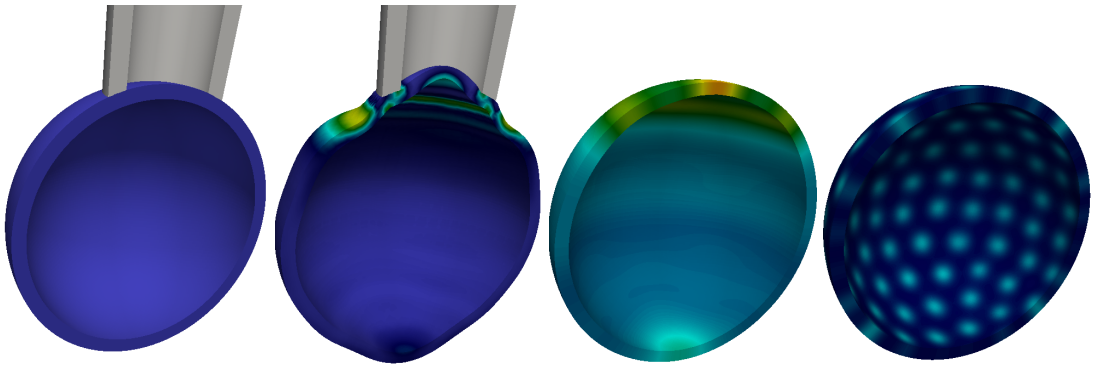

(B) Feedback loop based on negative strain

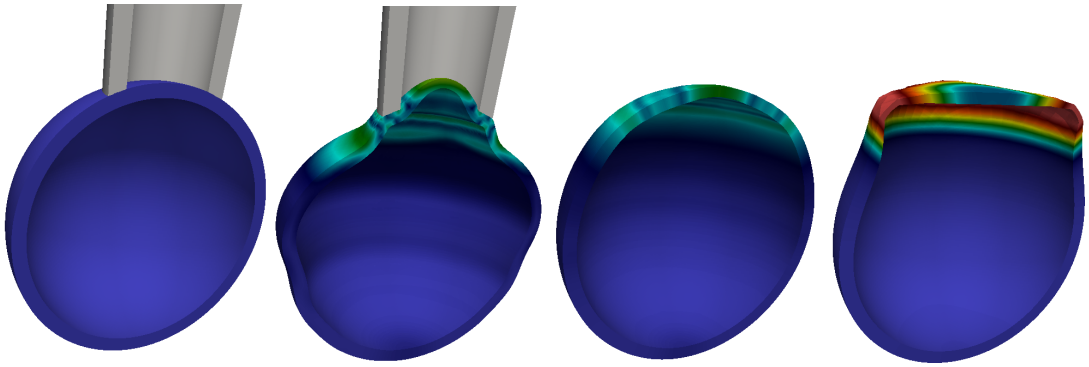

(a) Initial values (b) 5 min (c) 22 h (d) 31 h

(C) Feedback loop based on the absolute value of all hydrostatic strain

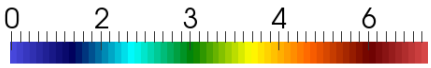

Morphogen concentration C

Figure 5.25: Simulation snapshots showing pattern formation during numerical experiments for the strain-mediated feedback loop with apico-basal shortening. The tissue sphere is sliced and a pipette is added for the sole purpose of a better visualization.

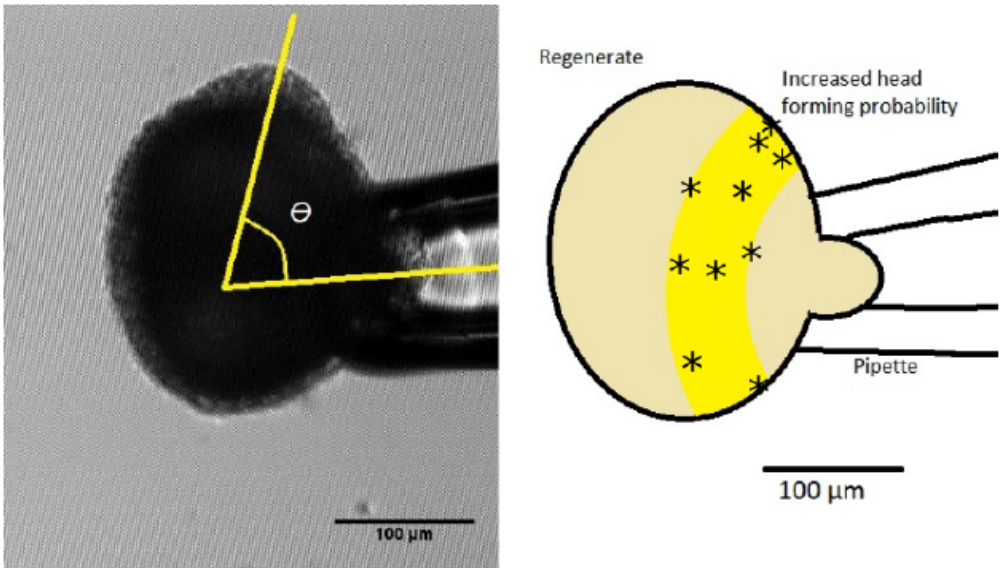

Figure 5.26: Left: Hydra aggregate during micropipette aspiration immediately after healing. The head forms at the angle θ seen from the center of the pipette. Right: Schematic representation of the *Hydra* and area of head formation (yellow). Head orientations in the experiments are marked with asterisks. Taken with permission from [133].

Regarding our feedback loop based on positive strain, we observe that morphogen is mainly produced in a single spot where the tissue is aspired into the pipette. Once the tissue is released, we obtain a single patch of co-localized morphogen and deformation, which becomes the center of head formation (cf. Fig. 5.25 (A)). This result corresponds well to our previous observation that positive strain is mainly produced inside the aspired tissue (cf. Fig. 5.24 (b)).

Next, in our feedback loop based on negative strain, we see that morphogen is primarily produced in a circular area around the (virtual) glass body of the micropipette as shown by the simulation snapshots in Fig. 5.25 (B) (after 5min). Based on our feedback, morphogen was expressed where the tissue experienced negative strain due to micropipette aspiration (cf. again Fig. 5.24 (b)). Here, we see a clear agreement of our numerical results to the micropipette experiments by Heike Sander [133]. Her experiments on mechanical stimuli induced by micropipette aspiration clearly show that head formation only occurs in a circular area around the pipette, see Fig. 5.26. In general, we might hence not only observe an increased head formation probability around the pipette but also morphogen production in these areas. Together, these findings might indeed inspire a close interplay of biological and numerical experiments for further investigations.

Interestingly, we see the formation of many but small co-localized morphogen and deformation patches, once the tissue is released by the micropipette (cf. Fig. 5.25 (B)). Similar results were observed in our application to embryogenesis, where larger morphogen production and diffusion rates lead to larger patterns as investigated and discussed for Fig. 5.9.

As an alternative, we propose a combination of the absolute value of negative and positive strains. Simulation snapshot regarding these results are shown in Fig. 5.24 (C). Again, a large circular pattern dominates and is preserved, once the micropipette is released. Here, a perturbation by prescribing an initial morphogen distribution might lead to a dominance of a single head in the area of increased head formation probability around the pipette, as ongoing numerical simulations indicate. Further, experiments show that *Hydra* aggregates are sensitive with regard to gravity and light, although the latter can be excluded by the experimental setup [133]. Hence, we might alternatively introduce an asymmetry by considering gravity which might lead to a single evolving head.

Finally, we conclude that our approach is flexible and well suited for modeling a broad range of predictive numerical experiments. Besides, our numerical results agree well with experimental observations and might inspire further cross-validation in the field of developmental biology. Alternatively, locally and ectopically over-expressing morphogen results in a local morphogen spot that in turn triggers our mechanochemical feedback loop (cf. our publication [103]).

6 Conclusion

In this thesis, we develop an efficient numerical method to robustly solve strongly coupled mechanochemical long-term problems that model pattern formation in biological tissues. More precisely, we consider embryogenesis, head formation in *Hydra* aggregates and growth pulsations in hydroids.

Firstly, we present a novel computational approach in 3D to model self-organized mechanochemical pattern formation in biological tissue. Based on recent experimental observations, we propose a flexible simulation framework and show how novel, simple mechanochemical feedback loops robustly lead to spontaneous pattern formation. The core of these mechanochemical interactions is the novel coupling of mechanical feedback via tensor invariants describing strain, stress and stretch on the morphogen dynamics. In turn, local morphogen concentrations lead to piecewise-defined, active deformations of individual biological cells. Hence, we blend a discrete description of active deformations while we benefit from continuous processes such as the elastic tissue description or inter-cellular diffusion. The strength of our approach lies in its flexibility. Namely, we apply our approach to various model organisms for different combinations of mechanical feedback and active deformations such as stretch and stress with apical/basal constriction (wedging) or strain apico-basal shortening (thinning) of biological cells. In particular, we contribute to the scientific understanding of gastrulation during embryogenesis, head formation during growth oscillations of *Hydra* aggregates or growth processes in the tips of colonial hydroids. We demonstrate that considering the full 3D representation of the tissue geometry is crucial to observe realistic mechanochemical tissue development, such as gastrulation events.

Secondly, numerical results in this thesis underline the crucial role of mechanics during pattern formation. A centerpiece of this thesis are our predictive numerical experiments where we study the sensitivity of biological tissue with respect to mechanical stimuli induced by micropipette aspiration. In particular, we highlight the importance of modeling the glass-body of the pipette by a Robin boundary condition: Then, negative mechanical strain results in a characteristic annulus around the pipette, which triggers our mechanochemical feedback loops and subsequent head formation in this area - analog to the experimental observations by Heike Sander [133]. Together, numerical and biological experiments advocate the strong interconnection between tissue mechanics and morphogen dynamics and might inspire future research. Besides, we demonstrate that merely studying the active deformations provides valuable insights into the processes involved in tissue morphogenesis, e.g. we compare active rotations and shearing during growth processes in tips of colonial hydroids to original experimental data shared by our colleague Igor Kosevich [81].

Thirdly, we developed efficient numerical solution techniques to handle the large, coupled systems of PDEs. Considering the full 3D geometry significantly increases the problem size compared to a 2D simplification and the strong coupling requires a monolithic solution approach with a parallel multigrid solver. We confirm the efficiency of our approach in a thorough numerical convergence analysis where we show quadratic and cubic convergence rates for linear (Q_1) and quadratic (Q_2) finite elements, respectively. Further, we present an adaptive mesh refinement strategy which significantly improves convergence in space by locally resolving mechanical feedback based on the growth-dependent and discontinuous Piola-Kirchhoff stress.

Regarding the parallel solution technique we show an impressive speedup by a factor 12 when the algebraic systems are solved in parallel on 14 CPU cores compared to the sequential multigrid method. It is crucial to employ a parallel multigrid solver for reducing the computation time necessary, as the bottleneck of our approach are the many time-steps necessary to attain a stationary solution. Here, we further propose a stabilization of the structural equation to mitigate numerical instabilities arising from the different timescales of tissue growth (days) and elasticity (seconds) while performing reasonably large time-steps. Here, we demonstrate that the introduced stabilization error is at least one scale below the dominating spatial discretization error.

Lastly, we contribute in various aspects to the finite element (FE) library GASCOIGNE3D [9] by implementing new features, most importantly the model itself. The implementation is based on template classes to dynamically switch between testing new ideas and models in 2D on the one hand and simulating pattern formation on the whole 3D geometry on the other. Further, we modify the parallelization process to track biological cells and propose a domain decomposition approach for distributing the finite element mesh. In the modified domain decomposition, we exploit the structure of the computational domain in the application to growth processes in colonial hydroids. Finally, we develop an adaptive mesh refinement strategy as well as finite element discretizations for spheres, cylinders and spheroids. Additional numerical techniques are required in the prescription of an internal pressure, which accounts for the fluid contained inside the blastula sphere and is crucial to ensure stationary solutions during gastrulation events. Also, we integrate the mechanical feedback over individual biological cells in an enhanced model. This novel approach is more accurate on a cellular level and provides valuable insights into the formation of mechanochemical patterns during gastrulation.

Outlook

In this thesis, we stress the importance of modeling mechanochemical interactions based on mechanical feedback being expressed by tensor invariants to observe realistic tissue development. A key strength of our approach are predictive numerical experiments by micropipette aspiration to assess the sensitivity of (*Hydra*) tissue to mechanical strain. Also, we compare different active deformation tensors prescribing growth in hydroid tips. With both numerical experiments, we hope to inspire new experiments and cross-validation with our results. In particular, these comparisons are enabled by new experimental insights elucidating the role of mechanochemistry in tissue development [37, 71, 95] and experimental techniques of visualization of mechanical

loads in biological tissues [76, 116, 131]. Hence, our approach may serve as a future basis to intensify the discussion between researchers from developmental biology and the numerics community to unravel one of the big mysteries in development together: the self-organized generation of patterns and shapes.

List of Abbreviations and Symbols

$(\cdot, \cdot)$	Scalar product of the space $L^2(\Omega)$ or $L^2(\Omega)^d$ for dimensions $d = 2, 3$
2D	Two dimensional
3D	Three dimensional
$\mathbf{a}$	A unit vector in $\mathbb{R}^d$, $d = 2, 3$
$\mathbf{A}$	A general, second-order tensor
α_0	Small constant in the Robin boundary conditions of our predictive numerical experiments
$c(\mathbf{x}, t)$	Concentration of signaling molecules (morphogens) given in Eulerian coordinates $\mathbf{x}$
$C(\mathbf{X}, t)$	Concentration of signaling molecules (morphogens) given in Lagrangian coordinates $\mathbf{X}$
$\mathbf{C}$	Symmetric and positive definite *right Cauchy-Green strain tensor* $\mathbf{C} \coloneqq \mathbf{F}^T\mathbf{F}$.
cf.	- from Latin: confer, "compare"
χ	*Deformation* (motion) of the particle $\mathbf{X}$ in the reference configuration Ω to the point $\mathbf{x}$ in the deformed domain $\Omega(t)$, i.e. $\mathbf{x} = \chi(\mathbf{X}, t)$
d	Number of dimensions, exclusively $d = 2, 3$
$\mathbf{D}(\mathbf{x})$	Diffusion coefficient matrix in $\mathbb{R}^{d\times d}$, $d = 2, 3$
$\mathrm{diag}(a_0, \cdots, a_n)$	Diagonal matrix with the entries $a_0, \cdots, a_n$ on the diagonal and zero entries elsewhere
E	Young's modulus, a constant with $E > 0$ and a measure for the stiffness of a solid material
$\mathbf{E}$	The *Green-Lagrange strain tensor* $\mathbf{E} \coloneqq \frac{1}{2}(\mathbf{C} - \mathbf{I}) = \frac{1}{2}(\mathbf{F}^T\mathbf{F} - \mathbf{I})$
$\mathbf{E}_e$	*Elastic* Green-Lagrange strain tensor based on the elastic tissue response $\mathbf{F}_e$ to active deformations with $\mathbf{E}_e \coloneqq \frac{1}{2}(\mathbf{F}_e^T\mathbf{F}_e - \mathbf{I})$
ECT	Ectodermal cell layer in the body of a colonial hydroid

END	Endodermal cell layer in the body of a colonial hydroid
ϵ	Scaling parameter $\epsilon > 0$ for the strength of the stabilization
$\boldsymbol{\epsilon}$	Linearized Green-Lagrange strain tensor $\boldsymbol{\epsilon} = \frac{1}{2}\left(\nabla \mathbf{u} + \nabla \mathbf{u}^T\right)$
$\mathbf{f}$	External volume forces in $\mathbb{R}^d$, $d = 2, 3$
$\mathbf{F}$	The *deformation gradient* with $\mathbf{F}(\mathbf{X}, t) := \nabla \boldsymbol{\chi}(\mathbf{X}, t) = \nabla \mathbf{u}(\mathbf{x}, t) + \mathbf{I}$ and the *multiplicative decomposition* $\mathbf{F} = \mathbf{F}_e \mathbf{F}_a$
$\mathbf{F}_a$	Active part of the decomposed deformation gradient $\mathbf{F}$ with $\mathbf{F}_a \colon \Omega \to \Omega_a(t)$
$\mathbf{F}_e$	Elastic part of the deformation gradient with $\mathbf{F}_e \colon \Omega_a(t) \to \Omega(t)$ and response to the active deformation $\mathbf{F}_a$
FEM	Finite element method
$\mathbf{g}$	External surface force acting on $\partial\Omega(t) \subset \mathbb{R}^3$
$\mathbf{G}$	External surface force in the reference configuration acting on $\partial\Omega \subset \mathbb{R}^3$
$\boldsymbol{\Gamma}$	A part of the boundary of a domain, i.e. $\Gamma \subset \partial\Omega$
h	Discretization parameter $h > 0$ which stems from the definition of the finite element subspace $V_h \subset V$
$H^1(\Omega)$	Sobolev space of square integrable functions $\mathbf{u} \in L^2(\Omega)$ with generalized first derivatives $\nabla \mathbf{u} \in L^2(\Omega)^d$ for $d = 2, 3$.
$\mathbf{I}$	Identity matrix in $\mathbb{R}^{d \times d}$, $d = 2, 3$
J	Determinant of the deformation gradient $J(\mathbf{X}, t) := \det(\mathbf{F}(\mathbf{X}, t))$
k	Scaling parameter which determines the strength of the coupling of signaling molecules (morphogen) on active deformations
k_1	Scaling parameter $k_1 > 0$ for the degradation rate of the concentration of signaling molecules (morphogens)
k_2	Scaling parameter $k_2 > 0$ for changing the maximal production rate of signaling molecules (morphogens)
k_m	Michaelis constant with $k_m > 0$
k_p	Scaling parameter $k_p > 0$ for the intensity of an internal pressure modeling the fluid inside the tissue sphere
K_i	Biological cell with index i
$L^2(\Omega)$	Lebesgue space of on Ω measurable square integrable functions

λ	First Lamé parameter which is essential in Hooke's material law
$\mathbf{m}_{K_i}$	Midpoint, i.e. centroid or origin, of the biological cell K_i in $\mathbb{R}^d$, $d = 2, 3$
μ	Second Lamé parameter $\mu > 0$ called *shear modulus* which is essential in Hooke's material law
$\mathbf{n}$	Eulerian outward unit normal in $\mathbb{R}^d$, $d = 2, 3$
$\mathbf{N}$	Lagrangian outward unit normal in $\mathbb{R}^d$, $d = 2, 3$
∇	The Nabla operator with $\nabla = \sum_{i=1}^{d} \mathbf{e}_i \frac{\partial}{\partial X_i}$, $\nabla f = \text{grad}(f)$ and $\nabla \cdot \mathbf{f} = \text{div}(\mathbf{f})$ for scalar and vector-valued differentiable functions f and $\mathbf{f}$
NI	Quotient of maximal and minimal number of cells in a subdomain during parallelization
ν	Poisson's ratio, a constant with $\nu > 0$ and a material property which defines the ratio of the transverse to the axial strain of a solid
Ω	Bounded reference domain, also denoted by *Lagrangian configuration*
$\Omega_a(t)$	An intermediate stress-free configuration that results from an active deformation. It is in general discontinuous, i.e. not a domain
$\Omega(t)$	Bounded Eulerian domain and the deformed configuration at time t
P	Short for *Perisarc* that is an organic skeleton made of chitin and the outer layer of tips in colonial hydroid
$\mathbf{P}$	The *first Piola-Kirchhoff stress tensor*, defined such that $\mathbf{PN}$ is the force in the current configuration per unit area in the reference configuration, related to the Cauchy stress tensor by $\mathbf{P} = J\boldsymbol{\sigma}\mathbf{F}^{-T}$
phase D	Phase of re-extension to the length of the previous peak during growth pulsations in colonial hydroids
$\partial\Omega$	Boundary of the reference domain Ω
$\boldsymbol{\varphi}$	Test function in $H^1(\Omega(t))$ defined in the Eulerian domain $\Omega(t) \subset \mathbb{R}^d$, $d = 2, 3$
$\boldsymbol{\Phi}$	Test function in $H^1(\Omega)$ defined in the Lagrangian domain $\Omega \subset \mathbb{R}^d$, $d = 2, 3$
PDE	Partial differential equation
$\mathbf{Q}$	Rotation matrix in $\mathbb{R}^{d\times d}$, $d = 2, 3$, with $\mathbf{Q}^T\mathbf{Q} = \mathbf{Q}\mathbf{Q}^T = \mathbf{I}$ and $\det(\mathbf{Q}) = 1$
Q_1-FE	Bilinear finite elements on quadrilaterals or hexahedra
Q_2-FE	Biquadratic finite elements on quadrilaterals or hexahedra

$\mathbf{r}(\mathbf{u}, \nabla\mathbf{u}, \mathbf{N})$	Robin boundary condition on $\partial\Omega$
R_0	Outer radius of the ectodermal tube in the growing tips of colonial hydroids
$R_i(I_j, C_i)$	Coupling term of the mechanical tensor invariants I_j on the concentration of signaling molecules (morphogens) C_i in the reaction-diffusion equation
$\mathbf{R}$	Orthogonal tensor in Cauchy's polar decompositions $\mathbf{F} = \mathbf{RU} = \mathbf{VR}$ of the deformation gradient $\mathbf{F}$
$\rho(\mathbf{x}, t)$	Mass distribution in the current Eulerian configuration
$\rho^0(\mathbf{X})$	Initial mass distribution in the Lagrangian configuration
$\boldsymbol{\sigma}$	Symmetric *Cauchy stress tensor*, defined such that $\boldsymbol{\sigma}\mathbf{n}$ is the force in the current configuration per unit area (also in the current configuration) with normal $\mathbf{n}$
$\boldsymbol{\Sigma}$	*Second Piola-Kirchhoff stress tensor* to express the stress in the reference configuration; related to the first Piola-Kirchhoff stress tensor and the Cauchy stress tensor by $\boldsymbol{\Sigma} = \mathbf{F}^{-1}\mathbf{P} = J\mathbf{F}^{-1}\boldsymbol{\sigma}\mathbf{F}^{-T}$
$\boldsymbol{\Sigma}_e$	*Elastic* second Piola-Kirchhoff stress tensor to express the stress in the intermediate configuration with $\boldsymbol{\Sigma} = J_a\mathbf{F}_a^{-1}\boldsymbol{\Sigma}_e\mathbf{F}_a^{-T}$
$\mathrm{span}(S)$	Linear span or linear hull of a set S
$\mathbf{t}(\mathbf{x}, t, \mathbf{n})$	The *surface stress density* or *Cauchy traction field* in direction $\mathbf{n}$ of the current configuration $\Omega(t)$
t	Parameter for the time measured in seconds, hours or days
T_{next}	time needed for the propagating deformation to affect one biological cell during growth processes in hydroid tips.
$\mathbf{T}(\mathbf{X}, t, \mathbf{N})$	*Surface stress density* or *first Piola-Kirchhoff traction field* in direction $\mathbf{N}$ of the reference configuration Ω
$\mathbf{T}$	Lagrangian unit vector tangential to the tissue sphere in the reference configuration $\Omega \subset \mathbb{R}^d$, $d = 2, 3$ which is orthogonal to the normal (or radial) direction $\mathbf{N}$
$\boldsymbol{\tau}$	Eulerian unit vector tangential to the deformed tissue sphere $\Omega(t) \subset \mathbb{R}^d$, $d = 2, 3$; orthogonal to the normal (or radial) direction $\mathbf{n}$
$THRES$	Threshold for the expression of morphogen due to mechanical feedback.
$\mathrm{tr}(\mathbf{A})$	Trace of a matrix $\mathbf{A}$, which is the sum over the elements a_{ii} for $i = 1, \cdots, n$ on the main diagonal i.e. $\mathrm{tr}(A) = \sum_{i=1}^{n} a_{ii}$

$\mathbf{u}(\mathbf{x}, t)$	*Displacement* field in Eulerian coordinates $\mathbf{x}$ defined as $\mathbf{u}(\mathbf{x}, t) = \mathbf{x} - \mathbf{X}(\mathbf{x}, t)$
$\mathbf{U}(\mathbf{X}, t)$	*Displacement* field in Lagrangian coordinates $\mathbf{X}$ with $\mathbf{u}(\mathbf{x}, t) = \mathbf{U}(\mathbf{X}, t)$
$\mathbf{U}, \mathbf{V}$	Unique, positive and symmetric tensors in Cauchy's polar decompositions $\mathbf{F} = \mathbf{RU} = \mathbf{VR}$ of the deformation gradient $\mathbf{F}$
$\mathbf{v}(\mathbf{x}, t)$	Velocity field in Eulerian coordinates defined as $\mathbf{v}(\mathbf{x}, t) \coloneqq \partial_t \boldsymbol{\chi}(\mathbf{X}, t) = \partial_t \mathbf{u}(\mathbf{x}, t)$
$\mathbf{V}(\mathbf{X}, t)$	Velocity field in Lagrangian coordinates $\mathbf{X}$ with $\mathbf{V}(\mathbf{X}, t) = \mathbf{v}(\mathbf{x}, t)$
V	Infinite-dimensional separable Hilbert space of ansatz- and test-functions with $V = H^1(\Omega)$ in general
V_h	Finite dimensional subspace $V_h \subset V$ obtained by a finite element discretization with bilinear or biquadratic finite elements
$\mathbf{x}$	Eulerian coordinates in the current deformed domain $\Omega(t) \subset \mathbb{R}^d$, $d = 2, 3$
$\mathbf{X}$	Lagrangian coordinates in the reference domain $\Omega \subset \mathbb{R}^d$, $d = 2, 3$
$\mathbf{y}$	Eulerian coordinates in the current deformed domain $\Omega(t) \subset \mathbb{R}^d$, $d = 2, 3$
$\mathbf{Y}$	Lagrangian coordinates in the reference domain $\Omega \subset \mathbb{R}^d$, $d = 2, 3$

Acknowledgments

Firstly, I thank my supervisor Prof. Dr. Thomas Richter for this interesting and challenging PhD topic and his continued support throughout my doctoral research project. You always have an open door/ear for me and you always have good advice on small and large mathematical or computational problems. Secondly, I express my gratitude to my co-supervisor Prof. Dr. Anna Marciniak-Czochra for our fruitful discussions and your constant support and advice. In addition, I thank Prof. Dr. Dr. h.c. Rannacher for his scientific support, the funding of my position for more than two years and the opportunity to assist in four of your lectures and in many of your seminars.

I want to express special thanks Dr. Moritz Mercker for conceiving the idea that lead to this thesis and for your advice and support throughout this project. You help in so many aspects, from the biological background over modeling questions and critical feedback to proofreading. This work would not be the same without your constant support.

I thank the Numerical Analysis Group by Prof. Dr. Dr. h.c. Rannacher Rannacher and the Numerical Optimization Group by Prof. Dr. Ekaterina A. Kostina for the great working atmosphere, the many "open doors" and all the fruitful conversations over the years.

In particular, I would like to thank my colleagues and fellow PhD Students, first of all Sven Wetterauer, Dr. Stefan Frei and Simon Dörsam. You are always a valuable source of advice and I enjoyed all our scientific or private discussions. In particular, I thank Sven Wetterauer for the proof reading of this thesis. Also, I thank Dr. Thomas Carraro, Alexander Drobny, Dr. Elfriede Friedmann, Dr. Michael Geiger, Dr. Daniel Gerecht, Dr. Christian Goll, Dr. Matthias Klinger, Dr. Sara Lee, Dr. Matthias Maier, Vladislav Olkhovskiy, Victoria Ponce, Marta Sauter, Florian Sonner, Robert Scholz, Matthias Schlöder, Anna Seitz, Ina Schüssler, Judith Stein and Hilke Stibbe for the great atmosphere and all the interesting discussions we had in our working group.

Finally, I am very grateful or the support by Dr. Igor Kosevich who kindly provided experimental data of growth pulsations in hydroids that verified my numerical simulations. Also, I express my gratitude to Heike Sander for the fruitful discussions and the image on micropipette aspiration of *Hydra* aggregates.

I gratefully acknowledge the financial support for traveling to conferences and the many other opportunities offered by the Heidelberg Graduate School of Mathematical and Computational Methods for the Sciences (HGS). Besides, I thank the Numerical Analysis Group, the Institute of Applied Mathematics and the Faculty of Mathematics and Computer Science, where I could write this thesis. Finally, I wand to express my gratitude to all the developers of the finite element library Gascoigne3D [9] for their great work which was the foundation of all my numerical simulations.

Ich danke meiner Familie und meinen Freunden, insbesondere Stephie, Liam und Nala für ihre Unterstützung während meiner Promotion und auch für ihr Verständnis in mancher Stunde der Frustration. Ihr seid die beste Familie, die ich mir wünschen kann!

Bibliography

[1] R. Allena, J. J. Muñoz, and D. Aubry. "Diffusion-reaction model for Drosophila embryo development." eng. In: *Comput Methods Biomech Biomed Engin* 16.3 (2013), pp. 235–248. URL: https://doi.org/10.1080/10255842.2011.616944 (cit. on pp. 24, 38, 39, 48, 98, 105, 108, 134, 137).

[2] Hans Wilhelm Alt. *Lineare Funktionalanalysis*. Springer-Verlag Berlin Heidelberg, 1999. URL: https://doi.org/10.1007/978-3-642-22261-0 (cit. on pp. 21, 58).

[3] Silvanus Alt, Poulami Ganguly, and Guillaume Salbreux. "Vertex models: from cell mechanics to tissue morphogenesis". In: *Phil. Trans. R. Soc. B* 372.1720 (2017), p. 20150520. URL: https://doi.org/10.1098/rstb.2015.0520 (cit. on p. 86).

[4] D. Ambrosi and F. Mollica. "On the mechanics of a growing tumor". In: *International Journal of Engineering Science* 40.12 (Mar. 2002), pp. 1297–1316. URL: https://doi.org/10.1016/S0020-7225(02)00014-9 (cit. on pp. 26, 35).

[5] Brendon M Baker and Christopher S Chen. "Deconstructing the third dimension–how 3D culture microenvironments alter cellular cues". In: *J Cell Sci* 125.13 (2012), pp. 3015–3024. URL: https://doi.org/10.1242/jcs.079509 (cit. on pp. 86, 89).

[6] Philip Ball. "Hits, Misses and Close Calls: An Image Essay on Pattern Formation in On Growth and Form". In: *Interdisciplinary Science Reviews* 38.1 (2013), pp. 74–88. URL: https://doi.org/10.1179/0308018813Z.00000000036 (cit. on pp. 87, 88).

[7] Peter Bastian. *Parallel adaptive multigrid methods*. Universität Heidelberg. Interdisziplinäres Zentrum für Wissenschaftliches Rechnen (IWR), 1993 (cit. on p. 78).

[8] Kirill Batmanov, Celine Kuttler, Cédric Lhoussaine, and Yasushi Saka. "Self-organized patterning by diffusible factors: roles of a community effect". In: *Fundamenta Informaticae* 118.4 (2012), pp. 419–461. ISSN: 0169-2968. URL: https://doi.org/10.3233/FI-2012-723 (cit. on p. 111).

[9] R. Becker, M. Braack, T. Dunne, D. Meidner, T. Richter, and B. Vexler. "Gascoigne 3D-a finite element toolbox". 2017. URL: https://www.uni-kiel.de/gascoigne/ (cit. on pp. 11, 14, 71, 75, 77, 78, 85, 89, 146, 155).

[10] L. V. Beloussov, L. A. Badenko, A. L. Katchurin, and L. F. Kurilo. "Cell movements in morphogenesis of hydroid polypes." In: *J Embryol Exp Morphol* 27.2 (Apr. 1972), pp. 317–337 (cit. on pp. 90, 92, 100).

[11] Lev V. Beloussov and Vassily I. Grabovsky. "Morphomechanics: goals, basic experiments and models." eng. In: *Int J Dev Biol* 50.2-3 (2006), pp. 81–92. URL: https://doi.org/10.1387/ijdb.052056lb (cit. on pp. 86, 111).

[12] Ilka B. Bischofs, Franziska Klein, Dirk Lehnert, Martin Bastmeyer, and Ulrich S. Schwarz. "Filamentous network mechanics and active contractility determine cell and tissue shape." eng. In: *Biophys J* 95.7 (Oct. 2008), pp. 3488–3496. URL: https://doi.org/10.1529/biophysj.108.134296 (cit. on pp. 48, 105, 134).

[13] Daria Bonazzi, Jean-Daniel Julien, Maryse Romao, Rima Seddiki, Matthieu Piel, Arezki Boudaoud, and Nicolas Minc. "Symmetry breaking in spore germination relies on an interplay between polar cap stability and spore wall mechanics." eng. In: *Dev Cell* 28.5 (Mar. 2014), pp. 534–546. URL: https://doi.org/10.1016/j.devcel.2014.01.023 (cit. on pp. 13, 40, 49, 88).

[14] Dietrich Braess. *Finite Elemente: Theorie, schnelle Löser und Anwendungen in der Elastizitätstheorie*. Springer, Berlin, Heidelberg, 2003. ISBN: 978-3-540-00122-5. URL: https://doi.org/10.1007/978-3-662-07232-5 (cit. on pp. 21, 62).

[15] James H. Bramble, Joseph E. Pasciak, and Jinchao Xu. "Parallel multilevel preconditioners". In: *Math. Comp.* (1990), pp. 1–22. ISSN: 1088-6842. URL: https://doi.org/10.1090/S0025-5718-1990-1023042-6 (cit. on p. 78).

[16] Achi Brandt. "MULTIGRID SOLVERS ON PARALLEL COMPUTERS". In: *Elliptic Problem Solvers*. Ed. by Martin H. Schultz. Academic Press, 1981, pp. 39–83. ISBN: 978-0-12-632620-8. URL: https://doi.org/10.1016/B978-0-12-632620-8.50008-5 (cit. on p. 78).

[17] Siobhan A. Braybrook and Alexis Peaucelle. "Mechano-chemical aspects of organ formation in Arabidopsis thaliana: the relationship between auxin and pectin." eng. In: *PLoS One* 8.3 (2013), e57813. URL: https://doi.org/10.1371/journal.pone.0057813 (cit. on pp. 48, 105, 110, 117, 134).

[18] Susanne Brenner and Ridgway Scott. *The Mathematical Theory of Finite Element Methods*. Springer-Verlag Berlin Heidelberg, 1994. URL: https://doi.org/10.1007/978-0-387-75934-0 (cit. on pp. 21, 61).

[19] S. C. van den Brink, P. Baillie-Johnson, T. Balayo, A.-K. Hadjantonakis, S. Nowotschin, D. A. Turner, and A. M. Arias. "Symmetry breaking, germ layer specification and axial organisation in aggregates of mouse embryonic stem cells". In: *Development* 141 (2014), pp. 4231–4242. URL: https://doi.org/10.1242/dev.113001 (cit. on pp. 86, 183).

[20] Felix Brinkmann, Moritz Mercker, Thomas Richter, and Anna Marciniak-Czochra. "Post-Turing tissue pattern formation: Advent of mechanochemistry". In: *PLoS Comput Biol* 14(7) (July 2018), e1006259. URL: https://doi.org/10.1371/journal.pcbi.1006259 (cit. on pp. 13–15, 41, 47, 49, 50, 53, 85, 88, 101, 105, 115, 134).

[21] J. Briscoe, P. A. Lawrence, and J.-P. Vincent, eds. *Generation and Interpretation of Morphogen Gradients*. Cold Spring Harbor Laboratory Press, 2010. ISBN: 978-0879698812 (cit. on p. 86).

[22] Regina Brockmann, Andreas Beyer, Jürgen J Heinisch, and Thomas Wilhelm. "Posttranscriptional expression regulation: what determines translation rates?" In: *PLoS computational biology* 3.3 (2007), e57. URL: https://doi.org/10.1371/journal.pcbi.0030057 (cit. on pp. 49, 50, 55).

[23] Mariya Broun, Lydia Gee, Beate Reinhardt, and Hans R. Bode. "Formation of the head organizer in hydra involves the canonical Wnt pathway." eng. In: *Development* 132.12 (June 2005), pp. 2907–2916. URL: https://doi.org/10.1242/dev.01848 (cit. on pp. 127, 138).

[24] Eric Brouzés and Emmanuel Farge. "Interplay of mechanical deformation and patterned gene expression in developing embryos." eng. In: *Curr Opin Genet Dev* 14 (2004), pp. 367–374. URL: https://doi.org/10.1016/j.gde.2004.06.005 (cit. on pp. 13, 40, 49, 88, 109).

[25] Yi-chao Chen and Anne Hoger. "Constitutive Functions of Elastic Materials in Finite Growth and Deformation". In: *Journal of elasticity and the physical science of solids* 59.1 (June 2000), pp. 175–193. ISSN: 1573-2681. URL: https://doi.org/10.1023/A:1011061400438 (cit. on p. 36).

[26] C. J. Chuong and Y. C. Fung. "Residual Stress in Arteries". In: *Frontiers in Biomechanics*. Ed. by G. W. Schmid-Schönbein, S. L-Y. Woo, and B. W. Zweifach. New York, NY: Springer New York, 1986, pp. 117–129. ISBN: 978-1-4612-4866-8. URL: https://doi.org/10.1007/978-1-4612-4866-8_9 (cit. on p. 34).

[27] P.G. Ciarlet. *Mathematical elasticity, Vol I: Three-Dimenstional Elasticity*. North Holland, Amsterdam, 1988. URL: https://doi.org/10.1002/zamm.19890691105 (cit. on pp. 14, 16, 24, 26, 49).

[28] P.G. Ciarlet. *The Finite Element Method for Elliptic Problems*. Society for Industrial and Applied Mathematics, 2002, pp. xxiii + 529. URL: https://doi.org/10.1137/1.9780898719208 (cit. on pp. 61, 62).

[29] Vito Conte, Jose J. Muñoz, and Mark Miodownik. "A 3D finite element model of ventral furrow invagination in the *Drosophila melanogaster* embryo." eng. In: *J Mech Behav Biomed Mater* 1 (2008), pp. 188–198. URL: https://doi.org/10.1016/j.jmbbm.2007.10.002 (cit. on pp. 13, 24, 26, 36–38, 107, 108, 118, 134).

[30] E. Cuthill and J. McKee. "Reducing the Bandwidth of Sparse Symmetric Matrices". In: *Proceedings of the 1969 24th National Conference*. ACM '69. New York, NY, USA: ACM, 1969, pp. 157–172. URL: https://doi.org/10.1145/800195.805928 (cit. on p. 78).

[31] Jamie A. Davies. *Mechanisms of Morphogenesis*. 2nd ed. Boston: Academic Press, Apr. 2013, p. 414. ISBN: 978-0-12-391062-2. URL: https://doi.org/10.1016/C2010-0-66323-1 (cit. on pp. 48, 107, 134).

[32] Andres Dekanty and Marco Milan. "The interplay between morphogens and tissue growth." eng. In: *EMBO Rep* 12.10 (Oct. 2011), pp. 1003–1010. URL: https://doi.org/10.1038/embor.2011.172 (cit. on pp. 48, 105, 134).

[33] Nicolas Desprat, Willy Supatto, Philippe-Alexandre Pouille, Emmanuel Beaurepaire, and Emmanuel Farge. "Tissue deformation modulates twist expression to determine anterior midgut differentiation in *Drosophila* embryos." eng. In: *Dev Cell* 15 (2008), pp. 470–477. URL: https://doi.org/10.1016/j.devcel.2008.07.009 (cit. on pp. 87, 127).

[34] Wolfgang Driever and Christiane Nüsslein-Volhard. "A gradient of bicoid protein in Drosophila embryos". In: *Cell* 54.1 (1988), pp. 83–93 (cit. on p. 86).

[35] J. Dumais. “Can mechanics control pattern formation in plants?” In: *Current Opinion in Plant Biology* 10 (1) (2007), pp. 58–62. URL: https://doi.org/10.1016/j.pbi.2006.11.014 (cit. on pp. 13, 40, 49, 88).

[36] Emmanuel Farge. “Mechanical induction of Twist in the Drosophila foregut/stomodeal primordium.” In: *Curr Biol* 13.16 (Aug. 2003), pp. 1365–1377. ISSN: 0960-9822. URL: https://doi.org/10.1016/S0960-9822(03)00576-1 (cit. on p. 24).

[37] Emmanuel Farge. “Mechanotransduction in development.” eng. In: *Curr Top Dev Biol* 95 (2011), pp. 243–265. URL: https://doi.org/10.1016/B978-0-12-385065-2.00008-6 (cit. on pp. 49, 88, 146).

[38] S. Frei, T. Richter, and T. Wick. “Long-term simulation of large deformation, mechano-chemical fluid-structure interactions in ALE and fully Eulerian coordinates”. In: *Journal of Computational Physics* 321 (2016), pp. 874–891. ISSN: 0021-9991. URL: https://doi.org/10.1016/j.jcp.2016.06.015 (cit. on pp. 39, 40).

[39] Y. C. Fung. *Foundations of Solid Mechanics*. English. Englewood Cliffs, N.J. : Prentice-Hall, 1965, p. 525. ISBN: 9780133299120 (cit. on p. 30).

[40] C. Fütterer, C. Colombo, F. Jülicher, and A. Ott. “Morphogenetic oscillations during symmetry breaking of regenerating *Hydra vulgaris* cells”. In: *Europhysics Letters* 64.1 (Oct. 2003), pp. 137–143. URL: https://doi.org/10.1209/epl/i2003-00148-y (cit. on p. 127).

[41] Giovanni P. Galdi and William J. Layton. “APPROXIMATION OF THE LARGER EDDIES IN FLUID MOTIONS II: A MODEL FOR SPACE-FILTERED FLOW”. In: *Mathematical Models and Methods in Applied Sciences* 10.3 (2000), pp. 343–350. URL: https://doi.org/10.1142/S0218202500000203 (cit. on p. 129).

[42] Brigitte Galliot. “Hydra, a fruitful model system for 270 years.” eng. In: *Int J Dev Biol* 56.6-8 (2012), pp. 411–423. URL: https://doi.org/10.1387/ijdb.120086bg (cit. on p. 126).

[43] Michael A. Gelbart, Bing He, Adam C. Martin, Stephan Y. Thiberge, Eric F. Wieschaus, and Matthias Kaschube. “Volume conservation principle involved in cell lengthening and nucleus movement during tissue morphogenesis”. In: *Proceedings of the National Academy of Sciences* 109.47 (2012), pp. 19298–19303. ISSN: 0027-8424. URL: http://www.pnas.org/content/109/47/19298 (cit. on p. 107).

[44] I. M. (Israel Moiseevich) Gelfand, Richard A Silverman, and S. V. (Sergei Vasilyevich) Fomin. *Calculus of variations*. English. Rev. English ed. / translated and edited by Richard A. Silverman. Includes index. Englewood Cliffs, N.J. : Prentice-Hall, 1963. ISBN: 978-0486414485 (cit. on pp. 22, 42).

[45] A. Gierer, S. Berking, H. Bode, C.N. David, K. Flick, G. Hansmann, H. Schaller, and E. Trenkner. “Regeneration of Hydra from reaggregated cells”. In: *Nature New Biology* 239: 91 (1972), pp. 98–101. URL: https://doi.org/10.1038/newbio239098a0 (cit. on pp. 86, 126, 127, 138, 183).

[46] A. Gierer and H. Meinhardt. “A theory of biological pattern formation.” eng. In: *Kybernetik* 12.1 (Dec. 1972), pp. 30–39. URL: https://doi.org/10.1007/BF00289234 (cit. on p. 87).

[47] S.F. Gilbert. *Developmental Biology*. Palgrave Macmillan, 2013. ISBN: 978-1605351735 (cit. on pp. 86, 101, 111).

[48] M. D. Gilchrist, Murphy J.G., W. Parnell, and B. Pierrat. "Modelling the slight compressibility of anisotropic soft tissue". In: *International Journal of Solids and Structures* 51: 23-24 (Nov. 2014), pp. 3857–3865. URL: https://doi.org/10.1016/j.ijsolstr.2014.06.018 (cit. on p. 24).

[49] Donatella Giuliani. "Gaussian curvature: A growth parameter for biological structures". In: *Mathematical and computer modelling* 42.11-12 (2005), pp. 1375–1384. URL: https://doi.org/10.1016/j.mcm.2004.05.015 (cit. on pp. 86, 89).

[50] Ananth Grama, Anshul Gupta, George Karypis, and Vipin Kumar. *Introduction to Parallel Computing, Second Edition*. Addison Wesley, Jan. 2003, p. 856. ISBN: 0-201-64865-2 (cit. on p. 79).

[51] Thomas Gregor, Eric F Wieschaus, Alistair P McGregor, William Bialek, and David W Tank. "Stability and nuclear dynamics of the bicoid morphogen gradient." eng. In: *Cell* 130 (2007), pp. 141–152. URL: https://doi.org/10.1016/j.cell.2007.05.026 (cit. on pp. 55, 123).

[52] Linda G Griffith and Melody A Swartz. "Capturing complex 3D tissue physiology in vitro". In: *Nature reviews Molecular cell biology* 7.3 (2006), p. 211. URL: https://doi.org/10.1038/nrm1858 (cit. on pp. 86, 89).

[53] C.J.P. Grimmelikhuijzen and H.C. Schaller. "Hydra as a model organism for the study of morphogenesis". In: *Trends in Biochemical Sciences* 4.12 (1979), pp. 265–267. ISSN: 0968-0004. URL: https://doi.org/10.1016/0968-0004(79)90296-2 (cit. on p. 126).

[54] William Grossman. "Cardiac hypertrophy: Useful adaptation or pathologic process?" In: *The American Journal of Medicine* 69.4 (1980), pp. 576–584. ISSN: 0002-9343. URL: https://doi.org/10.1016/0002-9343(80)90471-4 (cit. on p. 35).

[55] Jun Guo, Frederick Sachs, and Fanjie Meng. "Fluorescence-based force/tension sensors: a novel tool to visualize mechanical forces in structural proteins in live cells." In: *Antioxidants & redox signaling* 20 (6 Feb. 2014), pp. 986–999. ISSN: 1557-7716. URL: https://doi.org/10.1089/ars.2013.5708 (cit. on pp. 12, 89, 117).

[56] Morton E. Gurtin. "The Linear Theory of Elasticity". In: *Linear Theories of Elasticity and Thermoelasticity: Linear and Nonlinear Theories of Rods, Plates, and Shells*. Ed. by C. Truesdell. Berlin, Heidelberg: Springer Berlin Heidelberg, 1973, pp. 1–295. ISBN: 978-3-662-39776-3. URL: https://doi.org/10.1007/978-3-662-39776-3_1 (cit. on p. 30).

[57] Wolfgang Hackbusch. *Multi-Grid Methods and Applications*. Springer, 1985. ISBN: 978-3-642-05722-9. URL: https://doi.org/10.1007/978-3-662-02427-0 (cit. on pp. 11, 75, 77).

[58] F. M. Harold. "From morphogens to morphogenesis." eng. In: *Microbiology* 141 (1995), pp. 2765–2778. URL: https://doi.org/10.1099/13500872-141-11-2765 (cit. on pp. 48, 105, 134).

[59] S. Härting and A. Marciniak-Czochra. "Spike patterns in a reaction-diffusion-ODE model with Turing instability". In: *Math. Methods Appl. Sciences* 37 (2013), pp. 1377–1391. URL: https://doi.org/10.1002/mma.2899 (cit. on p. 87).

[60] Steffen Härting, Anna Marciniak-Czochra, and Izumi Takagi. "Stable patterns with jump discontinuity in systems with Turing instability and hysteresis". In: *Disc. Cont. Dyn. Syst. A* 37 (2016), pp. 757–800. URL: https://doi.org/10.3934/dcds.2017032 (cit. on p. 87).

[61] W. Helfrich. "Elastic properties of lipid bilayers: theory and possible experiments." In: *Z Naturforsch [C]* 28 (Dec. 1973), pp. 693–703. URL: https://doi.org/10.1515/znc-1973-11-1209 (cit. on p. 40).

[62] J.H Henderson and D.R Carter. "Mechanical induction in limb morphogenesis: the role of growth-generated strains and pressures". In: *Bone* 31.6 (2002), pp. 645–653. ISSN: 8756-3282. URL: https://doi.org/10.1016/S8756-3282(02)00911-0 (cit. on pp. 127, 138).

[63] G. Himpel, Ellen Kuhl, Andreas Menzel, and Paul Steinmann. "Computational modelling of isotropic multiplicative growth". eng. In: *CMES: Computer Modeling in Engineering and Sciences* 8.2 (June 2005), pp. 119–134. URL: https://doi.org/10.3970/cmes.2005.008.119 (cit. on pp. 13, 26, 32, 35).

[64] Tom W. Hiscock and Sean G. Megason. "Mathematically guided approaches to distinguish models of periodic patterning." eng. In: *Development* 142.3 (Feb. 2015), pp. 409–419. URL: https://doi.org/10.1242/dev.107441 (cit. on pp. 13, 87, 88).

[65] B. Hobmayer, F. Rentzsch, K. Kuhn, C. M. Happel, C. C. von Laue, P. Snyder, U. Rothbächer, and T. W. Holstein. "WNT signalling molecules act in axis formation in the diploblastic metazoan Hydra." eng. In: *Nature* 407.6801 (Sept. 2000), pp. 186–189. URL: https://doi.org/10.1038/35025063 (cit. on pp. 110, 127, 138).

[66] G. A. Holzapfel. *Nonlinear Solid Mechanics - A continuum approach for engineering*. John Wiley & Sons, LTD, 2010, p. 470. ISBN: 978-0-471-82319-3 (cit. on pp. 15, 16, 19–24, 49, 177).

[67] Shuang Hong et al. "Self-assembly of renal cells into engineered renal tissues in collagen/Matrigel scaffold in vitro." eng. In: *J Tissue Eng Regen Med* 6.10 (Nov. 2012), pp. 786–792. URL: https://doi.org/10.1002/term.484 (cit. on pp. 86, 183).

[68] Jonathon Howard, Stephan W. Grill, and Justin S. Bois. "Turing's next steps: the mechanochemical basis of morphogenesis." eng. In: *Nat Rev Mol Cell Biol* 12.6 (June 2011), pp. 392–398. URL: https://doi.org/10.1038/nrm3120 (cit. on pp. 13, 87, 88).

[69] Martin Hülskamp, Christine Pfeifle, and Diethard Tautz. "A morphogenetic gradient of hunchback protein organizes the expression of the gap genes Krüppel and knirps in the early Drosophila embryo". In: *Nature* 346.6284 (1990), p. 577. URL: https://doi.org/10.1038/346577a0 (cit. on p. 86).

[70] Javier E Irazoqui, Amy S Gladfelter, and Daniel J Lew. "Scaffold-mediated symmetry breaking by Cdc42p". In: *Nature cell biology* 5.12 (2003), p. 1062. URL: https://doi.org/10.1038/ncb1068 (cit. on p. 87).

[71] Thomas Iskratsch, Haguy Wolfenson, and Michael P. Sheetz. "Appreciating force and shape - the rise of mechanotransduction in cell biology." eng. In: *Nat Rev Mol Cell Biol* (Oct. 2014). URL: https://doi.org/10.1038/nrm3903 (cit. on pp. 88, 146).

[72] Johannes Jaeger, David H. Sharp, and John Reinitz. "Known maternal gradients are not sufficient for the establishment of gap domains in Drosophila melanogaster." In: *Mech Dev* 124.2 (Feb. 2007), pp. 108–128. URL: https://doi.org/10.1016/j.mod.2006.11.001 (cit. on p. 183).

[73] Volker John. "Slip with friction and penetration with resistance boundary conditions for the Navier-Stokes equations-numerical tests and aspects of the implementation". In: *Journal of Computational and Applied Mathematics* 147.2 (2002), pp. 287–300. URL: https://doi.org/10.1016/S0377-0427(02)00437-5 (cit. on pp. 129, 130).

[74] G.W. Jones and S.J. Chapman. "Modeling Growth in Biological Materials". In: *SIAM Review* 54 (1) (2012), pp. 52–118. URL: https://doi.org/10.1137/080731785 (cit. on p. 27).

[75] Sanna Junttila, Ulla Saarela, Kimmo Halt, Aki Manninen, Heikki Pärssinen, M. Rita Lecca, André W. Brändli, Sunder Sims-Lucas, Ilya Skovorodkin, and Seppo J. Vainio. "Functional Genetic Targeting of Embryonic Kidney Progenitor Cells Ex Vivo". In: *Journal of the American Society of Nephrology* 26.5 (2015), pp. 1126–1137. ISSN: 1046-6673. URL: https://doi.org/10.1681/ASN.2013060584 (cit. on pp. 86, 183).

[76] Carol Jurchenko and Khalid S. Salaita. "Lighting Up the Force: Investigating Mechanisms of Mechanotransduction Using Fluorescent Tension Probes." eng. In: *Mol Cell Biol* 35.15 (Aug. 2015), pp. 2570–2582. URL: https://doi.org/10.1128/MCB.00195-15 (cit. on p. 147).

[77] George Karypis and Vipin Kumar. "A fast and highly quality multilevel scheme for partitioning irregular graphs". In: *SIAM Journal on Scientific Computing* 20 (Jan. 1999), pp. 359–392 (cit. on pp. 78, 79).

[78] M. Kimmritz and T. Richter. "Parallel multigrid method for finite element simulations of complex flow problems on locally refined meshes". In: *Numerical Linear Algebra with Applications* 18.4 (2010), pp. 615–636. URL: https://doi.org/10.1002/nla.744 (cit. on pp. 11, 79).

[79] Tyler J Kirby and Jan Lammerding. "Cell mechanotransduction: Stretch to express". In: *Nature materials* 15.12 (2016), pp. 1227–1229. URL: https://doi.org/10.1038/nmat4809 (cit. on pp. 49, 51, 109).

[80] Shigeru Kondo and Takashi Miura. "Reaction-diffusion model as a framework for understanding biological pattern formation." eng. In: *Science* 329.5999 (Sept. 2010), pp. 1616–1620. URL: https://doi.org/10.1126/science.1179047 (cit. on pp. 13, 87).

[81] I. A. Kosevich. "Mechanics of growth pulsations as the basis of growth and morphogenesis in colonial hydroids". In: *Russian Journal of Developmental Biology* 37.2 (Mar. 2006), pp. 90–101. ISSN: 1608-3326. URL: https://doi.org/10.1134/S1062360406020056 (cit. on pp. 12, 85, 90–98, 100, 101, 145).

[82] Igor A. Kosevich. "Branching in Colonial Hydroids". In: *Branching Morphogenesis*. Boston, MA: Springer US, 2006, pp. 91–112. ISBN: 978-0-387-30873-9. URL: https://doi.org/10.1007/0-387-30873-3_5 (cit. on p. 90).

[83] Michel Labouesse. *Forces and Tension in Development*. Academic Press, 2011, p. 328. ISBN: 9780123850652 (cit. on pp. 24–26).

[84] Benoît Landrein, Annamaria Kiss, Massimiliano Sassi, Aurélie Chauvet, Pradeep Das, Millan Cortizo, Patrick Laufs, Seiji Takeda, Mitsuhiro Aida, Jan Traas, et al. "Mechanical stress contributes to the expression of the STM homeobox gene in Arabidopsis shoot meristems". In: *eLife* 4 (Dec. 2015). Ed. by Christian S Hardtke, e07811. URL: https://doi.org/10.7554/eLife.07811 (cit. on p. 110).

[85] R. Lefever. "Dissipative structures in chemical systems". In: *J. Chem. Phys.* 49 (1968), pp. 4977–4978. URL: https://doi.org/10.1063/1.1669986 (cit. on p. 87).

[86] Wesley R Legant. *Microscale measurements of cell and tissue mechanics in three dimensions*. University of Pennsylvania, 2012 (cit. on pp. 86, 89).

[87] Loïc LeGoff, Hervé Rouault, and Thomas Lecuit. "A global pattern of mechanical stress polarizes cell divisions and cell shape in the growing Drosophila wing disc." eng. In: *Development* 140.19 (Oct. 2013), pp. 4051–4059. URL: https://doi.org/10.1242/dev.090878 (cit. on p. 117).

[88] Tobias Lengfeld, Hiroshi Watanabe, Oleg Simakov, Dirk Lindgens, Lydia Gee, Lee Law, Heiko A. Schmidt, Suat Ozbek, Hans Bode, and Thomas W. Holstein. "Multiple Wnts are involved in Hydra organizer formation and regeneration." eng. In: *Dev Biol* 330.1 (June 2009), pp. 186–199. URL: https://doi.org/10.1016/j.ydbio.2009.02.004 (cit. on pp. 127, 138).

[89] Maria Leptin. "Gastrulation in Drosophila: the logic and the cellular mechanisms". In: *The EMBO journal* 18.12 (1999), pp. 3187–3192. URL: https://doi.org/10.1093/emboj/18.12.3187 (cit. on pp. 48, 105, 109).

[90] Bin Li, Fang Li, Kathleen M Puskar, and James H-C Wang. "Spatial patterning of cell proliferation and differentiation depends on mechanical stress magnitude." eng. In: *J Biomech* 42 (2009), pp. 1622–1627. URL: https://doi.org/10.1016/j.jbiomech.2009.04.033 (cit. on pp. 49, 51).

[91] Martin Loose, Elisabeth Fischer-Friedrich, Jonas Ries, Karsten Kruse, and Petra Schwille. "Spatial regulators for bacterial cell division self-organize into surface waves in vitro". In: *Science* 320.5877 (2008), pp. 789–792. URL: https://doi.org/10.1126/science.1154413 (cit. on p. 87).

[92] V.A. Lubarda and A. Hoger. "On the mechanics of solids with a growing mass". In: *International Journal of Solids and Structures* 39 (2002), pp. 4627–4664. URL: https://doi.org/10.1016/S0020-7683(02)00352-9 (cit. on pp. 13, 26, 27, 32, 35).

[93] Holley E Lynch, Sarah M Crews, Brett Rosenthal, Elliott Kim, Robert Gish, Karl Echiverri, and M Shane Hutson. "Cellular mechanics of germ band retraction in Drosophila". In: *Developmental biology* 384.2 (2013), pp. 205–213. URL: https://doi.org/10.1016/j.ydbio.2013.10.005 (cit. on p. 25).

[94] Akiko Mammoto, Sui Huang, and Donald E. Ingber. "Filamin links cell shape and cytoskeletal structure to Rho regulation by controlling accumulation of p190RhoGAP in lipid rafts." eng. In: *Journal of Cell Science* 120.3 (Feb. 2007), pp. 456–467. ISSN: 0021-9533. URL: https://doi.org/10.1242/jcs.03353 (cit. on pp. 49, 51).

[95] Akiko Mammoto, Tadanori Mammoto, and Donald E. Ingber. "Mechanosensitive mechanisms in transcriptional regulation." eng. In: *J Cell Sci* 125.13 (July 2012), pp. 3061–3073. URL: https://doi.org/10.1242/jcs.093005 (cit. on pp. 49, 88, 146).

[96] Tadanori Mammoto et al. "Mechanochemical control of mesenchymal condensation and embryonic tooth organ formation." eng. In: *Dev Cell* 21.4 (Oct. 2011), pp. 758–769. URL: https://doi.org/10.1016/j.devcel.2011.07.006 (cit. on p. 110).

[97] Anna Marciniak-Czochra, G. Karch, and K. Suzuki. "Instability of Turing patterns in reaction-diffusion-ODE systems". In: *J. Math. Biol.* 74.90 (2017), pp. 583–618. URL: https://doi.org/10.1007/s00285-016-1035-z (cit. on p. 87).

[98] Adam C. Martin and Bob Goldstein. "Apical constriction: themes and variations on a cellular mechanism driving morphogenesis." eng. In: *Development* 141.10 (May 2014), pp. 1987–1998. URL: https://doi.org/10.1242/dev.102228 (cit. on pp. 48, 51, 105, 107, 109).

[99] H. Meinhardt and A. Gierer. "Pattern formation by local self-activation and lateral inhibition." eng. In: *Bioessays* 22 (2000), pp. 753–760. URL: https://doi.org/10.1002/1521-1878(200008)22:8%3C753::AID-BIES9%3E3.0.CO;2-Z (cit. on p. 87).

[100] Hans Meinhardt. "Turing's theory of morphogenesis of 1952 and the subsequent discovery of the crucial role of local self-enhancement and long-range inhibition". In: *Interface Focus* 2 (2012), pp. 407–416. ISSN: 2042-8898. URL: https://doi.org/10.1098/rsfs.2011.0097 (cit. on p. 87).

[101] Fanjie Meng, Thomas M. Suchyna, Elena Lazakovitch, Richard M. Gronostajski, and Frederick Sachs. "Real Time FRET Based Detection of Mechanical Stress in Cytoskeletal and Extracellular Matrix Proteins." In: *Cell Mol Bioeng* 4.2 (June 2011), pp. 148–159. URL: https://doi.org/10.1007/s12195-010-0140-0 (cit. on pp. 12, 89, 117).

[102] Fanjie Meng, Thomas M. Suchyna, and Frederick Sachs. "A fluorescence energy transfer-based mechanical stress sensor for specific proteins in situ." eng. In: *FEBS J* 275.12 (June 2008), pp. 3072–3087. URL: https://doi.org/10.1111/j.1742-4658.2008.06461.x (cit. on pp. 12, 89, 117).

[103] Moritz Mercker, Felix Brinkmann, Anna Marciniak-Czochra, and Thomas Richter. "Beyond Turing: mechanochemical pattern formation in biological tissues". In: *Biology Direct* 11.1 (2016), pp. 1–15. ISSN: 1745-6150. URL: https://doi.org/10.1186/s13062-016-0124-7 (cit. on pp. 13–15, 41, 47, 50, 86, 88, 89, 102, 117, 126, 138, 143, 173, 181, 183).

[104] Moritz Mercker, Dirk Hartmann, and Anna Marciniak-Czochra. "A mechanochemical model for embryonic pattern formation: coupling tissue mechanics and morphogen expression." eng. In: *PLoS One* 8.12 (2013), e82617. URL: https://doi.org/10.1371/journal.pone.0082617 (cit. on pp. 13, 40, 41, 48, 88, 89, 105, 117, 134).

[105] Moritz Mercker, Alexandra Köthe, and Anna Marciniak-Czochra. "Mechanochemical symmetry breaking in Hydra aggregates." eng. In: *Biophys J* 108.9 (May 2015), pp. 2396–2407. URL: https://doi.org/10.1016/j.bpj.2015.03.033 (cit. on pp. 13, 40, 41, 49, 88, 89, 110, 126, 127, 136).

[106] Jose J. Muñoz, Kathy Barrett, and Mark Miodownik. "A deformation gradient decomposition method for the analysis of the mechanics of morphogenesis." eng. In: *J Biomech* 40.6 (2007), pp. 1372–1380. URL: https://doi.org/10.1016/j.jbiomech.2006.05.006 (cit. on pp. 13, 26, 36–38, 105).

[107] J. D. Murray and G.F. Oster. "Generation of Biological Pattern and Form". In: *Mathematical Medicine and Biology: A Journal of the IMA* 1.1 (1984), pp. 51–75. URL: https://doi.org/10.1093/imammb/1.1.51 (cit. on p. 88).

[108] James D Murray. "On the mechanochemical theory of biological pattern formation with application to vasculogenesis." In: *C R Biol* 326 (2003), pp. 239–252. URL: https://doi.org/10.1016/S1631-0691(03)00065-9 (cit. on p. 88).

[109] J.D. Murray. *Mathematical Biology I: An Introduction*. 3rd ed. Vol. 17. Springer-Verlag Berlin, Heidelberg, 2002. ISBN: 978-0-387-95223-9. URL: https://doi.org/10.1007/b98868 (cit. on pp. 49, 50, 55).

[110] J.D. Murray. *Mathematical Biology II: Spatial models and biomedical applications*. Springer-Verlag Berlin, Heidelberg, 2003. ISBN: 978-0-387-95228-4. URL: https://doi.org/10.1007/b98869 (cit. on p. 87).

[111] J.D. Murray and G.F. Oster. "Cell traction models for generating pattern and form in morphogenesis". In: *J. Math. Biol.* 19 (1984), pp. 265–279. URL: https://doi.org/10.1007/BF00277099 (cit. on p. 88).

[112] Sundar R Naganathan and Andrew C Oates. "Mechanochemical coupling and developmental pattern formation". In: *Current Opinion in Systems Biology* 5 (Oct. 2017), pp. 104–111. URL: https://doi.org/10.1016/j.coisb.2017.09.007 (cit. on pp. 88, 117).

[113] Martina Nagel, Emilios Tahinci, Karen Symes, and Rudolf Winklbauer. "Guidance of mesoderm cell migration in the Xenopus gastrula requires PDGF signaling". In: *Development* 131.11 (2004), pp. 2727–2736. ISSN: 0950-1991. URL: https://doi.org/10.1242/dev.01141 (cit. on p. 111).

[114] Marcos Nahmad. "Steady-state invariant genetics: probing the role of morphogen gradient dynamics in developmental patterning." In: *Journal of The Royal Society Interface* 8.63 (Mar. 2011), pp. 1429–1439. ISSN: 1742-5689. URL: https://doi.org/10.1098/rsif.2010.0738 (cit. on p. 111).

[115] Jeremy Nance, Jen-Yi Lee, and Bob Goldstein. "Gastrulation in C. elegans". In: *WormBook, ed The C. elegans Research Community* (2005). URL: https://doi.org//10.1895/wormbook.1.23.1 (cit. on pp. 48, 105, 109).

[116] Celeste M. Nelson. "Geometric control of tissue morphogenesis." eng. In: *Biochim Biophys Acta* 1793.5 (May 2009), pp. 903–910. URL: https://doi.org/10.1016/j.bbamcr.2008.12.014 (cit. on pp. 49, 51, 147).

[117] Celeste M Nelson, Ronald P Jean, John L Tan, Wendy F Liu, Nathan J Sniadecki, Alexander A Spector, and Christopher S Chen. "Emergent patterns of growth controlled by multicellular form and mechanics." eng. In: *PNAS* 102 (2005), pp. 11594–11599. URL: https://doi.org/10.1073/pnas.0502575102 (cit. on pp. 13, 40, 49, 51, 88, 117).

[118] W James Nelson. "Remodeling epithelial cell organization: transitions between front–rear and apical–basal polarity". In: *Cold Spring Harbor perspectives in biology* 1.1 (2009), a000513. URL: https://doi.org/10.1101/cshperspect.a000513 (cit. on pp. 48, 105, 109).

[119] G. Odell, G.F. Oster, P. Alberch, and B. Burnside. "The mechanical basis for morphogenesis : I. Epithelial folding and invagination". In: *Dev. Biol.* 85.2 (1981), pp. 446–462. URL: https://doi.org/10.1016/0012-1606(81)90276-1 (cit. on pp. 88, 89).

[120] Satoru Okuda, Yasuhiro Inoue, Tadashi Watanabe, and Taiji Adachi. "Coupling intercellular molecular signalling with multicellular deformation for simulating three-dimensional tissue morphogenesis." In: *Interface Focus* 5.2 (Apr. 2015), p. 20140095. URL: https://doi.org/10.1098/rsfs.2014.0095 (cit. on pp. 48, 105, 134).

[121] A. Wayne Orr, Brian P Helmke, Brett R Blackman, and Martin A Schwartz. "Mechanisms of mechanotransduction." In: *Dev Cell* 10 (2006), pp. 11–20. URL: https://doi.org/10.1016/j.devcel.2005.12.006 (cit. on p. 88).

[122] Parth Patwari and Richard T Lee. "Mechanical control of tissue morphogenesis." eng. In: *Circ Res* 103 (2008), pp. 234–243. URL: https://doi.org/10.1161/CIRCRESAHA.108.175331 (cit. on p. 88).

[123] Isabelle Philipp, Roland Aufschnaiter, Suat Ozbek, Stefanie Pontasch, Marcell Jenewein, Hiroshi Watanabe, Fabian Rentzsch, Thomas W. Holstein, and Bert Hobmayer. "Wnt/beta-catenin and noncanonical Wnt signaling interact in tissue evagination in the simple eumetazoan Hydra." In: *Proceedings of the National Academy of Sciences* 106.11 (Mar. 2009), pp. 4290–4295. ISSN: 0027-8424. URL: https://doi.org/10.1073/pnas.0812847106 (cit. on pp. 48, 134, 138).

[124] Rolf Rannacher. *Numerik 1: Numerik gewöhnlicher Differentialgleichungen*. Lecture Notes. Heidelberg: Heidelberg University Publishing, 2017. ISBN: 978-3-946054-31-3. URL: https://doi.org/10.17885/heiup.258.342 (cit. on pp. 60, 64).

[125] Rolf Rannacher. *Numerik 2: Numerik partieller Differentialgleichungen*. Lecture Notes. Heidelberg: Heidelberg University Publishing, 2017. ISBN: 978-3-946054-37-5. URL: https://doi.org/10.17885/heiup.281.370. (cit. on pp. 58, 62).

[126] T. Richter. *Fluid-structure Interactions. Models, Analysis and Finite Elements.* Vol. 118. Lecture notes in computational science and engineering. Springer, 2017. ISBN: 978-3-319-63969-7. URL: https://doi.org/10.1007/978-3-319-63970-3 (cit. on pp. 15, 16, 18–20, 60).

[127] T. Richter. "Parallel Multigrid for Adaptive Finite Elements and its Application to 3D Flow Problem". urn:nbn:de:bsz:16-opus-57433. PhD thesis. Universität Heidelberg, 2005 (cit. on pp. 11, 78–80, 82).

[128] E. K. Rodriguez, A. Hoger, and A. D. McCulloch. "Stress-dependent finite growth in soft elastic tissues." eng. In: *J Biomech* 27.4 (Apr. 1994), pp. 455–467. URL: https://doi.org/10.1016/0021-9290(94)90021-3 (cit. on pp. 11, 13, 15, 26, 27, 30, 34, 35).

[129] M.L. Rodriguez, P.J. McGarry, and N.J. Sniadecki. "Review on cell mechanics: Experimental and modeling approaches". In: *Applied Mechanics Reviews* 65 (2013), doi: 10.1115/1.4025355. URL: https://doi.org/10.1115/1.4025355 (cit. on p. 89).

[130] Anne-Gaëlle Rolland-Lagan, Lauren Remmler, and Camille Girard-Bock. "Quantifying shape changes and tissue deformation in leaf development". In: *Plant physiology* 165.2 (2014), pp. 496–505. ISSN: 0032-0889. URL: https://doi.org/10.1104/pp.113.231258 (cit. on pp. 86, 89).

[131] Anne-Lise Routier-Kierzkowska, Alain Weber, Petra Kochova, Dimitris Felekis, Bradley J. Nelson, Cris Kuhlemeier, and Richard S. Smith. "Cellular Force Microscopy for in Vivo Measurements of Plant Tissue Mechanics". In: *Plant Physiology* 158.4 (2012), pp. 1514–1522. ISSN: 0032-0889. URL: https://doi.org/10.1104/pp.111.191460 (cit. on p. 147).

[132] Yousef Saad. *Iterative Methods for Sparse Linear Systems*. PWS Publishing Company, 1996. URL: https://doi.org/10.1137/1.9780898718003 (cit. on pp. 11, 75, 77).

[133] Heike Sander. "Symmetry breaking in regenerating hydra: The role of fluctuations and cell mechanics". PhD thesis. Universität des Saarlandes, 2016. URL: https://doi.org/10.22028/D291-26882 (cit. on pp. 11, 12, 14, 85, 126–128, 142, 143, 145).

[134] Jacob M. Sawyer, Jessica R. Harrell, Gidi Shemer, Jessica Sullivan-Brown, Minna Roh-Johnson, and Bob Goldstein. "Apical constriction: a cell shape change that can drive morphogenesis." In: *Dev Biol* 341.1 (May 2010), pp. 5–19. URL: https://doi.org/10.1016/j.ydbio.2009.09.009 (cit. on p. 105).

[135] G. C. Schoenwolf. "Cutting, pasting and painting: experimental embryology and neural development". In: *Nature Reviews Neuroscience* 2 (2001), pp. 2, 763–771. URL: https://doi.org/10.1038/35097549 (cit. on pp. 86, 111).

[136] Natalie S. Scholes, David Schnoerr, Mark Isalan, and Michael P. H. Stumpf. "Turing patterns are common but not robust". In: *bioRxiv* (2018). URL: https://doi.org/10.1101/352302 (cit. on pp. 13, 87).

[137] Maisa Seppala, Gareth J Fraser, Anahid A Birjandi, Guilherme M Xavier, and Martyn T Cobourne. "Sonic Hedgehog Signaling and Development of the Dentition". In: *Journal of Developmental Biology* 5.2 (2017), p. 6. URL: https://doi.org/10.3390/jdb5020006 (cit. on p. 110).

[138] Richard Skalak, Stephen Zargaryan, Rakesh K. Jain, Paolo A. Netti, and Anne Hoger. "Compatibility and the genesis of residual stress by volumetric growth". In: *Journal of Mathematical Biology* 34.8 (1996), pp. 889–914. ISSN: 1432-1416. URL: https://doi.org/10.1007/BF01834825 (cit. on pp. 14, 30).

[139] Jordi Soriano, Sten Rüdiger, Pramod Pullarkat, and Albrecht Ott. "Mechanogenetic coupling of Hydra symmetry breaking and driven Turing instability model." eng. In: *Biophys J* 96.4 (Feb. 2009), pp. 1649–1660. URL: https://doi.org/10.1016/j.bpj.2008.09.062 (cit. on pp. 48, 110, 126, 127, 134, 138).

[140] Mansi Srivastava, Claire Larroux, Daniel R Lu, Kareshma Mohanty, Jarrod Chapman, Bernard M Degnan, and Daniel S Rokhsar. "Early evolution of the LIM homeobox gene family". In: *BMC biology* 8.1 (2010), p. 4. URL: https://doi.org/10.1186/1741-7007-8-4 (cit. on pp. 111, 112).

[141] Norbert Stoop, Romain Lagrange, Denis Terwagne, Pedro M Reis, and Jörn Dunkel. "Curvature-induced symmetry breaking determines elastic surface patterns". In: *Nature materials* 14.3 (2015), p. 337. URL: https://doi.org/10.1038/nmat4202 (cit. on p. 88).

[142] Ju Swift and Pierre C Hohenberg. "Hydrodynamic fluctuations at the convective instability". In: *Physical Review A* 15.1 (1977), p. 319. URL: https://doi.org/10.1103/PhysRevA.15.319 (cit. on p. 87).

[143] Larry A. Taber and Daniel W. Eggers. "Theoretical Study of Stress-Modulated Growth in the Aorta". In: *Journal of Theoretical Biology* 180.4 (1996), pp. 343–357. ISSN: 0022-5193. URL: https://doi.org/10.1006/jtbi.1996.0107 (cit. on p. 35).

[144] Larry A. Taber and Renato Perucchio. "Modeling Heart Development". In: *Journal of elasticity and the physical science of solids* 61.1 (July 2000), pp. 165–197. ISSN: 1573-2681. URL: https://doi.org/10.1023/A:1011082712497 (cit. on pp. 26, 35).

[145] Toshio Takahashi, Masayuki Hatta, Seungshic Yum, Lydia Gee, Masahiro Ohtani, Toshitaka Fujisawa, and Hans R. Bode. "Hym-301, a novel peptide, regulates the number of tentacles formed in hydra". In: *Development* 132.9 (2005), pp. 2225–2234. ISSN: 0950-1991. URL: https://doi.org/10.1242/dev.01792 (cit. on pp. 110, 138).

[146] D'Arcy Wentworth Thompson. *On Growth and Form*. Cambridge University Press, 1917, p. 793 (cit. on pp. 86–88).

[147] Mark W Tibbitt and Kristi S Anseth. "Hydrogels as extracellular matrix mimics for 3D cell culture". In: *Biotechnology and bioengineering* 103.4 (2009), pp. 655–663. URL: https://doi.org/10.1002/bit.22361 (cit. on pp. 86, 89).

[148] Clifford Truesdell. *A first course in rational continuum mechanics*. Academic Press, Inc., 1977, p. 304. ISBN: 9781483220482 (cit. on pp. 16, 18–20, 28).

[149] Clifford Truesdell and Walter Noll. *The Non-Linear Field Theories of Mechanics*. 3rd ed. Springer Berlin Heidelberg, 2004, p. 579. ISBN: 978-3-642-05701-4. URL: https://doi.org/10.1007/978-3-662-10388-3 (cit. on p. 22).

[150] C. D. Tsiairis and A. Aulehla. "Self-Organization of Embryonic Genetic Oscillators into Spatiotemporal Wave Patterns". In: *Cell* 164(4) (2016), pp. 656–667. URL: https://doi.org/10.1016/j.cell.2016.01.028 (cit. on pp. 86, 183).

[151] A. M. Turing. "The chemical basis of morphogenesis." In: *Phil Trans R Soc London B* 237 (Aug. 1952), pp. 37–72. URL: https://doi.org/10.1098/rstb.1952.0012 (cit. on pp. 87, 89).

[152] Séverine Urdy. “On the evolution of morphogenetic models: mechano-chemical interactions and an integrated view of cell differentiation, growth, pattern formation and morphogenesis.” eng. In: *Biol Rev Camb Philos Soc* 87.4 (Nov. 2012), pp. 786–803. URL: https://doi.org/10.1111/j.1469-185X.2012.00221.x (cit. on pp. 10, 13, 88).

[153] T. Vignaud, L. Blanchoin, and M. Théry. “Directed cytoskeleton self-organization.” In: *Trends Cell Biol* 22.12 (Dec. 2012), pp. 671–682. URL: https://doi.org/10.1016/j.tcb.2012.08.012 (cit. on pp. 49, 51).

[154] Josef Wloka. *Partielle Differentialgleichungen : Sobolevräume und Randwertaufgaben*. Vieweg & Teubner Verlag, Mar. 1982. ISBN: 9783519022251 (cit. on pp. 21, 61, 120, 130).

[155] Lewis Wolpert. “Positional information and the spatial pattern of cellular differentiation”. In: *Journal of Theoretical Biology* 25.1 (1969), pp. 1–47. URL: https://doi.org/10.1016/S0022-5193(69)80016-0 (cit. on pp. 86, 87).

[156] Lewis Wolpert. *The Triumph of the Embryo*. Dover books on biology, psychology and medicine. Dover Publications, 2008, p. 211. ISBN: 9780486469294 (cit. on p. 40).

[157] Matthew A. Wyczalkowski, Zi Chen, Benjamen A. Filas, Victor D. Varner, and Larry A. Taber. “Computational models for mechanics of morphogenesis.” In: *Birth Defects Research Part C: Embryo Today: Reviews* 96.2 (June 2012), pp. 132–152. URL: https://doi.org/10.1002/bdrc.21013 (cit. on p. 89).

[158] Charles R. Wyttenbach. “The dynamics of stolon elongation in the hydroid, Campanularia flexuosa”. In: *Journal of Experimental Zoology* 167.3 (1968), pp. 333–351. URL: https://doi.org/10.1002/jez.1401670306 (cit. on pp. 90–92, 95, 97, 98, 100).

[159] Chao Yang, Xiaohan Zhang, Yichen Guo, Fanjie Meng, Frederick Sachs, and Jun Guo. “Mechanical dynamics in live cells and fluorescence-based force/tension sensors.” In: *Biochimica et biophysica acta* 1853 (8 Aug. 2015), pp. 1889–1904. URL: https://doi.org/10.1016/j.bbamcr.2015.05.001 (cit. on pp. 12, 89, 117).

Colophon

This thesis was created with LaTeX 2$_\varepsilon$ and BibTeX using the TeX Live distribution and it was typeset in *Latin Modern*. Our numerical simulations were visualized in paraview, shematic illustrations were drawn in xfig and plots were created in gnuplot.

Appendix

In this appendix, we present derivations and numerical results that were omitted in the main part of this thesis for the sake of brevity and readability. Nonetheless, these results will provide further insights into the numerical implementation and the robustness of our efficient methods to reliably solve our coupled system of PDEs. This appendix is divided into three major parts:

Firstly, in Section A.1, we give a detailed derivation of the active deformation tensors that we employed in modeling growth processes in hydroids as well as embryonic development. Secondly, in Section A.2, we present further results on the robustness of the stretch-mediated feedback loop including active constriction in the application to embryogenesis. Ultimately, in Section A.3, we show numerical result for the application of our prototypical systems of PDEs to embryogenesis in 2D. We have published similar results in Mercker *et al.* [103]. In this thesis, we present a modified system of PDEs and new calculations on the robustness of our model that closely correspond to our novel results in 3D.

A.1 Derivation of the active deformation tensors

The derivation of the active deformation tensors prescribed in our three applications is certainly interesting for the practical implementation of our models. We postponed the (geometrical) derivation of these tensors to the appendix for the sake of brevity in the main manuscript above. These tensors were specified when we applied our prototypical system of PDEs to the chosen model organisms.

A.1.1 Active deformations in growth processes in hydroid tips

Firstly, we focus on the active deformation gradient describing a shearing that was presented in Eq. (5.1). So let us consider a point $\mathbf{X}$ in the ectodermal cell layer and its radius $r = \sqrt{X_0^2 + X_1^2}$ inside the hydroid cylinder. Further, R_0 denotes the constant distance of the cell membrane, located between the ectodermal layer and the perisarc, to the X_2-axis (i.e. the axis of the cylindrical hydroid body). Then, an active deformation that describes a shearing of the ectodermal cells (ECT) that is largest towards the endodermal layer (END) and zero towards the perisarc (P) (compare again Fig. 5.4) can be expressed by

$$\mathbf{u}_a = \begin{pmatrix} 0 \\ 0 \\ (R_0 - r)\, k(t) \end{pmatrix}, \tag{A.1}$$

where the deformation linearly depends on time via $k(t)$ (cf. Eq. (5.3)). The desired active deformation gradient describing a shearing of the ectodermal cells is given by $\mathbf{F}_a = \nabla \mathbf{u}_a + \mathbf{I}$, see Eq. (5.1) for the differentiated result.

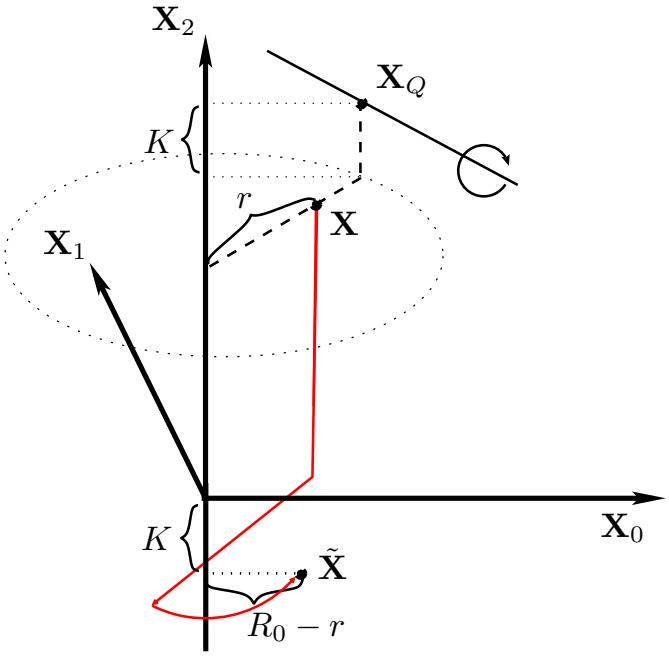

Figure A.1: Derivation of the active deformation tensor describing a rotation: Translation and rotation of $\mathbf{X}$ to the X_0X_2-plane with rotation point $\mathbf{X}_Q$ transformed to the origin such that the rotation axis coincides with the X_1-axis.

Secondly, we derive the active deformation tensor prescribing a rotating motion. Again, let us consider a point $\mathbf{X}$ in the ectodermal cell layer and the notation introduced above. We intend to rotate this point around an axis through $\mathbf{X}_Q$ that is orthogonal to $\mathbf{X}$ as illustrated in Fig. A.1. The cardinal point $\mathbf{X}_Q := \left(X_0R_0r^{-1}, X_1R_0r^{-1}, X_2 + K\right)$ lies on the membrane between the ectodermal cell layer and the perisarc with radius R_0 in cylindrical coordinates and offset K in X_2-direction with respect to $\mathbf{X}$, cf. Fig. A.1. In the first step, we translate $\mathbf{X}$ by the rotation point $\mathbf{X}_Q$ such that the latter coincides with the origin (first red zigzag arrow in this figure), which yields

$$\mathbf{X} - \mathbf{X}_Q = \begin{pmatrix} X_0(1 - R_0r^{-1}) \\ X_1(1 - R_0r^{-1}) \\ -K \end{pmatrix}.$$

Secondly, we rotate this difference to the X_0X_2-plane. This gives

$$\tilde{\mathbf{X}} = \mathbf{Q}_2(\mathbf{X} - \mathbf{X}_Q) = \begin{pmatrix} R_0 - r \\ 0 \\ -K \end{pmatrix}, \tag{A.2}$$

which is easy to verify geometrically and illustrated by the red, curved arrow in Fig. A.1. The rotation matrix around the X_2-axis is given by

$$\mathbf{Q}_2 = \begin{pmatrix} -X_0r^{-1} & -X_1r^{-1} & 0 \\ X_1r^{-1} & -X_0r^{-1} & 0 \\ 0 & 0 & 1 \end{pmatrix}.$$

Please mind the shift of the rotation angle by π due to the preceeding translation by $\mathbf{X}_Q$. At this point, the rotation axis for $\mathbf{X}$ coincides with the X_1-axis. In a third step, we can hence apply our rotation by the angle $\alpha(t)$, where we had specified the nature of the time dependence for our application to colonial hydroids in Eq. (5.3). This rotation reads:

$$\mathbf{Q}_1 = \begin{pmatrix} \cos(\alpha(t)) & 0 & -\sin(\alpha(t)) \\ 0 & 1 & 0 \\ \sin(\alpha(t)) & 0 & \cos(\alpha(t)) \end{pmatrix},$$

which results in

$$\mathbf{Q}_1\tilde{\mathbf{X}} = \begin{pmatrix} \cos(\alpha(t))(R_o - r) + K\sin(\alpha(t)) \\ 0 \\ \sin(\alpha(t))(R_o - r) - K\sin(\alpha(t)) \end{pmatrix}. \tag{A.3}$$

Finally, this intermediate result has to be rotated and translated back, i.e. we use the inverse rotation $\mathbf{Q}_2^T$ around the X_2-axis and a translation by $\mathbf{X}_Q$ to obtain the active deformation $\mathbf{u}_a$:

$$\mathbf{u}_a = \mathbf{Q}_2^T\mathbf{Q}_1\tilde{\mathbf{X}} + \mathbf{X}_Q - \mathbf{X} = \begin{pmatrix} (R_0 - \cos(\alpha(t))(R_o - r) - K\sin(\alpha(t)))X_0 r^{-1} - X_0 \\ (R_0 - \cos(\alpha(t))(R_o - r) - K\sin(\alpha(t)))X_1 r^{-1} - X_1 \\ \sin(\alpha(t))(R_o - r) - K\sin(\alpha(t)) + K \end{pmatrix}. \tag{A.4}$$

Then, the desired active deformation gradient describing a rotation of the ectodermal cells is given by $\mathbf{F}_a = \nabla\mathbf{u}_a + \mathbf{I}$. The resulting gradient was presented in Eq.(5.2).

A.1.2 Active deformations for mechanochemical pattern formation in embryogenesis

In the application to mechanochemical pattern formation in embryonic development, we mainly consider morphogen dependent apical/basal constriction. A schematic illustration of an active deformation tensor describing basal constriction is shown in Fig. 5.8. The basic idea of the multiplicative deformation gradient decomposition implicates that the continuity of the overall deformation is preserved by the elastic response (which we also depicted in Fig. 5.8 and Fig. 2.1).

To define the active deformation tensor $\mathbf{F}_a$, we first introduce local coordinate systems $\hat{\mathbf{X}}$ in the origin of every biological cell. These coordinate systems are oriented such that $\hat{\mathbf{X}}_1$ in 2D and $\hat{\mathbf{X}}_2$ in 3D, respectively, point in the radial direction, see Fig. A.2 for an illustration in the two-dimensional case. With these preparations, the parametric coordinates located in the centroid of an arbitrary biological cell K_i can be obtained from the reference coordinates $\mathbf{X}$ by

$$\hat{\mathbf{X}} = \mathbf{Q}_i\mathbf{X} + \mathbf{m}_i \tag{A.5}$$

with continuous rotations $\mathbf{Q}_i$ with $\mathbf{Q}_i^T\mathbf{Q}_i = \mathbf{Q}_i\mathbf{Q}_i^T = \mathbf{I}$ and translation vectors $\mathbf{m}_i$ (cf. Fig. A.2(a)). The indices indicate that the rotation and the translation depend on the biological cell K_i under consideration. Thus, we define a cell-wise continuous global matrix $\mathbf{Q}$ and a cell-wise constant global vector $\mathbf{m}$ with the properties:

$$\mathbf{Q}|_{K_i} = \mathbf{Q}_i, \quad \mathbf{m}|_{K_i} = \mathbf{m}_i. \tag{A.6}$$

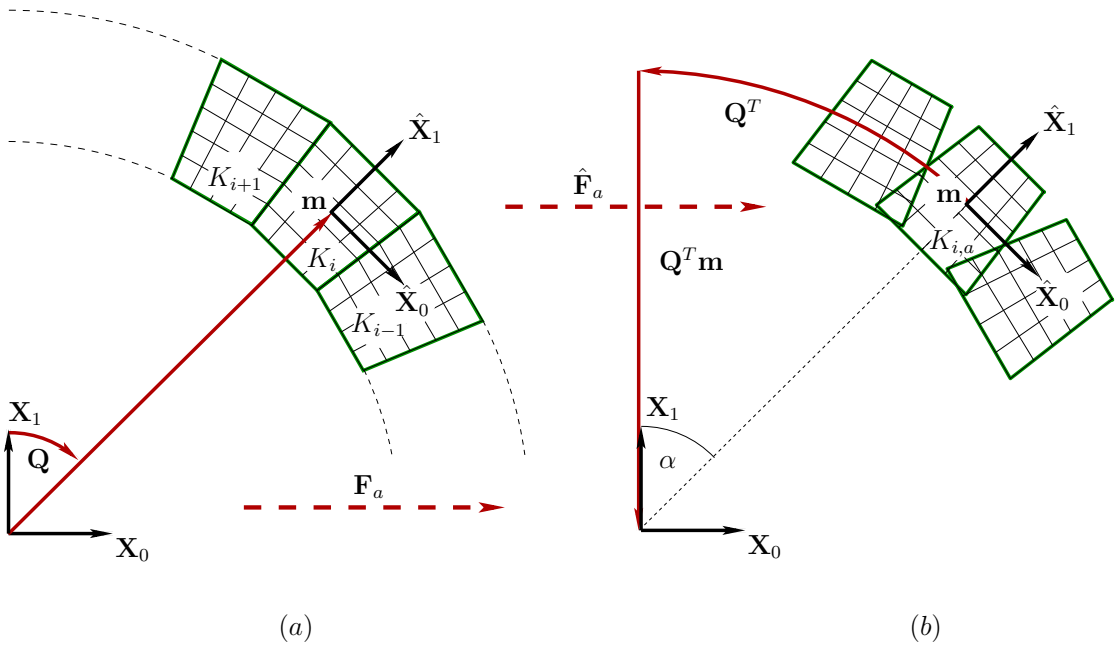

Figure A.2: Schema of the transformation between the reference system $\mathbf{X}$ and the parametric local coordinate system $\hat{\mathbf{X}}$ located in the centroid $\mathbf{m}$ of an arbitrary biological cell K_i (green): (a) Transformation from $\mathbf{X}$ to $\hat{\mathbf{X}}$ by a rotation $\mathbf{Q}$ and a translation by $\mathbf{m}$. (b) Inverse transformation from $\hat{\mathbf{X}}$ to $\mathbf{X}$ by $\mathbf{Q}^T$ and the translation $\mathbf{Q}^T\mathbf{m}$ of the argument.

Then, the active deformation gradient in the parametric coordinate systems $\hat{\mathbf{X}}$ is defined as

$$\begin{aligned}\hat{\mathbf{F}}_a(\hat{\mathbf{X}}, C) &:= \begin{pmatrix} 1 + kC\hat{X}_1 & kC\hat{X}_0 \\ 0 & 1 \end{pmatrix} && \text{in 2D,} \\ \hat{\mathbf{F}}_a(\hat{\mathbf{X}}, C) &:= \begin{pmatrix} 1 + kC\hat{X}_2 & 0 & kC\hat{X}_0 \\ 0 & 1 + kC\hat{X}_2 & kC\hat{X}_1 \\ 0 & 0 & 1 \end{pmatrix} && \text{in 3D}\end{aligned} \tag{A.7}$$

with k being a constant, $\hat{\mathbf{X}}(\hat{\mathbf{X}}_0, \hat{\mathbf{X}}_1)^T$ in 2D and $\hat{\mathbf{X}} = (\hat{\mathbf{X}}_0, \hat{\mathbf{X}}_1, \hat{\mathbf{X}}_2)^T$ in 3D. Positive values of k result in an apical constriction and negative values in a basal one. Without loss of generality, let us consider the biological cell K_i with local coordinate system $\hat{\mathbf{X}}$ in its centroid (midpoint) $\mathbf{m}$. This local coordinate system is transformed to the reference configuration $\mathbf{X}$ by

$$\mathbf{X} = \mathbf{Q}_i^T\hat{\mathbf{X}} - \mathbf{Q}_i^T\mathbf{m}_i = \mathbf{Q}_i^T(\hat{\mathbf{X}} - \mathbf{m}_i),$$

which is the inverse transformation of the transformation given in Eq. (A.5) and is illustrated in Fig. A.2 (b) for the two-dimensional setting.

Further, this figure shows that $\cos(\alpha) = m_1|\mathbf{m}|^{-1}$ and $\sin(\alpha) = m_0|\mathbf{m}|^{-1}$ where $|\mathbf{m}| = \sqrt{m_0^2 + m_1^2}$. Then, the rotation of the system $\hat{\mathbf{X}}$ around the origin of the system $\mathbf{X}$ by the angle α is given by

$$\mathbf{Q}_i^T := \begin{pmatrix} \cos(\alpha) & \sin\alpha \\ -\sin(\alpha) & \cos(\alpha) \end{pmatrix} = \frac{1}{|\mathbf{m}|}\begin{pmatrix} m_1 & m_0 \\ -m_0 & m_1 \end{pmatrix} \quad \text{in 2D.}$$

The rotated coordinate system with regard to the reference one is then located in the position $\mathbf{Q}_i\mathbf{m}_i = (0, (Qm)_1)^T$.

In 3D, we proceed analogously to the two-dimensional derivation (cf. Fig. A.2 (b)): We rotate the local coordinate system $\hat{\mathbf{X}}_a$ to the position $\mathbf{Q}_i\mathbf{m}_i = (0, 0, (Qm)_2)^T$ by a rotation $\mathbf{Q}_i$, which is composed of a clockwise rotation $\mathbf{Q}_{X_2}$ around the X_2-axis followed by a counter-clockwise rotation $\mathbf{Q}_{i,X_1}$ around the X_1-axis. The first rotation $\mathbf{Q}_{i,X_2}$ takes place in the X_0X_1-plane and is thus analog to the rotation matrix $\mathbf{Q}_i^T$ in two dimensions: We simply take the length of $\mathbf{m}_i$ projected to this plane, i.e. $|\mathbf{m}_{01}| := \sqrt{m_0^2 + m_1^2}$. Then, we obtain for the rotation by the angle α of the local coordinate system $\hat{\mathbf{X}}_a$ around the X_2-axis

$$\mathbf{Q}_{i,X_2}^T = \frac{1}{|\mathbf{m}_{01}|}\begin{pmatrix} m_0 & -m_1 & 0 \\ m_1 & m_0 & 0 \\ 0 & 0 & |\mathbf{m}_{01}| \end{pmatrix},$$

using $\cos(\alpha) = m_0|\mathbf{m}_{01}|^{-1}$ and $\sin(\alpha) = m_1|\mathbf{m}_{01}|^{-1}$. Similarly, the rotation around the X_1-axis can be derived as

$$\mathbf{Q}_{i,X_1}^T = \frac{1}{|\mathbf{m}|}\begin{pmatrix} m_2 & 0 & |\mathbf{m}_{01}| \\ 0 & |\mathbf{m}| & 0 \\ -|\mathbf{m}_{01}| & 0 & m_2 \end{pmatrix}.$$

Overall, the rotation of the local coordinate system $\hat{\mathbf{X}}_a$ around the origin of the reference coordinates $\mathbf{X}$ to the position $\mathbf{Q}_i\mathbf{m}_i = (0, 0, (Qm)_2)^T$ is given by

$$\mathbf{Q}_i = \mathbf{Q}_{i,X_1}\mathbf{Q}_{i,X_2}.$$

This result is the analogon to the two-dimensional rotation matrix such that we can proceed to the formulation of the general active deformation tensor prescribing apical/basal constriction.

Therefor, we use the notation for the discontinuous, globally defined rotation $\mathbf{Q}$ and translation $\mathbf{m}$ defined in Eq. (A.6). Also, notice that an arbitrary tensor $\mathbf{A}$ given in $\hat{\mathbf{X}}$ transforms as $\mathbf{Q}^T\mathbf{A}\mathbf{Q}$ into a rotated system $\mathbf{X}$, see the tensorial transformation law in Section 1.5 in Holzapfel [66]. Then, the active deformation tensor $\mathbf{F}_a(\mathbf{X}, C)$ in the reference configuration can be expressed by rotating $\hat{\mathbf{F}}_a$ such that the orientation of the local coordinate system $\hat{\mathbf{X}}$ coincides with the orientation of $\mathbf{X}$. Finally, the active deformation gradient acts in the desired way if its rotated argument $\mathbf{QX}$ is also translated by $\mathbf{Qm}$. It reads

$$\mathbf{F}_a(\mathbf{X}, c) = \mathbf{Q}^T\hat{\mathbf{F}}_a(\mathbf{QX} - \mathbf{Qm}, C)\mathbf{Q}. \tag{A.8}$$

An illustration of these transformations is given in Fig. A.2.

Notably, we have assumed that every biological cell constricts in the same manner, i.e. $\hat{\mathbf{F}}_a$ remains identical for each cell K_i, whereas the rotation matrix $\mathbf{Q}$ and the translation vector $\mathbf{m}$ depend on the biological cell under consideration. In particular, $\mathbf{F}_a$ is a piecewise-defined tensor that maps the biological cells $K_i \subset \Omega$ to their actively deformed counterparts $K_{i,a} \subset \Omega_a(t)$. Whereas the local inverse $\mathbf{F}^{-1}_{a,K_{a,i}}$ is always well-defined, its global representation $\mathbf{F}_a^{-1}$ is not a function, since there might be gaps or superpositions in the intermediate configuration (see again Subsection 2.2.2). Overall, this results in a semi-discrete coupled system of model equations (5.4), which was entirely continuous up to this point. Mathematically, this system has to be understood as being continuously defined on each biological cell.

Indeed, this specific choice of $\hat{\mathbf{F}}_a$ and thus $\mathbf{F}_a$ (since $\det(\mathbf{Q}) = 1$) is volume-preserving. For the volume $\hat{V}_{i,a}$ deformed by $\hat{\mathbf{F}}_a$ and the initial volume $\hat{V}_i$ of any biological cells K_i it holds

$$\begin{aligned}\hat{V}_{i,a} &= \int_{K_{i,a}} \mathrm{d}\hat{X}_1\mathrm{d}\hat{X}_0 = \int_{K_i} |\det(\hat{\mathbf{F}}_a)|\mathrm{d}\hat{X}_1\mathrm{d}\hat{X}_0 \\ &= \int_{K_i} (1 + kC\hat{X}_1)\mathrm{d}\hat{X}_1\mathrm{d}\hat{X}_0 = \hat{V}_i + kC\int_{K_i} \hat{X}_1\mathrm{d}\hat{X}_1\mathrm{d}\hat{X}_0 = \hat{V}_i,\end{aligned}$$

where the last integral vanishes since the centroid of the biological cell under consideration was transformed to the origin. Consequently, integration over X_1 cancels out. In the three-dimensional case, we follow the same line of argument and transform the integrals by

$$\begin{aligned}\hat{V}_{i,a} &= \int_{K_{i,a}} \mathrm{d}\hat{X}_2\mathrm{d}\hat{X}_1\mathrm{d}\hat{X}_0 = \int_{K_i} |\det(\hat{\mathbf{F}}_a)|\mathrm{d}\hat{X}_2\mathrm{d}\hat{X}_1\mathrm{d}\hat{X}_0 \\ &= \int_{K_i} (1 + kC\hat{X}_2)^2\mathrm{d}\hat{X}_2\mathrm{d}\hat{X}_1\mathrm{d}\hat{X}_0 = \hat{V}_i + kC\int_{K_i} \hat{X}_2(2 + kc\hat{X}_2)\mathrm{d}\hat{X}_2\mathrm{d}\hat{X}_1\mathrm{d}\hat{X}_0 = \hat{V}_i,\end{aligned}$$

where the last integral vanishes since the centroid of K_i has been transformed to the origin and integration with respect to $\hat{X}_1$ and $\hat{X}_0$ cancels out.

A.2 Further results on the robustness of mechanochemical pattern formation

In this section, we present additional results on the robustness of our numerical simulations. These results are vital as they confirm the robustness of our prototypical system to produce mechanochemical patters, e.g. if the initial conditions or diffusion rates are changed. Yet, we postponed these results to the appendix for the sake of a readable presentation of our numerical results in Subsection 5.3.4. In the following, we give a short overview of these findings.

Firstly, we show that we obtain approximately the same number and size of mechanochemical patterns regardless weather a single morphogen spot or uniformly distributed random concentrations for each biological cell are used as initial conditions, compare Fig. A.3 and Fig. 5.9 (of the main manuscript). Secondly, in the case of apical constriction, the gastrulation event also seems to be insensitive to the initial conditions (cf. Fig. A.4 and Fig. 5.10 (of the main manuscript)).

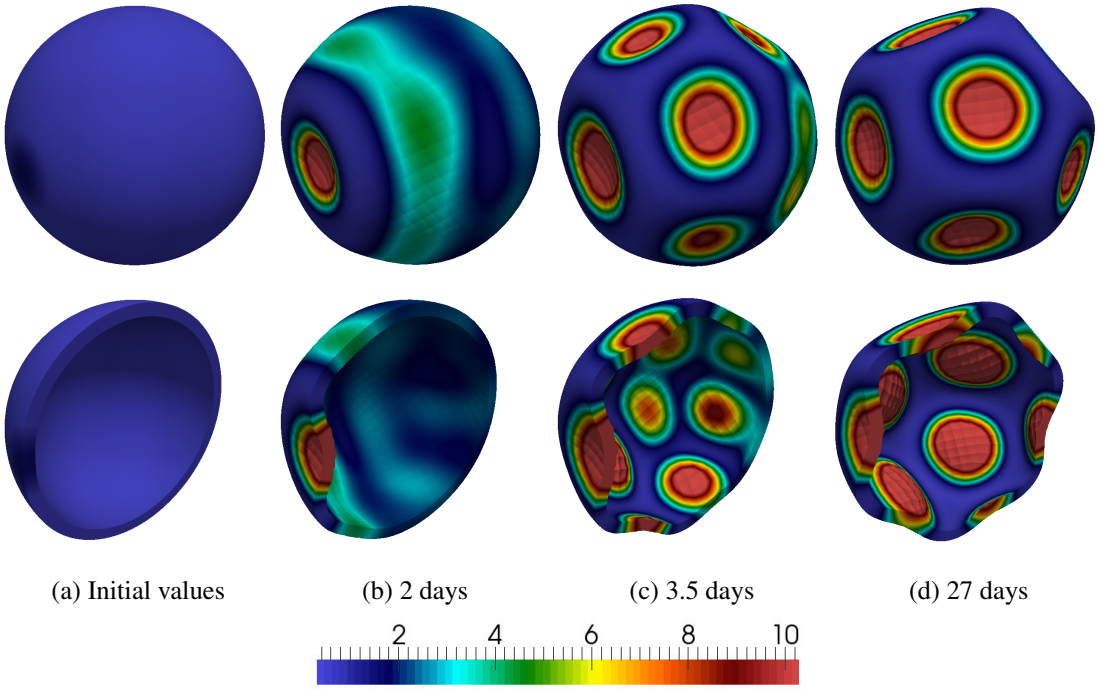

(a) Initial values (b) 2 days (c) 3.5 days (d) 27 days

Figure A.3: Simulation snapshot showing spontaneous pattern formation for the stretch-mediated feedback loop including basal constriction. Morphogen is initially distributed within a spot at one side of the sphere. The tissue sphere has been sliced for the sole purpose of a better visualization.

Finally, we observe that quartering the lateral diffusion for the stretch-mediated feedback loop based on basal constriction still leads to patterns (cf. Fig. A.5) with slightly more and smaller curvature/morphogen patches in the final, stationary result. In particular, diffusion seems to speed up the initial development of patterns which leads to larger patterns on the one hand but also results in a longer consolidation process (of stronger patterns dissolving weaker ones). Overall, both developments take similar time to reach a stationary state, compare Fig. 5.9 from the main part of the thesis with Fig. A.5. Overall, we find that smaller lateral diffusion and thinner domains as well as lower morphogen production result in more patterns; larger diffusion, thicker domains and higher morphogen levels lead, in contrast, to fewer and larger patterns.

Ultimately, we want to interest the reader in the complexity of our research: One might wonder why some tenor invariants are suitable as mechanical feedback and why some, such as tr($\mathbf{F}$) or det($\mathbf{E}$) are not. The main reason is that feedback based on the latter invariants leads to morphogen production around (and not only within) the range of the current patterns. In extensive numerical tests (usually in 2D first) including these tensor invariants, we observed that localized initial patterns expand and merge until an equilibrium of constant deformation and morphogen concentrations in the entire domain is reached. On the other hand, any feedback that was suitable

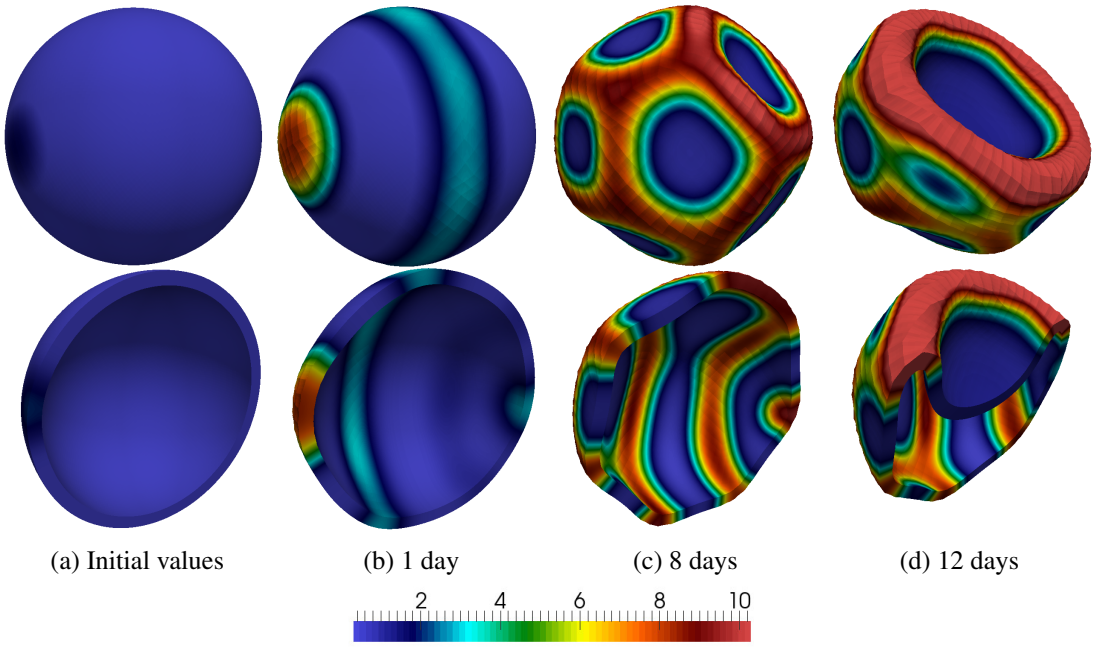

(a) Initial values (b) 1 day (c) 8 days (d) 12 days

Figure A.4: Simulation snapshot that show spontaneous pattern formation for the stretch-mediated feedback loop including apical constriction. Morphogen is initially distributed within a spot at one side of the sphere.

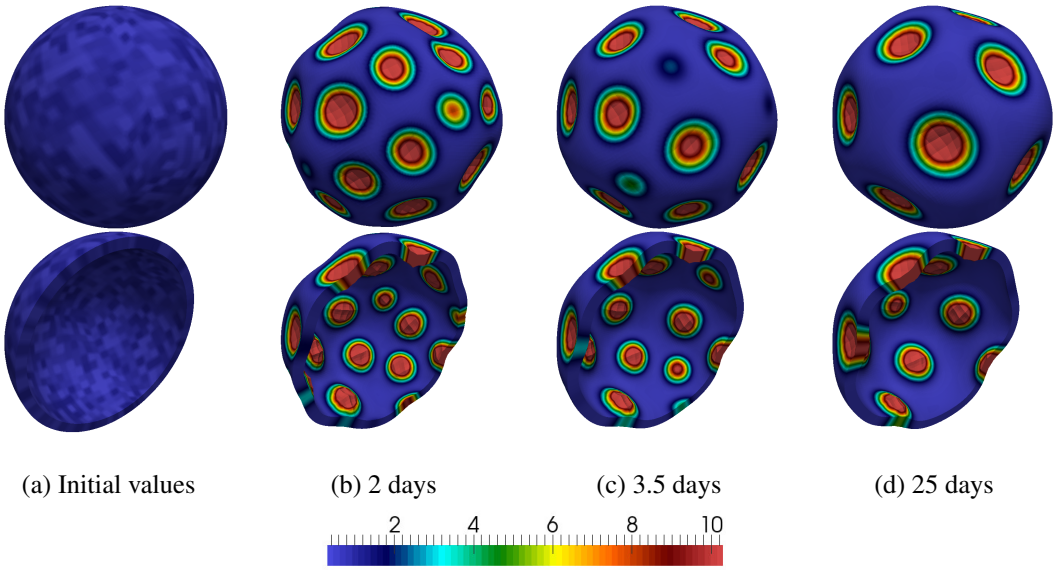

(a) Initial values (b) 2 days (c) 3.5 days (d) 25 days

Figure A.5: Simulation snapshots that show spontaneous pattern formation for the stretch-mediated feedback loop including basal constriction with quartered tangential diffusion rate. The sphere has been sliced for the sole purpose of a better visualization.

in 2D interestingly also lead to stable mechanochemical patterns in the corresponding simulation in 3D.

A.3 Numerical results and discussion in 2D

In this thesis, we have developed a unified approach where one prototypical model of PDEs is suitable for simulations on the full 3D geometry, 2D cross-sections or other simplifications. The main reason is the vast numerical effort to perform simulations in the full 3D configuration. In this approach, it is fairly simple to find and test suitable feedback loops, parameters and geometries in a 2D setting first and to subsequently leverage these models to the full 3D scope. Nonetheless, our numerical simulations clearly show that the full 3D geometry is vital to obtain realistic numerical results such as gastrulation events, as discussed in Chapter 5. Further, we will see in the following that other numerical observations in 2D do not in general translate to the three-dimensional regime, most importantly the influence of diffusion.

We have included the following results in 2D for the sake of completion and a comparison of our findings to an enhanced model (cf. Subsection 5.3.6), where we integrate the mechanical feedback over the biological cells.

We point out that we have already published some of the following computational results in 2D Mercker *et al.* [103]. In particular, this applies to Fig. A.6 and Fig. A.7 and the corresponding discussions. In contrast to the results in Mercker *et al.* [103], new calculations with different diffusion rates in radial and tangential direction (analog to the 3D settings) were performed. Also, we corrected an error in the transformations of our model equations from the Eulerian to the reference coordinate system made in the derivation of our model equations and in the numerical simulations in Mercker *et al.* [103]. We point out this error did not impact that the quality or correctness of the results in this publication. Finally, we extended the discussion on the robustness of our approach (in 2D) and contrasted these results with our more recent findings in the three-dimensional regime.

In this section, we present and discuss our numerical results for our mechanochemical feedback loops leading to mechanochemical pattern formation. These feedback loops are based on a single morphogen species that locally leads to apical/basal constriction in combination with strain-, stress- and stretch-based mechanical feedback. These are commonly observed combinations which were discussed in Section 2.3.

In Fig. A.6 we present simulation snapshots for the stretch-mediated feedback loop including basal constriction (first row) and the strain-mediated one including apical constriction (second row). We prescribed uniformly distributed, random morphogen concentrations for each biological cell. For both feedback loops, we obtain stationary solutions of co-localized morphogen/curvature patterns after two days, see the deformed elliptic tissue in Fig. A.6 (d) or the peanut-shaped result in Fig. A.6 (i). In both stationary results, the actively deformed parts are towards the top left and the bottom right of the simulation snapshot but basal constriction seems to produce softer but larger curvature patterns compared to apical constriction.

Also here, *de novo* pattern formation seems to be very robust with regard to the initial conditions analog to our results in 3D. On 2D cross-sections, identical symmetric patterns are also ob-

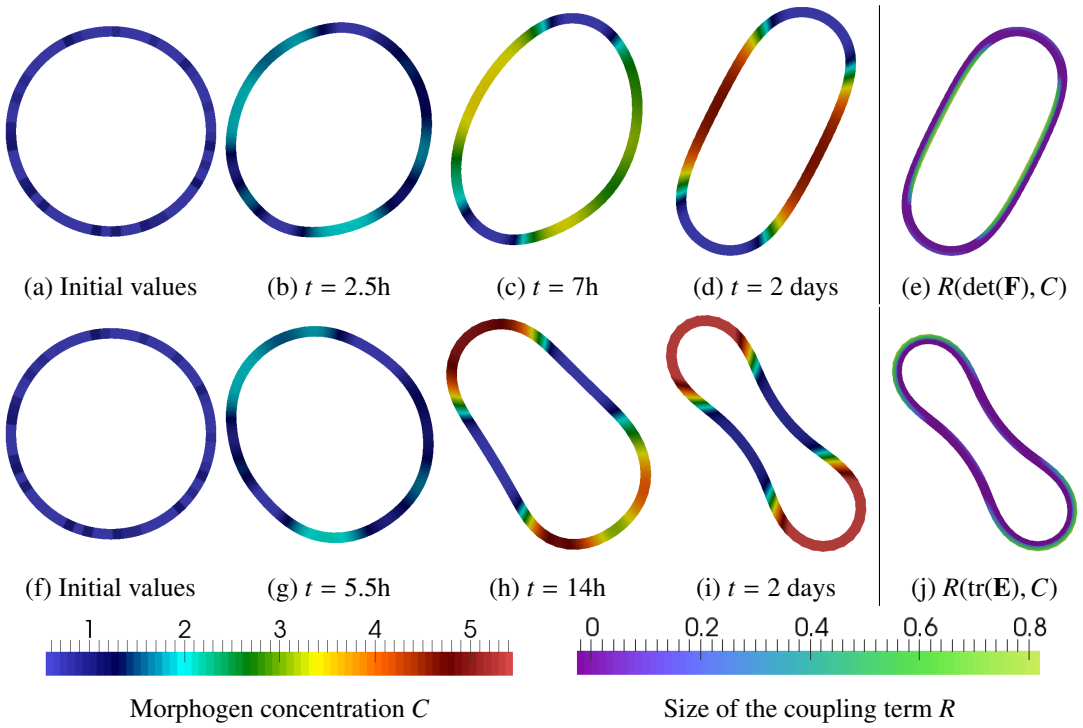

Figure A.6: Simulation snapshots showing spontaneous pattern formation. (a)-(e): Stretch-mediated feedback loop with basal constriction. (f)-(j): Strain-mediated feedback loop with apical constriction. As initial conditions, we prescribe uniformly distributed random morphogen concentrations for each biological cell.

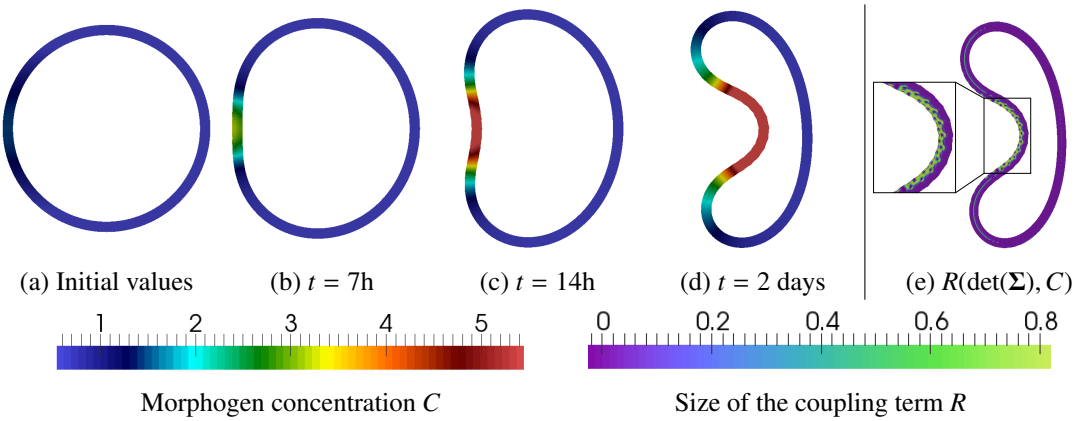

Figure A.7: Simulation snapshots showing pattern formation based on the stress-mediated feedback loop with basal constriction. Initially, morphogen is distributed with a spot at one side of the sphere.

served when we start with a single, initial morphogen gradient. Correspondingly, self-organized pattern formation from dissociated and re-arranged cells (e.g. *Hydra* aggregates) is observed in an increasing number of biological systems [19, 45, 67, 75, 150] but may also align with a predetermined gradient, e.g. in *Drosophila* [72].

In Fig. A.7, simulation snapshots for the stress-mediated feedback loop including basal constriction are shown. Here, we observe a single invagination which resembles gastrulation events during embryogenesis. Although the stress-mediated feedback loop seems like a suitable candidate leading to gastrulation events from a 2D perspective, we point out that this results is only obtained if a single morphogen spot at one side of the tissue sphere is initially prescribed. Any morphogen that is initially distribution on the side opposing the invagination will once again result in a symmetric and peanut-shaped deformation as in Fig. A.6 (i). Further, the solution in Fig. A.7 (d) represents a stationary result for a small parameter range only. In addition to our previous publication Mercker *et al.* [103], we hence propose an internal volume constraint which accounts for the fluid contained inside the tissue sphere. Not only does this internal pressure reliably stop the invagination process, but also we saw that it facilitates stable stationary solutions over a wide parameter range (cf. Subsection 5.3.5 for a discussion of these results).

If, in contrast, the full 3D geometry is considered, saddle points with negative Gaussian curvature promote single invaginations whereas the geometry of the remaining tissue remains more robust with regard to a second invagination as discussed in Subsection 5.3.4. Here, gastrulation was also observed for a stretch-mediated feedback loop. Again, this stresses the importance of considering the full 3D representation of the biological tissue. Apparently, the tissue, which takes the role of long range inhibition, cannot prevent the establishment of a second pattern on the opposing side of the 2D tissue section - at least for the given tissue geometry. The robustness of our approach with regard to the model geometry, initial conditions or parameters are discussed in the following.

A.3.1 Robustness

In the following, we further investigate the robustness of our approach with regard to the diffusion rates, the model geometry, the system size and the (material) parameters. In comparison to our publication Mercker *et al.* [103], we considered different diffusion rates in tangential and radial direction and new simulations to view the results from a 2D setting in the light of our 3D experiences. In comparison to the results that were already published, the interplay between diffusion, stiffness and the number of biological cells was further investigated.

The presented approach is robust with regard to changes in the parameters and we generally observe stable patterns over large parameter ranges, i.e. bisecting the diffusion rate does not change the number of patterns.

In Fig. A.8 we present simulation snapshots for the stretch-mediated feedback loop including basal constriction. In this numerical setup, we prescribe only one-tenth of the tangential diffusion rate compared to the simulations for the standard setup shown Fig. A.6 (a)-(d). In Fig. A.8 (a), simulations were performed on the standard model geometry. Here, we observe a stationary solution after about six days with an increased number of (seven) patterns due to the reduced

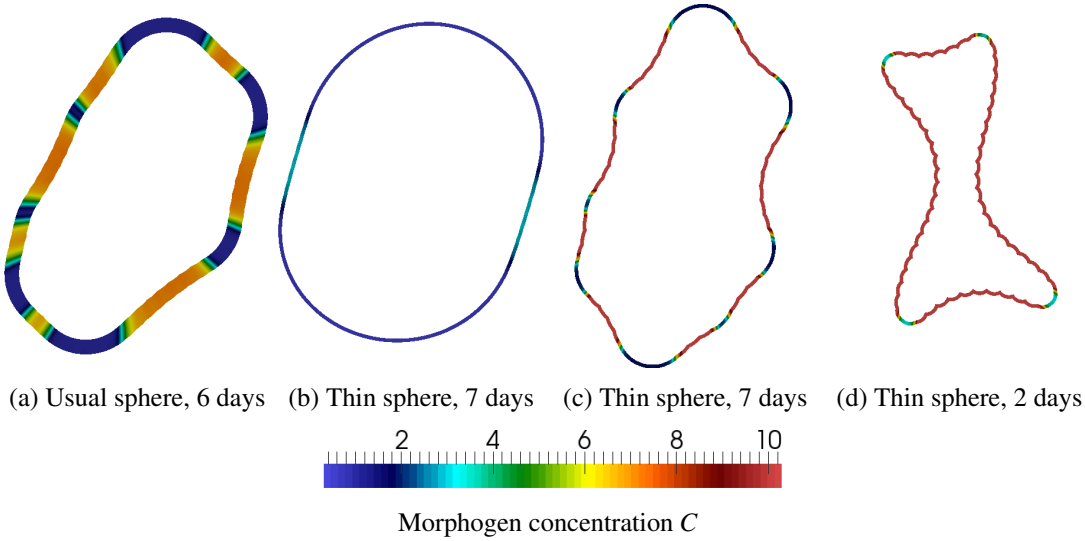

(a) Usual sphere, 6 days (b) Thin sphere, 7 days (c) Thin sphere, 7 days (d) Thin sphere, 2 days

Figure A.8: Simulation snapshots investigating the robustness of pattern formation for the stretch-mediated feedback loop including basal constriction for one-tenth of the tangential diffusion rate. (c)-(d) For larger and even further increased morphogen production rate.

diffusion rate. In the second snapshot Fig. A.8 (b), all parameters were kept the same but the tissue thickness was quartered which results in only two co-localized morphogen/curvature patterns. Presumably, a comparably smaller part of the tissue is stretched such that morphogen production is reduced and only two patterns on opposing sides prevail due to mechanically-transmitted long-range inhibition. Besides, we increased the morphogen production rate: We obtain a stationary solution of eight morphogen patches which strongly resembles the final result on the usual domain for less morphogen production, compare Fig. A.8 (c) and (a). Further, in Fig. A.8 (d), even larger morphogen production leads to large deformations, such that strong morphogen/curvature patches dominate the pattern formation process. These strong patterns suppress weaker ones via the passively bending material (long-range inhibition) and reduce the number of patterns once again. Note that in Fig. A.8 (d), we observe a sawlike structure of the tissue sphere due to the actively constricting individual biological cells.

Further, we summarize that large diffusion and morphogen degradation as well as stronger patterns due to increased morphogen production reduces the overall number of mechanochemical patterns. This process cannot be continued at will and large diffusion rates eventually blur any patterns. Notably, pattern formation seems to be less sensitive to changes in the geometry or the diffusion rates if the whole 3D tissue geometry is considered (compare with our discussion in Subsection 5.3.4).

Finally, the number of morphogen/curvature patches does not depend on the number of biological cells, which can be cut in half, doubled or quadrupled (results not shown). Additionally, the choice of the material parameters does not significantly alter the results as argued in Subsection 5.3.3. Yet, despite all discussed modifications and numerical simulations, symmetry

breaking or gastrulation events could not be observed in a 2D setting.

In summary, the observed robustness of pattern formation with regard to changes in the model geometry, the initial conditions or the parameters on 2D cross-sections of the tissue sphere essentially translates to the three dimensional regime. Interestingly, we observe at least two morphogen/curvature patterns in two dimensions (the stress-mediated feedback loop with one initial morphogen spot being the only exception). Overall, this robustness study hence underlined the importance of considering the full 3D nature of the tissue sphere to observe realistic mechanochemical patterns such as gastrulation.